A Numerical and Experimental Investigation into Multi-Ionic Reactive Transport Behaviour in Cementitious Materials

Brubeck Lee Freeman

Thesis submitted in candidature for the degree of Doctor of Philosophy at Cardiff University

2017

Acknowledgements

The research presented in this thesis would not have been possible without the financial support of Cardiff University School of Engineering and the EPSRC, this is gratefully acknowledged.

Firstly I would like to thank my supervisors, Tony Jefferson and Peter Cleall, for providing me with this opportunity and for your continuous help and guidance throughout the PhD. In particular I would like to thank you for your understanding, support and encouragement during the difficult times, without which I feel certain that I would not have made it to this point.

I would also like to thank my colleagues in offices W1.31 and W1.32, Stefani, Tom, Waled, Rob, Martins, Chuansan, Monica, Toby, Olly, Adriana and Tharmesh for their help and advice and for creating an enjoyable work environment.

In addition, I would like to thank the laboratory technical staff, Carl Wadsworth and Jack Morgan for their assistance and guidance with the ion transport experiments.

I would like to thank my friends and family for all of their support and encouragement throughout. I would particularly like to thank my wife Mitra, my mother and my mother-in-law for their support and encouragement during the most difficult moments.

Finally I would like to specially thank all of my family, my mother, Kenny, my granddad, my brothers and sisters and all of my in-laws for being amazing and for always being there for me no matter what and Mitra for being the best partner I could have wished for.

Declaration

This work has not been submitted in substance for any other degree or award at this or any other university or place of learning, nor is being submitted concurrently in candidature for any degree or other award

Signed …… (candidate) Date ……

STATEMENT 1

This thesis is being submitted in partial fulfillment of the requirements for the degree of PhD

Signed …… (candidate) Date ……

STATEMENT 2

This thesis is the result of my own independent work/investigation, except where otherwise stated, and the thesis has not been edited by a third party beyond what is permitted by Cardiff University's Policy on the Use of Third Party Editors by Research Degree Students. Other sources are acknowledged by explicit references. The views expressed are my own.

Signed …… (candidate) Date ……

STATEMENT 3

I hereby give consent for my thesis, if accepted, to be available online in the University's Open Access repository and for inter-library loan, and for the title and summary to be made available to outside organisations.

Signed …….. (candidate) Date ……

Table of Contents

Summary

This thesis describes a FE approach to the simulation of reactive transport problems and a simple experimental procedure for the determination of transport parameters in cementitious materials.

A comprehensive fully coupled reactive-thermo-hygro-chemical model was developed based on the governing equations of mass and enthalpy balance. The model takes into consideration advective-dispersive transport of solutes, heat flow, advective-diffusive moisture flow, and chemical reactions. The FEM, Euler backward difference scheme and Newton-Raphson iteration procedure were employed to solve the system of nonlinear equations. To address the numerical challenge associated with such coupled simulations, three problem reduction schemes were proposed, each of which uses a reduced set of species, termed 'indicators', for full computation. The response of the remaining species is computed at each time step from the transport of the indicators. The difference between the schemes lies in the number of indicator species used and in the method employed for calculating the transport of the remaining species.

Firstly the development of the experimental procedure is presented including the design of a porous concrete mix, a discussion of the problems encountered and the results of an advective-diffusive case. Following this, the model is validated and verified against a number of problems, beginning with a moisture transport problem and ending with a multi-ionic reactive transport problem. It was found that the model was able to accurately capture the transport behaviour. The range of applicability of each of the reduction schemes is then investigated through an example problem concerning the reactive transport of 16 chemical species, before verifying each of the schemes against the full model through the consideration of three example problems. The reduction schemes were found to perform well in accurately capturing the transport behaviour whilst greatly reducing the number of coupled equations to be solved, and the computational cost of the simulation.

Nomenclature

Symbols

$a_{1\text{-}5}$, a_c	Material parameters
$A_{1\text{-}3}$, A_k, A_v, A_w, A_λ	Material parameters
A^ϕ	Debye-Hückel parameter
A', A'_2	Reaction parameter
act_i	Solution activity
b, $b_{1\text{-}5}$	Material parameters
b_p	Universal parameter
B_v	Material parameter
B_{ma}, B_{mx}, B'_{ca}, B^ϕ_{mx}	Virial coefficients
c_i	Concentration of species i
C	Global secant matrix
C_i	Specific heat of phase i
C_{ma}, C_{mx}, C^ϕ_{mx}	Virial coefficients
D_i^j	j diffusion/dispersion of type i
f_i	Global body force vector of phase i
f_s	Material parameter
$f(T)$, F^ϕ	Pitzer functions
F	Faraday's constant
g	Gravity vector
$g(x)$, $g'(x)$	Pitzer functions
H_c^j	Heat of reaction i
H_v	Heat of vaporisation
I	Ionic strength of solution
J_i^j	j flux of type i
k_a, k_d, k_{da}	Reaction rate parameters
k_t	Thermal conductivity
K	Global mass matrix
K_i	Permeability of type i
K^{eq}	Equilibrium constant of reaction
m_i^j	j mass of type i
M_i	Molecular mass of type i
$\boldsymbol{n}$	Unit normal vector
n_i	Porosity of type i
N	Shape function matrix
$ndof$	Number of degrees of freedom
$nelem$	Number of elements
nr	Number of reactions
ns	Number of species
P_i	Pressure of phase i
q_i	Flux of phase i
$q_{1\text{-}6}$	Pitzer parameters
R	Molar gas constant
S	Solution Supersaturation ratio
S_i	Degree of saturation of phase i

t	Time
T_{cc}	Total chloride content
T	Temperature
T_r	Reference temperature
v_i	Velocity of type i
v^i	Valence of type i
W	Weighting function
z_i	Charge of species i
Z	Charge function
α_1, α_2	Virial coefficient parameters
α_c	Boundary mass transfer coefficient
α_L, α_T	Longitudinal and transverse dispersivities
β_c	Boundary mass transfer coefficient
$\beta_{mx}^0, \beta_{mx}^1, \beta_{mx}^2$	Virial coefficient parameters
γ_c	Boundary mass transfer coefficient
γ_m, γ_x	Activity coefficient of an anion and cation
Γ	Problem boundary
δ_{ij}	Kronecker delta
ε	Dielectric permittivity
λ	Order of reaction
μ_i	Viscosity of phase i
ξ	Free surface energy
ρ	Charge density
ρ_i	Density of phase i
$\overline{\rho_i}$	Mass averaged density of phase i
$\overline{\rho C}$	Heat capacity
τ	Tortuosity
φ	Residual from approximation
ϕ	Osmotic coefficient
Φ	Vector of primary variables
ψ	Electric potential
Ω	Problem domain

Subscripts/Superscripts/Abbreviations

0	Initial
atm	Atmospheric
c	Cauchy
C	Capillary
d	Dispersive
da	Dry air
di	Dirichlet
$diff$	Diffusive
e	Element
env	Environment
es	Electrostatic double layer
g	Gas
ind	Indicator

ind,l	Lower indicator
ind,m	Middle indicator
ind,u	Upper indicator
i	Intrinsic
k	Iteration
m	Anion
mol	Molecular
mv	Moisture vapour
p	Precipitated/sorbed
PRS	Problem reduction scheme
q	Heat
r	Reference
rg	Relative gas
RH	Relative humidity
rw	Relative water
s	Solid
t	Time
qi	Boundary flux i
v	Vapour
vs	Vapour saturated
w	Water
x	Cation
Γ	Boundary

Chapter 1. Introduction

1.1 Background and Motivation for Research

The prediction of thermo, hygro, and chemical transport behaviour in porous materials is of great importance in a wide range of engineering applications. To this end, a large number of analytical and numerical transport models have been developed. Typically these are coupled models which consider the advective-dispersive transport of a solute, heat flow, the advective-diffusive moisture flow, and often mechanical behaviour of the medium. In addition to these flow and deformation processes, the solute can be considered as reactive or non-reactive, depending on the application.

These models have existed for a number of decades, with a number of reactive models having been developed in the 1970's and 80's (Rubin and James 1973; Valocchi et al. 1981; Rubin 1983; Lichtner 1985). The application of these models has varied considerably, with much of the previous work concentrating on geochemical problems such as modelling groundwater systems (Yeh and Tripathi 1991; Walter et al. 1994; Parkhurst and Wissmeier 2015), assessing the performance of engineered barriers (Gens et al. 2004; Cleall et al. 2007; Thomas et al. 2012), or attenuation of mine water tailings (Zhu et al. 1999; Bertocchi et al. 2006). The application of these models to cementitious materials has most often investigated the ingress of chloride ions (Song et al. 2008; Baroghel-Bouny et al. 2009; Koniorczyk and Gawin 2012), or calcium leaching (Kuhl et al. 2004; Gawin et al. 2009). However, recently these models have also been used for investigating self-healing concrete (Aliko-Benítez et al. 2015; Chitez and Jefferson 2016).

The problem with these types of models is that the computational demand can be very high, depending on the chemical system. Cleall et al. (2006) suggest that this is governed by the following three main aspects of a problem:

1. Domain size, which affects not only the memory storage required but also the computational cost of solving large sets of simultaneous equations.

2. Timescale, which affects the number of times that this set of simultaneous equations need to be solved, and which for geochemical problems can be many years, with a fine resolution required to accurately capture the behaviour.
3. Complexity of the analysis, which can be split into four factors:
    a. The number of variables (affecting memory storage requirements and the computational cost of solving large sets of simultaneous equations).
    b. Degree of coupling between the variables, i.e. if the chemicals are involved in many reactions with one another (affecting whether a fully coupled solution is required).
    c. Non-linearity of the system (affecting the number of times the set of simultaneous equations need to be solved in one time step).
    d. The number of processes considered.

An example of this high computational demand can be seen in the hypothetical Tokyo bay case study, modelled by Yamamoto et al. (2009; 2014). This case study was of the geological storage of CO_2 in a 60×70 km area centred in Tokyo Bay. The authors used an efficient parallel simulator TOUGH2-MP/ECO2N (Zhang et al. 2007) and ran the simulations on the Earth Simulator (ES) supercomputer which consists of a total of 5120 processors and 10 TB memory. The domain was discretised into 10 million grid cells, with 3 degrees of freedom per node for the multi-phase flow problem, leading to a total of 30 million degrees of freedom. The time period considered was 1000 years and the authors found that the simulations generally took 1-2 days.

The high computational demand is commonly dealt with in one of two ways in the literature. The first, termed 'operator splitting', separates the calculation of the transport and the chemical reactions in a time step, effectively decoupling the chemical transport equations from the reaction equations, with a number of models then iterating between the two. The chemical reaction equations, however, may still be coupled in this approach. In addition to this, the splitting of the calculations has been found to introduce mass balance errors for certain boundary conditions (Valocchi and Malmstead 1992) and the iterative methods may require a prohibitively small time step or large number of iterations to converge (Hoffmann et al. 2012). The second approach is to reformulate the system of equations, using the problem stoichiometry,

and introduce transformed variables. The aim is to decouple a number of the transport equations and eliminate some local (spatially invariant) equations. The amount of reduction that can be achieved is often limited by the problem chemistry (for example if there are a large number of kinetic reactions considered). Many also impose the assumption of equal diffusion coefficients for all species, which has been found to be inaccurate for certain chemical systems (Thomas et al. 2012). One of the aspects of this study is to consider the development of methods which allows a greater reduction of problem size, whilst also allowing for species dependent diffusion coefficients.

In order to predict the transport behaviour, these models rely on a number of parameters that need to be determined experimentally. These include the permeability and conductivity of the medium, the ion diffusion and dispersion coefficients, and the chemical reaction parameters, including the order and rate of the reactions. These issues have been investigated experimentally for soil leaching problems over a number of years (Robbins 1989; Wierenga and Van Genuchten 1989; Khan and Jury 1990; Krueger et al. 1998; Hartley et al. 2004; Liu et al. 2017). These experiments use columns, usually made from Perspex, which are filled with the soil. Chemical solutions are then added to the top of the column and their concentrations measured either throughout the length of the column or at the outflow location. An idealised depiction of a typical setup can be seen in Figure 1.1 (Robbins 1989), used in this case for the determination of longitudinal and transverse dispersion coefficients. The columns are filled with the soil, and a water flow of constant velocity applied. The tracer is then injected, either continuously or as a point injection, and its migration through the column measured with a probe. The dispersion coefficients are then determined from this data through application of the advective dispersive equation. A setup like this allows for different flow conditions and pressure heads, as well as the measurement of the concentration without removal of the soil sample.

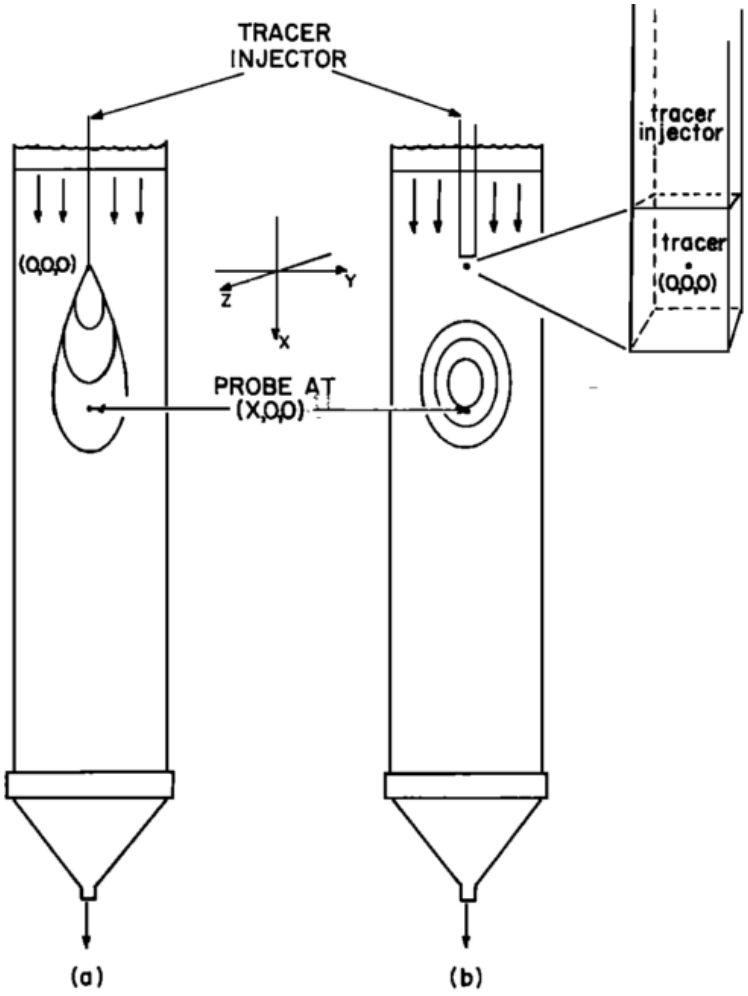

Figure 1.1 – Idealised column set up for a) Continuous injection and b) Point injection (after Robbins (1989))

A different experimental arrangement has been used for investigating transport processes in concrete specimens (Francy 1998; Baroghel-Bouny et al. 2007a; Song et al. 2014); a typical example of which can be seen in Figure 1.2 (Baroghel-Bouny et al. 2007a). This setup does not allow for the adjustment of the pressure head, limiting the range of flow conditions that can be investigated. In addition, the measurements taken require the removal and grinding down of the specimen prior to the analysis of the resultant dust, meaning that many specimens would be needed for the proper characterisation of transient behaviour.

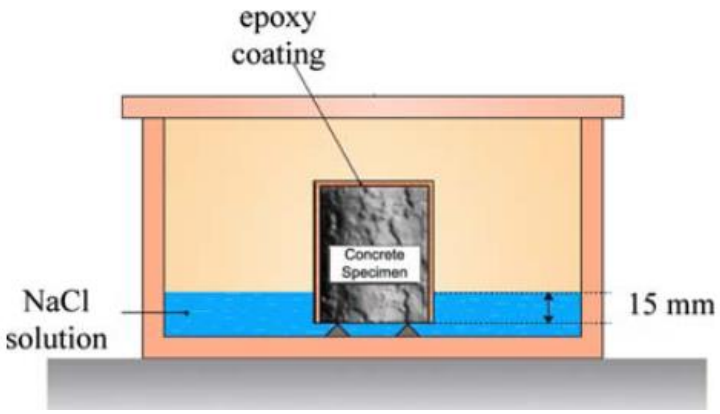

Figure 1.2 – Diffusion/wetting test setup (after Baroghel-Bouny et al. (2007))

Another aspect of this study is to consider the development of a simple ion transport experimental procedure for cementitious materials, which allows the application of different pressure heads, and allows the measurement of the concentration profile without the removal of the specimen, making it simpler to investigate the transient chemical behaviour.

1.2 General Aims, Objectives, Scope and Limitations

The work of this thesis had two main aims which are as follows:

1. Develop a numerical approach to enable problem size reduction that would reduce the computational demand associated with the simulation of reactive transport problems.
2. Develop an experimental test procedure for the investigation of transport behaviour in cementitious materials, which allows for different flow conditions and the measurement of transient behaviour, without requiring the removal of the specimen from the test setup.

These will be met by satisfaction of the following detailed objectives:

1. Develop a coupled model based on a reliable mathematical framework for the simulation of reactive transport problems in porous media.
2. Investigate the behaviour of the coupled model for different chemical systems, including different boundary conditions, a range of transport behaviour and various reactions to determine the validity of the model.

3. Propose a problem reduction scheme for use in complex multi-ionic systems in order to reduce the computational cost of the simulations.
4. Investigate the problem reduction scheme to determine the range of applicability of each of the approaches, before investigating the behaviour of the schemes for different chemical systems including different boundary conditions, a range of transport behaviour and various reactions to determine the validity of the approach.
5. Develop a simple alternative to column leaching tests for cementitious materials using lab scale concrete beams and carry out tests in order to determine different chemical parameters such as dispersion coefficients, as well as providing data for the validation of the proposed model.

The scope and limitations of this study are as follows:

1. It is assumed that the domain is isotropic.
2. The reactions considered throughout are kinetic, such that chemical equilibrium conditions are not assumed.
3. No investigation is made into temperature changes, including warming/cooling of the medium and the enthalpy change of chemical reactions.
4. Diffusion coefficients are considered to be constant irrespective of chemical concentrations and moisture content.
5. The chemical activity of the pore water is assumed to have no effect on the transport of ions or moisture.
6. Gas pressure changes are assumed to be negligible such that they are neglected in the model.
7. The chemical concentration is assumed to have no effect on the moisture retention characteristics of the medium.
8. The porous matrix is assumed to be rigid.

1.3 Outline of Thesis

This thesis is divided into 8 chapters and 1 appendix. Chapter 2 provides a review of the literature including an overview of the theory behind the physical processes and chemical reactions that are used for simulating the chemical behaviour in porous

media. A review of current models that have been developed by other authors is presented, with particular attention being directed towards current approaches to problem size reduction. Finally, a brief overview of current ion transport experimental procedures used for both soils and cementitious materials is given.

Chapter 3 details the theoretical formulations required for the development of a coupled transport model, including the description of chemical reactions and ion activity.

Chapter 4 details the numerical formulation and the application of the finite element method to the governing equations derived in Chapter 3. Both the spatial and temporal discretisation are discussed, as well as the iteration procedure employed to deal with the problem non-linearity. The chapter ends with the proposal and description of a series of problem reduction schemes.

The development of an experimental procedure for chemical transport in cementitious materials is presented in Chapter 5 beginning with a description of the methodology, and concluding with results and a description of the problems encountered during the investigation.

The verification and validation of the full coupled model is detailed in Chapter 6. The model is first verified against numerical results found in the literature, before being validated against drying experiments and the results of the experiments presented in the previous chapter.

In Chapter 7 the behaviour of the proposed problem reduction schemes will be investigated. This begins with an investigation into the range of validity of each of the methods through the consideration of a 16 ion reactive transport problem. Following this, each of the three reduction schemes are verified through comparison with the full model on the simulation of three example problems.

Finally, Chapter 8 gives the general conclusions of the thesis and provides suggestions for future research.

Chapter 2. Literature Review

2.1 Introduction

Transport models have been used for the prediction of chemical behaviour in porous media for a number of years. A great deal of research has been focused on geochemical problems; however, there is an increasing amount of work being done on construction materials such as masonry, mortar and cement (Gawin et al. 2006; Baroghel-Bouny et al. 2011; Koniorczyk 2012; Song et al. 2014; Chitez and Jefferson 2016). A key problem with these types of models, as recognised by a number of authors (Yeh and Tripathi 1989; Molins et al. 2004; Cleall et al. 2006; Hoffmann et al. 2012; Huo et al. 2014), is their large computational demand. This has been reported to be driven by the domain size, time period and complexity of the analysis including the number of chemical species and reactions (Cleall et al. 2006). This thesis proposes a coupled transport model for the simulation of chemical behaviour, and three problem reduction schemes for increasing the efficiency of their solution. To do this, the various physical phenomena involved in these types of problem need to be reviewed, along with the solution methods and approaches to the problem size reduction of previous authors.

Section 2.2 details the physical processes in porous media that need consideration. These include the advection and diffusion of the moisture phase, conduction and generation of heat, advection and dispersion of a solute and the chemical reactions considered (including the reaction rates and ion activity).

A review of existing numerical models developed for simulating the reactive transport in cementitious materials can be found in section 2.3. The reactions considered include the non-equilibrium sorption and precipitation of various chemicals, which is directly relevant to how chemical reactions are modelled within this thesis.

In section 2.4 a review of the different approaches to increasing the efficiency of transport models can be found. This section is split into two sections, (i) a review of models taking the operator splitting approach and (ii) a review of approaches that reformulate the global system of equations.

In section 2.5 a review of the existing approaches to the determination of transport parameters in porous media is presented.

Finally section 2.6 provides a summary of the findings and resulting conclusions.

2.2 Physical Processes in Porous Media

Transport models are transient in nature and consider the changes that the primary variables undergo with time within the system. The physical processes describe the mechanisms which cause this change, such as the conduction of heat through the sample -driven by temperature gradients- that change the temperature distribution. The primary variables commonly considered for transport models include the capillary pressure P_C(which is related to the degree of saturation S_w), the gas pressure P_g, the temperature T, the dissolved chemical concentration c and the displacement u. In this thesis, the mechanical behaviour of the system is not considered and, following the approach of Chitez and Jefferson (2016), it is assumed that the gas pressure remains constant. The physical processes reviewed here therefore are those which describe the degree of saturation, the temperature and the dissolved chemical concentration.

2.2.1 Moisture Transport

The mechanisms of moisture transfer in porous media can be split into two main parts, the advection of the liquid moisture phase and the diffusion of the moisture vapour.

2.2.1.1 Advection

The transport of the liquid moisture in porous media is driven by gradients in capillary potential, as first defined by Buckingham (1907). This capillary potential can be made up of a number of different potentials, as observed by Hillel (1980) and Nitao and Bear (1996) including matric, osmotic, gravitational and pressure. Richards (1931) asserted that the most common capillary potential is that of the pressure difference between the liquid moisture and air phases, caused by the surface tension of the meniscus. The advective flow of the capillary liquid can be modelled using Darcy's law which was extended to unsaturated conditions by Richards (1931) and has been used by a number of authors (Gawin et al. 2006; Cleall et al. 2007; Koniorczyk 2010; Baroghel-Bouny et al. 2011; Koniorczyk et al. 2015).

$$v_w = -K(\nabla \cdot \Psi + yg) \qquad (2.1)$$

where v_w is the liquid velocity, K is the conductivity or coefficient of permeability, y is the height above a datum, g is the acceleration due to gravity and Ψ is the capillary potential. It should be noted, however, that this equation describes the flow of the capillary liquid, which is the liquid that is not adsorbed to the solid matrix (Richards 1931). For liquid moisture coming into a dry medium, the initial liquid transport is driven by adhesive forces between the molecules until the solid is wetted, covering the solid in a thin film (pendular state); it is after this that liquid transport due to other forces can take place (funicular state). It can be said then that eq. (2.1) is only valid for moisture in the funicular state, and therefore there is no moisture transport below a particular value of saturation (which describes the adsorbed water content). In investigating heat and moisture transport at high temperature in cementitious materials, Davie et al. (2006) found that ignoring the adsorbed water content can have a significant effect on the prediction of moisture fluxes, vapour contents and gas pressures.

The coefficient of permeability in eq. (2.1) is dependent on a number of different variables including porosity, damage, degree of saturation and temperature and has a wide range of values for porous media ranging from 10^{-9} m^2 for clean sand (Bear and Verruijt 1987) to 10^{-21} m^2 (or lower) for cementitious materials (Baroghel-Bouny et al. 2011; Koniorczyk et al. 2015). The effective permeability therefore can be given by the multiple of the intrinsic permeability K_i (which is dependent on the medium) and the relative permeability K_{rw} as follows:

$$K = K_i K_{rw} \tag{2.2}$$

where the relative permeability takes into account the effects of the aforementioned variables. For the dependence of the relative permeability on the degree of saturation, there are two schools of thought (Mualem 1976), the first being that the relative permeability is a power function of the degree of saturation. An expression of this first type has been derived analytically by Irmay (1954), who found that a cubic function was appropriate. This approach has been adopted by a number of authors (Gawin et al. 1999; Cleall et al. 2007; Koniorczyk and Gawin 2011). The second group derive analytical expressions for the relative permeability based on the moisture retention

curve for a given medium. Examples of such approaches can be found in (Brooks and Corey 1964; Mualem 1976; van Genuchten 1980); which have also been used by a number of authors (Koniorczyk 2010; Baroghel-Bouny et al. 2011; Koniorczyk 2012).

The moisture vapour advection can also be described using the eq. (2.1); however, according to Chitez and Jefferson (2016), the gas pressure quickly reaches steady state and so therefore this is neglected.

2.2.1.2 Retention

It was mentioned in the previous section that the capillary potential (or capillary pressure) mainly arose as a result of the pressure difference between the liquid moisture and air phases. The magnitude of this pressure depends on both the surface tension and the curvature of the separating meniscus which in turn depends on the moisture content of the medium (Bear and Verruijt 1987). There is a relationship then between the capillary pressure and the moisture content of the medium, which is dependent on the pore structure of the medium (Richards 1931; Bear and Verruijt 1987; Baroghel-Bouny et al. 2011). In initial work undertaken by Buckingham (1907), measurements were made of the soil-moisture retention curves for various types of soil. In his classic paper, van Genuchten (1980) proposed an analytical relationship between the two, using just two fitting parameters to take into account different pore structures. This relationship is given by:

$$P_C = a\left(S_w^{-\frac{1}{m}} - 1\right)^{1-m} \qquad (2.3)$$

where P_C is the capillary pressure, S_w is the degree of liquid saturation and a and m are material parameters. Some authors have also included the effects of chemical concentration or temperature on this retention curve. For example, Koniorczyk and Wojciechowski (2009) used neural networks to model the influence of salt concentration on this retention curve and found that at high saturations (or high salt content) these effects can be significant. By contrast, Baroghel-Bouny et al. (2011) found that for the cement mortars, at the concentrations and degrees of hydration considered, these effects (temperature and chemical concentration) had a negligible influence on the retention curve parameters. For the temperature dependence, Cleall

(1998) describes an approach following work by Edlefsen and Anderson (1943) and Fredlund and Rahardjo (1993) in which the capillary pressure can be related to the free surface energy which is a function of temperature; stating that the relative change in free surface energy with temperature is equal to the relative change in capillary pressure.

2.2.1.3 Diffusion

The diffusion of moisture vapour within a porous medium is caused by molecular diffusion and as such is assumed to be governed by Fick's law (Philip and De Vries 1957; Gawin et al. 2006):

$$J_v = -D_m \nabla \cdot \rho_v \qquad (2.4)$$

where J_v is the vapour flux, D_m is the moisture vapour diffusivity and ρ_v is the density of the moisture vapour phase. Tie-hang and Li-jun (2009) state that the transfer of moisture vapour is driven by both capillary pressure and temperature gradients. The effect of temperature gradients was discussed in detail in the classic paper by Philip and De Vries (1957) who also noted that, at low moisture contents, transport via diffusion was dominant. Gawin et al. (1999) reports that, like the permeability, the vapour diffusion through a porous medium is also dependent on the properties of that medium; including the porosity, degree of saturation and tortuosity (Knudsen effect).

2.2.2 Heat Flow

2.2.2.1 Conduction

The behaviour of heat transport in porous media has been subject to a great deal of investigation. These investigations range from heat loss from ground source heat transfer (Rees et al. 2000) to the heat of hydration of cementitious materials (De Schutter and Taerwe 1995). Gawin et al. (2011a; 2011b) studied the effects of high temperature on concrete structures in order to determine the effect of the different heat phenomena, concluding that convective heat transfer could be ignored with little loss of model accuracy. The conduction of heat is assumed to follow Fourier's law and is given as (Gawin et al. 2006):

$$J_q = -k_t \nabla \cdot T \qquad (2.5)$$

where J_q is the heat flux, $k_t$is the thermal conductivity and T is the temperature. The thermal conductivity is reported to depend on the temperature, moisture content and porosity of the medium (Gawin et al. 1999).

2.2.2.2 Heat Generation

Another key consideration in the heat behaviour of a porous medium is the heat generation; this can be heat change from external sources or heat change due to chemical reactions. The heat change due to a chemical reaction is caused by the change in enthalpy in a system caused by the chemical reaction. For example, if we consider the formation of NaCl:

$$Na(s) + \frac{1}{2}Cl_2(g) \rightarrow NaCl(s), \quad \Delta H = -411.3\ kJ/mol \tag{2.6}$$

where ΔH is the enthalpy of the reaction and a negative value indicates that this is an exothermic reaction, meaning that heat is released. The effects of this enthalpy change has been included in the models of a number of authors (De Schutter and Taerwe 1995; Gawin et al. 2006; Gawin et al. 2009; Thomas et al. 2009; Koniorczyk 2010; Koniorczyk 2012). De Schutter and Taerwe (1995) considered the heat generated from the hydration reaction of Portland cement and blast furnace slag cement; predicting the heat generation rate based on the temperature and degree of hydration. Koniorczyk (2010; 2012) included in his model the heat generated from precipitation of salt in cement mortar and bricks and suggested that integration of the temperature profiles compared with pure water profiles, could serve as an indication of the amount of precipitated salt within the system. The change in temperature caused by reactions can also induce pore water movement due to the temperature gradients; this was taken into account by Thomas et al. (2009), who considered the cryogenic suction caused by the interface between ice and water in permafrost and frozen soils.

2.2.3 Ion Transport

The transport of chemical ions in pore water is split into two parts, the advection caused by the movement of the pore water and the hydrodynamic dispersion which accounts for the movement of ions within the pore water.

2.2.3.1 Advection

The advection of dissolved chemical ions is due to the pore water velocity and therefore the physical processes that govern this behaviour have been described in section 2.2.1.1. There are, however, some differences which may arise as a result of the presence of the ions. The most widely considered is the effect of the chemical concentration on the viscosity of the pore liquid which has been included in the models of a number of authors (Koniorczyk and Wojciechowski 2009; Baroghel-Bouny et al. 2011). Some authors take things further and include the flow of pore water due to chemical concentration gradients, known as osmotic flow (Cleall et al. 2007).

2.2.3.2 Hydrodynamic Dispersion

The next key transport process of dissolved chemical ions is the hydrodynamic dispersion. This is considered in two key ways, the first is a multi-species model which takes into account the differential molecular diffusion coefficients of each species allowing for different rates of transport for each ion (Samson and Marchand 2007; Baroghel-Bouny et al. 2011; Song et al. 2014). The second assumes that all species have the same diffusion coefficient and so the rate of transport is equal for all ions (Zhu et al. 1999; Cleall et al. 2007; Hoffmann et al. 2012). The justification for the second approach is that in the system under consideration the molecular diffusion coefficient is small in comparison to the mechanical dispersion (Zhu et al. 1999; Kräutle and Knabner 2007; Hoffmann et al. 2012). The hydrodynamic dispersion is composed of two different phenomena, the molecular diffusion, which is the spreading of the ions due to their random movement in the pore water and the mechanical dispersion (Bear and Verruijt 1987). The mechanical dispersion is the spreading of the ions due to the pore water flow; this is split into two parts, the spreading of the pore water as it flows around solid particles, and the spreading due to the velocity distribution within the pores. The effects of these phenomena can be seen in Figure 2.1.

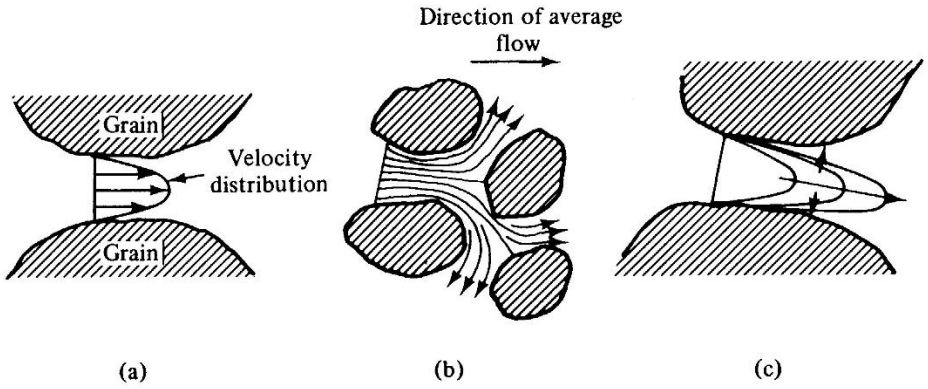

Figure 2.1 – Dispersion mechanisms, a) and b) show the mechanical dispersion and c) shows the molecular diffusion (after Bear and Verruijt (1987))

The effects of these phenomena however can be described by a single coefficient known has the coefficient of hydrodynamic dispersion and can be described using Fick's law and is given as (Bear and Bachmat 1990):

$$D_d = (\alpha_T|v_w| + nS_w D_{mol})\delta_{ij} + (\alpha_L - \alpha_T)\frac{v_w^i v_w^j}{|v_w|},\ \delta_{ij} = \begin{cases} 1\ if\ i = j \\ 0\ if\ i \neq j \end{cases} \qquad (2.7)$$

where D_d is the dispersion coefficient, D_{mol} is the molecular diffusion coefficient, n is the porosity, δ_{ij} is the kronecker delta and α_L and α_T represent the longitudinal and transverse dispersivities respectively.

2.2.3.3 Charge Neutrality

The problem of the first approach mentioned previously is that the charge of the solution could become unbalanced if all of the ions dispersed at different rates. Lasaga (1981) states that the movement of the ions is not independent as Coulomb forces act between all pairs of ions and the diffusion of the ions creates an electric potential ψ which balances their flux (Song et al. 2014). The description of flux can be given by the Nernst Planck equation (eq. 2.8) and the electrical potential can be given by Poisson's equation (eq. 2.9):

$$J_{diff}^i = -nS_w\rho_w D_{mol}^i \left(\nabla \cdot c_i \pm c_i \frac{z_i F}{RT}\nabla \cdot \psi\right) \qquad (2.8)$$

$$\varepsilon\nabla^2 \cdot \psi + F[\sum_{i=1}^{ns}(|z_{i+}|c_{i+} - |z_{i-}|c_{i-}) + \rho] = 0 \qquad (2.9)$$

where J^i_{diff} is the diffusive flux of an ion i, ρ_w is the liquid density, R is the molar gas constant, F is Faraday's constant, ns is the number of chemical species, ρ is the charge density and ε is the dielectric permittivity of the liquid phase. This approach has been included in the models of a number of authors (Samson and Marchand 2007; Baroghel-Bouny et al. 2011; Thomas et al. 2012; Song et al. 2014), most of whom substitute Poisson's equation into the Nernst Planck formula to eliminate ψ (Thomas et al. 2012; Song et al. 2014), while some solve for ψ as an additional primary variable (Samson and Marchand 2007; Baroghel-Bouny et al. 2011). In studies on ion transport in cementitious materials, Baroghel-Bouny et al. (2011) and Samson and Marchand (2007) also took into account the effect of chemical activity gradients on the diffusion, while others have considered the effect of temperature gradients, known as the Soret effect (Cleall et al. 2007; Thomas et al. 2012).

2.2.4 Chemical Reactions

The final key considerations of chemical behaviour in porous media are any chemical reactions which may occur. There are a great number of different chemical reactions that are of importance in porous media ranging from salt precipitation in bricks (Koniorczyk 2012), to the hydration reaction of cement (Chitez and Jefferson 2016), to the large number of geochemical reactions that are of great importance in contaminant transport and remediation problems (Walter et al. 1994; Zhu et al. 1999; Cleall et al. 2007; Yapparova et al. 2017).

2.2.4.1 Reaction Classes

The first step in modelling chemical reactions in porous media is determining the reaction type or class. The reaction classes considered in chemical models were proposed by Rubin in his classic paper (Rubin 1983), who stated that the nature of the chemical reaction will have a direct effect on the formulation of the ion transport problem. Rubin (1983) proposed a 3 level scheme to determine the reaction class and therefore the appropriate way of modelling it. This scheme leads to 6 different reaction classes and can be seen in Figure 2.2.

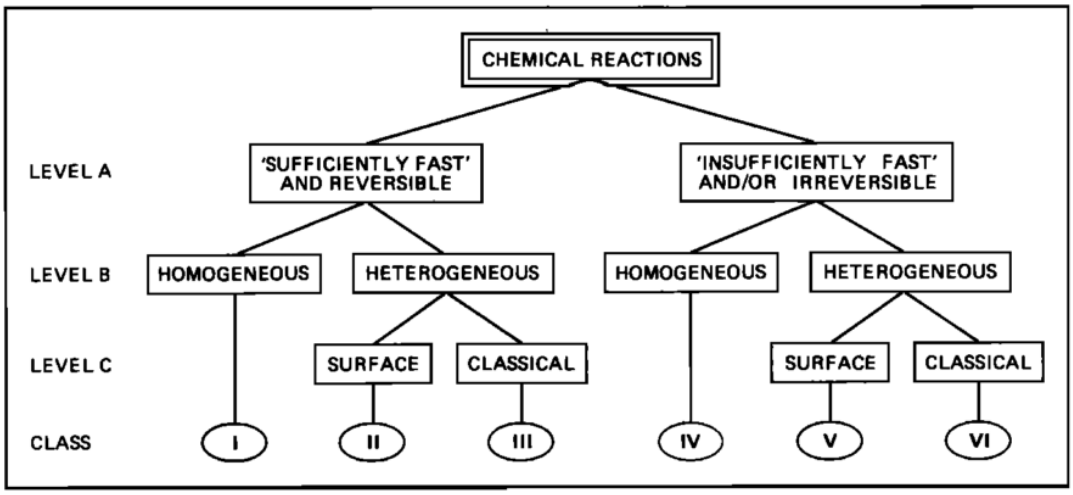

Figure 2.2 – Classification of chemical reactions (after Rubin (1983))

The first sub-level, level A divides the reactions into categories of 'sufficiently fast and reversible' and 'insufficiently fast and/or irreversible'. The first category describes reactions whose rates are faster than the transport of the ions, meaning that at all points the LEA (local equilibrium assumption) can be used and that those reactions are reversible. The second category therefore means that the reaction rates are not fast enough for this assumption to be made or simply that the reactions are irreversible. According the Rubin (1983), this distinction is pragmatic and often depends on the allowable error considered. In their paper, Walter et al. (1994) developed a transport model to be linked with the geochemical model MINTEQA2 (Allison et al. 1991), based on the equilibrium assumption. They found that this assumption allowed an efficient two-step solution to the problem and that accurate results were found when comparing the model predictions to field data from Valocchi et al. (1981), which considered the transport of 5 chemical species, 3 of which were involved in ion exchange reactions. In considering ion transport in cementitious materials, Baroghel-Bouny et al. (2011) found that if the chloride binding was considered under the local equilibrium assumption, the model greatly overestimated near surface chloride content and underestimated its penetration; but a non-equilibrium approach was found to give good agreement to experimental data. The second sub-level, level B, divides the reactions into either 'homogeneous' or 'heterogeneous'; meaning simply that the reaction either takes place within a single phase (for example an aqueous

complexation) or between two or more phases (for example salt precipitation). The final sub-level, level C, then divides the heterogeneous reactions into two types, 'surface' or 'classical', a surface reaction could involve adsorption onto the solid matrix or ion exchange, whereas a classical reaction could include precipitation/dissolution, complex formation or oxidation/reduction (Rubin 1983).

2.2.4.2 Ion Activity

An important consideration in the calculation of chemical reactions is the activity of the chemical species. The activity of a chemical is a measure of the chemical potential in non-ideal solutions. A non-ideal solution is a solution within which interactions between molecules have an effect on its chemical properties. In such systems the equilibrium constants (the ratio of products to reactants in equilibrium reactions) and reactions rates for non-equilibrium reactions depend then on the activity of the chemical species instead of their concentration. The activity coefficient is used as a measure of the deviation of the solution from the standard state (ideal solution) (Lewis et al. 1961). The deviation of a system from ideality depends upon the mole fraction. Figure 2.3 shows the fugacity plotted against pressure for both a perfect gas and a real gas (Lewis et al. 1961). It should be noted that this behaviour is analogous to a solute where the fugacity is equal to the activity and the dependence would be on mole fraction or molality instead of pressure (Lewis et al. 1961).

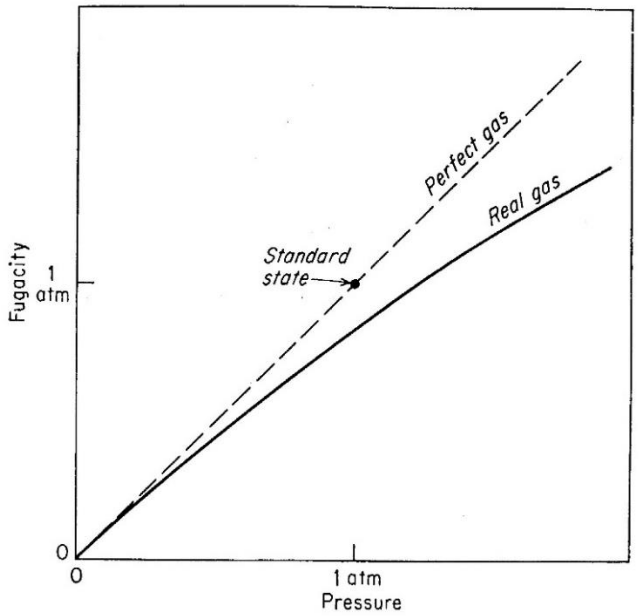

Figure 2.3 – Comparison of fugacity as a function of pressure for a perfect and real gas (after Lewis et al. (1961))

It can be seen then that the calculation of chemical activity can be of great importance for chemical reaction calculations. To this end, theories of electrolyte solutions have been proposed that seek to quantify the interactions between ions and hence the effect these will have on the ideality of the solution. The most commonly used are extended versions the Debye-Hückel theory such as the Davies equation (Allison et al. 1991; Samson and Marchand 2007b). Debye and Hückel (1923) assumed that the solution consisted of a dielectric medium where the ions interact according to Coulomb's law. The theory assumes that the effect of the charge on an ion can be calculated from a charge density given by Boltzmann's law, and a charge distribution described by Poisson's equation, where there is spherical symmetry around an ion. In solving these equations, a truncated Taylor series is used including only one term which corresponds to 1-1 electrolytes such as NaCl (Lewis et al. 1961). The extended Debye-Hückel law is given as (Koniorczyk 2012):

$$ln\gamma_{\pm} = \frac{-A|z_+ z_-|\sqrt{I}}{1+\sqrt{I}} \qquad (2.10)$$

where A is a constant which depends on the solvent, I is the ionic strength and $\gamma_{\pm}$ is the average activity coefficient. As a result of these assumptions, and the fact that short range interactions between ions are ignored, the Debye-Hückel theory is only valid for dilute solutions (Koniorczyk 2012) and therefore at higher concentrations a more comprehensive set of equations are needed. One such set of equations are the Pitzer equations (Pitzer 1973). The Pitzer equations are formed through the virial expansion of the Gibbs free energy of the solution, including a term representing the extended Debye-Hückel theory and higher order terms which account for short range interactions (Koniorczyk 2012). The simplified form of the Pitzer equation for calculating the activity for an ion i is given as (Pitzer 1973):

$$ln\gamma_i = \frac{z_i^2}{2} F^{\phi} + 2\sum_j \lambda_{ij} m_j + \frac{z_i^2}{2}\sum_{j.k} \lambda'_{jk}\, m_j m_k + 3\sum_{j,k} \mu_{ijk} m_j m_k \qquad (2.11)$$

where F^{ϕ} is a Debye-Hückel term, m are molalities and λ, λ' and μ are terms which represent the interactions between ions. The second order terms in the expansion represent all possible interactions between two ions, the third order terms representing all possible interactions between three ions and so on (Koniorczyk 2012).

For this reason, the Pitzer equations are valid for higher concentrations than the Debye-Hückel equations, with ranges of validity up to 6 M (Pitzer and Mayorga 1973) for some electrolytes in comparison to 0.1 M for the extended Debye-Hückel law (Koniorczyk 2012). In a study into salt transport in porous materials, Koniorczyk (2012) made a comparison of the average activity coefficients as predicted by the Debye-Hückel theories and the Pitzer equations to show the errors at higher concentrations. This can be seen in Figure 2.4.

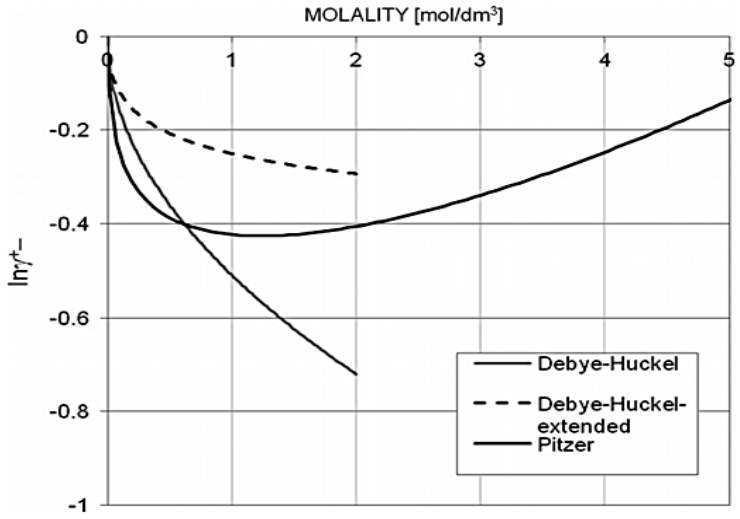

Figure 2.4 – Average activity coefficients as predicted by different electrolyte theories (after Koniorczyk (2012))

2.3 Coupled Models in Porous Media

The previous section dealt with the physical processes in porous media, the next step therefore is to review existing coupled models that have been developed based upon these processes.

In their 2011 paper Baroghel-Bouny et al. (2011) presented a coupled transport model for predicting moisture-ion transport in cementitious materials. The primary variables considered were the concentration of four chemical species, Na^+, OH^-, K^+ and Cl^-, the capillary pressure P_C, gas pressure P_g and the electrical potential ψ. The electrical potential was considered to describe the flux of the chemical species caused by the electrical interactions of ions; it is this flux that maintains the charge neutrality of the solution. The flux was described using the Nernst Planck equation and the Poisson

equation was used to describe the electrical potential. The ion activity was included in the model and its effect on the water/water vapour equilibrium was taken into account. The ion activities were calculated based on a combination of long range effects (Debye-Hückel and Davies equations) and short range (Pitzer equations). The concentration of the chemical species was assumed not to have any effect on the moisture retention curve based on the results of experimental adsorption data; their effect was, however, taken into account on both the viscosity of the fluid -via a Jones-Doyle type equation- and the fluid density. The permeability of the moisture phase was calculated using Mualem's model (Mualem 1976), as opposed to the analytical form derived by van Genuchten (van Genuchten 1980), as the former is valid for both adsorption and desorption, when the latter is valid for adsorption only. Following experimental results on desorption it was found that for moisture contents of $S_w<0.4$ the relative permeability greatly dropped and so liquid transport was assumed not to take place below this value. The reactions considered were of the chloride binding onto the C-S-H and the formation of Freidel's salt. These reactions were calculated with assumptions of both equilibrium and non-equilibrium conditions and compared to experimental data for the total chloride content. It was found that under the equilibrium assumption the model greatly over predicted the chloride content at the surface and under predicted its penetration into the mortar samples, the best results were found when the chloride binding was considered kinetically and the Freidel's salt formation as instantaneous.

In investigating the transport and precipitation of salt in porous building materials, Koniorczyk (2010; 2012) developed a finite element model based on the volume averaged governing balance equations. These included the mass balance of moisture, dry air and solute, the enthalpy balance equation for temperature and the linear momentum conservation equation for deformation. The chosen primary variables were capillary pressure P_C, gas pressure P_g, chemical concentration c, temperature T and displacement u. The mathematical model was an extension of previous work (Gawin et al. 1996; Lewis and Schrefler 1998). The salt concentration was assumed here to affect the dynamic viscosity and density of the fluid as well as the moisture retention curve, the effect of which was studied in an earlier paper (Koniorczyk and

Wojciechowski 2009). In the latter paper (Koniorczyk 2012), the salt crystallisation was taken into account with an assumption of non-equilibrium conditions and the rate of precipitation is given by the Freundlich type isotherm based on the supersaturation of the solution. The supersaturation was calculated as function of ion activity and the equilibrium constant of the reaction K. Due to its accuracy at the concentration levels found during the drying of porous media investigated; the Pitzer model was chosen to calculate the activities of the ions. Three further phenomena were considered, the first of which is the heat of reaction -as salt precipitation is an exothermic reaction- which was included in the enthalpy balance equation. The second is the reduction in pore space due to the presence of the salt crystals, this was taken into account through a simplified method developed by the author in an earlier paper (Koniorczyk and Gawin 2008). The third is the crystallisation pressure on the solid skeleton. This arises as a result of the fact that the solid skeleton confines the salt crystal between the pore walls. The crystallisation pressure was calculated as the difference between the pressure on the loaded crystal face and the hydrostatic pressure. The value of this crystallisation pressure was derived from the chemical potential of the unloaded and loaded sides of the crystal and of the solute, leading to the pressure as a function of the activity, molar volume of the crystal and the equilibrium constant.

In 2014, Song et al. (2014) presented a finite difference model to study the diffusion and reaction of six chemical species namely OH^-, Na^+, K^+, Cl^-, Ca^{2+} and SO_4^{2-}, whilst also taking into account the interaction between ions. The interaction between the ions was taken into account through the diffusive flux of ions due to the local electrical field, described by the Nernst Planck equation, and the local electric field is described by the Poisson equation, as in (Baroghel-Bouny et al. 2011). The difference here is that, instead of solving for the electrical potential ψ as a primary variable, Song et al. (2014) asserted that if the initial solution is charge neutral then the charge neutrality condition is the condition of zero current. This allowed the rearrangement of the sum of the diffusive flux of all chemicals for the gradient of electrical potential, which was then substituted into the Nernst Planck equation. The effect of electrostatic double layers was also taken into account by applying a factor to the molecular diffusion coefficients. There were a number of chemical reactions that were considered, all

based on an assumption of non-equilibrium conditions. The rates of reaction were empirical but all based on mass action law or something like mass action law, where the Freundlich type isotherm was used for their calculation. There were a number of chemical reactions that were taken into consideration including the dissolution of the cement phases. The dissolution of portlandite was included, which occurs due to the concentration difference in calcium between the pore and source solutions as was the dissolution of calcium and hydroxide from the C-S-H phases. The chemical chloride bindings onto the AFm phases were considered, including formation of Freidel's salt and Kuzel's salt, both of which are said to be just special formulas of the AFm phases, meaning that the chemical chloride binding can be seen as just the creation or transformation of this phase (Song et al. 2014). The physical absorption of the chloride ions onto the C-S-H phases was also taken into account; however, their chemical binding onto the same phase was not considered. Finally, the alkali bindings onto both the C-S-H and AFm phases have been included, the former of which is said to have a significant effect on the chloride diffusion.

2.4 Reduced Models in Porous Media

The computational cost of solving the coupled models used for this kind of transport problem can become quite large for particular chemical systems. According to Cleall et al. (2006) this is driven by three main areas, the domain size, time scale and complexity of the analysis; where the complexity of the analysis is dependent on the number of variables and degree of coupling between them, the non-linearity of the system and the number of processes considered. A number of authors deal with this problem by using an operator splitting scheme, changing the numerical treatment of the problem from a GIA (Global Implicit Approach) to an SIA or SNIA (Sequential Iterative Approach or Sequential Non-iterative Approach) (Yeh and Tripathi 1991; Walter et al. 1994; Cleall et al. 2007; Beisman et al. 2015; Yapparova et al. 2017).

GIAs are one step methods that solve the governing equations of transport (PDE's, which are coupled through reaction terms) and chemical reactions (ODE's, which are also coupled through reaction terms or AE's) simultaneously. Two common methods of doing this are the DAE (mixed differential and algebraic equation) method, where the mixed differential and algebraic equations are solved simultaneously for the primary

dependant variables, and the DSA (direct substitution approach), in which -where possible- the nonlinear chemical reactions are substituted directly into the transport equations, reducing the system to a set of nonlinear PDE's (Yeh and Tripathi 1989). In the latter method the AE's can be solved for certain variables, which can then be eliminated from the differential equations (Kräutle and Knabner 2005).

SIA/SNIA methods are two step methods which solve the governing equations of transport first and then calculate the chemical reactions, where the SIA will then iterate between the two over a time step. One of the attractions of SIA/SNIA methods is that they have been found to reduce the computational cost, placing less demand on CPU memory and CPU time (Yeh and Tripathi 1989). The problem with operator splitting approaches is that the SNIA can introduce a splitting error and the SIA can require a prohibitively small time step and a large number of iterations in order to converge (Kräutle and Knabner 2007; Hoffmann et al. 2012). The accuracy of operator splitting was discussed in detail by Valocchi and Malmstead (1992) who found that for continuous mass influx boundary conditions there is an inherent mass balance error that was proportional to the time step size and the decay constant (for a first order decay problem). It was found however that with a reversal of order of the steps at each time step this error could be reduced to less than 10 % of its value.

Due to the potential problems with operator splitting methods, a number of authors have instead turned their attention to approaches that can reduce the computational cost of the global methods, usually through reformulating the system to reduce the number of coupled PDE's and eliminating a number of local equations (Friedly and Rubin 1992; Molins et al. 2004; Hoffmann et al. 2012; Huo et al. 2014). The reformulation of the system is usually achieved using the stoichiometric matrix and variable transforms. The problem with this approach is that the amount of reduction that can be achieved often depends on the problem chemistry and many impose the condition of equal diffusion coefficients. A review of some operator splitting models and reduced order global models will be presented in the following subsections.

2.4.1 Operator Splitting

In 1991 Yeh and Tripathi (1991) presented a numerical model based on the governing mass balance equations of aqueous and sorbed concentration and cation exchange capacity. The chemical reactions were considered with an assumption of equilibrium conditions, based on the laws of mass action, taking into account the deviation from ideality of the solution through the activity coefficients. The activity coefficients were calculated using the Davies equation which is valid up to concentrations of 0.3 M. The model was developed such that a number of different types of chemical reactions could be considered including complexation, adsorption, ion exchange, precipitation/dissolution, redox, and acid-base reactions. The SIA method was chosen for the numerical treatment of the problem, where the transport was separated from the chemical reactions. The algorithm employed calculated any sorption reactions at the beginning of the time step, and then iterated between the transport, and remaining reactions until a convergence tolerance was met. Yeh and Tripathi (1991) assert that the choice of primary dependant variables (PDV's) is of great importance as it can determine how practically it can be used for realistic problems and how many of the different types of chemical reactions it can model. The total analytical concentrations were chosen here as the PDV's as this allows for precipitation/dissolution reactions.

Walter et al. (1994) presented a numerical model for predicting the reactive chemical transport in groundwater systems, called MINTRAN in 1994. This model was a combination of a transport model PLUME2D (Frind et al. 1990) and a geochemical model, namely MINTEQA2 (Allison et al. 1991). The numerical treatment of the model was considered in two ways, both a SIA and a SNIA. The SIA method solved the transport of the components first taking the reaction as constant, then the reactions, taking the physical terms as constant. The spatial terms in this method were centrally weighted for greater accuracy, and for consistency so was the reaction term. For the SNIA method the transport is again calculated first, with the central weighting for the spatial terms; however, this time the reaction term was not included. Following this, the chemical reactions were calculated at the end of the time step. The accuracy of the two approaches was compared and it was found that the SNIA took 1 hour and the SIA

3.5 hours CPU time on an IBM 6000/560, with only 2 % difference in the results profiles. The governing equations were considered for the component concentrations in order to reduce the size of the system, as the components are the minimum number of species that are needed to solve the system. The chemical reactions were considered with an assumption of non-equilibrium conditions and were calculated based on the mass action laws, as a function of the activity coefficients.

A coupled Thermo/Hydro/Chemical/Mechanical model was presented by Cleall et al. (2007) for unsaturated soils. The primary variables considered were the pore water pressure P_w, pore air pressure P_a, temperature T, dissolved chemical concentration c, and the displacement u. The mathematical development of the model was based on previous work by Thomas and He (1995; 1997).The liquid moisture transfer considered the advection described using Darcy's law as well as the osmotic flow, which is the diffusion of the liquid driven by the chemical concentration gradients, where the fluid will diffuse to areas of higher concentration. The relative permeability of the medium was calculated using Kozeny's approach. Concerning the heat transfer, the conduction and convection were taken into account whilst the radiation and the transfer of heat due to chemical concentration gradients were neglected following the conclusions of previous authors as to their significance (Mitchell 1993). The chemical mass balance considered the advection, dispersion and reaction of the solutes, where the temperature dependence of the diffusion coefficients as well as the Soret effect, or chemical diffusion due to temperature gradients was included. The chemical reactions were assumed to be sufficiently fast such that the local equilibrium assumption could be made and were calculated through coupling the model to the geochemical model MINTEQA2. Both the SIA and SNIA methods were used for the numerical treatment of the problem. The model was then tested against an example problem involving dolomisation, where a 1D domain saturated with an aqueous solution was flushed by water of a different chemical composition. The predicted profiles were then compared to the results of Engesgaard and Kipp (1992). It was found that the models agreed very closely, with the exception of the sharp mineral fronts. It was thought that this difference was attributable to the fact that Engesgaard and Kipp (1992) included an algorithm in their model to avoid numerical instabilities.

A parallel reactive transport model, ParCrunchFlow, for application to heterogeneous porous media was presented in 2015 by Beisman et al. (2015). The model was created by sequentially coupling the existing geochemical model CrunchFlow (Steefel et al. 2015) with the parallel hydrologic model ParFlow (Ashby and Falgout 1996). ParCrunchFlow was developed as part of a larger project for subsurface reactive transport problems and in this first step is capable of modelling isothermal, saturated, steady state problems. ParFlow was chosen for its ability to model complex flow and field heterogeneities as well its efficient parallelism. ParFlow allows for parallel computation through a domain decomposition approach and has a number of built-in statistical tools which allow for stochastic simulations. CrunchFlow is a multi-species reactive transport code that incorporates both GIA and OS solvers, though it was the OS approach that was used by Beisman et al. (2015). The reactions found in CrunchFlow include equilibrium homogeneous reactions, kinetic homogeneous and heterogeneous reactions and biologically mediated reactions. A flow chart detailing the program structure and linking of the two models can be seen in Figure 2.5.

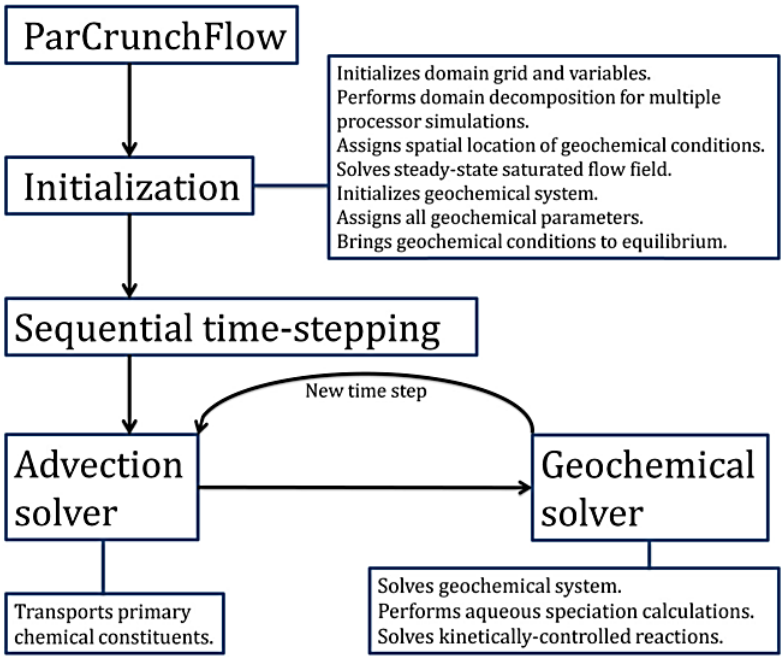

Figure 2.5 – Program structure (after Beisman et al. (2015))

Two example problems were considered to verify the developed model, an advective problem and a geochemical problem. The advective case was chosen to show the ability of the model to capture sharp concentration fronts. In comparing the model to an analytical solution the difference found was less than 0.001 % in chemical mass. The second example concerned 1D reactive transport and compared the results of the code with those of the existing code CrunchFlow. The steady state profiles predicted by each of the models were in good agreement with the maximum difference being less than 3 %. Finally an investigation into the parallel performance of the model was made. The investigation included the consideration of both the strong and weak scaling (where strong scaling is a measure of the decrease in simulation time with increase in processor numbers and weak scaling is a measure of the efficiency of the code with increasing problem size). With strong scaling, it was found that the relative speedup was nearly ideal up to around 125 processes, but began to breakdown thereafter. This can be seen in Figure 2.6.

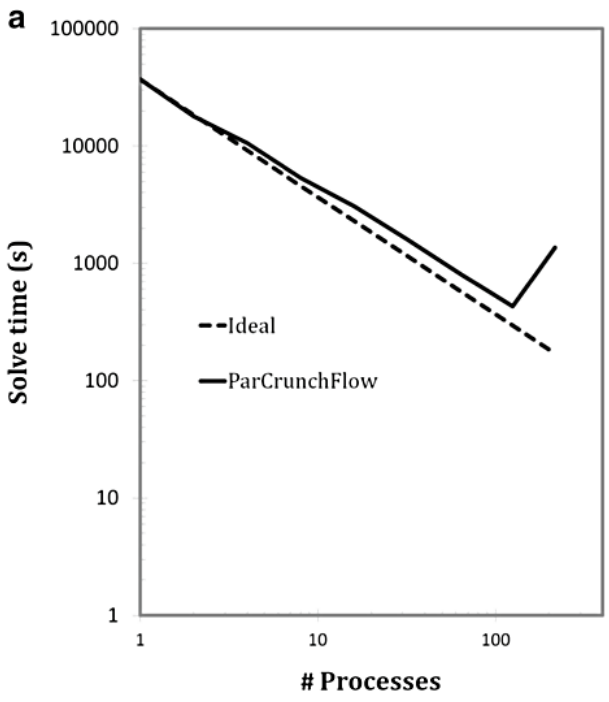

Figure 2.6 – Strong scaling performance (after Beisman et al. (2015))

With weak scaling it was found that the performance was very good, with deviation from ideal behaviour attributed to hardware, numerical and algorithmic inefficiencies. This can be seen in Figure 2.7.

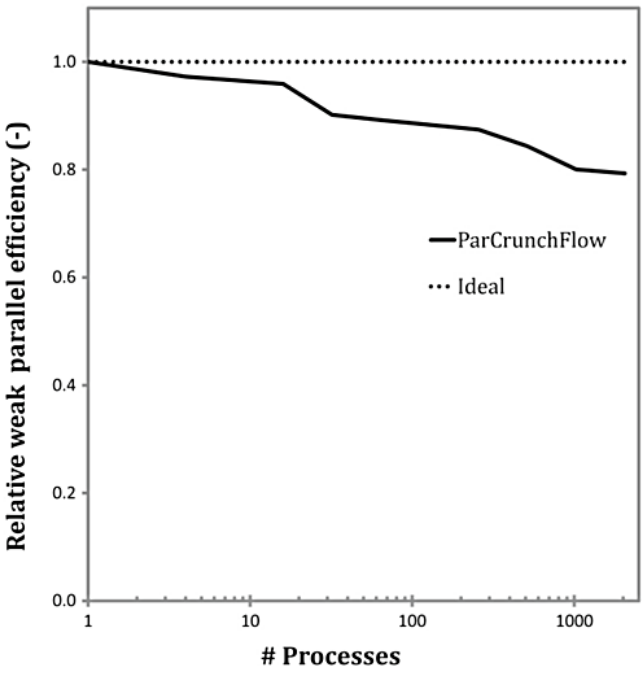

Figure 2.7 – Weak scaling performance (after Beisman et al. (2015))

The development of the reactive transport model CSMP++GEM was presented in 2017 by Yapparova et al. (2017). The authors used a SNIA to combine the best features of the existing codes CSMP++ (Matthäi et al. 2001) and GEMS3K (Kulik et al. 2012). CSMP++ is an object oriented C++ code developed to solve partial differential equations using the finite element-finite volume method. GEMS3K is a C++ code for calculating chemical reactions using the Gibbs energy minimisation technique (GEM). In many reactive transport codes the speciation is calculated using LMA (law of mass action) method (Allison et al. 1991; Xu et al. 2012; Song et al. 2014). The LMA method requires the categorising of the chemical species into master species and product species. The mass balance equations are solved for the master species and the LMA chemical reaction equations are used to calculate the product species concentrations. The LMA method imposes the assumptions that the solid phase is not predominant in the system and that a certain number of chemical properties are known *a priori*

including the redox state of stable phases. In contrast the GEM calculates the speciation based on the elemental bulk composition of the system, through the minimisation of the systems total Gibbs energy. The advantage of the GEM over the LMA is that it does not hold the aforementioned assumptions. The model was then applied to two 1D benchmarking problems involving dolomisation. The latter case involved the dolomisation by sea water and considered mineral kinetics. The authors compared the results of their model to those of TOUGHREACT (Xu et al. 2012) and found that the results were similar. The minor differences were put down to the following (i) TOUGHREACT uses a finite difference method whereas CSMP++GEM uses a finite element-finite volume method, (ii) chemical reactions were calculated differently (LMA vs GEM), (iii) different thermodynamic databases were used with different aqueous activity and mineral kinetic rate models and (iv) there are differences in the equations of state for the aqueous fluid.

2.4.2 Reduced Order GIA

Friedly and Rubin (1992) in 1992 presented an approach to simulate reactive chemical transport that resulted in a compact form of the governing equations. The approach is based on the consideration of the concentration and reactions as vector spaces and uses the stoichiometry of the problem to reduce the system of equations. This approach was based on the work for batch systems by Thompson (1982a; 1982b) and its extension to flow by Friedly (1991). The model is applicable to both equilibrium and non-equilibrium reactions, but requires that the advection-dispersion operator acts on all solutes in the same way. The first step to the development was to define vectors of the concentrations of mobile species, concentrations of immobile species, reaction rates, and stoichiometric coefficients of both mobile and immobile species. Then defining a vector of all concentrations and a matrix of all stoichiometric coefficients S, the mass balance equations for mobile and immobile species can be written in vector form.

$$\dot{X} = L \begin{bmatrix} \boldsymbol{I} & 0 \\ 0 & 0 \end{bmatrix} X + Sr \qquad (2.12)$$

where L is the transport operator and $\boldsymbol{I}$ is the identity matrix. This is done in order to take advantage of linear algebra of vector spaces. The next step was to break down the

vector of concentration X, which represents the concentration space into a set of basis vectors, given for the example of the choice of Cartesian coordinates as the basis vectors as:

$$X = \begin{bmatrix}1\\0\\\vdots\end{bmatrix} c_1 + \begin{bmatrix}0\\1\\\vdots\end{bmatrix} c_2 + \cdots \tag{2.13}$$

In actuality, any complete set of linearly independent vectors may be chosen, and following the approach for batch reaction systems the columns of the stoichiometric matrix S are chosen by the author, representing the reaction space. These alone are not enough and are supplemented by the orthogonal matrix $S^{\perp}$, giving:

$$X = S\xi + S^{\perp}\eta \tag{2.14}$$

where ξ and η are factors analogous to c_1 and c_2 and represent the extent of the reactions and the reaction invariants respectively. This can be applied similarly to the mobile species only to give ξ_m and η_m, where the m subscript denotes mobile contributions. This leads to the equivalent form of X as:

$$\begin{bmatrix}c\\\bar{c}\end{bmatrix} X = S\xi + S^{\perp}\eta + \begin{bmatrix}s\xi_m + s^{\perp}\eta_m\\0\end{bmatrix} \tag{2.15}$$

where the overbar indicates immobile species. This can then be substituted into the original mass balance equation, leading to the following set of equations to be solved:

$$\dot{\xi} = r(\xi, \eta, \xi_m, \eta_m) \tag{2.16}$$

$$\dot{\xi_m} = L(\xi_m + A\xi) \tag{2.17}$$

$$\dot{\eta_m} = L\eta_m \tag{2.18}$$

where the superior dot denotes the time derivative, A is a matrix depending on the stoichiometry and ξ, ξ_m and η_m are the PDV's of the system, η is not considered as a variable as it can often be determined from the initial conditions alone and, for a spatially uniform initial state remain unchanged, and so is often neglected. This reformulation of the equations has eliminated the reaction rates and immobile species concentrations from the PDE's. Leading to a system of J chemical reaction equations

(one for each reaction) for ξ, J_{mind} (number of linearly independent reactions in their mobile phase stoichiometry) linear PDE's for ξ_m -coupled indirectly through the reaction extent ξ- and I-J_{mind} (where I is the number of mobile species) linear uncoupled PDE's for $\eta_{m.}$ The chemical concentrations can then be calculated from the PDV's.

A decoupling method for application to both SIA and DSA methods was presented by Molins et al. (2004) in 2004. Molins et al. (2004) point to the fact that difficulties are caused by the coupling between the transport equations, causing the DSA to be inefficient for large systems (Yeh and Tripathi 1989) and convergence issues for the SIA for some systems such that the DSA is preferred (Saaltink et al. 2001). The beginning of their approach is to set the problem into vector space following the work of Friedly and Rubin (1992) discussed previously, before defining components to eliminate any coupling terms. The approach is split into four distinct paradigms, where a different construction of the component matrix is proposed for each, depending on the chemical treatment of the system. The first paradigm is the tank paradigm and considers only mobile species with equilibrium reactions that take place within the aqueous phase. The second is the canal paradigm, which is the tank paradigm with some kinetic reactions. The third is a river paradigm in which heterogeneous reactions are now included, but are kinetically controlled. The final paradigm is of an aquifer in which heterogeneous reactions can also be considered as equilibrium reactions. For the tank system the governing equations are simply multiplied by the equilibrium component matrix (made up of the identity matrix and equilibrium stoichiometry), eliminating the reaction rates and thus uncoupling the system. Leading to a system of J_e (where J_e is the number of equilibrium equations) AE's describing the reactions and of I-J_e linear uncoupled PDE's for conservative components given as:

$$\eta_m^{\dot{tank}} = L\eta_m^{tank} \tag{2.19}$$

where η_m^{tank} are the chemical components for this paradigm. The transport of the components can therefore be solved separately and the nonlinear system of AE's for the chemical reactions solved for each node separately. For the canal system, the governing equations can then be multiplied by the kinetic component matrix (made up

of the identity matrix and kinetic stoichiometry) which leads to a system of J_e(where J_e is the number of equilibrium equations) AE's describing the equilibrium reactions, J_k (where J_k is the number of kinetic reactions) ODE's describing the kinetic reactions, I-J_e-$J_k$linear uncoupled PDE's for conservative components and J_kPDE's. The system is given as:

$$\eta_m^{\dot{canal}} = L\eta_m^{canal} \tag{2.20}$$

$$\xi_m^{\dot{canal}} = L\xi_m^{canal} - r_k \tag{2.21}$$

where η_m^{canal} and ξ_m^{canal} are the chemical components for this paradigm and r_k are the kinetic reaction rates. For the river system a factor matrix is developed to eliminate the immobile kinetic species from the components. This factor matrix is derived by splitting of the component matrix into two arbitrary groups of conservative components and mobile and immobile groups of the kinetic components. The factor matrix can then be found as the inverse of this component matrix. This factor matrix and the component matrix from the canal paradigm can then be multiplied by the governing equations to decouple them, leading to a reduction to a system of J_e(where J_e is the number of equilibrium equations) AE's describing the equilibrium reactions, J_k+J_{ki} ODE's describing the kinetic reactions, I-J_e-J_k-J_{ki} (where J_{ki} is the number of kinetic reactions involving immobile species) linear uncoupled PDE's for conservative components and J_kPDE's. The system is given as:

$$\eta_m^{\dot{river}} = L\eta_m^{river} \tag{2.22}$$

$$\xi_m^{\dot{river}} = ML\xi_m^{river} - \begin{pmatrix} u_k^{\parallel} r_k^i \\ -r_k^a \end{pmatrix} \tag{2.23}$$

where η_m^{river} and ξ_m^{river} are the chemical components for this paradigm, M is a matrix of coefficients of 1 for mobile and 0 for immobile species, r_k^a are the kinetic reaction rates for aqueous species, r_k^i are the reaction rates for immobile species and $u_k^{\parallel}$ is the kinetic component matrix for immobile species. The final paradigm is the aquifer system, the treatment of which is similar to that of the river paradigm in that a matrix is derived based on the restructuring of the components matrix and multiplied by the

system to eliminate some species. The species being eliminated in this paradigm are the fixed activity species such as minerals.

$$\eta_m^{\dot{aquifer}} = L\eta_m^{aquifer} \tag{2.24}$$

$$\xi_m^{\dot{aquifer}} = ML\xi_m^{aquifer} - \begin{pmatrix} u_k^{\parallel} r_k^i \\ -r_k^a \end{pmatrix} \tag{2.25}$$

where $\eta_m^{aquifer}$ and $\xi_m^{aquifer}$ are the chemical components for this paradigm. It should be noted that this only applies to fixed activity species and so any adsorbed species would not be eliminated as their activity is not fixed. An investigation into the efficiency of the approach when implemented into a DSA and an SIA was made and the authors found that both benefited from the decoupling, but especially the DSA.

In 2012, Hoffman et al. (2012) presented a general reduction scheme for reactive transport based on linear transformation of the equations and variables. The model was an extension on the previous work of two of the authors (Kräutle and Knabner 2005; Kräutle and Knabner 2007; Kräutle 2008). The model assumes that the diffusion coefficient is the same for all species, and is justified by the fact that the molecular diffusion is usually small in comparison to the mechanical dispersion. The stoichiometric matrix is filled in in a particular order and is split into four parts, a) mobile species with equilibrium reactions, b) mobile species with kinetic reactions, c) immobile species with equilibrium reactions and d) immobile species with kinetic reactions. These sections are then also filled in a particular order; section a) starts with the reactions with only mobile species, followed by sorption reactions and then mineral reactions. Section c) is ordered similarly but without the mobile species reactions. The reformulation begins by defining two matrices, S_1 and S_2 that represent the maximal system of linearly independent columns of the mobile and immobile sections of the stoichiometric matrix respectively. The decoupling of some PDE's results from the multiplication of the governing equations by matrices $S_1^{\perp T}$ and C_1^T, followed by a transformation of variables. The matrices are not defined but instead a list of conditions for their choice is presented including the linear dependence of all of the columns of each and the fact that all of the columns of $S_1^{\perp T}$ are orthogonal to all columns of S_1. Following their multiplication by the system of PDE's transformed

variables are chosen ξ_m and η_m, where η_m are reaction invariants. This leads to the elimination of the mobile species equilibrium reaction rates, reducing the system. The next step was to apply this to the system of ODE's for the immobile species, which lead to another set of transformed variables ξ and η, where η are reaction invariant. The equations for reaction invariants are decoupled and linear and the mobile equilibrium reaction rates have been eliminated, however the sorption and mineral equilibrium reaction rates remain. The elimination of these reaction rates is achieved by the introduction of additional variables $\tilde{\xi}$, these new variables allow equations to be solved for the aforementioned reaction rates, which can then be substituted into the PDE's. The final reduction of the system is made through the consideration of the local equations. Using a resolution function a number of these local equations can also be eliminated. This leads to a system of equations of I_m-J_m-J_{sorp}-J_{min}-J_{kin} (where I_m is the number of mobile species, J_m is the number of chemical reactions involving only mobile species, J_{sorp} is the number of sorption reactions, J_{min} is the number of mineral reactions and J_{kin} is the number of kinetic reactions) PDE's for η_m, I-J_{sorp}-J_{min}-J_{kin} (where I is the number of immobile species) PDE's for η and $J_{sorp}+J_{min}+J_{kin}$ PDE's and $J_{sorp}+J_{min}+J_{kin}$ AE's for $\tilde{\xi}$ given as:

$$\dot{\eta_m} = L\eta_m \tag{2.26}$$

$$\dot{\eta} = L\eta \tag{2.27}$$

$$\dot{\tilde{\xi}} = L\xi_* + A_*\widetilde{r_{kin}}(\tilde{\xi}) \tag{2.28}$$

$$\tilde{\xi} = \xi_* - R\widetilde{\xi_{het}}(\tilde{\xi}) \tag{2.29}$$

The efficiency of the resultant scheme was tested on the MoMaS benchmark (Carrayrou et al. 2010) 2D advective easy test case, and compared against the results from the code HYTEC (SIA) (Lagneau and van der Lee 2010) and MIN3P (DSA) (Mayer and MacQuarrie 2010). The proposed reduction scheme was found to be five times faster than those of both HYTEC and MIN3P when comparing the normalised CPU time.

In 2014 Huo et al. (2014) presented a decoupling approach for application to reactive transport in heterogeneous porous media. The idea of the approach was to split the domain into a number of sub-domains based on the spatial variance of the physical

and chemical properties of the medium. The decoupling approach developed by Molins et al. (2004) is then applied to each of the sub-domains based on their chemical properties, before they are assembled to give the entire study area through the appropriate boundary conditions. The boundary conditions between the adjacent sub-domains are set as the Neumann boundary condition for inflow and the Dirichlet boundary condition for out flow, and are given for sub-domains A and B as:

$$-\boldsymbol{n} \cdot D\nabla\eta_A = 0 \qquad ,\Gamma_{AB}^1 \tag{2.30}$$

$$\eta_A = S_A^{\perp} \cdot c_A = S_A^{\perp} \cdot c_B = S_A^{\perp} \cdot f(\eta_B, K_B) \qquad ,\Gamma_{AB}^0 \tag{2.31}$$

where $\boldsymbol{n}$ is the unit normal vector, D is the dispersion coefficient, η are the components, c are the concentrations and $f(\eta_B, K_B)$ indicates that c_B can be calculated from the equilibrium constant K_B and η_B. The decoupling approach was summarised into the following 5 steps (Huo et al. 2014):

1. Split the study area into sub-domains based on the potential chemical reactions and express $S^{\perp}$ and η for each.
2. Calculate the kinetic reaction rate as a function of η for each sub-domain.
3. Set the boundary conditions between sub-domains.
4. Solve the model for the several component transport equations (with the same number of sub-domains).
5. Calculate species concentrations.

Following the description of the approach the model was applied to a 2D test problem. The medium was split into two parts, one containing non-reactive quartz and one containing quartz and reactive permanganate. Fluid circulation involved flow of deionised water through two inlets and out through one outlet. The whole domain was assumed to be saturated with KCl solution. The schematic of the test problem can be seen in Figure 2.8.

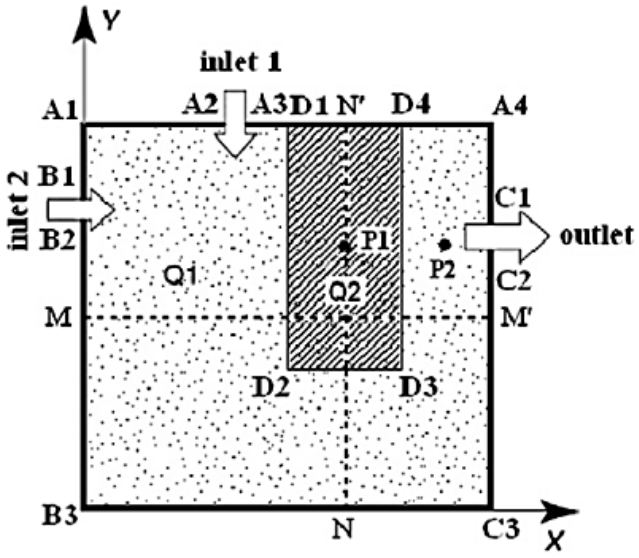

Figure 2.8 – Schematic of the test problem (after Huo et al. (2014))

The decoupled approach was solved in COMSOL Multi-physics and the results compared to those of the reactive multi-component transport model PHAST (Parkhurst et al. 2010). It was found that all of the species concentration profiles, as well as transient behaviour were similar to those predicted by PHAST. The subtle differences found were attributed to the following (i) PHAST uses the finite difference method, whereas COMSOL uses a finite element method, (ii) PHAST uses an operator splitting approach, whereas Huo et al. (2014) use a global approach, and (iii) differences in the setting of the boundary condition.

It can be seen from the review of reduced order GIAs that in all schemes a number of the kinetic reaction rates remain, meaning that many species involved in kinetic reactions remain coupled (at least through the reaction rates).

2.5 Ion Transport Experiments

Ion transport experiments are important for determining the number of parameters needed for the implementation of any numerical model, ranging from the dispersivity values (Robbins 1989), to effective diffusion coefficients (Truc et al. 2000; Sun et al. 2011), to chemical reaction data such as sorption amounts (Boggs and Adams 1992), and reaction rates for empirically based kinetic reactions (Baroghel-Bouny et al. 2011). These experiments can be carried out at the laboratory scale such as column leaching

experiments (Wierenga and Van Genuchten 1989; Krueger et al. 1998; Hartley et al. 2004; Liu et al. 2017) used for geochemical data, or at the field scale, for example, to determine the scale effect of dispersion (Domenico and Robbins 1984). It is the laboratory scale experiments that are of interest here as this is the scale of the experimental procedure developed in this thesis.

For the determination of these parameters in soils, column leaching experiments have been used by a number of authors (Robbins 1989; Wierenga and Van Genuchten 1989; Krueger et al. 1998; Hartley et al. 2004; Liu et al. 2017). In 1989 Wierenga and van Genutchen (1989) published a study into solute transport into small and large soil columns to determine the dispersion coefficients, dispersivity coefficients and retardation factors for the transport of a $Ca(NO_3)_2$ solution through columns, filled with a Berino loamy fine sand, at four different moisture contents. The retardation factor accounts for interactions between the solute and the soil matrix, for example the physical adsorption. The experimental procedure was to apply a tracer to the columns at a constant rate and measure the concentration in the effluent collected from the outflow, the parameters can then be determined through an optimisation program. For the small column experiments, Plexiglas columns of 5.1 cm diameter and 30 cm length were used. The ends of the columns were sealed with porous stainless steel plates, held in place by Plexiglas end plates. The soil was air dried and passed through a 1 mm sieve before placement. A vacuum was applied to the base of the column, which was used to adjust the pressure to give equal pressure heads at the top and the bottom of the column. The large column experiments were carried out in a 6 m long column made from galvanised highway culverts, with the setup being similar to that of the small columns, with the main difference here being that suction candles were placed at 6 depths through the column, allowing measurement at different depths. The setup can be seen in Figure 2.9.

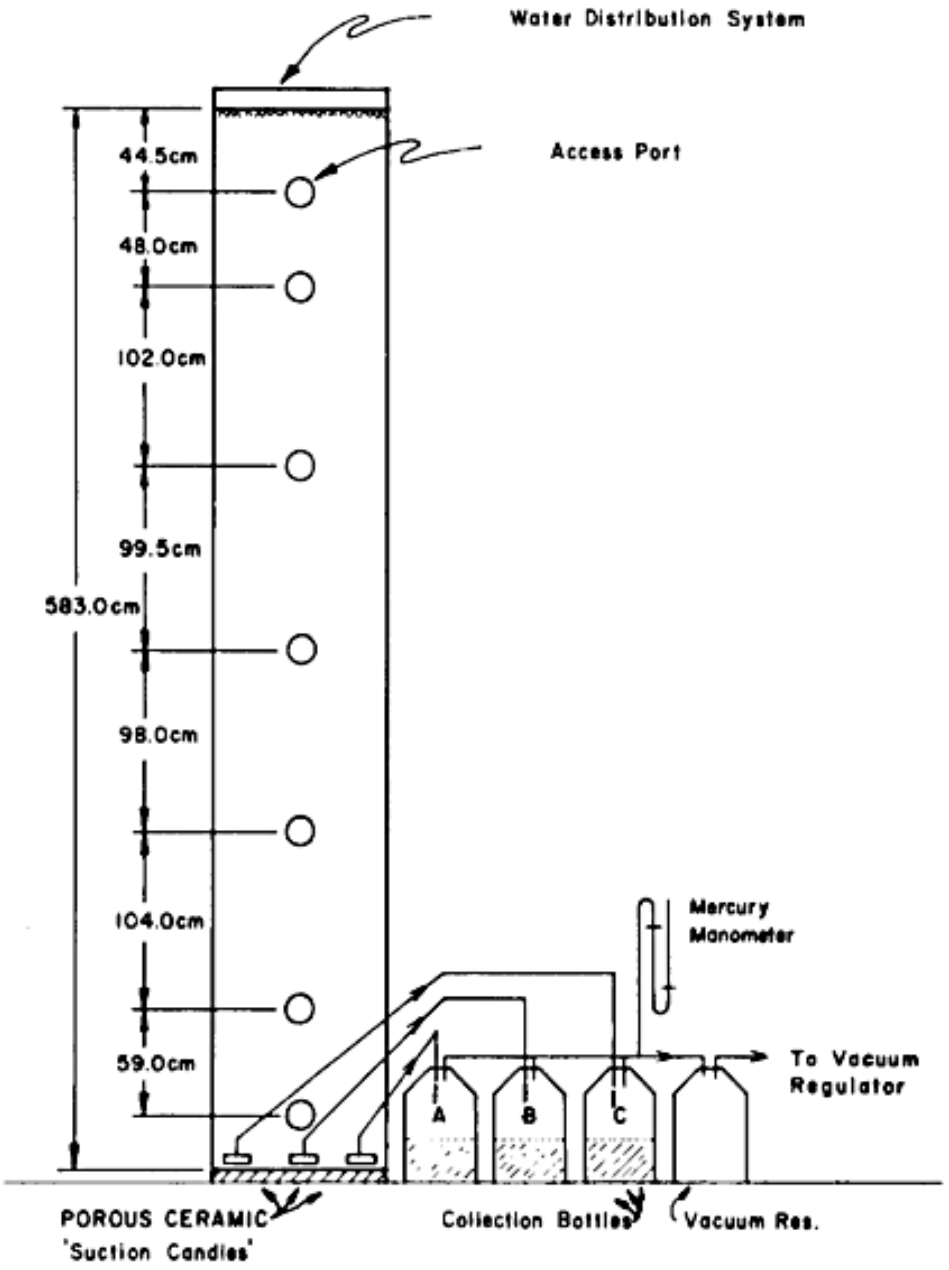

Figure 2.9 – Large column leaching setup (after Wierenga and Van Genuchten (1989))

In 2004 Hartley et al. (2004) presented a series of leaching tests to assess the mobility of arsenic and heavy metals in contaminated soils, following amendment by various iron oxides. Three different UK soils were tested, collected from the following sites: Merton Bank (NGR, SJ 523 961), Kidsgrove near Stoke-on- Trent (NGR, SJ 844 543) and Warrington, Cheshire (NGR, SJ 621 885). The samples were air dried for one week before being crushed to a particle size of less than 4 mm. The iron oxides used for the

amendments were α-$FeOOH$ (goethite), iron grit type 31051, iron (II) sulphate heptahydrate ($FeSO_4 \cdot 7H_2O$) + lime and iron (III) sulphate pentahydrate ($Fe_2(SO_4)_3 \cdot 5H_2O$) + lime. The leaching tests used were the UK Environment Agency (UKEA) leaching test, the American Society of Testing and Materials (ASTM) leaching test and the Modified Dutch Environmental Agency column test (NEN 7473 1995). For the UKEA test, a 10 g sample of soil was leached with 50 cm^3 deionised water for 1 h, whilst being occasionally agitated, before being filtered and analysed. For the ASTM test, a 25 g sample of soil was leached with 100 cm^3 of deionised water for 48 h whilst being continuously agitated on a shaker platform, before being filtered and analysed. Finally the NEN 7473 test glass columns of length 20 cm and diameter 5 cm were filled with the contaminated soil, before being leached with acidic deionised water. The leaching consisted of the continuous flow of water from a peristaltic pump. Filters were placed at the top of the column and an acrylic jacket was fitted to maintain the temperature. Samples were taken over a three week period to be analysed. A depiction of the NEN 7473 leaching test column can be seen in Figure 2.10. The arsenic content was measured using a hydride generation atomic absorption spectrometry (HG-AAS) technique.

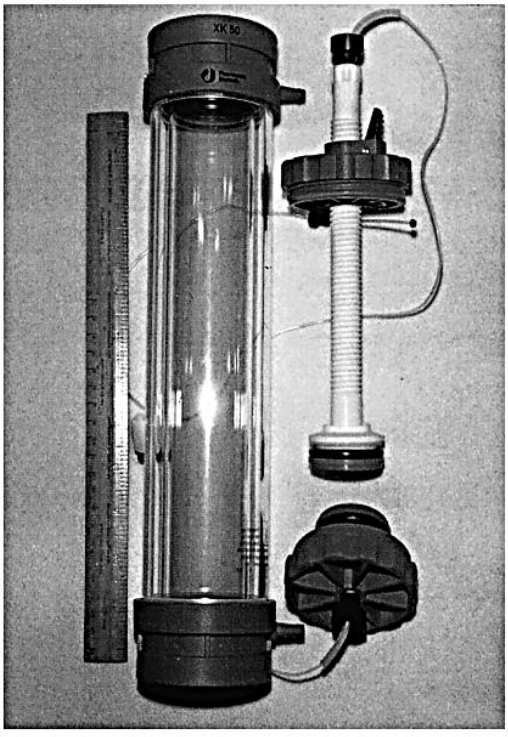

Figure 2.10 – NEN 7473 leaching test apparatus (after Hartley et al. (2004))

Liu et al. (2017) presented an experimental and numerical study into the non-Fickian transport of Sr^{2+} in laboratory columns in 2017. Their study was motivated by the fact that there are a limited number of investigations into the reactive, non-Fickian transport of Sr^{2+}, which is a hazardous chemical that has been reported to increase the risk of bone cancer and leukaemia (Liu et al. 2017). The non-Fickian transport is reported to be characterised by "early breakthrough times and long late time tails in measured breakthrough curves (BTCs), which deviate from the Gaussian distributions of species concentration" (Liu et al. 2017). The column experiments simulated rainfall infiltration with the contaminant and measured the concentrations in the effluent at the outflow. A depiction of the experimental setup can be seen in Figure 2.11.

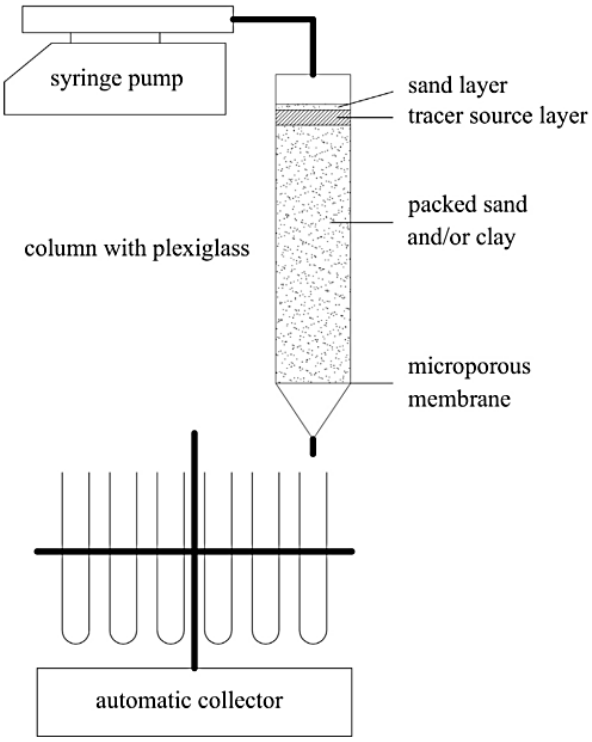

Figure 2.11 – Experimental setup (after Liu et al. (2017))

The columns were 20 cm long and 3 cm in diameter and were packed with either sand or clay. In total eight different test cases were investigated with varying sand content and volumetric flow rates. Membranes were placed at the bottom of the column to prevent soil loss and a conservative tracer of Br^- was used for the moisture flow. The concentrations of the effluent were measured using ion chromatography and

inductively coupled plasma-atomic emission spectrometry. Two different transport models were tested to determine their validity, the first was based on the advection-diffusion equation (ADE), and the second was a continuous time random walk (CTRW) model. The transport parameters required for each model were then determined through an inverse analysis carried out using a non-linear least squares inversion program. It was found in their results that the Sr^{2+} transport does exhibit non-Fickian transport behaviour, particularly for the test case labelled 'd' and that the CTRW model was able to more accurately reproduce the measured profiles, particularly for the test case labelled 'h'. This can be seen in Figure 2.12.

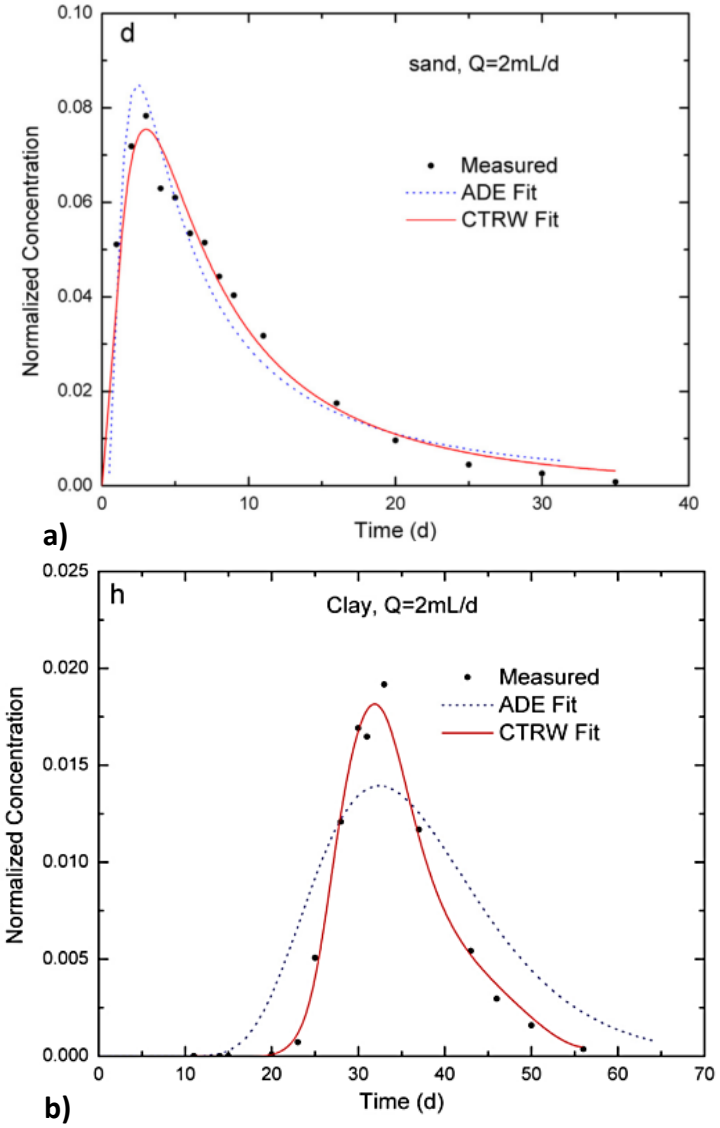

Figure 2.12 – Experimental and modelling results a) test case d and b) test case h (after Liu et al. (2017))

For the determination of these parameters in cementitious materials, the approach is quite different, with different test setups being used for depending on the parameter in question. For the determination of effective diffusion coefficients the most common method is the non-steady-state (*nss*) migration test. The *nss* migration test involves the diffusion of ions from a solution through a concrete specimen, under the influence of an applied electric field. The electric field is used to speed up the transport of ions and therefore reduce the length of the test. This test has been used by Baroghel-Bouny and co-authors in a series of papers investigating durability parameters and binding isotherms (Baroghel-Bouny et al. 2007a; Baroghel-Bouny et al. 2007b; Baroghel-Bouny et al. 2011). The test setup can be seen in Figure 2.13.

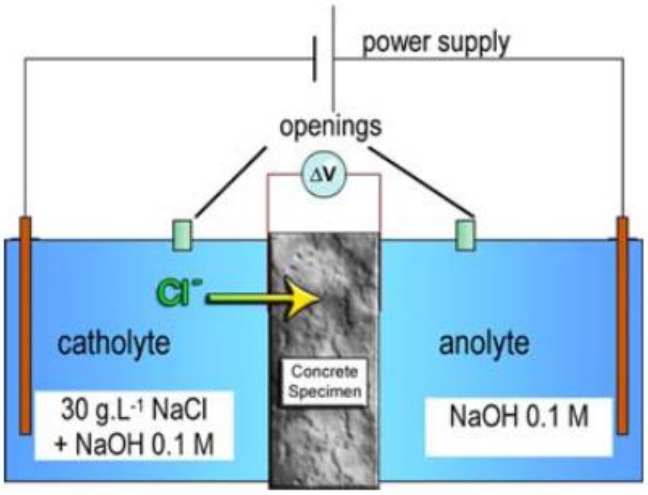

Figure 2.13 – Migration test setup (after Baroghel-Bouny et al. (2007b))

The samples are first vacuum saturated with a 0.1 M $NaOH$ solution before sealing the relevant sides with epoxy resin, mounting the sample into the migration cell and sealing the cell-specimen interface. A potential difference was then applied and the test was left for between one and a few days. The penetration depth was then measured (for example as described in (Baroghel-Bouny et al. 2007b)) and the diffusion coefficient calculated from:

$$D_{Cl} = \frac{RT}{ZF} \cdot \frac{e}{\Delta E} \cdot \frac{x_d - \alpha \cdot \sqrt{x_d}}{t} \qquad (2.32)$$

where Z is the valence of the ion, e is the thickness of the sample, t is the test duration, ΔE is the applied potential, α is a function of the test conditions, x_d is the penetration depth and D_{Cl} is the effective chlorine diffusion coefficient. This test can also be left to reach steady state (*ss*) if prefered. In this case, the monitoring is done by potentiometric titration of the chloride ion concentration vs time in the anolyte. Assuming very dilute solutions and no interaction between ions, the effective diffusion coefficient can then be calculated by:

$$D_{Cl} = \frac{RT}{ZF} \cdot \frac{e}{\Delta E} \cdot \frac{Q}{\gamma c_0 t} \tag{2.33}$$

where c_0 is the chloride concentration in the catholyte, γ is the activity coefficient of the chloride in the catholyte and Q is the cumulative amount of chloride ions arriving in the anolyte in time t. These tests however can suffer from edge effects, such that it is recommended that the first 10 mm of penetration is ignored. In addition to this when a large voltage is applied the penetration can be highly effected by the size of aggregates or presence of defects (Baroghel-Bouny et al. 2007b). A similar test setup was used by Conciatori et al. (2013) in analysing the statistical variance of concrete transport properties. A number of concrete mixes –produced in the lab or sampled in the field- were tested for a range of transport parameters including porosity, permeability, diffusion coefficient and water content at 50 % RH. The tests included porosity measurements, drying tests and migration tests. The parameters were then analysed using a point estimator method. It was found that there was good agreement between the predicted and observed values with correlation coefficients being of the range 0.9475-0.9824.

The Nordtest method NT Build 492 (1999) describes a standardised version of the *nss* migration test for the determination of chloride diffusion coefficients in concrete, mortar or cement based repair materials. The test uses 100x50 mm (diameter x length) cylindrical specimens which are first vacuum saturated in a $Ca(OH)_2$ solution. A typical arrangement of the migration setup can be seen below in Figure 2.14. The sample is mounted into the migration cell, a potential difference is applied and the setup is left for 6-96 hours depending on the initial current. The sample is then removed and split

into two before a 0.1 M silver nitrate solution is used to facilitate measurement of the penetration depth. Finally the diffusion coefficient is calculated from eq. (2.32).

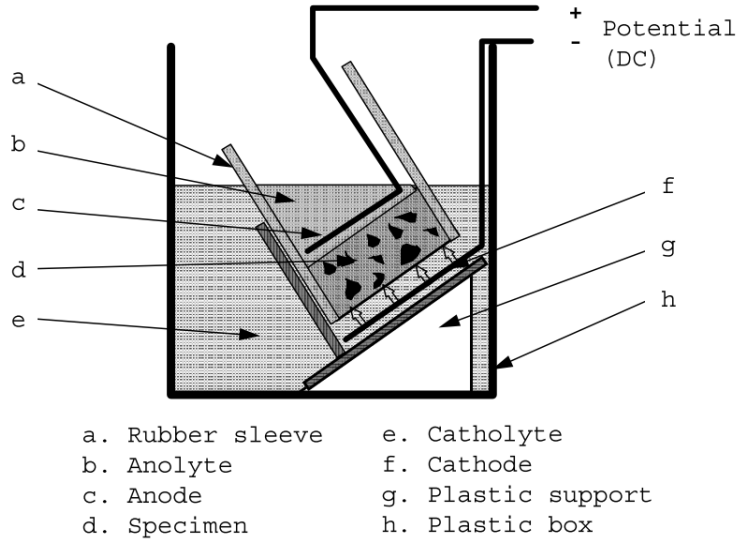

Figure 2.14 – Typical migration test setup (after NT Build 492 (1999))

The problem with migration tests is they do not allow for different flow conditions and they require the removal of the sample to measure the chloride penetration.

For the determination of binding parameters, two different experimental approaches can be used, as described in (Baroghel-Bouny et al. 2012). Immersion tests on crushed specimens can be used for equilibrium binding parameters, to this end samples are moist cured before oven drying at 40 ^{o}C for 3 days, and being crushed (size 200 µm-2.5 mm). The crushed samples are then soaked in $NaCl$ solutions for 2 months (long enough for equilibrium to be reached), before using titration to analyse the bound chlorine amounts. In concretes however, chloride adsorption onto the aggregates can induce large variability of results, and the sample can be a poor representation of the material. The second approach is the profile method, which is the measurement of total (tcc) and free (fcc) chloride profiles following a nss or ss migration or diffusion/wetting test and which can be applied to both equilibrium and non-equilibrium chloride binding. In their paper Baroghel-Bouny et al. (2007a) used a nss diffusion test, the setup of which can be seen in Figure 2.15.

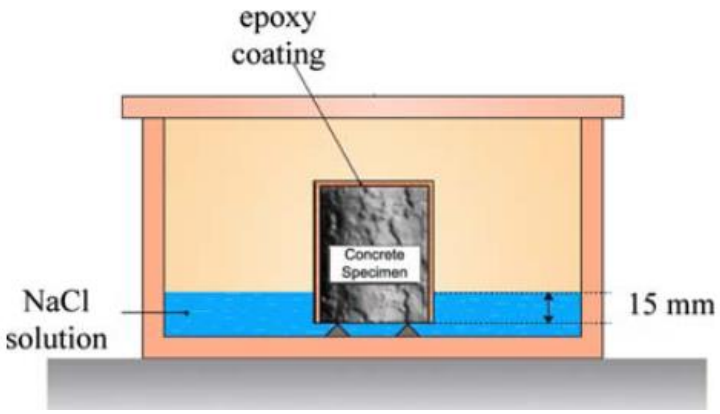

Figure 2.15 – *nss* diffusion/wetting test setup (after Baroghel-Bouny et al. (2007a))

A sample was vacuum dried with a 0.1 M $NaOH$ solution before being sealed on 5 sides and immersed in a $NaCl$ solution, in a sealed container. After a period of time the *tcc* and *fcc* profiles were measured by grinding the specimen, layer by layer and applying chloride extraction and potentiometric titration to the resultant dust. A numerical inverse analysis was then carried out to determine the binding parameters, through optimisation until the least squared error function is minimised. A similar test setup was used by Song et al. (2014) in investigating multi-phase reactions in concretes immersed in $NaCl$ and $CaCl_2$ solutions.

The problem with this setup, as with migration tests, is that it does not allow for many different flow conditions and the sample needs to be removed in order to measure the concentration profiles.

2.6 Conclusions

This chapter has provided a review of the modelling and underlying physical phenomena of the behaviour of transport models. The transport of moisture was found to be driven by the advection of the liquid and diffusion of the moisture vapour. The relation between the degree of saturation and capillary pressure was discussed and most authors used a form derived by van Genuchten (1980). This retention curve was found to depend upon the medium, the temperature and the chemical concentration at high concentrations. Heat transfer models normally consider heat conduction, driven by the temperature gradients, and heat generation from chemical

reactions. The transport of a chemical ion is assumed to be driven by liquid advection, mechanical dispersion and diffusion of the ions, where the diffusion is coupled through an electrical potential term, described by Poisson's equation, to prevent the break-up of electro neutrality. The chemical reactions were also considered including the reaction classes which affect the mathematical treatment of the reaction. In this case, the kinetic reactions were assumed to be described by a Freundlich isotherm, where the reaction rate is driven by the chemical concentration or solution supersaturation. Different methods for calculating ion activity were discussed, where the Pitzer model is preferred for higher concentrations due to its greater range of applicability.

A review of coupled models found in the literature for modelling transport was made including a review of the approaches to increasing the efficiency of their solution. It was found that there are two schools of thought with regard to this; one uses operator splitting approaches whilst the other employs reformulation techniques. It was found, however, that operator splitting techniques can introduce errors or have convergence problems and reformulation techniques are limited in the amount of reduction that can be achieved (i.e. overall reduction in the number of coupled equations to be solved), depending on the chemical system. It was therefore concluded that there is a need for a new set of efficient reduction approaches that can be applied –without modification- to a range of chemical systems.

Finally a review of the current approaches to determining transport parameters was made, including those applied to both soils and cementitious materials. It was found that there were a number of drawbacks with current approaches for cementitious materials, including the inability to allow for different flow conditions and the requirement of the removal of the sample for concentration measurements. It is therefore concluded that there is a need for a new approach to determining transport parameters in cementitious materials that allows for different flow conditions and the in situ measurement of concentrations.

Chapter 3. Theoretical Formulation

3.1 Introduction

This chapter presents the theoretical formulation of the governing equations describing mass and energy balance and physical laws describing the various physical processes considered. The primary variables considered here are the capillary pressure (P_C), the temperature (T) and the dissolved chemical concentration (c_i) of each species.

Section 3.2 describes the governing equation for moisture transfer, which is split into two parts; liquid moisture flux and moisture vapour flux. For each part the governing equation of mass balance is presented and the various mechanisms of transport including the advection, diffusion and phase change between the two described.

The enthalpy balance equation and mechanisms of heat transfer including conduction is covered in section 3.3.

The theoretical formulation that describes the physical processes of ion transport will then be presented in section 3.4 including the advection with the liquid phase, hydrodynamic dispersion and the condition of charge neutrality based on the Nernst Planck and Poisson equations considering the no current condition.

Section 3.5 is dedicated to the description of the chemical reactions that may take place. The chemical reactions presented are considered as non-equilibrium reactions described with a Freundlich type isotherm. Following this, the calculation of ion activity, used at times in the place of concentration for reaction rates, using the Pitzer equations is discussed.

Finally, in section 3.6, the chapter is summarised.

3.2 Moisture Flow

The flow of moisture in porous materials is considered to be composed of two main transfer mechanisms, the advection of the liquid water and the diffusion of the moisture vapour. The governing mass balance equations for each will be derived below.

3.2.1 Governing Equation for Moisture Flow

The mass balance equation considered here is the macroscopic volume averaged balance equation, which for a phase π has the general form (Hassanizadeh and Gray 1979), (full details of the averaging procedure can be found in (Hassanizadeh and Gray 1979; Lewis and Schrefler 1998)), can be expressed as:

$$\dot{\overline{\rho_\pi}} + \nabla \cdot (\overline{\rho_\pi} v_\pi) - \nabla \cdot i^\pi + f^\pi = G^\pi + \dot{m}_\pi \tag{3.1}$$

where $\overline{\rho_\pi}$ is the phase averaged density, v_π is the mass averaged velocity, i^π is the surface flux vector, f^π is the phase averaged external supply of mass π, G^π is the phase averaged production, $\dot{m}_\pi$ is the mass change between phases, and the superior dot indicates the time derivative. The phase averaged density is given by:

$$\overline{\rho_\pi} = n \rho_\pi S_\pi \tag{3.2}$$

where $\overline{\rho_\pi}$ denotes the average density of phase π, n denotes the porosity of the medium and S_π denotes the degree of saturation of phase π. Assuming i^π, f^π and G^π are all equal to zero the mass balance equation for liquid moisture is given by:

$$\dot{\overline{\rho_w}} + \nabla \cdot (\overline{\rho_w} v_w) + \dot{m}_v = 0 \tag{3.3}$$

where $\dot{m}_v$ denotes the rate of phase change between liquid moisture and moisture vapour. The gaseous phase consists of dry-air and moisture vapour, which are miscible and so following (Lewis and Schrefler 1998) are assumed to have the same volume fraction S_g the mass balance equations for dry-air and moisture vapour are given as:

$$\dot{\overline{\rho_v}} + \nabla \cdot (\overline{\rho_v} v_v) - \dot{m}_v = 0 \tag{3.4}$$

$$\dot{\overline{\rho_{da}}} + \nabla \cdot (\overline{\rho_{da}} v_{da}) = 0 \tag{3.5}$$

However, the mass balance of dry-air is neglected here following Bary et al. (2008) and de Morais et al. (2009), who found that a model based on the assumption that the gas phase consisted of moisture vapour only was able to accurately capture the moisture transport behaviour when compared to results of a full model, while reducing the computational cost of the simulation. The assumption used here is that the combined gas pressure of moisture vapour and dry-air remains constant at atmospheric pressure,

following the approach of Chitez and Jefferson (2015). This is justified as Gardner et al. (2008) found that the time to reach steady state of the gas flow is relatively short and so any excess pressures would be negligible in all but short time scales. Introducing a diffusive dispersive flux J_v for the moisture vapour gives:

$$\dot{\overline{\rho_v}} + \nabla \cdot (\overline{\rho_v} v_v) + \nabla \cdot J_v - \dot{m}_v = 0 \tag{3.6}$$

3.2.2 Mechanisms of Liquid Moisture Transport

The velocity of the liquid moisture phase is given by a generalised form of Darcy's law (Gawin et al. 2006), which is given as:

$$v_w = -\frac{K_i K_{rw}}{n S_w \mu_w} (\nabla \cdot P_w - \rho_w g) \tag{3.7}$$

where K_i is the intrinsic permeability of the medium, K_{rw} is the relative permeability of the liquid moisture phase, μ_w is the dynamic viscosity of water, g is the gravity vector and P_w is the liquid pressure. The capillary pressure is the chosen primary variable for the moisture phase, following the approach of Gawin et al. (2006). The capillary pressure, P_C, arises as a result of the interfacial tension between the liquid and gas phases and is defined as the difference between the gas pressure, P_g, and liquid pressure and can be expressed as:

$$P_C = P_g - P_w \tag{3.8}$$

Following Dalton's law of partial pressures this gives the combined pressure of dry-air and moisture vapour to be equal to atmospheric:

$$P_g = P_{da} + P_v = P_{atm} \tag{3.9}$$

Noting eq. (3.8), eq. (3.7) can be rewritten as:

$$v_w = -\frac{K_i K_{rw}}{n S_w \mu_w} (\nabla \cdot P_g - \nabla \cdot P_C - \rho_w g) \tag{3.10}$$

as the gas pressure is assumed to be constant then the first term in the bracket of eq. (3.10) is equal to zero giving:

$$v_w = \frac{K_i K_{rw}}{n S_w \mu_w} (\nabla \cdot P_C + \rho_w g) \tag{3.11}$$

The capillary pressure can be linked to the external relative humidity (RH) through the Kelvin equation (Gawin et al. 2006) given as:

$$P_c = \frac{-\rho_w RT}{M_w} \ln\left(\frac{P_v}{P_{vs}}\right) = \frac{-\rho_w RT}{M_w} \ln(RH) \tag{3.12}$$

where R is the ideal gas constant, T is the temperature, M_w is the molar mass of water, P_v is the vapour pressure and P_{vs} is the saturated vapour pressure which is related to the saturated vapour density through the ideal gas law (Gawin et al. 2006), which is given for a phase π as:

$$P_\pi = \frac{\rho_\pi RT}{M_\pi} \tag{3.13}$$

and ρ_{vs} is a function of temperature and is given by Antione's equation as:

$$\rho_{vs} = b_1 \cdot 10^{b_2 - \frac{b_3}{b_4 + T - b_5}} \tag{3.14}$$

where $b_{1\text{-}5}$ are material parameters. The moisture density ρ_w depends on temperature, and the relationship proposed by McCutcheon (1993) is considered here:

$$\rho_w = a_1 \left[1 - \frac{(T - a_2)\cdot(T - a_3)^2}{a_4(T - a_5)}\right] \tag{3.15}$$

where $a_{1\text{-}5}$ are material parameters.

The remaining terms from eq. (3.7), as yet undefined, are the relative permeability of the medium K_{rw} and the dynamic viscosity of water μ_w and these are considered in the following paragraph. The dynamic viscosity has been reported to depend on both the temperature and solute concentration (Gawin et al. 1999; Koniorczyk 2010) and is given by:

$$\mu_w = 0.6612\left(1 + A_1 \sum_{i=1}^{ns} c_i - A_2 \left(\sum_{i=1}^{ns} c_i\right)^2 + A_3 \left(\sum_{i=1}^{ns} c_i\right)^3\right) \cdot (T - 229)^{-1.562} \tag{3.16}$$

where $A_{1\text{-}3}$ are material parameters, c_i is the chemical concentration of a species i and ns is the number of chemical species. The intrinsic permeability is reported to depend

upon the hydration degree and temperature; however hydration is not considered here and so is ignored. The relationship is given as (Gawin et al. 1999):

$$K_i = K_{i0} 10^{A_k(T-T_r)} \tag{3.17}$$

where T_r is the reference temperature and A_k is a material parameter. A number of different relationships have been used for the relative permeability of the liquid moisture phase in the literature (Mualem 1976; Koniorczyk 2010; Baroghel-Bouny et al. 2011); the relationship used here however is based on Kozeny's approach (Mualem 1976; Cleall et al. 2007; Koniorczyk and Gawin 2011):

$$K_{rw} = S_w^{A_w} \tag{3.18}$$

where A_w is a material parameter with reported values between 1 and 6 (Koniorczyk and Gawin 2011). This relationship is shown for $A_w = 3$ (Irmay 1954; Cleall et al. 2007) in Figure 3.1.

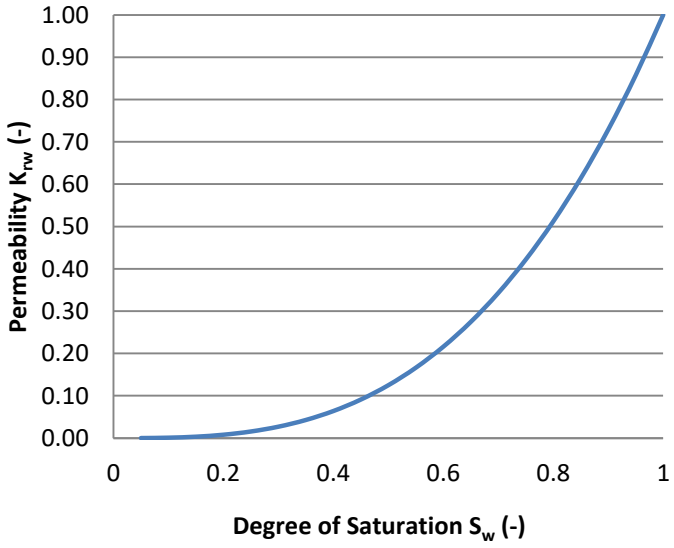

Figure 3.1 – Typical variation of Relative Permeability with Moisture Content (A_w=3)

The final important element to consider is the relationship between the capillary pressure P_C and degree of saturation S_w. which is referred to hereafter as the moisture retention curve. The form used here was originally derived for partially saturated soils by van Genuchten (1980):

$$S_w = \left[1 + \left(\frac{P_c \xi_0}{a_c P_{atm} \xi}\right)^{\frac{b}{b-1}}\right]^{\frac{-1}{b}} \quad (3.19)$$

where a_c and b are experimentally determined parameters and ξ and ξ_0 are free surface energy at T and a reference temperature T_r. Figure 3.2 shows the retention curve for a typical concrete using values of $b = 2.27$, $a_c = 183.765$ and $P_{atm} = 101325\ Pa$ (Koniorczyk and Gawin 2012; Chitez and Jefferson 2015).

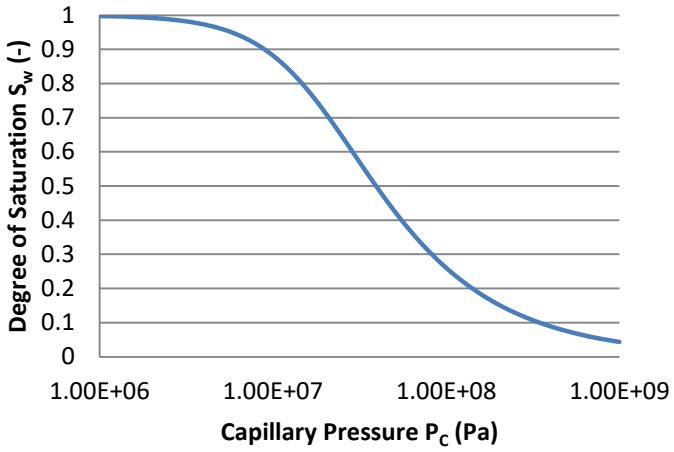

Figure 3.2 – Moisture retention curve

The temperature dependence of this moisture retention curve follows an approach derived for partially saturated soil mechanics and applied to cementitious materials by Chitez and Jefferson (2015), where the free surface energy ξ is given by Edlefsen and Anderson (1943) as:

$$\xi = 0.1171 - 0.00001516T \quad (3.20)$$

It should be noted that this moisture retention curve and definition of capillary pressure may not be valid at low moisture contents at which no liquid moisture is present (Lewis and Schrefler 1998). An allowance for a residual adsorbed moisture content can be included in the moisture retention curve (van Genuchten 1980), it is assumed here however that the residual moisture content is zero and that eq. (3.19) is valid over the moisture ranges considered. This is justified as the only problem considered in this study which reaches low moisture contents was the numerical

experiment found in Koniorczyk (2010), which did not take this phenomenon into account.

3.2.3 Mechanisms of Water Vapour Transport

The velocity of the moisture vapour phase is given by generalised Darcy's law (Gawin et al. 2006) given as:

$$v_v = -\frac{K_i K_{rg}}{n S_g \mu_g}(\nabla \cdot P_g + \rho_g g) \tag{3.21}$$

where K_{rg} is the relative permeability of the gas phase, μ_g is the dynamic viscosity of the gas, and P_g is the gas pressure. It is assumed in this thesis however as previously mentioned that the gas pressure remains constant at atmospheric pressure, following the approach of Chitez and Jefferson (2015). The first term in the bracket in (eq. 3.21) therefore is zero. In addition to this the advection of the moisture vapour due to gravity is also neglected here following the approach of previous authors (Gawin et al. 1999; de Morais et al. 2009). The advection of moisture vapour therefore is neglected in this thesis, meaning that the main transport mechanism for moisture vapour considered is the diffusion of the moisture vapour through the gas phase. This diffusive flux is assumed to follow Fick's law (Gawin et al. 2006) and is given by:

$$J_v = -\rho_g D_m \nabla \cdot \left(\frac{\rho_v}{\rho_g}\right) \tag{3.22}$$

taking into account the assumption that $P_g = P_{atm}$ and converting the gas density to gas pressure through the ideal gas law eq. (3.13), eq. (3.22) becomes:

$$J_v = -\frac{M_v}{RT} D_m \nabla \cdot P_v \tag{3.23}$$

where D_m is the effective moisture vapour diffusivity which following (Gawin et al. 1999) is given by:

$$D_m = n(1 - S_w)^{A_v} f_s D_{v0} \left(\frac{T}{T_r}\right)^{B_v} \frac{P_{atm}}{P_g} \tag{3.24}$$

where A_v and B_v are material parameters, f_s is a factor to take into account the Knudsen effect and D_{v0} is the free air diffusivity. Equation (3.23) can be simplified to:

$$J_v = -D_{mv} \nabla \cdot P_v \tag{3.25}$$

where the moisture vapour diffusivity is given as:

$$D_{mv} = \frac{M_v}{RT} D_m \tag{3.26}$$

3.3 Heat Flow

The energy balance equation that governs heat flow is given as:

$$\overline{\rho C}\dot{T} + \nabla \cdot (\overline{\rho_w} C_w v_w) + \nabla \cdot J_q + \dot{m}_v H_v + \sum_{i=1}^{nr} \dot{m}_c^i H_c^i = 0 \tag{3.27}$$

where $\overline{\rho C}$ is the heat capacity, J_q the heat flux, $\dot{m}_v H_v$ and $\dot{m}_c^i H_c^i$ represent the latent heat of vaporisation and the heat generated by chemical reactions respectively and nr represents the number of chemical reactions.

The heat capacity $\overline{\rho C}$ is given as (Koniorczyk 2010):

$$\overline{\rho C} = (1-n)\rho_s C_s + (1-S_p) n S_g \rho_g C_g + (1-S_p) n S_w \rho_w C_w + \sum_{i=1}^{nr} n_0 S_p^i \rho_p^i C_p^i \tag{3.28}$$

where C_π represents the specific heat of phase π, with the s subscript representing the solid matrix, the p subscript the precipitated or sorbed material and n_0 is the initial porosity of the medium.

The third term in eq. (3.27), the heat flux represents heat conduction which is assumed to follow Fourier's law and is given by (Gawin et al. 2006):

$$J_q = -k_t \nabla \cdot T \tag{3.29}$$

where k_t is the thermal conductivity of the medium which depends on temperature, void ratio and degree of saturation following (Gawin et al. 1999) and can be defined as:

$$k_t = k_{t0}[1 - A_\lambda (T - T_r)] \left[1 + \frac{4 n \rho_w S_w}{(1-n)\rho_s}\right] \tag{3.30}$$

where k_{t0} and A_λ are material parameters.

The remaining term to be defined in eq. (3.27) is the second term which represents the convective heat transfer. It is assumed in this thesis however following de Morais et al.

(2009), Davie et al. (2010) and Gawin et al. (2011a; 2011b) that this term can be neglected with little loss of accuracy and so it is ignored hereafter.

3.4 Ion Transport

The mass balance equation that governs the transport of a solute within the liquid moisture phase is given as:

$$\overline{\rho_w}\dot{c_\iota} + \nabla.(\overline{\rho_w}c_i v_w) + \nabla.J_d^i - \dot{m}_c^\iota = 0 \tag{3.31}$$

where J_d represents the chemical flux and the final term on the left hand side represents any sources/sinks due to chemical reactions and is discussed in more detail in the following section. The second term in eq. (3.31) represents the advection of the solute which is driven by the liquid moisture velocity and has been discussed in the previous section. The third term represents the flux of the solute; this represents the hydrodynamic dispersion of the solute and is given as (Koniorczyk 2010):

$$J_d^i = -\rho_w D_d^i \nabla.c_i + J_{diff}^i \tag{3.32}$$

where J_{diff}^i is the diffusive flux of species i and D_d^i is the coefficient of mechanical dispersion, which can be described following Bear and Bachmat (1990) as:

$$D_d^i = \alpha_T|v_w|\delta_{kj} + (\alpha_L - \alpha_T)\frac{v_w^k v_w^j}{|v_w|},\ \delta_{kj} = \begin{cases} 1\ if\ k = j \\ 0\ if\ k \neq j \end{cases} \tag{3.33}$$

where α_T and α_L are the transverse and longitudinal dispersivities.

An important consideration in the transport of chemical species is the charge neutrality condition (Lasaga 1981; Baroghel-Bouny et al. 2011; Song et al. 2014). Pore solutions tend towards being charge neutral as any areas of net charge would attract ions of the opposite charge until the solution was balanced. If ions of opposite charge were transported at different rates the charge of the solution could become unbalanced, this leads to the development of an electric field that acts to balance the diffusive flux of the ions and is described by the Poisson and Nernst-Planck equations (Lasaga 1981; Baroghel-Bouny et al. 2011; Song et al. 2014):

$$J_{diff}^i = -nS_w\rho_w D_{mol}^i\left(\nabla \cdot c_i \pm c_i\frac{z_i F}{RT}\nabla \cdot \psi\right) \tag{3.34}$$

$$\varepsilon\nabla^2 \cdot \psi + F[\sum_{i=1}^{ns}(|z_{i+}|c_{i+} - |z_{i-}|c_{i-}) + \rho] = 0 \quad (3.35)$$

where D_{mol}^{i} is the molecular diffusion coefficient of a positively or negatively charged ion i, z is the charge of an ion, F is Faraday's constant, ψ is the electrical potential, ρ is the charge density, ns is the number of chemical species and ε is the dielectric permittivity of the liquid phase. The first term in eq. (3.35) is often small with comparison to the second and ρ can be taken as zero following (Song et al. 2014), reducing the Poisson equation to:

$$\sum_{i=1}^{ns}(|z_{i+}|c_{i+} - |z_{i-}|c_{i-}) = 0 \quad (3.36)$$

If the initial pore solution in the medium is initially neutral then eq. (3.36) means that the current in the medium should be zero giving the diffusion of the ion i as:

$$J_{diff}^{i} = -nS_w\rho_w D_{mol}^{i}\left(\nabla \cdot c_i \pm z_i c_i \frac{\sum_{i=1}^{ns} z_{i-} D_{mol}^{i-}\nabla\cdot c_{i-} - \sum_{i=1}^{ns} z_{i+} D_{mol}^{i+}\nabla\cdot c_{i+}}{\sum_{i=1}^{ns} z_{i+}^2 D_{mol}^{i+} c_{i+} + \sum_{i=1}^{ns} z_{i-}^2 D_{mol}^{i-} c_{i-}}\right) \quad (3.37)$$

Taking this into account the total flux of an ion i can be given by:

$$J_d^i = -\rho_w D_d^i \nabla . c_i - nS_w\rho_w D_{mol}^{i}\left(\nabla \cdot c_i \pm z_i c_i \frac{\sum_{i=1}^{ns} z_{i-} D_{mol}^{i-}\nabla \cdot c_{i-} - \sum_{i=1}^{ns} z_{i+} D_{mol}^{i+}\nabla \cdot c_{i+}}{\sum_{i=1}^{ns} z_{i+}^2 D_{mol}^{i+} c_{i+} + \sum_{i=1}^{ns} z_{i-}^2 D_{mol}^{i-} c_{i-}}\right) \quad (3.38)$$

3.5 Chemical Reactions

The chemical reactions considered throughout this thesis are class 5 ('insufficiently fast surface') or class 6 ('insufficiently fast classical') reactions (Rubin 1983) following the scope of this thesis. The term 'insufficiently fast' means that the rate of transport of the ions is faster than the rates of reaction, such that the local equilibrium assumption is not valid. The terms 'surface' and 'classical' refer to adsorption/desorption and precipitation/dissolution reactions respectively. The reaction rates are considered in two ways here, empirical rates based on the literature (eq. 3.39) and reaction rates based on a combination of empirical values and the activity of the ions in the solution (eqs. 3.40 & 3.41). The first type considered based on empirical rates use a Freundlich type description (Baroghel-Bouny et al. 2011; Song et al. 2014) of the general form:

$$\frac{\dot{m_c^i}}{n_0 \rho_p} = \dot{S_p^i} = -k_d S_p^i + k_a c_i^\lambda \tag{3.39}$$

where k_d and k_a are the desorption and adsorption (or dissolution and precipitation) rates respectively, and λ is the order of the reaction. A plot of a typical Freundlich isotherms for three different reaction orders is shown in Figure 3.3 assuming $k_a = 1$ and $S_p^i = 0$.

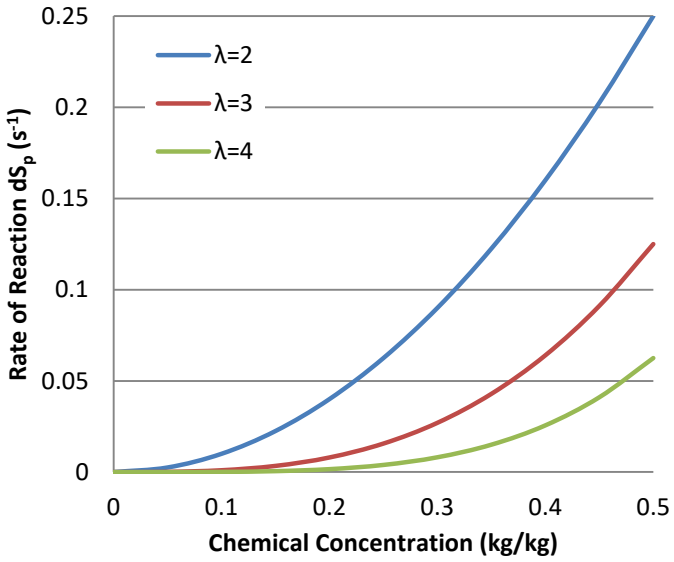

Figure 3.3 – Rate of reaction as calculated by Freundlich isotherm

The calculation of the activity of ions is undertaken in order to take into account the deviation of the solution from an ideal solution. This deviation arises from the fact that the charge of the ions affects their distribution within the solvent, with ions of like charges repelling each other and opposite attracting; meaning that they are not randomly distributed throughout the solvent. The reactions which consider the activity of the solution have a similar form to eq. (3.39) and are also based on a Freundlich type description which is given for precipitation and dissolution (or adsorption and desorption) by Koniorczyk (2012):

$$\dot{S_p^i} = S_w k_{da} (S_i - A')^\lambda, \quad S_i \geq A' \wedge S_p^i < 1 \tag{3.40}$$

$$\dot{S_p^i} = -S_w k_{da} |S_i - 1|^\lambda, \quad S_i < 1 \wedge 0 < S_p^i < 1 \tag{3.41}$$

where k_{da} is a reaction rate, A' is a constant which depends on the reaction and porous medium and S_i is the solution supersaturation ratio which is given as the quotient of the solution activity a_i, and the equilibrium constant for the considered reaction K:

$$S_i = \frac{a_i}{K} \tag{3.42}$$

The Pitzer equations are used here to calculate the activity coefficient of the ions (Pitzer 1973; Steiger et al. 2008; Koniorczyk 2012), which is an extension of Debye-Hückel Theory. The Debye-Hückel equation calculates the activity coefficient of the solution based on the ionic strength of the solution whereas the Pitzer equations also take into account the binary interactions of individual ions and can include higher terms for interaction between three ions and more. The extended Debye-Hückel theory is valid for concentrations up to 0.1 M (Koniorczyk 2012) whereas the Pitzer equations are valid to 6 M for certain ions (Pitzer and Mayorga 1973). The activity coefficients for an anion m and a cation x as predicted by the Pitzer equations are given as:

$$ln\gamma_m = z_m^2 F^{\phi} + m_a(2B_{ma} + ZC_{ma}) + |z_m| m_c m_a C_{ca} \tag{3.43}$$

$$ln\gamma_x = z_x^2 F^{\phi} + m_c(2B_{cx} + ZC_{cx}) + |z_x| m_c m_a C_{ca} \tag{3.44}$$

where γ_π, z_π and m_π are the activity coefficient, charge and mass respectively for an anion or cation, B_π and C_π are the second and third virial coefficients, Z is a function given as:

$$Z = \sum_i m_i |z_i| \tag{3.45}$$

and F^{ϕ} is a function which depends on the ionic strength given as:

$$F^{\phi} = -A^{\phi}\left[\frac{I^{0.5}}{1+bI^{0.5}} + \frac{2}{b} ln(1 + bI^{0.5})\right] + m_c m_a B'_{ca} \tag{3.46}$$

where A^{ϕ} is the Debye-Hückel parameter for the osmotic coefficient, b is a universal parameter and I is the ionic strength of the solution given as:

$$I = \frac{1}{2}\sum_i m_i z_i^2 \tag{3.47}$$

The second virial coefficients found in eq. (3.43) and eq. (3.44) are given as:

$$B_{mx}^{\phi} = \beta_{mx}^{0} + \beta_{mx}^{1} e^{-\alpha_1 I^{0.5}} + \beta_{mx}^{2} e^{-\alpha_2 I^{0.5}} \quad (3.48)$$

$$B_{mx} = \beta_{mx}^{0} + \beta_{mx}^{1} g(\alpha_1 I^{0.5}) + \beta_{mx}^{2} g(\alpha_2 I^{0.5}) \quad (3.49)$$

$$B'_{mx} = \frac{\beta_{mx}^{1} g'(\alpha_1 I^{0.5})}{I} + \frac{\beta_{mx}^{2} g'(\alpha_2 I^{0.5})}{I} \quad (3.50)$$

where α_1 and α_2 are parameters depending on the type of electrolyte and g and g' are functions given as:

$$g(x) = \frac{2}{x^2}(1 - (1 + x)e^{-x}) \quad (3.51)$$

$$g'(x) = \frac{-2}{x^2}(1 - (1 + x + 0.5x^2)e^{-x}) \quad (3.52)$$

The third virial coefficient is given as:

$$C_{mx} = \frac{C_{mx}^{\phi}}{2|z_m z_x|^{0.5}} \quad (3.53)$$

The coefficients in eqs. (3.48, 3.49, 3.50 & 3.53) depend on the temperature and pressure and are given by:

$$f(T) = q_1 + q_2\left(\frac{1}{T} - \frac{1}{T_r}\right) + q_3 \ln\left(\frac{T}{T_r}\right) + q_4(T - T_r) + q_5(T^2 - T_r^2) + q_6 \ln(T - 225) \quad (3.54)$$

where $q_{1\text{-}6}$ are experimentally determined parameters. Given the activity coefficients the activity of any salt can be calculated by:

$$ln a_i = v_m \ln m_m + v_x \ln m_x + v_m \ln \gamma_m + v_x \ln \gamma_x + v_0 \ln a_w \quad (3.55)$$

where a_w is the activity of water which can be calculated from:

$$ln a_w = \frac{-M_w}{1000}(\sum_i m_i)\phi \quad (3.56)$$

where ϕ is the osmotic coefficient of the solution and is given as:

$$\phi = \frac{2}{\sum_i m_i}\left[-\frac{A^{\phi} I^{1.5}}{1 + bI^{0.5}} + m_a m_c\left(B_{ca}^{\phi} + ZC_{ca}\right)\right] + 1 \quad (3.57)$$

An example of how the chemical activity varies with chemical concentration can be seen in Figure 3.4 (Koniorczyk 2012).

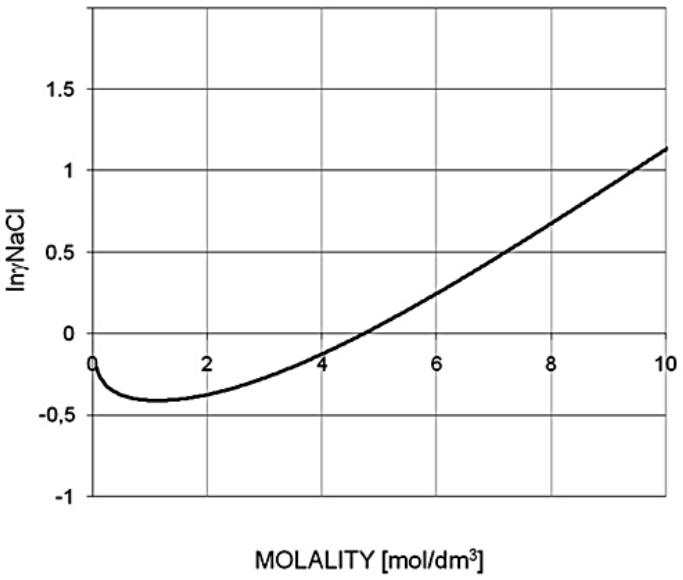

Figure 3.4 – Activity of NaCl in solution (after Koniorczyk (2012))

3.6 Summary

This chapter has detailed the development of a theoretical formulation representing the various phenomena that take place in chemical transport problems. Governing equations of mass and enthalpy balance were considered based on the volume averaging theorem with hybrid mixture theory and were given for the moisture, moisture vapour, temperature and solute mass as:

$$\dot{\overline{\rho_w}} + \nabla \cdot (\overline{\rho_w} v_w) + \dot{m}_v = 0 \tag{3.58}$$

$$\dot{\overline{\rho_v}} + \nabla \cdot J_v - \dot{m}_v = 0 \tag{3.59}$$

$$\overline{\rho C}\dot{T} + \nabla \cdot J_q + \dot{m}_v H_v + \sum_{i=1}^{nr} \dot{m}_c^{\iota} H_c^i = 0 \tag{3.60}$$

$$\overline{\rho_w} \dot{c}_\iota + \nabla \cdot (\overline{\rho_w} c_i v_w) + \nabla \cdot J_d^i - \dot{m}_c^{\iota} = 0 \tag{3.61}$$

The chosen primary variables were the capillary pressure (P_C) for the moisture phase, temperature (T), and chemical concentration (c_i) of each species. The secondary variables are the degrees of saturation of precipitated or sorbed mass resulting from the various chemical reactions. The chemical reactions considered were based on the non-equilibrium assumption and are described using a Freundlich type isotherm. The model developed allows this reaction rate to be calculated from the chemical

concentrations, or for concentrated solutions the ion activities. For the ion activities the Pitzer model was chosen following the approach by Koniorczyk (2012) for its ability to accurately predict the activities at higher concentrations than Debye-Hückel type theories allow.

Chapter 4. Numerical Formulation

4.1 Introduction

The previous chapter presented the theoretical formulation of both the governing equations of mass and energy balance and the constitutive equations describing the physical phenomena. This chapter details the derivation of a numerical procedure used for the solution of the governing system of equations. This type of equation system is usually dealt with using a coupled solution procedure due to the strong interdependence of the primary variables (for example the dependence of solute transport on the liquid moisture advection, which in turn depends on the solute concentration through the liquid density and in some cases viscosity).

The finite element method (FEM) is chosen for the spatial discretisation of the system, where the Galerkin method was employed for choice of the weighting functions. An implicit Euler backward difference scheme was chosen for the temporal discretisation, before finally a Newton-Raphson iteration procedure is employed to solve the system of nonlinear equations. Section 4.2 begins with the formulation of the boundary value problem, before providing a brief explanation of the approach of the FEM and the choice of the weighting functions in section 4.3. The temporal discretisation is detailed in section 4.4 along with the description of the Newton-Raphson procedure.

The model was implemented in FORTRAN and was developed from the starting point of a linear elastic FORTRAN code, written to the coding standard of the research group.

One of the aims of the research of this thesis is to develop a numerical reduction scheme to reduce the computational cost of simulations, whilst maintaining suitable accuracy. Three reduction techniques are proposed each of which reduces the number of chemical species considered in the global system of equations, by calculating the transport of only a number of indicator species (up to 3 depending on the particular technique). The transport of the non-indicator species is then calculated at the end of a time step as a function of the transport of the indicator species. The description of these techniques is presented in section 4.5, before finally a summary of the numerical approach is made in section 4.6.

4.2 Formulation of Boundary Value Problem

The governing equations of mass and energy balance presented in Chapter 3 (from eqs. 3.58, 3.59, 3.60 & 3.61) for the liquid moisture, moisture vapour, temperature and chemical species are recalled here, as follows:

$$\dot{\overline{\rho_w}} + \nabla \cdot (\overline{\rho_w} v_w) + \dot{m}_v = 0 \tag{4.1}$$

$$\dot{\overline{\rho_v}} + \nabla \cdot J_v - \dot{m}_v = 0 \tag{4.2}$$

$$\overline{\rho C}\dot{T} + \nabla \cdot J_q + \dot{m}_v H_v + \sum_{i=1}^{nr} \dot{m}_c^{\iota} H_c^i = 0 \tag{4.3}$$

$$\overline{\rho_w}\dot{c}_{\iota} + \nabla \cdot (\overline{\rho_w} c_i v_w) + \nabla \cdot J_d^i - \dot{m}_c^{\iota} = 0 \tag{4.4}$$

Summing together eq. (4.1) and eq. (4.2) to give the total moisture mass balance equation results in:

$$\dot{\overline{\rho_w}} + \dot{\overline{\rho_v}} + \nabla \cdot (\overline{\rho_w} v_w) + \nabla \cdot J_v = 0 \tag{4.5}$$

and rearranging eq. (4.1) to give the value of the rate of mass change from liquid to vapour, $\dot{m}_v$ gives:

$$\dot{m}_v = -\dot{\overline{\rho_w}} - \nabla \cdot (\overline{\rho_w} v_w) \tag{4.6}$$

this can then be substituted into the enthalpy balance equation (eq. 4.3) to give:

$$\overline{\rho C}\dot{T} + \nabla \cdot J_q + (-\dot{\overline{\rho_w}} - \nabla \cdot (\overline{\rho_w} v_w))H_v + \sum_{i=1}^{nr} \dot{m}_c^{\iota} H_c^i = 0 \tag{4.7}$$

this gives the governing system of equations to be solved for the principal variables P_C, T and c as:

$$\dot{\overline{\rho_w}} + \dot{\overline{\rho_v}} + \nabla \cdot (\overline{\rho_w} v_w) + \nabla \cdot J_v = 0 \tag{4.8}$$

$$\overline{\rho C}\dot{T} + \nabla \cdot J_q + (-\dot{\overline{\rho_w}} - \nabla \cdot (\overline{\rho_w} v_w))H_v + \sum_{i=1}^{nr} \dot{m}_c^{\iota} H_c^i = 0 \tag{4.9}$$

$$\overline{\rho_w}\dot{c}_{\iota} + \nabla \cdot (\overline{\rho_w} c_i v_w) + \nabla \cdot J_d^i - \dot{m}_c^{\iota} = 0 \tag{4.10}$$

subject to (i) initial conditions which specify the values of the primary variables at the beginning of the analysis of:

$$P_C = P_C^0 \quad T = T_0 \quad c_i = c_i^0 \quad in\ \Omega\ and\ on\ \Gamma \tag{4.11}$$

(ii) the Dirichlet boundary conditions of:

$$P_c(t) = P_{c\Gamma} \quad on \quad \Gamma_{di1} \tag{4.12}$$

$$T(t) = T_\Gamma \quad on \quad \Gamma_{di2} \tag{4.13}$$

$$c_i(t) = c_{i\Gamma} \quad on \quad \Gamma_{di3} \tag{4.14}$$

and (iii) the Cauchy type boundary conditions given as:

$$(\overline{\rho_w} v_w + J_v)\boldsymbol{n} - q_{wv} - \beta_c(\rho_v - \rho_v^{env}) = 0 \quad on\ \Gamma_{q1} \tag{4.15}$$

$$\left(J_q - H_v\overline{\rho_w} v_w\right)\boldsymbol{n} - q_t - \alpha_c(T - T^{env}) = 0 \quad on\ \Gamma_{q2} \tag{4.16}$$

$$\left(\overline{\rho_w} c_i v_w + J_d^i\right)\boldsymbol{n} - q_c - \gamma_c(c_i - c_i^{env}) = 0 \quad on\ \Gamma_{q3} \tag{4.17}$$

where $\boldsymbol{n}$ is the unit normal vector to the boundary Γ, q_{wv}, q_t and q_c are the applied moisture, heat and chemical fluxes respectively and β_c, α_c and γ_c are the convective boundary transfer coefficients for moisture, heat and chemical species respectively. ρ_v^{env}, T^{env} and c_i^{env} are the environmental values of moisture vapour density, temperature and chemical concentration respectively.

4.3 Finite Element Solution

4.3.1 General Solution

The next step is to apply the spatial discretisation of the above system. In this thesis, the finite element method is chosen for this following the approach of many other authors (Lewis and Schrefler 1998; Gawin et al. 2006; Cleall et al. 2007; Koniorczyk 2012; Thomas et al. 2012; Chitez and Jefferson 2016). A brief description of the finite element method will be presented here; however, for full details refer to Zienkiewicz et al. (2013). To demonstrate the finite element approach we can consider a general boundary value problem of the form:

$$A(\boldsymbol{u}) = 0 \quad in\ \Omega \tag{4.18}$$

$$B(\boldsymbol{u}) = 0 \quad on\ \Gamma \tag{4.19}$$

in which A and B are arbitrary differential operators. Integrating over the domain and boundary we can make the following statement:

$$\int_{\Omega} WA(u)d\Omega + \int_{\Gamma} WB(u)d\Gamma = 0 \quad (4.20)$$

where W is an arbitrary weighting function. Assuming that the integrands can be evaluated there are some restrictions on the choice of functions for W, full details of which can be found in (Zienkiewicz et al. 2013). Once the equations are set in this form we can apply the integral over a number of finite elements, which are summed together to form the global discretised system:

$$\int_{\Omega} WA(u)d\Omega + \int_{\Gamma} WB(u)d\Gamma = \sum_{i=1}^{nelem}\left(\int_{\Omega_e} WA(u)d\Omega_e + \int_{\Gamma_e} WB(u)d\Gamma_e\right) \quad (4.21)$$

noting that the finite element method is an approximation method the solution will be of the form:

$$u \approx \hat{u} = \sum_{i=1}^{n} N_i \bar{u}_i = N\bar{u} \quad (4.22)$$

where N is a vector of shape functions defined in terms of local coordinates in section 4.3.4. From this we then obtain the weighted residual equation:

$$\sum_{i=1}^{nelem}\left(\int_{\Omega_e} WA(N\bar{u})d\Omega_e + \int_{\Gamma_e} WB(N\bar{u})d\Gamma_e\right) = 0 \quad (4.23)$$

where $A(N\bar{u})$ and $B(N\bar{u})$ represent the residual error and the boundary residual error respectively that arise from the approximation (eq. 4.22). The approach of the finite element method is to minimise this residual.

4.3.2 Application to the System of Governing Equations

Applying the above discretisation to the governing equations of mass and energy balance (eqs. 4.3, 4.4 & 4.5) gives:

$$\int_{\Omega_e} W\left(\dot{\overline{\rho_w}} + \dot{\overline{\rho_v}} + \nabla\cdot(\overline{\rho_w}v_w) + \nabla\cdot J_v\right)d\Omega_e - \int_{\Gamma_{q1e}} W\Big((\overline{\rho_w}v_w + J_v)\boldsymbol{n} - q_{wv} - \beta_c(\rho_v - \rho_v^{env})\Big)\Gamma_{q1e} = 0 \quad (4.24)$$

$$\int_{\Omega_e} W\left(\overline{\rho C}\dot{T} + \nabla\cdot J_q - H_v\left(\dot{\overline{\rho_w}} + \nabla\cdot(\overline{\rho_w}v_w)\right) + \sum_{i=1}^{nr}\dot{m}_c^{\iota}H_c^i\right)d\Omega_e - \int_{\Gamma_{q2e}} W\Big(\big(J_q - H_v\overline{\rho_w}v_w\big)\boldsymbol{n} - q_T - \alpha_c(T - T^{env})\Big)\Gamma_{q2e} = 0 \quad (4.25)$$

$$\int_{\Omega_e} W\left(\overline{\rho_w}\dot{c_\iota} + \nabla\cdot(\overline{\rho_w}c_i v_w) + \nabla.J_d^i - \dot{m_c^\iota}\right)d\Omega_e - \int_{\Gamma_{q3e}} W\left(\left(J_d^i + \overline{\rho_w}c_i v_w\right)\boldsymbol{n} - q_c - \gamma_c(c_i - c_i^{env})\right)\Gamma_{q3e} = 0 \quad (4.26)$$

which can be rearranged into a more convenient form:

$$\int_{\Omega_e} W\left(\dot{\overline{\rho_w}} + \dot{\overline{\rho_v}}\right)d\Omega_e + \int_{\Omega_e} W\nabla\cdot\left((\overline{\rho_w}v_w) + J_v\right)d\Omega_e - \int_{\Gamma_{q1e}} W\left((\overline{\rho_w}v_w + J_v)\boldsymbol{n}\right)\Gamma_{q1e} + \int_{\Gamma_{q1e}} W\left(q_{wv} + \beta_c(\rho_v - \rho_v^{env})\right)\Gamma_{q1e} = 0 \quad (4.27)$$

$$\int_{\Omega_e} W\left(\overline{\rho C}\dot{T} - H_v\dot{\overline{\rho_w}} + \sum_{i=1}^{nr}\dot{m_c^\iota}H_c^i\right)d\Omega_e + \int_{\Omega_e} W\nabla\cdot\left(J_q - H_v(\overline{\rho_w}v_w)\right)d\Omega_e - \int_{\Gamma_{q2e}} W\left(\left(J_q - H_v\overline{\rho_w}v_w\right)\boldsymbol{n}\right)\Gamma_{q2e} + \int_{\Gamma_{q2e}} W(q_T + \alpha_c(T - T^{env}))\Gamma_{q2e} = 0 \quad (4.28)$$

$$\int_{\Omega_e} W\left(\overline{\rho_w}\dot{c_\iota} - m_c^i\right)d\Omega_e + \int_{\Omega_e} W\nabla\cdot\left((\overline{\rho_w}c_i v_w) + J_d^i\right)d\Omega_e - \int_{\Gamma_{q3e}} W\left(\left(J_d^i + \overline{\rho_w}c_i v_w\right)\boldsymbol{n}\right)\Gamma_{q3e} + \int_{\Gamma_{q3e}} W(q_c + \gamma_c(c_i - c_i^{env}))\Gamma_{q3e} = 0 \quad (4.29)$$

if we then apply the Gauss-Green divergence theorem by performing integration by parts on the divergent terms we can obtain the weak form of the equations which will allow us to cancel the boundary flux terms:

$$\int_{\Omega_e} W\left(\dot{\overline{\rho_w}} + \dot{\overline{\rho_v}}\right)d\Omega_e + \cancel{\int_{\Gamma_{q1e}} W\left((\overline{\rho_w}v_w + J_v)\boldsymbol{n}\right)\Gamma_{q1e}} - \int_{\Omega_e}\nabla W\left((\overline{\rho_w}v_w) + J_v\right)d\Omega_e - \cancel{\int_{\Gamma_{q1e}} W\left((\overline{\rho_w}v_w + J_v)\boldsymbol{n}\right)\Gamma_{q1e}} + \int_{\Gamma_{q1e}} W\left(q_{wv} + \beta_c(\rho_v - \rho_v^{env})\right)\Gamma_{q1e} = 0 \quad (4.30)$$

$$\int_{\Omega_e} W\left(\overline{\rho C}\dot{T} - H_v\dot{\overline{\rho_w}} + \sum_{i=1}^{nr}\dot{m_c^\iota}H_c^i\right)d\Omega_e + \cancel{\int_{\Gamma_{q2e}} W\left(\left(J_q - H_v\overline{\rho_w}v_w\right)\boldsymbol{n}\right)}\Gamma_{q2e} - \int_{\Omega_e}\nabla W\left(J_q - H_v(\overline{\rho_w}v_w)\right)d\Omega_e - \cancel{\int_{\Gamma_{q2e}} W\left(\left(J_q - H_v\overline{\rho_w}v_w\right)\boldsymbol{n}\right)}\Gamma_{q2e} + \int_{\Gamma_{q2e}} W(q_T + \alpha_c(T - T^{env}))\Gamma_{q2e} = 0 \quad (4.31)$$

$$\int_{\Omega_e} W\left(\overline{\rho_w}\dot{c_\iota} - \dot{m_c^\iota}\right)d\Omega_e + \cancel{\int_{\Gamma_{q3e}} W\left(\left(J_d^i + \overline{\rho_w}c_i v_w\right)\boldsymbol{n}\right)}\Gamma_{q3e} - \int_{\Omega_e}\nabla W\left((\overline{\rho_w}c_i v_w) + J_d^i\right)d\Omega_e - \cancel{\int_{\Gamma_{q3e}} W\left(\left(J_d^i + \overline{\rho_w}c_i v_w\right)\boldsymbol{n}\right)}\Gamma_{q3e} + \int_{\Gamma_{q3e}} W(q_c + \gamma_c(c_i - c_i^{env}))\Gamma_{q3e} = 0 \quad (4.32)$$

leading to:

$$\int_{\Omega_e} W\,(\dot{\overline{\rho_w}} + \dot{\overline{\rho_v}})d\Omega_e - \int_{\Omega_e} \nabla W\left((\overline{\rho_w} v_w) + J_v\right)d\Omega_e + \int_{\Gamma_{q1e}} W\big(q_{wv} + \beta_c(\rho_v - \rho_v^{env})\big)\Gamma_{q1e} = 0 \quad (4.33)$$

$$\int_{\Omega_e} W\left(\overline{\rho C}\dot{T} - H_v\dot{\overline{\rho_w}} + \sum_{i=1}^{nr} \dot{m}_c^{\iota} H_c^i\right)d\Omega_e - \int_{\Omega_e} \nabla W\left(J_q - H_v(\overline{\rho_w} v_w)\right)d\Omega_e + \int_{\Gamma_{q2e}} W(q_T + \alpha_c(T - T^{env}))\Gamma_{q2e} = 0 \quad (4.34)$$

$$\int_{\Omega_e} W\left(\overline{\rho_w}\dot{c}_{\iota} - \dot{m}_c^{\iota}\right)d\Omega_e - \int_{\Omega_e} \nabla W\left((\overline{\rho_w} c_i v_w) + J_d^i\right)d\Omega_e + \int_{\Gamma_{q3e}} W(q_c + \gamma_c(c_i - c_i^{env}))\Gamma_{q3e} = 0 \quad (4.35)$$

The next step is to define the time derivatives of the phase averaged densities, which are functions of the chosen principal variables. This is accomplished using the chain rule of differentiation, as follows:

$$\dot{\overline{\rho_w}} = \frac{\partial\overline{\rho_w}}{\partial P_C}\dot{P}_C + \frac{\partial\overline{\rho_w}}{\partial T}\dot{T} + \sum_{i=1}^{ns}\frac{\partial\overline{\rho_w}}{\partial c_i}\dot{c}_{\iota} + \sum_{i=1}^{nr}\frac{\partial\overline{\rho_w}}{\partial S_p}\dot{S}_p \quad (4.36)$$

$$\dot{\overline{\rho_v}} = \frac{\partial\overline{\rho_v}}{\partial P_C}\dot{P}_C + \frac{\partial\overline{\rho_v}}{\partial T}\dot{T} + \sum_{i=1}^{ns}\frac{\partial\overline{\rho_v}}{\partial c_i}\dot{c}_{\iota} + \sum_{i=1}^{nr}\frac{\partial\overline{\rho_v}}{\partial S_p}\dot{S}_p \quad (4.37)$$

similarly recalling that the moisture vapour dispersive flux is given as (eq. 3.25):

$$J_v = -D_{mv}\nabla\cdot P_v \quad (4.38)$$

the spatial variability of the vapour pressure is given as:

$$\nabla\cdot P_v = \frac{\partial P_v}{\partial P_C}\nabla\cdot P_C + \frac{\partial P_v}{\partial T}\nabla\cdot T \quad (4.39)$$

introducing a description of the rate of mass transfer caused by chemical reactions given by:

$$\dot{m}_c^{\iota} = n_0\rho_p^i\dot{S}_p^{\iota} \quad (4.40)$$

and defining the permeability of the medium $K_w$as:

$$K_w = \frac{K_i K_{rw}}{\mu_w} \quad (4.41)$$

then recalling eqs. (3.11, 3.25 ,3.29 & 3.38) and substituting them into eqs. (4.33-4.35) leads to:

$$\int_{\Omega_e} W\left(\left(\frac{\partial\overline{\rho_w}}{\partial P_C}+\frac{\partial\overline{\rho_v}}{\partial P_C}\right)\dot{P_C}+\left(\frac{\partial\overline{\rho_w}}{\partial T}+\frac{\partial\overline{\rho_v}}{\partial T}\right)\dot{T}+\sum_{i=1}^{ns}\left(\frac{\partial\overline{\rho_w}}{\partial c_i}+\frac{\partial\overline{\rho_v}}{\partial c_i}\right)\dot{c_\iota}+\sum_{i=1}^{nr}(\frac{\partial\overline{\rho_w}}{\partial S_p^i}+\frac{\partial\overline{\rho_v}}{\partial S_p^i})\dot{S_p^\iota}\right)d\Omega_e-\int_{\Omega_e}\nabla W\left(\rho_w K_w(\nabla\cdot P_C+\rho_w g)-D_{mv}\frac{\partial P_v}{\partial P_C}\nabla\cdot P_C-D_{mv}\frac{\partial P_v}{\partial T}\nabla\cdot T\right)d\Omega_e+\int_{\Gamma_{q1e}}W\left(q_{wv}+\beta_c(\rho_v-\rho_v^{env})\right)\Gamma_{q1e}=0 \quad (4.42)$$

$$\int_{\Omega_e} W\left(-H_v\frac{\partial\overline{\rho_w}}{\partial P_C}\dot{P_C}+\left(\overline{\rho C}-H_v\frac{\partial\overline{\rho_w}}{\partial T}\right)\dot{T}-H_v\sum_{i=1}^{ns}\frac{\partial\overline{\rho_w}}{\partial c_i}\dot{c_\iota}+\sum_{i=1}^{nr}\left(-H_v\frac{\partial\overline{\rho_w}}{\partial S_p^i}+n_0\rho_p^i H_c^i\right)\dot{S_p^\iota}\right)d\Omega_e-\int_{\Omega_e}\nabla W\left(-k_t\nabla\cdot T-H_v\rho_w K_w(\nabla\cdot P_C+\rho_w g)\right)d\Omega_e+\int_{\Gamma_{q2e}}W(q_T+\alpha_c(T-T^{env}))\Gamma_{q2e}=0 \quad (4.43)$$

$$\int_{\Omega_e} W\left(\frac{\partial\overline{\rho_w c_i}}{\partial P_C}\dot{P_C}+\frac{\partial\overline{\rho_w c_i}}{\partial T}\dot{T}+\frac{\partial\overline{\rho_w c_i}}{\partial c_i}\dot{c_\iota}+(\frac{\partial\overline{\rho_w c_i}}{\partial S_p^i}-n_0\rho_p^i)\dot{S_p^\iota}\right)d\Omega_e-\int_{\Omega_e}\nabla W\left(\rho_w K_w c_i(\nabla\cdot P_C+\rho_w g)-\rho_w D_d^i\nabla\cdot c_i-nS_w\rho_w D_{mol}^i\left(\pm z_i c_i\frac{\sum_{i=1}^{ns}z_{i-}D_{mol}^{i-}\nabla\cdot c_{i-}-\sum_{i=1}^{ns}z_{i+}D_{mol}^{i+}\nabla\cdot c_{i+}}{\sum_{i=1}^{ns}z_{i+}^2D_{mol}^{i+}c_{i+}+\sum_{i=1}^{ns}z_{i-}^2D_{mol}^{i-}c_{i-}}\right)\right)d\Omega_e+\int_{\Gamma_{q3e}}W(q_c+\gamma_c(c_i-c_i^{env}))\Gamma_{q3e}=0 \quad (4.44)$$

which can be written using matrix notation as:

$$\int_{\Omega_e} W\left(C_{11}\dot{P_C}+C_{12}\dot{T}+\sum_{i=1}^{ns}C_{13}^i\dot{c_\iota}+\sum_{i=1}^{nr}C_{1Sp}^i\dot{S_p^\iota}\right)d\Omega_e+\int_{\Omega_e}\nabla W\left(K_{11}\nabla\cdot P_C+K_{12}\nabla\cdot T-\rho_w K_w\rho_w g\right)d\Omega_e+\int_{\Gamma_{q1e}}W\left(q_{wv}+\beta_c(\rho_v-\rho_v^{env})\right)\Gamma_{q1e}=0 \quad (4.45)$$

$$\int_{\Omega_e} W\left(C_{21}\dot{P_C}+C_{22}\dot{T}+\sum_{i=1}^{ns}C_{23}^i\dot{c_\iota}+\sum_{i=1}^{nr}C_{2Sp}^i\dot{S_p^\iota}\right)d\Omega_e+\int_{\Omega_e}\nabla W\left(K_{21}\nabla\cdot P_C+K_{22}\nabla\cdot T+H_v\rho_w K_w\rho_w g\right)d\Omega_e+\int_{\Gamma_{q2e}}W(q_T+\alpha_c(T-T^{env}))\Gamma_{q2e}=0 \quad (4.46)$$

$$\int_{\Omega_e} W\left(C_{31}^i\dot{P_C}+C_{32}^i\dot{T}+C_{33}^i\dot{c_\iota}+C_{3Sp}^i\dot{S_p^\iota}\right)d\Omega_e+\int_{\Omega_e}\nabla W\left(K_{31}^i\nabla\cdot P_c+K_{33}^i\nabla\cdot c_i-\rho_w K_w c_i\rho_w g+nS_w\rho_w D_{mol}^i\left(\pm z_i c_i\frac{\sum_{i=1}^{ns}z_{i-}D_{mol}^{i-}\nabla\cdot c_{i-}-\sum_{i=1}^{ns}z_{i+}D_{mol}^{i+}\nabla\cdot c_{i+}}{\sum_{i=1}^{ns}z_{i+}^2D_{mol}^{i+}c_{i+}+\sum_{i=1}^{ns}z_{i-}^2D_{mol}^{i-}c_{i-}}\right)\right)d\Omega_e+\int_{\Gamma_{q3e}}W(q_c+\gamma_c(c_i-c_i^{env}))\Gamma_{q3e}=0 \quad (4.47)$$

in which:

$$C_{11} = \frac{\partial \overline{\rho_w}}{\partial P_C} + \frac{\partial \overline{\rho_v}}{\partial P_C} \qquad C_{12} = \frac{\partial \overline{\rho_w}}{\partial T} + \frac{\partial \overline{\rho_v}}{\partial T} \qquad C_{13}^i = \frac{\partial \overline{\rho_w}}{\partial c_i} + \frac{\partial \overline{\rho_v}}{\partial c_i}$$

$$C_{21} = -H_v \frac{\partial \overline{\rho_w}}{\partial P_c} \qquad C_{22} = \overline{\rho C} - H_v \frac{\partial \overline{\rho_w}}{\partial T} \qquad C_{23}^i = -H_v \frac{\partial \overline{\rho_w}}{\partial c_i}$$

$$C_{31}^i = \frac{\partial \overline{\rho_w} c_i}{\partial P_c} \qquad C_{32}^i = \frac{\partial \overline{\rho_w} c_i}{\partial T} \qquad C_{33}^i = \frac{\partial \overline{\rho_w} c_i}{\partial c_i}$$

$$C_{1Sp}^i = \frac{\partial \overline{\rho_w}}{\partial S_p^i} + \frac{\partial \overline{\rho_v}}{\partial S_p^i} \qquad C_{2Sp}^i = -H_v \frac{\partial \overline{\rho_w}}{\partial S_p^i} + n_0 \rho_p^i H_c^i \qquad C_{3Sp}^i = \frac{\partial \overline{\rho_w} c_i}{\partial S_p^i} - n_0 \rho_p^i$$

$$K_{11} = -\rho_w K_w + D_{mv} \frac{\partial P_v}{\partial P_C} \qquad K_{12} = D_{mv} \frac{\partial P_v}{\partial T} \qquad K_{13}^i = 0$$

$$K_{21} = H_v \rho_w K_w \qquad K_{22} = k_t \qquad K_{23}^i = 0$$

$$K_{31}^i = -\rho_w K_w c_i \qquad K_{32}^i = 0 \qquad K_{33}^i = \rho_w D_d^i$$

4.3.3 Weighting by Galerkin Method

Many sets of functions can be chosen to be used as the weighting functions W, here however the Galerkin method (Galerkin 1915) is chosen and as such the weighting functions W are chosen to be equal to the shape functions used in eq. (4.22) in the original approximation. The Galerkin method is preferred here due to the fact that this method often leads to symmetric matrices. Applying this and the approximation of eq. (4.22) gives the following system of equations in matrix form (considering a single chemical species):

$$\begin{bmatrix} \widetilde{K_{11}} & \widetilde{K_{12}} & 0 \\ \widetilde{K_{21}} & \widetilde{K_{22}} & 0 \\ \widetilde{K_{31}^i} & 0 & \widetilde{K_{33}^i} \end{bmatrix} \begin{bmatrix} \overline{P_c} \\ \overline{T} \\ \overline{c_i} \end{bmatrix} + \begin{bmatrix} \widetilde{C_{11}} & \widetilde{C_{12}} & \widetilde{C_{13}^i} \\ \widetilde{C_{21}} & \widetilde{C_{22}} & \widetilde{C_{23}^i} \\ \widetilde{C_{31}^i} & \widetilde{C_{32}^i} & \widetilde{C_{33}^i} \end{bmatrix} \begin{bmatrix} \dot{\overline{P_C}} \\ \dot{\overline{T}} \\ \dot{c}_i \end{bmatrix} = \begin{bmatrix} f_1 \\ f_2 \\ f_3^i \end{bmatrix} \tag{4.48}$$

where the primary variables are approximated as:

$$P_C = N\overline{P_C} \qquad T = N\overline{T} \qquad c_i = N\overline{c_i} \tag{4.49}$$

the global matrices K and C are given by:

$$\check{K} = \sum_{i=1}^{nelem} \int_{\Omega_e} \nabla N^t K \nabla N \, d\Omega_e \qquad \check{C} = \sum_{i=1}^{nelem} \int_{\Omega_e} N^t C N \, d\Omega_e \tag{4.50}$$

the global right hand side vector is given by:

$$f = \sum_{i=1}^{nelem} f_e \tag{4.51}$$

where the right hand side vector for each of the variables is given as:

$$f_1 = \int_{\Omega_e} \nabla N^t \, (\rho_w K_w \rho_w g) d\Omega_e - \int_{\Gamma_{q1e}} N^t \left(q_{wv} + \beta_c(\rho_v - \rho_v^{env})\right) \Gamma_{q1e} - \int_{\Omega_e} N^t \left(\sum_{i=1}^{nr} C_{1Sp}^i \dot{S_p^i}\right) d\Omega_e \tag{4.52}$$

$$f_2 = -\int_{\Omega_e} \nabla N^t \, (H_v \rho_w K_w \rho_w g) d\Omega_e - \int_{\Gamma_{q2e}} N^t \left(q_t + \alpha_c(T - T^{env})\right) \Gamma_{q2e} - \int_{\Omega_e} N^t \left(\sum_{i=1}^{nr} C_{2Sp}^i \dot{S_p^i}\right) d\Omega_e \tag{4.53}$$

$$f_3^i = \int_{\Omega_e} \nabla N^t \left(c_i \rho_w K_w \rho_w g - n S_w \rho_w D_{mol}^i \left(\pm z_i c_i \frac{\sum_{i=1}^{ns} z_{i-} D_{mol}^{i-} \nabla \cdot c_{i-} - \sum_{i=1}^{ns} z_{i+} D_{mol}^{i+} \nabla \cdot c_{i+}}{\sum_{i=1}^{ns} z_{i+}^2 D_{mol}^{i+} c_{i+} + \sum_{i=1}^{ns} z_{i-}^2 D_{mol}^{i-} c_{i-}} \right) \right) d\Omega_e - \int_{\Gamma_{q3e}} N^t \left(q_c + \gamma_c(c_i - c_i^{env})\right) \Gamma_{q3e} - \int_{\Omega_e} N^t \left(C_{3Sp}^i \dot{S_p^i}\right) d\Omega_e \tag{4.54}$$

It can be seen in the chemical balance equation above that the flux term relating to the charge neutrality condition has been moved to the right hand side, this is because here it is to be dealt with explicitly. This global system of equations can be written in condensed form as:

$$K\Phi + C\dot{\Phi} = f \tag{4.55}$$

where Φ is the vector of primary variables.

4.3.4 Shape Functions and Numerical Integration

As seen in the previous section, a vector of shape functions is used both in the approximation of eq. (4.22) and through the choice of weighting functions. It is therefore necessary to define these shape functions and describe the means of evaluating the above integrals. Bilinear quadrilaterals are chosen here as the element type, it can be noted however that other element types can be chosen depending on the continuity required and on the geometry of the problem domain. The shape functions of a bilinear quadrilateral are given as:

$$N = \begin{bmatrix} 0.25(1-\xi)(1-\eta) \\ 0.25(1+\xi)(1-\eta) \\ 0.25(1+\xi)(1+\eta) \\ 0.25(1-\xi)(1+\eta) \end{bmatrix} \quad (4.56)$$

where ξ and η are local parametric coordinates with values range -1< ξ, η <+1, which are mapped to the Cartesian coordinates using interpolation, known as isoparametric mapping.

The integrals are evaluated in a numerical fashion using a Gauss-Legendre rule (Zienkiewicz et al. 2013). The Gauss-Legendre method calculates the value of the function at discrete points and sums them to give the approximation to the integral. The 2x2 Gauss-Legendre rule is used here due to its ability to exactly evaluate the integrals considered and due to convergence and stability criteria (Zienkiewicz et al. 2013). This rule uses 4 sampling points with local coordinates of (-1/√3 , -1/√3), (1/√3 , -1/√3), (1/√3 , 1/√3) and (-1/√3 , 1/√3), each with a weight of 1. Using this rule the approximation of an integral I, is given by:

$$I = \int_{-1}^{+1}\int_{-1}^{+1} f(\xi,\eta)d\xi d\eta = \sum_{i=1}^{4} f(\xi_i,\eta_i)W_i \quad (4.57)$$

4.4 Temporal Discretisation and Non-linearity

Following the spatial discretisation of the last section, the next step is to carry out the temporal discretisation. The method chosen here was the implicit backward difference scheme following Gawin et al. (2006), which when applied to eq. (4.55) gives:

$$\check{K}\Phi^{t+1} + \frac{1}{\Delta t}\check{C}(\Phi^{t+1} - \Phi^{t}) = \check{f} \quad (4.58)$$

equation (4.58) is non-linear as the matrices depend on the values of the primary variables Φ; the error due to an approximation of these values is given by:

$$\varphi = \Delta t\check{K}\Phi^{t+1} + \check{C}(\Phi^{t+1} - \Phi^{t}) - \Delta t\check{f} \quad (4.59)$$

To deal with this non-linearity the Newton-Raphson iteration procedure has been used following Gawin et al. (2006), to minimise this approximation error. This approach minimises this error by expanding eq. (4.59) as a Taylor's series, ignoring higher order terms and equating to zero, which gives:

$$\varphi + \left[\frac{\partial \varphi}{\partial \Phi_k^{t+1}}\right] \delta\Phi_{k+1}^{t+1} = 0 \tag{4.60}$$

which can be rearranged to give the change in primary variables $\delta\Phi$:

$$\delta\Phi_{k+1}^{t+1} = \left[\frac{\partial \varphi}{\partial \Phi_k^{t+1}}\right]^{-1} (-\varphi) \tag{4.61}$$

the iteration updates the primary variables as follows:

$$\Phi_{k+1}^{t+1} = \Phi_k^{t+1} + \delta\Phi_{k+1}^{t+1} \tag{4.62}$$

differentiating the error with respect to the primary variables and substituting into eq. (4.59) gives the system of equations in matrix form:

$$\left\{ \Delta t \begin{bmatrix} \Delta\widetilde{K_{11}} & \Delta\widetilde{K_{12}} & 0 \\ \Delta\widetilde{K_{21}} & \Delta\widetilde{K_{22}} & 0 \\ \Delta\widetilde{K_{31}^{l}} & 0 & \Delta\widetilde{K_{33}^{l}} \end{bmatrix} + \begin{bmatrix} \Delta\widetilde{C_{11}} & \Delta\widetilde{C_{12}} & \Delta\widetilde{C_{13}^{l}} \\ \Delta\widetilde{C_{21}} & \Delta\widetilde{C_{22}} & \Delta\widetilde{C_{23}^{l}} \\ \Delta\widetilde{C_{31}^{l}} & \Delta\widetilde{C_{32}^{l}} & \Delta\widetilde{C_{33}^{l}} \end{bmatrix} - \Delta t \begin{bmatrix} \Delta f_1 \\ \Delta f_2 \\ \Delta f_3^i \end{bmatrix} \right\} \begin{bmatrix} \delta\overline{P_c} \\ \delta\overline{T} \\ \delta\overline{c_l} \end{bmatrix} = \begin{bmatrix} -\varphi_s \\ -\varphi_T \\ -\varphi_C^i \end{bmatrix} \tag{4.63}$$

where ΔK, ΔC and Δf are tangent matrices and are given by:

$$\widetilde{\Delta K} = \sum_{i=1}^{nelem} \int_{\Omega_e} \nabla N^t \Delta K \nabla N \, d\Omega_e \qquad \widetilde{\Delta C} = \sum_{i=1}^{nelem} \int_{\Omega_e} N^t \Delta C N \, d\Omega_e \tag{4.64}$$

and:

$$\Delta K_{i,j} = K_{i,j} + \sum_{k=1}^{ndof} \frac{\partial K_{i,k}}{\partial \Phi_k} \Phi_k^{t+1} \tag{4.65}$$

$$\Delta C_{i,j} = C_{i,j} + \sum_{k=1}^{ndof} \frac{\partial C_{i,k}}{\partial \Phi_k} \Phi_k^{t+1} \tag{4.66}$$

The equations presented so far have been written for the consideration of one chemical species, however this was just for brevity and the formulation remains the same for two or more. The system of equations for ns chemical species would be given as:

$$\begin{bmatrix} \widetilde{K_{11}} & \widetilde{K_{12}} & 0 & \dots & 0 \\ \widetilde{K_{21}} & \widetilde{K_{22}} & 0 & \dots & 0 \\ \widetilde{K_{31}^{l}} & 0 & \widetilde{K_{33}^{l}} & \dots & 0 \\ \vdots & \vdots & \vdots & \ddots & 0 \\ \widetilde{K_{31}^{ns}} & 0 & 0 & 0 & \widetilde{K_{33}^{ns}} \end{bmatrix} \begin{bmatrix} \overline{P_C} \\ \overline{T} \\ \overline{c_l} \\ \vdots \\ \overline{c_{ns}} \end{bmatrix} + \begin{bmatrix} \widetilde{C_{11}} & \widetilde{C_{12}} & \widetilde{C_{13}^{l}} & \dots & \widetilde{C_{13}^{ns}} \\ \widetilde{C_{21}} & \widetilde{C_{22}} & \widetilde{C_{23}^{l}} & \dots & \widetilde{C_{23}^{ns}} \\ \widetilde{C_{31}^{l}} & \widetilde{C_{32}^{l}} & \widetilde{C_{33}^{l}} & \dots & 0 \\ \vdots & \vdots & \vdots & \ddots & 0 \\ \widetilde{C_{31}^{ns}} & \widetilde{C_{32}^{ns}} & 0 & 0 & \widetilde{C_{33}^{ns}} \end{bmatrix} \begin{bmatrix} \dot{\overline{P_C}} \\ \dot{\overline{T}} \\ \dot{\overline{c_l}} \\ \vdots \\ \dot{\overline{c_{ns}}} \end{bmatrix} = \begin{bmatrix} f_1 \\ f_2 \\ f_3^i \\ \vdots \\ f_3^{ns} \end{bmatrix} \tag{4.67}$$

it can be noted here that in this thesis, since only kinetic reactions have been considered, it is assumed that any coupling between chemical species can only be found in the right hand side vector through the kinetic reaction rates and the charge neutrality condition.

4.5 Problem Reduction Scheme

One of the main aims of this thesis is to address the computational demand posed by certain reactive transport problems. In this section to reduce the size of the governing system of equations three different reduction schemes, denoted PRS1, PRS2 and PRS3 are proposed and detailed. In each of these schemes, a reduced set of species is chosen for full computation. These selected species are termed 'indicators' and the response of the remaining species is computed at each time step based upon the calculated transport of the indicators. The difference between the three reduction approaches (PRS 1 to 3) lies in both the number of indicator species used and in the method employed for calculating the transport of the remaining species.

The rate of transport of an ion depends on the moisture velocity (which is the same for all ions), the concentration gradient and the diffusion coefficient. The three approaches proposed here aim to estimate the transport of an ion relative to indicator species, considering the differences in diffusion coefficient and the maximum concentration gradient. For each PRS bounds checking was also implemented to prevent physically meaningless results (i.e. negative concentrations).

4.5.1 PRS 1

The first reduction scheme is an extrapolation technique which uses just one indicator species. The transport of all other species is computed from the incremental change in the concentration of the indicator species multiplied by a concentration gradient ratio and diffusion coefficient ratio, according to eq. (4.68). The concentration gradient multiplier is the ratio of the maximum concentration gradients (initial concentration – boundary concentration) of the current and indicator species respectively. The diffusion coefficient ratio is defined in a similar manner. The concentration of a non-indicator species i is given as:

$$c_i^{t+1} = c_i^t + \frac{\left(c_i^0 - c_i^b\right)}{\left(c_{ind}^0 - c_{ind}^b\right)} \frac{D_{mol}^i}{D_{mol}^{ind}} \Delta c_{ind} \quad (4.68a)$$

where c_i is the concentration of a chemical species, Δc_{ind} is the change of concentration of the indicator species due to transport over a time step, c^0 and c^b refer to the initial and boundary concentrations respectively, D_{mol}^i and D_{mol}^{ind} are the diffusion coefficients a species and the indicator respectively and the t superscript denotes time. Letting w denote the weighting function for the indicator species, eq. (4.68a) can be written in condensed form as:

$$c_i^{t+1} = c_i^t + w(c^0, c^b, D_{mol}) \cdot \Delta c_{ind} \quad (4.68b)$$

A depiction of the use of indicators can be seen in Figure 4.1a. Figure 4.1b shows the weighting function w (for a case where $c_i^0 = c_i^b$ and $c_{ind}^0 = c_{ind}^b$).

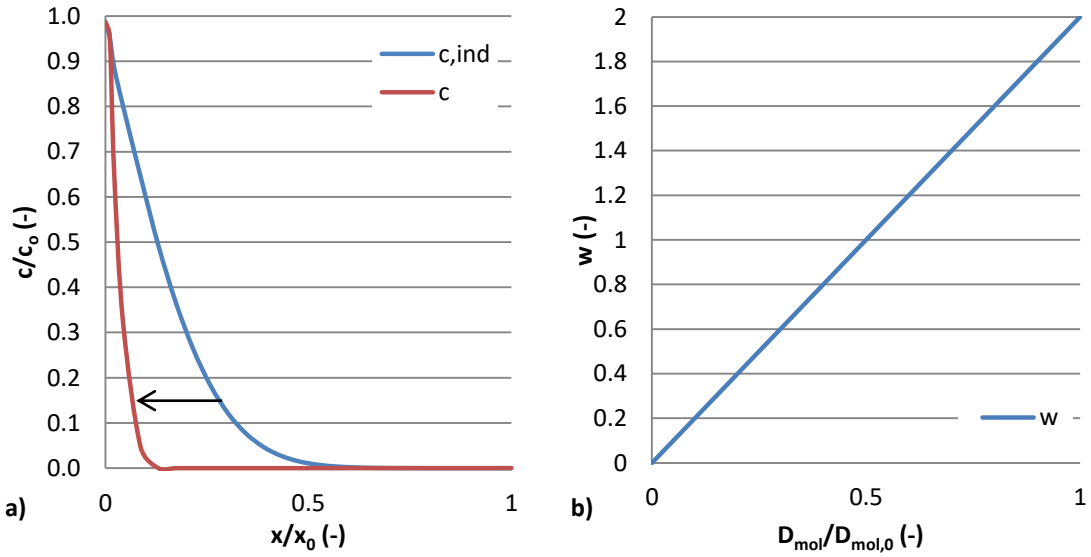

Figure 4.1 – PRS 1 a) Use of indicator species and b) Weighting function

4.5.2 PRS 2

The second method uses two indicator species, which are those with the largest and smallest diffusion coefficients. In this case, the solution is bounded by the response of the two indicators. For each non-indicator species, the weighting given to the transport of each indicator species is based on the concentration gradient ratio and a

linear interpolation between the diffusion coefficients. The concentration of a non-indicator species i is given as:

$$c_i^{t+1} = c_i^t + \frac{\left(c_i^0 - c_i^b\right)}{\left(c_{ind,l}^0 - c_{ind,l}^b\right)}\left(\frac{D_{mol}^{ind,u} - D_{mol}^i}{D_{mol}^{ind,u} - D_{mol}^{ind,l}}\right)\Delta c_{ind,l} + \frac{\left(c_i^0 - c_i^b\right)}{\left(c_{ind,u}^0 - c_{ind,u}^b\right)}\left(\frac{D_{mol}^i - D_{mol}^{ind,l}}{D_{mol}^{ind,u} - D_{mol}^{ind,l}}\right)\Delta c_{ind,u} \quad (4.69a)$$

which can be written in condensed form as:

$$c_i^{t+1} = c_i^t + w_1(c^0, c^b, D_{mol}) \cdot \Delta c_{ind,l} + w_2(c^0, c^b, D_{mol}) \cdot \Delta c_{ind,u} \quad (4.69b)$$

where subscripts l and u denote lower and upper indicator species respectively (i.e. the species with the smallest (l) and greatest (u) diffusion coefficients) and w_1 and w_2 denote the weighting functions for the lower and upper indicators respectively.

A depiction of the use of indicators can be seen in Figure 4.1a. Figure 4.1b shows the weighting functions (for a case where $c_i^0 = c_i^b$ and $c_{ind}^0 = c_{ind}^b$).

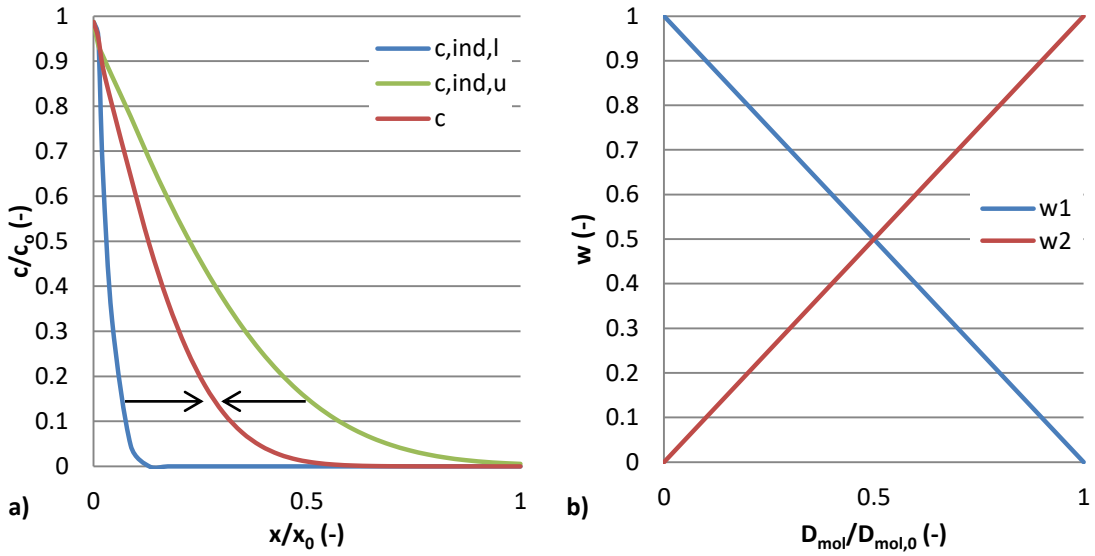

Figure 4.2 - PRS 2 a) Use of indicator species and b) Weighting functions

4.5.3 PRS 3

The third method uses three indicator species, two of which are the species with the largest and smallest diffusion coefficients and the third species has an intermediate diffusion coefficient (it was found here that using the mean value of the diffusion

coefficients gave the best results). The updated concentration of non-indicator species i is given by the following quadratic interpolation function:

$$c_i^{t+1} = c_i^t + \frac{\left(c_i^0 - c_i^b\right)}{\left(c_{ind,l}^0 - c_{ind,l}^b\right)} \left(\frac{\left(D_{mol}^{ind,m} - D_{mol}^i\right)\left(D_{mol}^{ind,u} - D_{mol}^i\right)}{\left(D_{mol}^{ind,m} - D_{mol}^{ind,l}\right)\left(D_{mol}^{ind,u} - D_{mol}^{ind,l}\right)} \right) \Delta c_{ind,l} + \frac{\left(c_i^0 - c_i^b\right)}{\left(c_{ind,m}^0 - c_{ind,m}^b\right)} \left(\frac{\left(D_{mol}^{ind,l} - D_{mol}^i\right)\left(D_{mol}^{ind,u} - D_{mol}^i\right)}{\left(D_{mol}^{ind,l} - D_{mol}^{ind,m}\right)\left(D_{mol}^{ind,u} - D_{mol}^{ind,m}\right)} \right) \Delta c_{ind,m} + \frac{\left(c_i^0 - c_i^b\right)}{\left(c_{ind,u}^0 - c_{ind,u}^b\right)} \left(\frac{\left(D_{mol}^{ind,l} - D_{mol}^i\right)\left(D_{mol}^{ind,m} - D_{mol}^i\right)}{\left(D_{mol}^{ind,l} - D_{mol}^{ind,u}\right)\left(D_{mol}^{ind,m} - D_{mol}^{ind,u}\right)} \right) \Delta c_{ind,u} \quad (4.70a)$$

which can be written in condensed form as:

$$c_i^{t+1} = c_i^t + w_1(c^0, c^b, D_{mol}) \cdot \Delta c_{ind,l} + w_2(c^0, c^b, D_{mol}) \cdot \Delta c_{ind,m} + w_3(c^0, c^b, D_{mol}) \cdot \Delta c_{ind,u} \quad (4.70b)$$

where the m subscript denotes the middle indicator species and w_1, w_2 and w_3 denote the weighting functions for the lower, middle and upper indicators respectively.

A depiction of the use of indicators can be seen in Figure 4.1a. Figure 4.1b shows the weighting functions (for a case where $c_i^0 = c_i^b$ and $c_{ind}^0 = c_{ind}^b$).

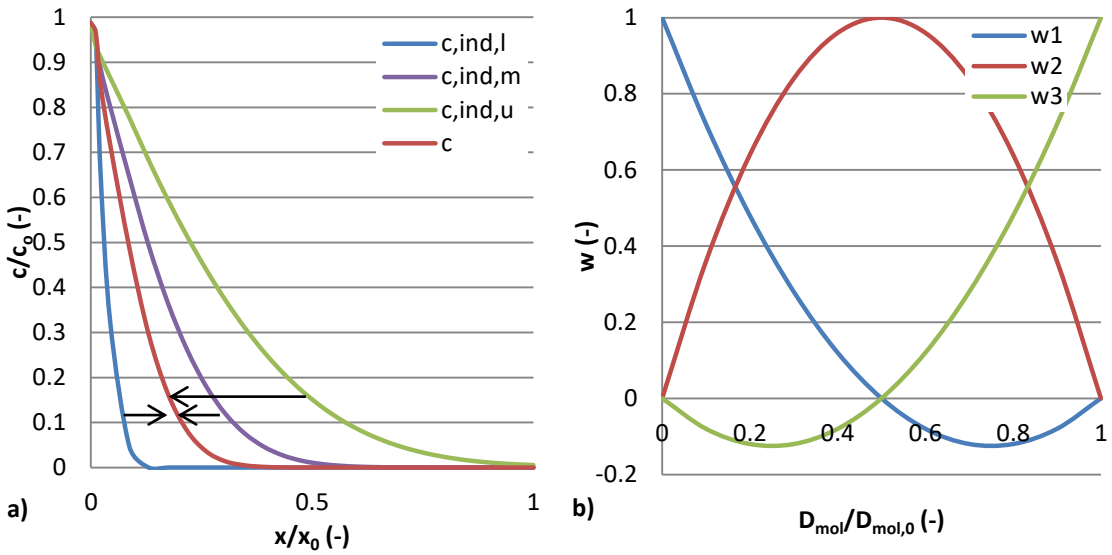

Figure 4.3 - PRS 3 a) Use of indicator species and b) Weighting functions

4.5.4 Boundary Conditions

The initial conditions for the PRS can be defined in the same way as the full model using eq. (4.11). The boundary conditions for the PRSs are also defined in the same way as the full model and should be of the same type for both 'indicator' and 'non-indicator' species, with the latter being calculated on a point wise basis.

4.5.5 Charge Neutrality

Another key consideration is how the charge neutrality condition is dealt with for the PRSs, since the transport of the non-indicator species is not calculated in the reduced system of governing equations. To deal with this, the diffusive flux due to the electric field is dealt with explicitly by using concentrations from the previous time step and moving these to the right hand side of the governing equations in a similar manner to the way that moisture flow under gravity is often included in transport computations. For non-indicator species this can then be calculated on a point wise basis and subtracted at the end of the PRS eqs. (4.68-4.70).

4.5.6 Chemical Reactions

The chemical reactions are considered in much the same way as in the full model with the reaction rates being calculated using the most recent chemical concentrations and moving them to the right hand side of the governing equations. For non-indicator species they are calculated on a point wise basis and subtracted at the end of the PRS eqs. (4.68-4.70).

A flow chart showing the pseudo-code of the algorithm of the solution procedure can be seen in Figure 4.4.

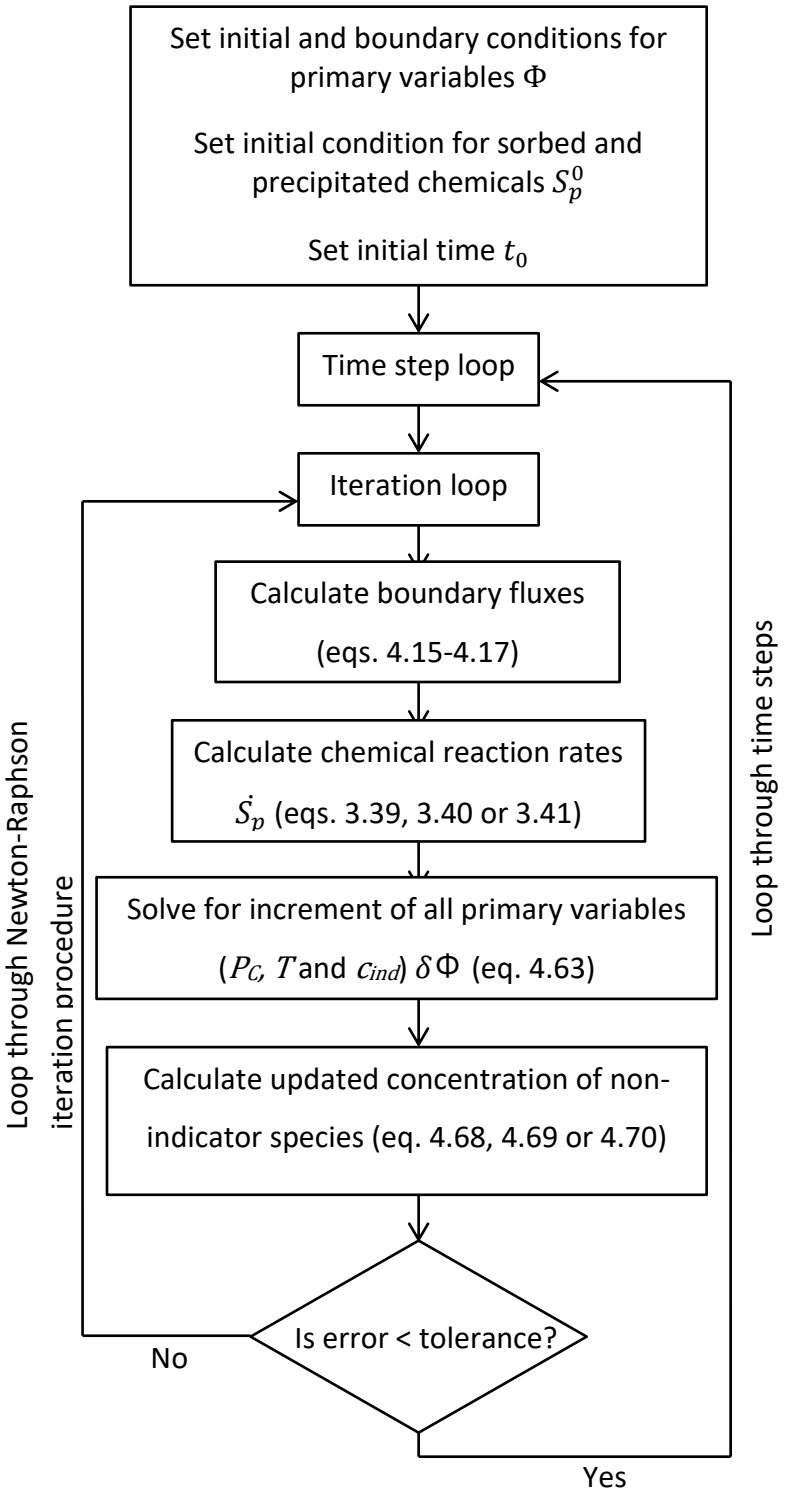

Figure 4.4 – Flow chart detailing the algorithm

4.6 Summary

The numerical treatment of the system of equations has been discussed and the algorithm of the solution procedure has been presented in a flow chart of the pseudo

code. The system of equations are treated as fully coupled and a numerical solution using the FEM for the spatial discretisation and an implicit backward difference method for the temporal discretisation has been developed. The nonlinearity of the system is dealt with using a Newton-Raphson iteration procedure which used the truncated Taylor series expansion to equate the error of approximation to the change in primary variables over a time step. This iteration procedure is continued until a convergence tolerance is reached for a given time step. This leads to the system of equations to be solved of:

$$\delta\Phi_{k+1}^{t+1} = \left[\frac{\partial\varphi}{\partial\Phi_k^{t+1}}\right]^{-1}(-\varphi) \tag{4.71}$$

$$\varphi = \Delta t\check{K}\Phi^{t+1} + \check{C}(\Phi^{t+1} - \Phi^t) - \Delta t\check{f} \tag{4.72}$$

The main contribution of this chapter was the development of a series of reduction schemes for computationally expensive chemical systems. A numerical approach was taken and in total three reduction schemes were presented; each of which has a different degree of reduction associated with them, as the number of indicator species for each is different. The reduction schemes were given as:

$$c_i^{t+1} = c_i^t + \frac{\left(c_i^0 - c_i^b\right)}{\left(c_{ind}^0 - c_{ind}^b\right)}\frac{D_{mol}^i}{D_{mol}^{ind}}\Delta c_{ind} \tag{4.73}$$

$$c_i^{t+1} = c_i^t + \frac{\left(c_i^0 - c_i^b\right)}{\left(c_{ind,l}^0 - c_{ind,l}^b\right)}\left(\frac{D_{mol}^{ind,u} - D_{mol}^i}{D_{mol}^{ind,u} - D_{mol}^{ind,l}}\right)\Delta c_{ind,l} + \frac{\left(c_i^0 - c_i^b\right)}{\left(c_{ind,u}^0 - c_{ind,u}^b\right)}\left(\frac{D_{mol}^i - D_{mol}^{ind,l}}{D_{mol}^{ind,u} - D_{mol}^{ind,l}}\right)\Delta c_{ind,u} \tag{4.71}$$

$$\begin{aligned} c_i^{t+1} = {} & \\ & c_i^t + \frac{\left(c_i^0 - c_i^b\right)}{\left(c_{ind,l}^0 - c_{ind,l}^b\right)}\left(\frac{\left(D_{mol}^{ind,m} - D_{mol}^i\right)\left(D_{mol}^{ind,u} - D_{mol}^i\right)}{\left(D_{mol}^{ind,m} - D_{mol}^{ind,l}\right)\left(D_{mol}^{ind,u} - D_{mol}^{ind,l}\right)}\right)\Delta c_{ind,l} + \\ & \frac{\left(c_i^0 - c_i^b\right)}{\left(c_{ind,m}^0 - c_{ind,m}^b\right)}\left(\frac{\left(D_{mol}^{ind,l} - D_{mol}^i\right)\left(D_{mol}^{ind,u} - D_{mol}^i\right)}{\left(D_{mol}^{ind,l} - D_{mol}^{ind,m}\right)\left(D_{mol}^{ind,u} - D_{mol}^{ind,m}\right)}\right)\Delta c_{ind,m} + \\ & \frac{\left(c_i^0 - c_i^b\right)}{\left(c_{ind,u}^0 - c_{ind,u}^b\right)}\left(\frac{\left(D_{mol}^{ind,l} - D_{mol}^i\right)\left(D_{mol}^{ind,m} - D_{mol}^i\right)}{\left(D_{mol}^{ind,l} - D_{mol}^{ind,u}\right)\left(D_{mol}^{ind,m} - D_{mol}^{ind,u}\right)}\right)\Delta c_{ind,u} \end{aligned} \tag{4.72}$$

It is thought that each of the schemes will have a different range of applicability, for which accurate results are predicted, for chemical systems based on the range of diffusion coefficients and perhaps the magnitude of the concentration gradients.

Chapter 5. Development of an Experimental Procedure for the Determination of Ion Transport Parameters for Cementitious Materials

5.1 Introduction

The ability to predict transport behaviour in cementitious materials is dependent on the knowledge of a number of parameters, which need to be determined experimentally. These parameters range from permeability coefficients to rates of reaction. Typically in soils these parameters have been determined experimentally using column leaching tests (Robbins 1989; Wierenga and Van Genuchten 1989; Khan and Jury 1990; Krueger et al. 1998; Hartley et al. 2004; Liu et al. 2017). These experiments use columns -usually made from Perspex- which are filled with a soil sample, before a chemical solution is added to the top and its concentration is measured either throughout the length of the column or in the effluent collected form the outflow. This setup allows for different flow conditions to be investigated and allows for proper characterisation of the transient behaviour. In concrete specimens however, the experimental arrangement is quite different, and does not allow for different flow conditions (Francy 1998; Baroghel-Bouny et al. 2011; Song et al. 2014). A typical example of this can be seen in Figure 5.1. In addition, the specimen needs to be removed to measure the chemical concentrations, requiring the use of many specimens for the proper characterisation of transient behaviour.

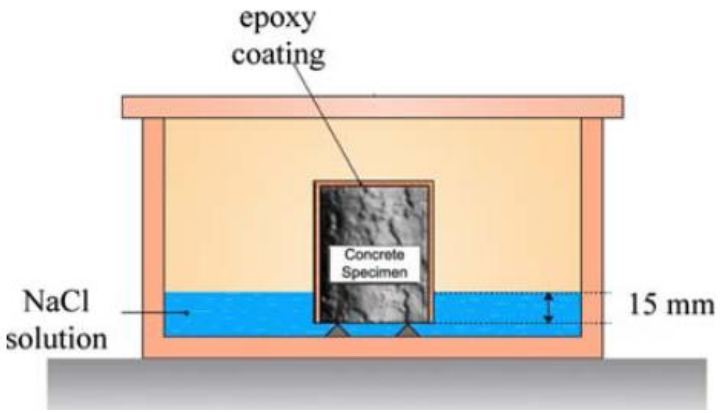

Figure 5.1 – Diffusion/wetting test setup (after Baroghel-Bouny et al. (2007))

This chapter presents the development of a methodology to undertake ion transport experiments in cementitious materials, including the experimental set up and methodology, the concrete mix design, the experimental results and the difficulties encountered. The objective of these experiments is to provide a simple means of obtaining transport parameters for cementitious materials that (i) are quick, (ii) allow for different flow conditions and (iii) allow for in situ measurements. The results of these experiments will then be used to validate the numerical model developed in Chapter 4.

The experimental setup and procedure are detailed in section 5.2 including the description of the basic premise of the experiments, the design of the tanks and the detailed description of the experimental procedure.

Section 5.3 details the design of a high porosity concrete, designed to reduce the amount of time required to carry out the experiments.

The results of an advective-diffusive reactive case concerning Cl^- and Na^+ are presented in section 5.4.

The difficulties that were encountered and the steps taken to circumvent them are presented in section 5.5.

Finally the conclusions on the success of the proposed experiments are made in section 5.6.

5.2 Experimental Setup and Methodology

The three problems with the current approaches found in the literature that this thesis aims to address are:

1. The experiments are slow due to the low permeability of concrete, requiring the use of short specimens.
2. The pressure head cannot be altered, limiting the flow conditions that may be investigated.

3. The specimen needs to be removed to measure concentration profiles; such that for transient behaviour to be investigated multiple specimens must be used.

The premise of the proposed experimental procedure is to have two plastic tanks, which can be filled with water or a chemical solution, connected near the bottom with a concrete beam. Different heads of water and different concentrations of chemical solution can be added to each of the tanks and their transport through the beam can be measured. This set up can be used for moisture transport or chemical transport including diffusive and advective-diffusive cases. The ability to apply different heads of water allows for different flow conditions to be investigated, addressing point 2. The ability to investigate different flow conditions is important as a number of parameters depend upon them, for example, the rate of chloride binding has been found to be effected by the rate of solute transport (Baroghel-Bouny et al. 2011). The measurements can be taken from a number of predrilled sampling points using humidity probes for moisture content measurements or by extracting a pore water sample for solute concentration measurements. The extraction of a sample prevents the specimen from being removed from the test setup, when measuring concentration profiles, addressing point 3. A basic depiction of the test setup can be seen in Figure 5.2. Finally, point 1 is addressed through the design of a high permeability concrete mix, designed to reduce the length of the test. It is thought that the resultant parameters could then be scaled up to lower permeability concrete using relationships found in the literature (see (Yang et al. 2006) or (Ahmad and Azad 2013)).

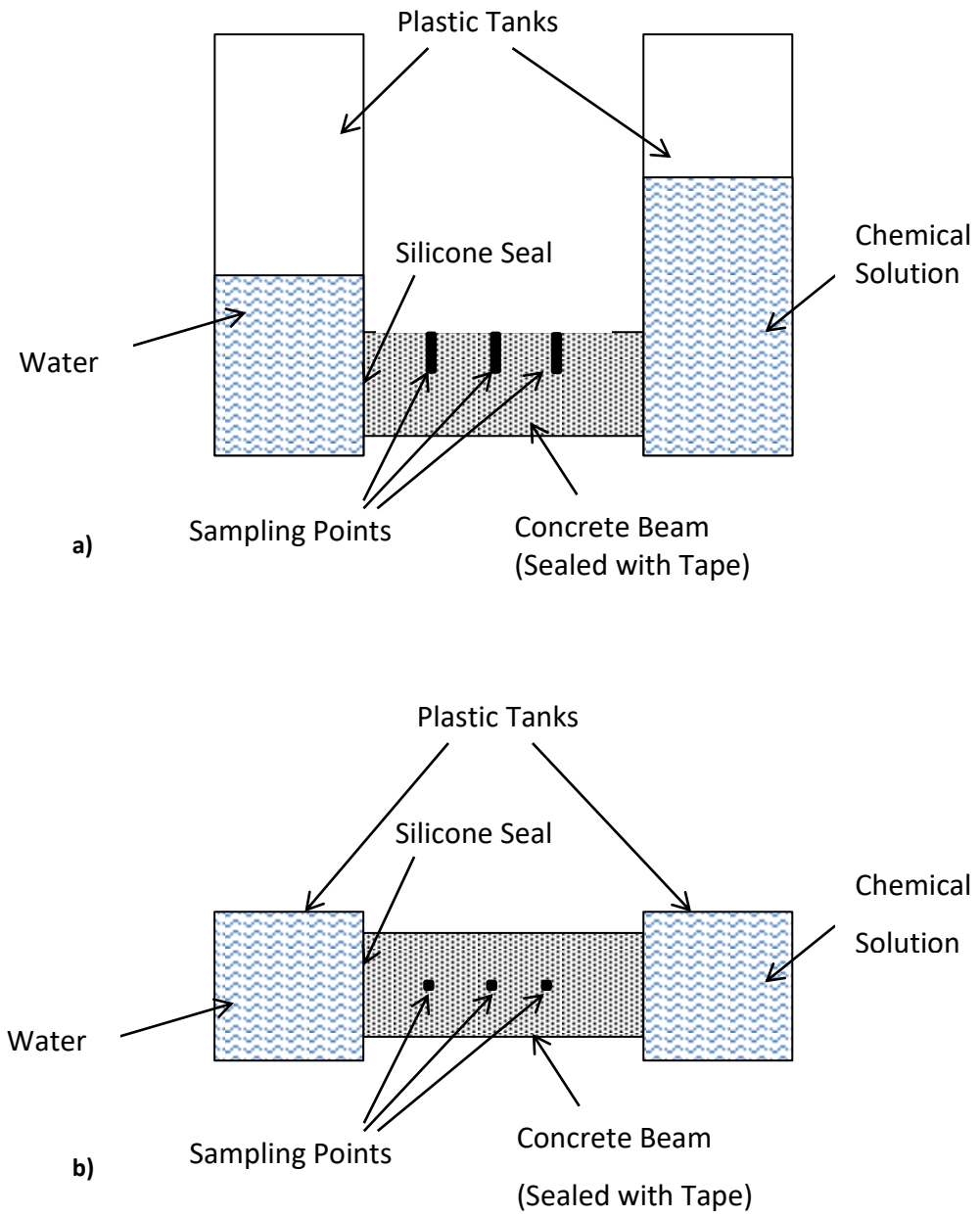

Figure 5.2 – Experimental setup a) elevation and b) plan view

The plastic tanks were designed to allow for a maximum pressure head of 0.5 m and to fit a concrete beam of cross-section 75x75 mm. The walls of the tank are 10 mm Perspex, designed to ensure the ability of the tanks to withstand the pressure head. Base plates were also added, with predrilled holes to increase the stability of the tanks by allowing them to bolted down if required. The plans showing the design and the dimensions can be seen in Figure 5.3. The tanks were manufactured by Dipec plastics.

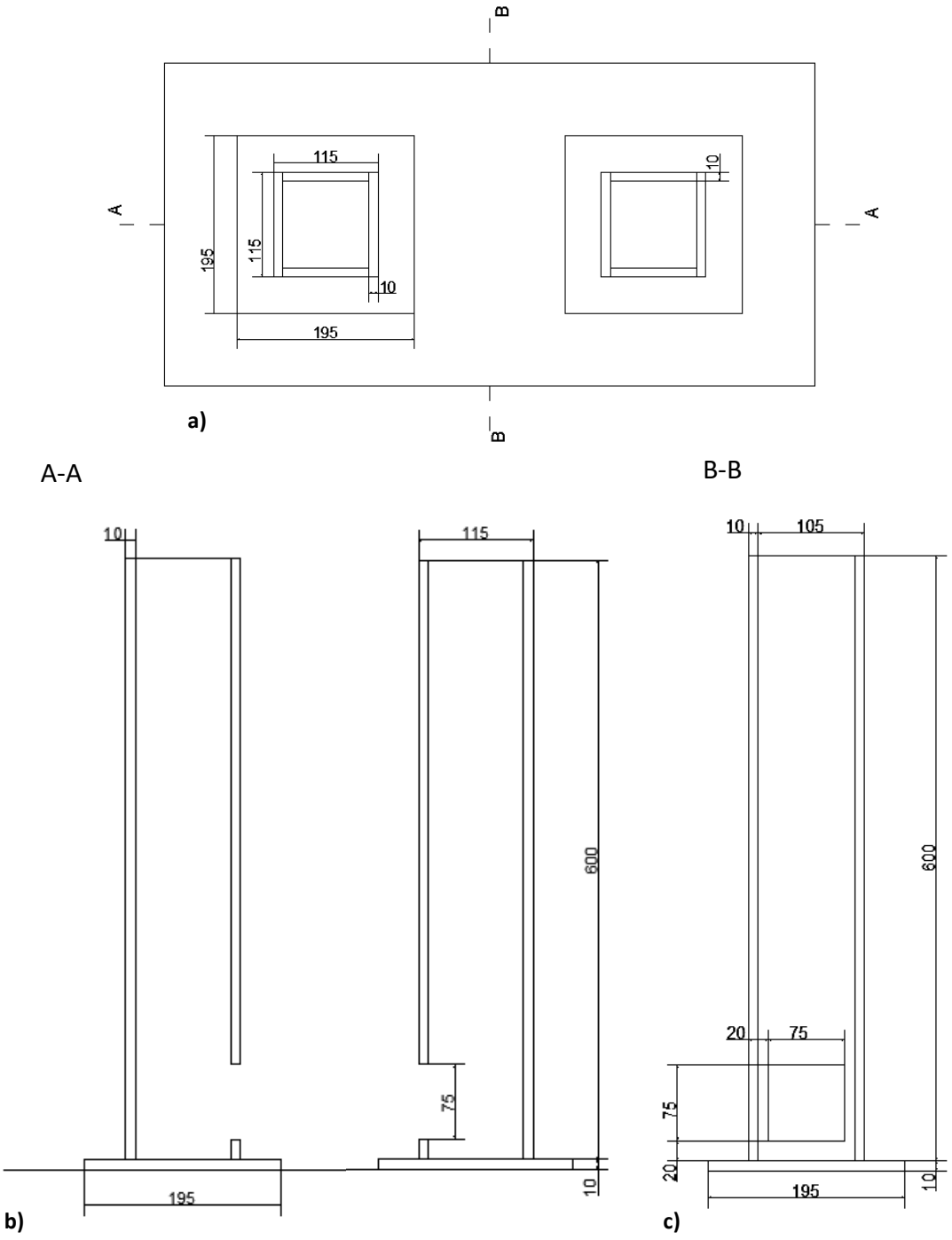

Figure 5.3 – Tank design drawings (not to scale, all dimensions in mm) a) Plan view, b) Elevation about cut A-A and c) Elevation about cut B-B

5.2.1 Experimental Procedure

5.2.1.1 Beam Preparation

The first step in the experimental procedure is the preparation of the concrete beams, beginning with the mixing and casting. All concrete mixes were made with a minimum volume of 10 litres to reduce the effect of moisture loss to the walls of the mixer. To cast the specimens the moulds were first oiled, to prevent any bonding between the concrete and the mould walls. Two concrete beams of size 255x75x75 mm and three concrete cubes of 100x100x100 mm for strength testing were cast each time. Typically, the strength of the concrete mix used was 15±1 MPa. The strength was measured as a parameter that could be used to scale the transport properties of the porous concrete mix to that of an ordinary (lower porosity) concrete (see for example (Al-amoudi et al. 2009)). The moulds were then filled in three layers, with each layer being compacted using a vibrating table before the next is added. Following a waiting period of 24 hours the specimens were de-moulded and placed into curing tanks to moist cure in tap water for 7 days at 19±2 ^{o}C.

After 7 days the specimens were taken out of the curing tanks to be prepared for the experiment. This included the drilling of the holes at the sampling points and the grinding down of the edge of the sample. This last step was introduced in order to facilitate the placement of the beams into the plastic tanks, as it was found that the cross-section of the beams and the cut outs in the plastic tanks were exactly the same size, making the beams impossible to place. To grind down the edges, an angle grinder was used, reducing the cross-section at the end of the beams until they fit into the cut outs of the tanks. Some example photos of a prepared beam can be seen in Figure 5.4 (it should be noted that this beam has been cut in half to reduce its size to 125x75x75 mm, in order to reduce the length of time of the experiment further).

Figure 5.4 – Prepared beam (not to scale)

Following this the specimens were placed in an oven at a temperature of 90±2 ^{o}C for 24 hours. The main purpose of this was to speed up the hydration reaction, allowing for shorter curing times, however this may also be used to reduce the moisture content of the specimen in preparation for test scenarios involving moisture transport.

5.2.1.2 Sealing

The next step was to seal the sides of the concrete beam and place the beam into the tanks. It was found that Duck 'Ultimate cloth tape mesh clear' was the most suitable for this, which was for two reasons, firstly the cloth tape had a good level of adhesion to the concrete (when compared to duct tape), and secondly the tape is clear so it allows a degree of observation (for example in a moisture transport test scenario the penetration of the wetting front can be seen). Some example photos of the beam sealed with the cloth tape can be seen in Figure 5.5.

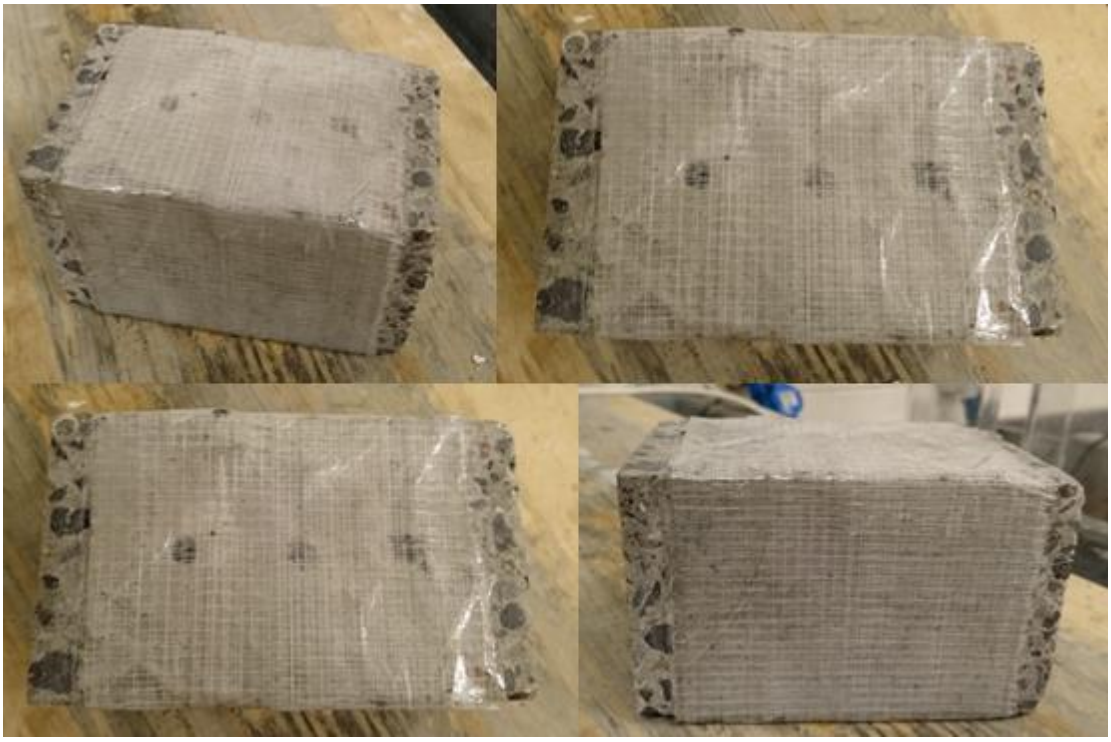

Figure 5.5 – Sealed beam (not to scale)

For the placement of the beams into the tanks a layer of silicone was first placed along the edges of the beam, before pushing each end into the tank cut outs, one by one. Following this an outer layer of silicone was added around the edge of the cut outs to seal the connection between the beam and the tanks. Different types of silicone were tested for their adhesion, with Geocel 'The Works' being found to give the best results (in terms of reduced occurrence of leaks) after a number of tests. Some example photos of the concrete beam in place in the tanks can be seen in Figure 5.6. This setup was then left for the silicone to cure for 24 hours. If the moisture transport is being measured it is at this point that humidity probes can be placed into the sampling holes and linked to a data logger to record the measurements. The moisture transport, however, was not measured in this study.

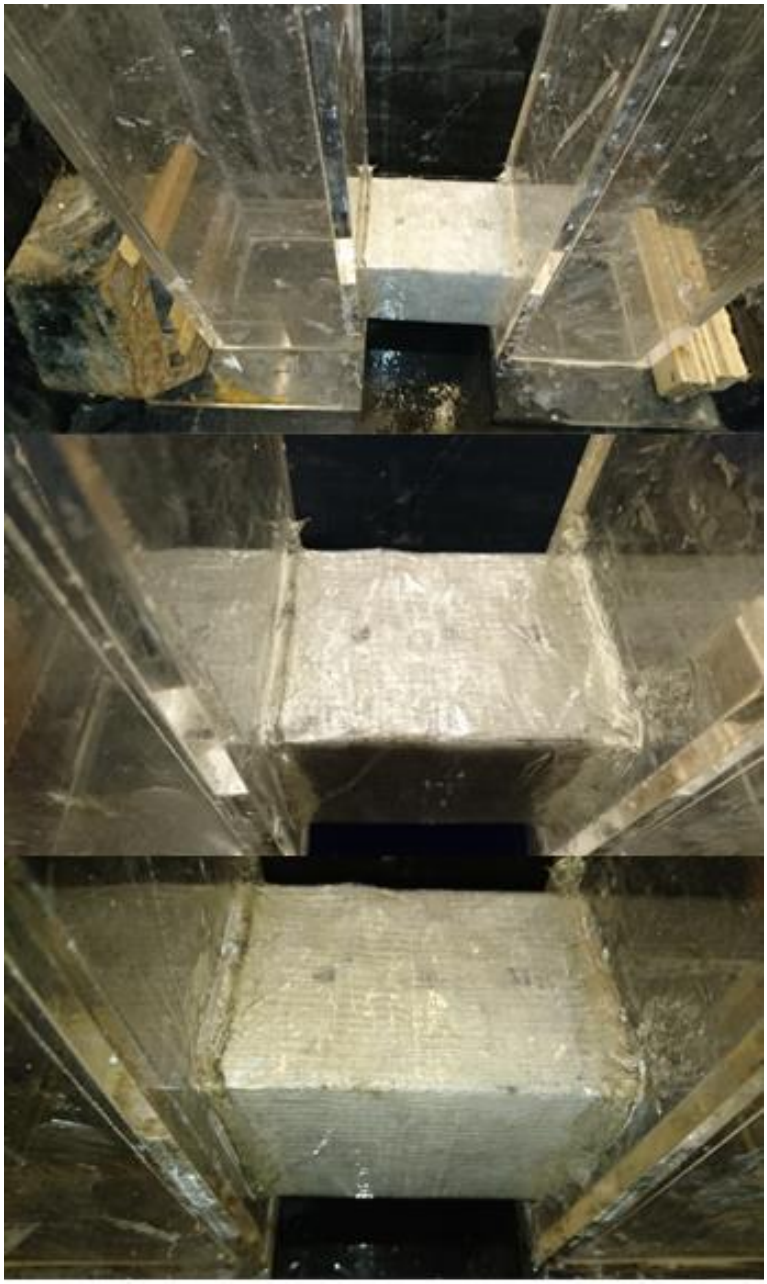

Figure 5.6 – Silicone seal between beam and tanks

5.2.1.3 Test Setup

Once the silicone was cured the test could be set up, beginning with the addition of water into the tanks at the desired levels. The next step depended upon the test scenario being investigated. If the test scenario considered ion transport beginning with the beam as unsaturated, the chemicals under consideration were added to the tanks –and stirred into the water to create a solution- as desired immediately. If the test scenario assumed a saturated beam at the beginning of the test, then this setup

was left for one week, to allow the beam to become saturated, before adding the chemicals. This is considered long enough for full saturation as in wetting tests cementitious materials have been reported to reach very high saturation after just 48 hours (Baroghel-Bouny et al. 2011). The specimen lengths were smaller (20mm compared with 125mm) in Baroghel-Bouny et al. (2011), however the porosity of the concrete used here was much higher, such that time to saturation can be expected to be lower. In addition to this moisture could be seen on the opposite face after just a few days. Some example photos of a test setup can be seen in Figure 5.7.

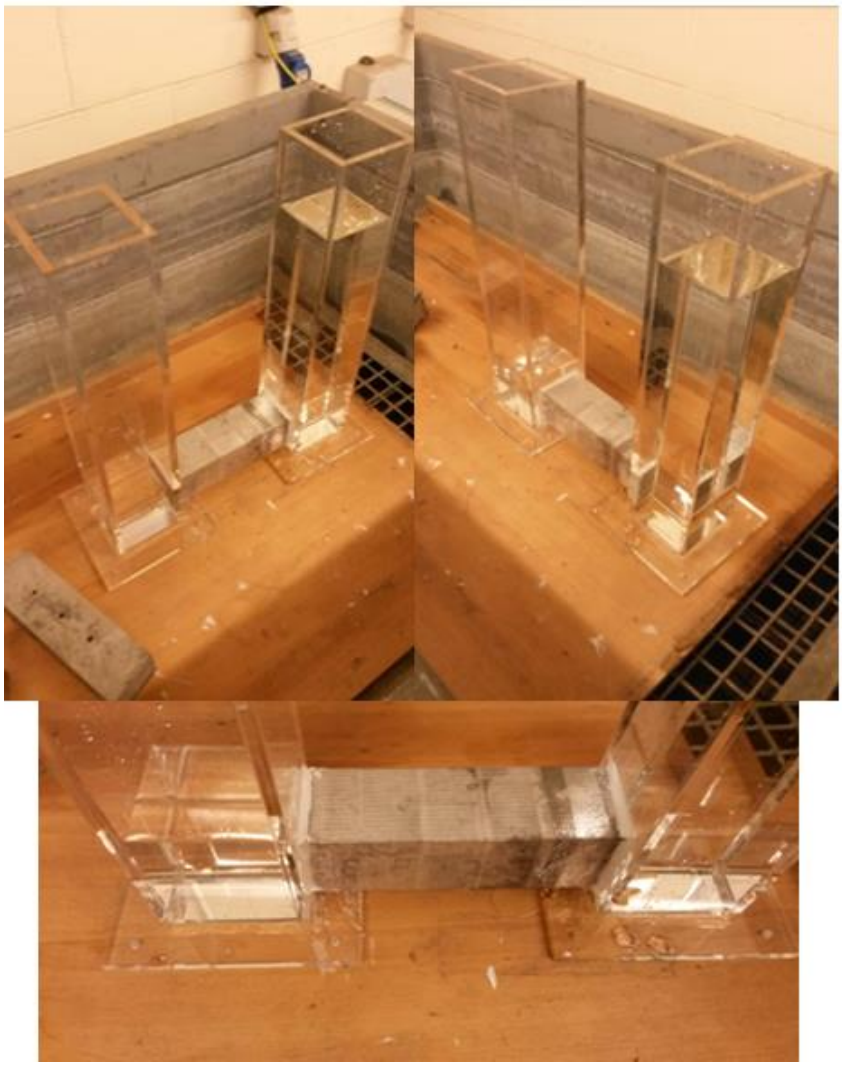

Figure 5.7 – Advective diffusive test setup

The final step was the taking of measurements of the chemical concentrations. Samples were taken through the extraction of 1 ml of pore fluid from the sampling

points, before the hole was resealed with cloth tape. The samples were then analysed for their chemical content. For salts this analysis was carried out using a Mettler Toledo SevenMulti, which was used to measure the total dissolved solids (TDS) content of the solution. The Toledo SevenMulti was calibrated against a control solution and has an accuracy of ±0.5 %. Due to the fact that some cementitious ions are present in the pore water phase, a control test was needed in order to determine what proportion of the measured TDS content represented the additional chemicals. The control case setup was the same as the test case, but this time no additional chemicals were added. The difference between the TDS of the test case and the TDS of the control gives the concentration of the chemicals added. For more complex chemical systems, the sample taken could be analysed using alternative methods such as spectroscopy; however this was not undertaken in this study.

The general procedure can be summarised into the following 10 steps:

1. Cast the concrete specimens.
2. Place the specimens in a curing tank for 7 days.
3. Cut the beams to size, prepare the edges and drill holes at the sampling points.
4. Place the specimens in oven at 90 ^{o}Cfor 24 hours.
5. Seal the beam with cloth tape before sealing into place in the tank cut outs with silicone.
6. Leave the silicone to cure for 24 hours.
7. Fill the tanks with desired levels of water.
8. Add the chemicals after 1 week for an initially saturated case or immediately for an initially unsaturated case.
9. Take samples from sampling points at desired times using a syringe, and reseal.
10. Measure the chemical concentrations using a conductivity measure or other method and compare this value with a control case.

5.3 Concrete Mix Design

The aim of the concrete mix design was to produce a concrete with a high porosity such that the time taken for each experiment was reduced but a low enough porosity that the concrete is still similar to an ordinary concrete mix as opposed to a pervious

concrete (which are no fines concretes developed for use as pavements, designed to allow the quick transfer of rainwater into the underlying soil (Yang and Jiang 2003)). It was thought that if the concrete mix is designed in this way then it will be possible to compare the results of the experiments with ordinary concrete mixes or to scale up the resultant parameters to higher strength/lower porosity concretes by using relationships found in the literature (see (Yang et al. 2006) or (Ahmad and Azad 2013)).

To achieve this balance in porosity between that of a pervious and an ordinary concrete, a very high w/c ratio of 0.9 was used, which has been found to increase the porosity (Kim et al. 2014), along with a low percentage of fine aggregate. Three different concrete mixes were tested, denoted as L, M and H, with fine aggregate contents of 10 %, 15 % and 20 % respectively. The full details of the concrete mixes can be seen in Table 5.1. The materials used were Portland-fly ash cement (CEM II/B-V 32,5R), 4-10 mm crushed limestone and 0-4 mm sea dredged sand. The grading curves for the aggregates, determined according to BS EN 12620:2013, are shown in Figure 5.8.

Table 5.1 – Mix parameters

Parameter	Mix		
	L	M	H
Fine Aggregate %age[a] (%)	10	15	20
W/C Ratio	0.9	0.9	0.9
Water Content (kg)	2.25	2.25	2.25
Cement Content (kg)	2.5	2.5	2.5
Coarse Aggregate Content (kg)	16.61	15.68	14.76
Fine Aggregate Content (kg)	1.85	2.77	3.69

[a]Percentage of total aggregate content

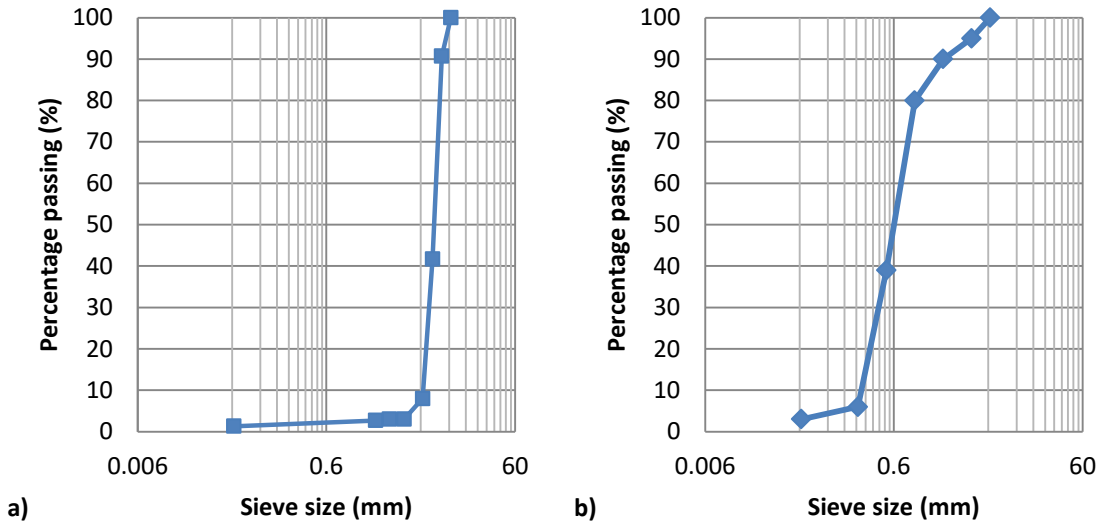

Figure 5.8 – Grading curves for a) Coarse aggregate and b) Fine aggregate

The main problem with using such a low fine aggregate content was that when the specimen was compacted, the fine aggregate sank to the bottom of the specimen, producing a beam with the bottom half containing all of the fine aggregate and the top half containing only coarse aggregate. Such aggregation of samples is shown in Figure 5.9 for the resultant specimens of the L mix.

The specimen photos of the M mix can be seen in Figure 5.10. It can be seen that the sinking of the fine aggregate was still a problem for this mix, albeit to a lesser extent.

Finally the specimen photos of the H mix can be seen in Figure 5.11. Here the sinking of fine aggregate is significantly less pronounced and can only be seen in one of the concrete cubes. These photos show that this mix is capable of producing a suitable concrete, and so it was this mix that was used in the experiments.

Figure 5.9 – Mix L specimens (not to scale)

Figure 5.10 – Mix M specimens (not to scale)

Figure 5.11 – Mix H specimens (not to scale)

To try and avoid the sinking of the fine aggregate hand compaction was also tested on the L and M mixes; however whilst the distribution of the fine aggregate throughout the sample was greatly improved, it was clear that there was simply not enough fine aggregate to produce an ordinary concrete. This can be seen in Figure 5.12.

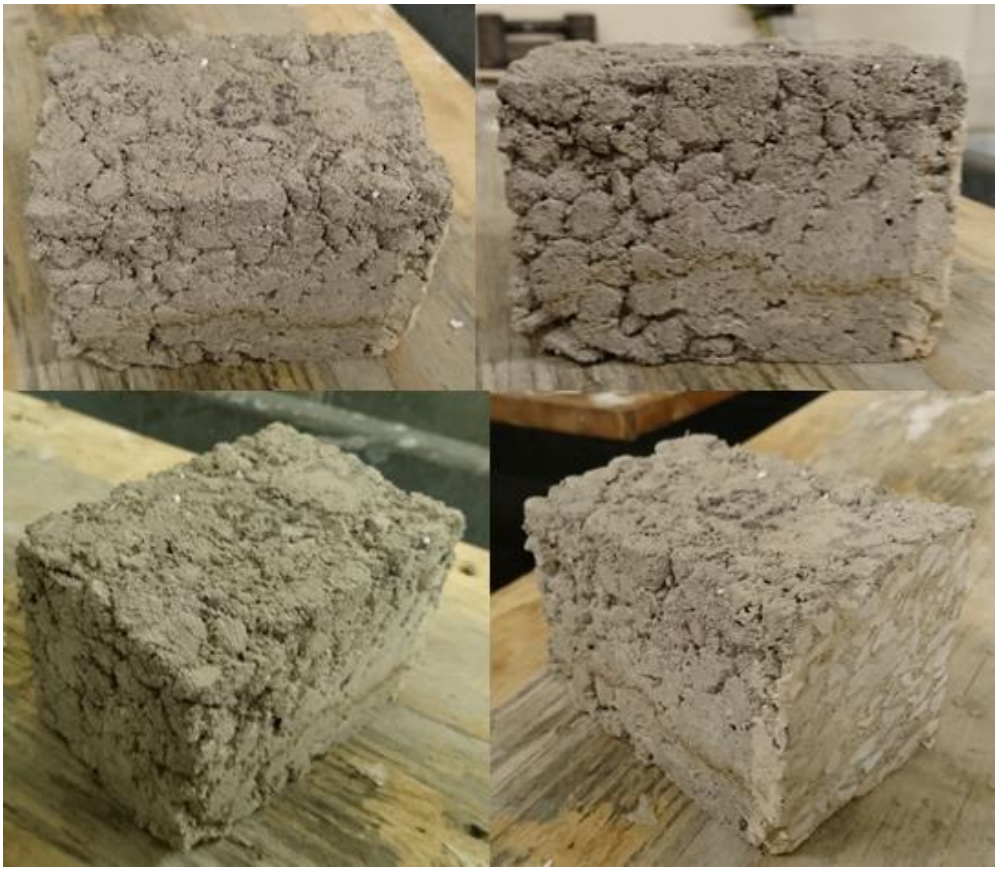

Figure 5.12 – Hand compacted specimen (not to scale)

5.4 Experimental Results

In this section the experimental results are presented. It should be noted that once results were obtained from the control test case the tanks were modified by attaching a second section on top of the first to allow for a greater pressure head. The tanks were attached by sealing them together with silicone before clamping a piece of Perspex to the joint to add stability as shown in Figure 5.13.

Figure 5.13 – Modified tanks (not to scale)

5.4.1 Advective Diffusive Reactive Case

The test setup for an advective-diffusive case can be seen in Figure 5.14 (where C1-3 denote the different sampling points). A 10.3 % $NaCl$ solution was added to the left hand tank at a head of 540 mm (above the bottom of the beam), whilst the right tank was left empty. Tap water was added to the left hand tank, before the setup was left for one week, to allow the beam to become saturated. The $NaCl$ was added to the water in the left hand tank and stirred with a rod until dissolved. The control case was setup in the same way, without the addition of the $NaCl$.

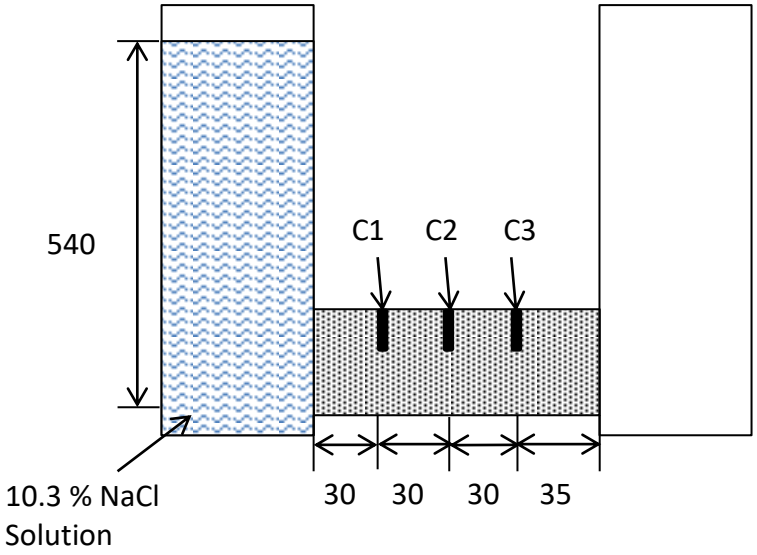

Figure 5.14- Test setup diagram (all dimensions in mm)

Samples were taken after 7 days and the concentration was measured using a Mettler Toledo SevenMulti, which has an accuracy of ±0.5 %. To facilitate the measurements, the extracted sample was diluted to give a large enough volume to take readings. The results along with those of an equivalent control case can be seen in Table 5.2.

Table 5.2 – Experimental results

Sample	Size (µL)	Diluted To (ml)	Conductivity (µS/cm)	TDS (mg/L)	TDS (kg/kg)	Cl^- Conc. (kg/kg)	Na^+ Conc. (kg/kg)
C1	100	10	843	426	0.0426	0.0193	0.0124
C2	100	10	647	325	0.0325	0.0132	0.0084
C3	100	10	448	224	0.0224	0.0070	0.0045
Control	100	10	214	109	0.0109	-	-

The Cl^- and Na^+ profiles as measured from the experiment after one week can be seen in Figure 5.15. It can be noted that due to the significant problems encountered with the experimental set up leaking these are the only set of viable results obtained.

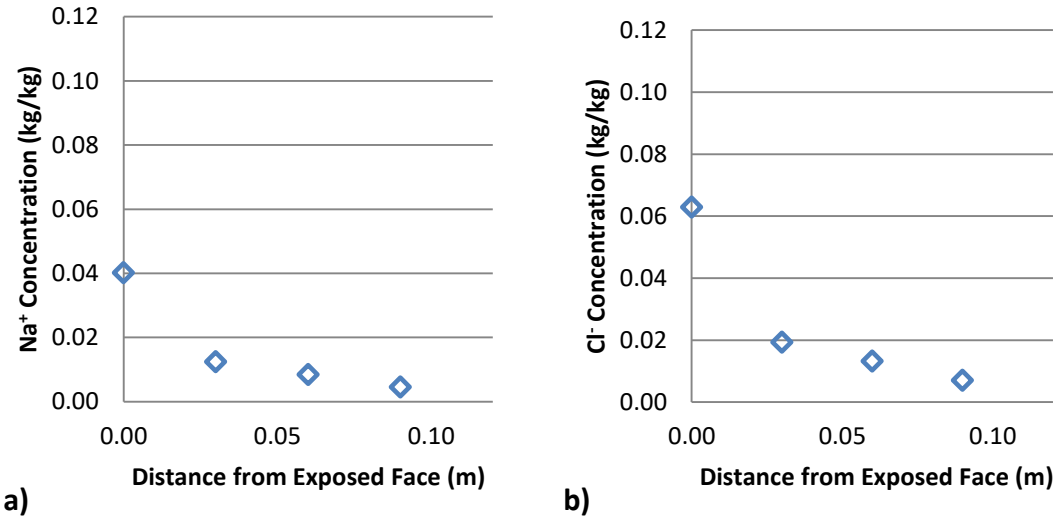

Figure 5.15 – Chloride profile as measured from the experiment (t=1week)

5.5 Difficulties and Problems Encountered

5.5.1 Test Cases Attempted

During the course of the experiments a number of different cases were considered including a diffusion case and two advective-diffusive cases. The test setup for each of these cases can be seen in Figure 5.16.

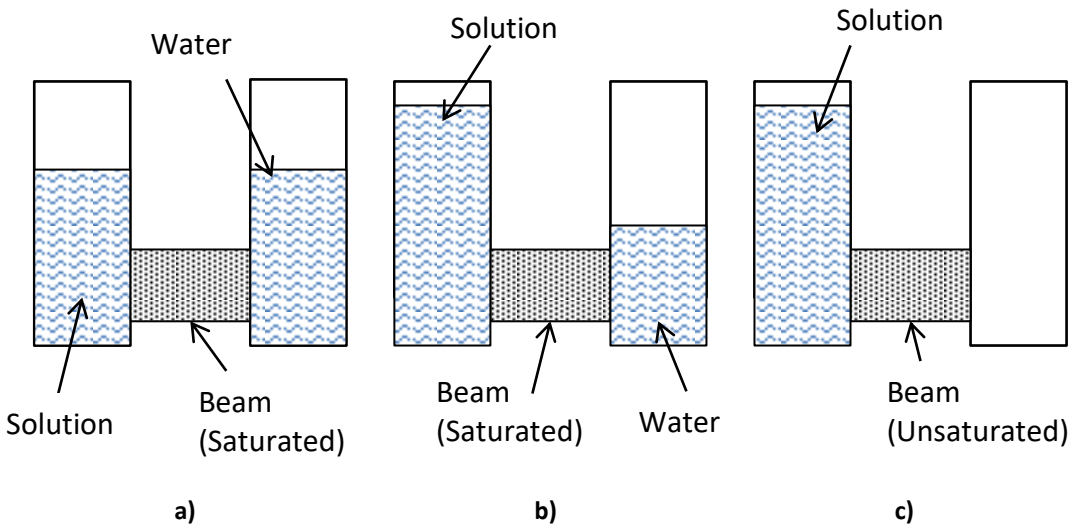

Figure 5.16 – Test cases considered a) Diffusive case, b) Advective-diffusive case (initially saturated beam) and c) Advective-diffusive case (initially unsaturated beam)

For all test cases the chemical solution under consideration was added to the left hand tank and the concentration profiles measured by extracting samples from predrilled holes in the beam. For the advective-diffusive cases adjustment of the head difference across the beam controls the degree of advection.

In addition to the different experimental arrangements a number of different chemical solutions were considered including $NaCl$, Na_2SiO_3 and $CaCl_2$. However due to the significant problems encountered with the experimental set up leaking the only set of viable results obtained was for the advective-diffusive case detailed in section 5.4.1.

5.5.2 Problems Encountered

During the process of undertaking the ion transport experiments a number of difficulties were encountered, such as the design of a suitable concrete mix, discussed previously. However the most significant problem encountered was of the tanks leaking through the connection to the concrete beam. A typical example of this can be seen in Figure 5.17.

Figure 5.17 – Leaking tanks (not to scale, leaks shown with arrows)

The first approach adopted to circumvent this leakage problem was to test different silicones to see if a different type or brand would perform any better. It was found through this testing that using Geocel 'The Works' provided a better seal. It was also

discovered that it was very difficult to seal the bottom edge, which is where many of the leaks were found. This was due to the fact that there was only a 20 mm gap between the bottom of the beam and the base plate of the plastic tanks. This gap did not allow enough access for sealing the bottom edge, and so to prevent this, the front of the base plate of the tanks was cut off. This can be seen in Figure 5.18. Another problem was the presence of old silicone on the tanks. Originally between tests the old silicone was removed with a Stanley blade. It was found however that this made the subsequent sealing more difficult as it was not possible to remove all of the old silicone, and the new silicone did not bond well to it. This was remedied by cleaning the area with a proprietary silicone remover, providing a much cleaner surface for the next attempt.

Figure 5.18 – Modified tanks (not to scale)

As some of the leaks encountered did not occur immediately but after some time, the third tactic was to reduce the amount of time that the test would take. This was already considered in the concrete mix design through the use of high porosity concrete, however other methods employed included the reduction in length of the beam from 255 mm to 125 mm and the aforementioned attaching together of the tanks to allow for a greater pressure head (it should be noted that this increase in

pressure head may have a detrimental effect due to the increase in pressure on the joints, however there is the option of not utilising the extra head available).

5.6 Conclusions

The purpose of this chapter was to detail the development of a simple approach to ion transport experiments that would allow the investigation of a range of different chemical species and flow conditions, with measurements being taken in situ, allowing the proper characterisation of transient behaviour. The current approaches and experimental procedures were reviewed in Chapter 2 for both soils and cementitious materials. It was found that the approaches used for cementitious materials were limited, requiring the use of short specimens to reduce the time taken, the removal of the specimen for the measurements, and having no allowance for a range of pressure heads, limiting the range of flow conditions that can be investigated. The need therefore for the new procedure presented here is justified.

The procedure developed here addressed the following issues:

1. Different pressure heads were available through the use of plastic tanks, connected by the specimen, allowing a maximum variation in pressure head across the sample of 0.5 m.
2. A high permeability concrete mix was designed that facilitated the reduction in test time.
3. Pore water samples were extracted to be analysed for their chemical content, allowing the specimen to remain in place.

It was found that the experiments were successful in investigating the advective salt transport through a concrete specimen. There were, however a number of problems encountered. The first of which was the design of a high permeability concrete mix, that still resembled an ordinary concrete. It was found that this could be achieved with a w/c ratio of 0.9 and a 20 % fine aggregate content. The second problem was the leaking of the water through the silicone seal between the tanks and the specimen. It was found that this was due to a difficulty in application of the silicone due to the design of the tanks, the presence of old silicone on the cut outs and the type of silicone used. This was rectified by the removal of the front part of the base plates of the tanks,

the use of a silicone remover between tests and the testing of different silicones until a suitable one was found.

It is recognised that, due to the problems encountered, a limited number of results were produced, however it has been shown that once these problems were addressed the experimental procedure was effective in providing a simple means of investigating ion transport through a concrete specimen under different flow conditions.

Chapter 6. Verification and Validation of the Coupled Model

6.1 Introduction

This chapter details the verification and validation of the full transport model through a series of numerical simulations of example problems found in the literature. This chapter is split into two main parts; the first part concerns the verification of the model, to this end the model is compared to a number of numerical simulations reported in the literature concerning the reactive transport of chemical species through concrete and mortar specimens. The second part concerns the validation of the model, which will be carried out by considering the experimental results of the drying of three different mixes of concrete specimens found in Kim and Lee (1999), and the experimental results obtained from the ion transport experiments, details of which were presented in Chapter 5.

Section 6.2 details the verification of the model. This section begins with examples from Koniorczyk (2010) and Koniorczyk and Gawin (2012), concerning the transport and precipitation of salt in building materials. Following these, examples from Baroghel-Bouny et al. (2011) and Song et el. (2014) concerning multiple ionic transport in cementitious specimens are then simulated.

The validation of the moisture flow and chemical transport can be found in section 6.3, where simulations were carried out based on the drying experiments reported by Kim and Lee (1999) and the results of the ion transport experiments reported in chapter 5.

Finally in section 6.4 the conclusions drawn on the ability of the model to accurately simulate the various transport problems are presented.

6.2 Verification of the Coupled Model

6.2.1 Introduction

In this section the verification of the full reactive transport model will be presented through a series of examples concerning reactive chemical transport in cementitious materials. The first two examples are taken from Koniorczyk (2010) and Koniorczyk and Gawin (2012), which concern the drying of building materials initially saturated with a salt solution. In both examples the precipitation of the salt was included with an

assumption of non-equilibrium conditions, with the difference being that in the first example the rate of reaction was calculated as a function of the concentration and in the second it was calculated instead as a function of the solution supersaturation ratio.

The final two examples were presented by Baroghel-Bouny et al. (2011) and Song et al. (2014) respectively. They concern the multi-ionic diffusion of chemical species from a source solution into a cementitious material. The chemical reactions found in both examples are modelled with an assumption of non-equilibrium conditions using a Freundlich type isotherm. In addition to this both examples also included a charge neutrality condition through the implementation of the Nernst Planck and Poisson equations, with the difference being that Baroghel-Bouny et al. (2011) solved for the electrical potential as a primary variable, whereas Song et al. (2014) substituted the condition of zero current directly into the diffusive flux equation, eliminating the electrical potential as a variable.

For all examples the mesh and time step sizes were chosen based on the results of a mesh convergence study.

6.2.2 Example – Koniorczyk (2010)

In 2010 Koniorczyk (2010) developed a model to simulate the transport and crystallisation of salt in porous building materials. The simulations undertaken included the drying of a mortar sample containing $NaCl$ and the cool-warming of a cement mortar containing Na_2SO_4. For the drying simulation, both the equilibrium and non-equilibrium approach to the salt precipitation were considered, with the equilibrium approach testing Freundlich, linear and Langmuir isotherms and the non-equilibrium approach testing a kinetic Freundlich isotherm. The results considered here were of the drying of the mortar sample containing $NaCl$ with non-equilibrium salt precipitation. The rate of reaction is of the general from of eq. (3.39) and is given as:

$$\dot{S}_p = S_w k_{da}(c - A' c_{max})^{\lambda} \qquad (6.1)$$

where k_{da} is a rate parameter, λ is the order of the reaction, A' is a supersaturation parameter given here as 1 and c_{max} is the solubility of $NaCl$.

6.2.2.1 Numerical Model Conditions

The mortar sample was a 100x50 mm beam. The time period considered was 100 hours, a time step of $\Delta t = 3.6\ s$ and a uniform mesh of 40 bilinear quadrilateral elements were used, with element size of $\Delta x = 0.00125\ m$ and $\Delta y = 0.05\ m$. The finite element mesh used and problem geometry can be seen in Figure 6.1, half of the domain was modelled due to the symmetry of the problem.

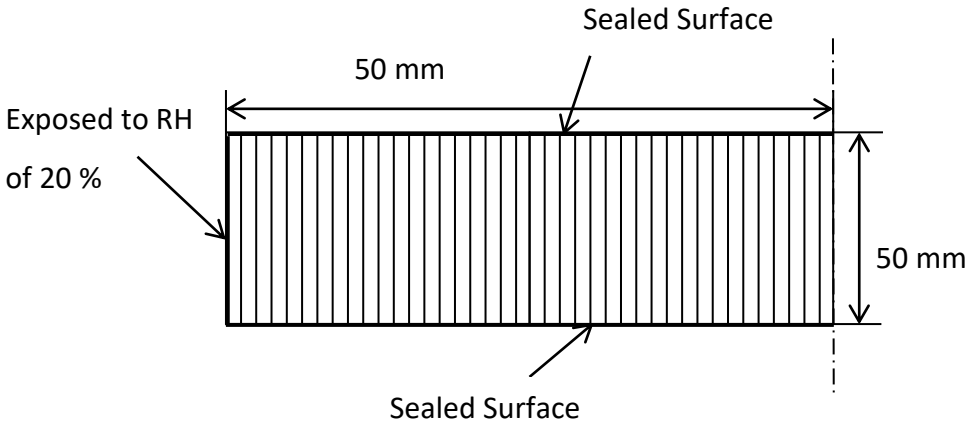

Figure 6.1 – Finite element mesh and problem geometry (not to scale)

The initial conditions along with the parameters used for the simulation can be seen in Table 6.1. The boundary conditions considered were of zero flux for the sealed sides and of the Cauchy type (eqs. 4.15-4.17) for the exposed surface, the values can be seen in Table 6.2. It should be noted that in this example it was found that a tortuosity factor τ was needed to correctly predict the chemical transport; this factor takes into account the tortuous pathways of the medium and is simply multiplied by the diffusion coefficient in eq. (3.38). In addition to this, it was found that a much lower value of the boundary mass transfer coefficient was needed, than the value reported by Koniorczyk (2010) ($8x10^{-2}$ m/s).

Table 6.1 – Model parameters

Parameter		Values
Permeability (eqs. 3.11 & 3.18)	K_{i0}[a] $(10^{-21}\ m^2)$	3.0
	A_w[b]	2.4
Moisture Retention (eq. 3.19)	a_c[c]	183.765
	b[c]	2.27
Porosity	n[a]	0.12
Boundary (eqs. 4.15-4.17)	$\alpha_c\ (W/Km^2)$	8.0
	$\beta_c\ (10^{-3}\ m/s)$	4.0
Initial Values	S_w[a]	0.687
	$c^a\ (kg/kg)$	0.15
	S_p[a]	0.0
Reaction (eq. 6.1)	A'[a]	1.0
	λ[a]	1.9
	k_{da}[a]	0.05
	c_{max}[c] (kg/kg)	0.264
Diffusion (eq. 3.38)	D_{mol}[a] $(10^{-9}\ m^2/s)$	1.0
	τ	0.7

[a]Taken from (Koniorczyk 2010)
[b]Reported values between 1 and 6 (Koniorczyk and Gawin 2011)
[c]Taken from (Koniorczyk and Gawin 2012)

Table 6.2 –Boundary conditions

Boundary	Boundary Type	Values
LHS	Cauchy	$RH=20\ \%$, $c=0\ kg/kg$, $T=293\ K$
Bottom	Sealed	-
RHS	q=0	-
Top	Sealed	-

6.2.2.2 Results and Discussions

The comparison of the results of the model and the results presented by Koniorczyk (2010) can be seen in Figure 6.2 for the liquid saturation and concentration profiles and Figure 6.3 for the salt profiles and the transient behaviour. The transient profiles are measured at a point on the exposed surface.

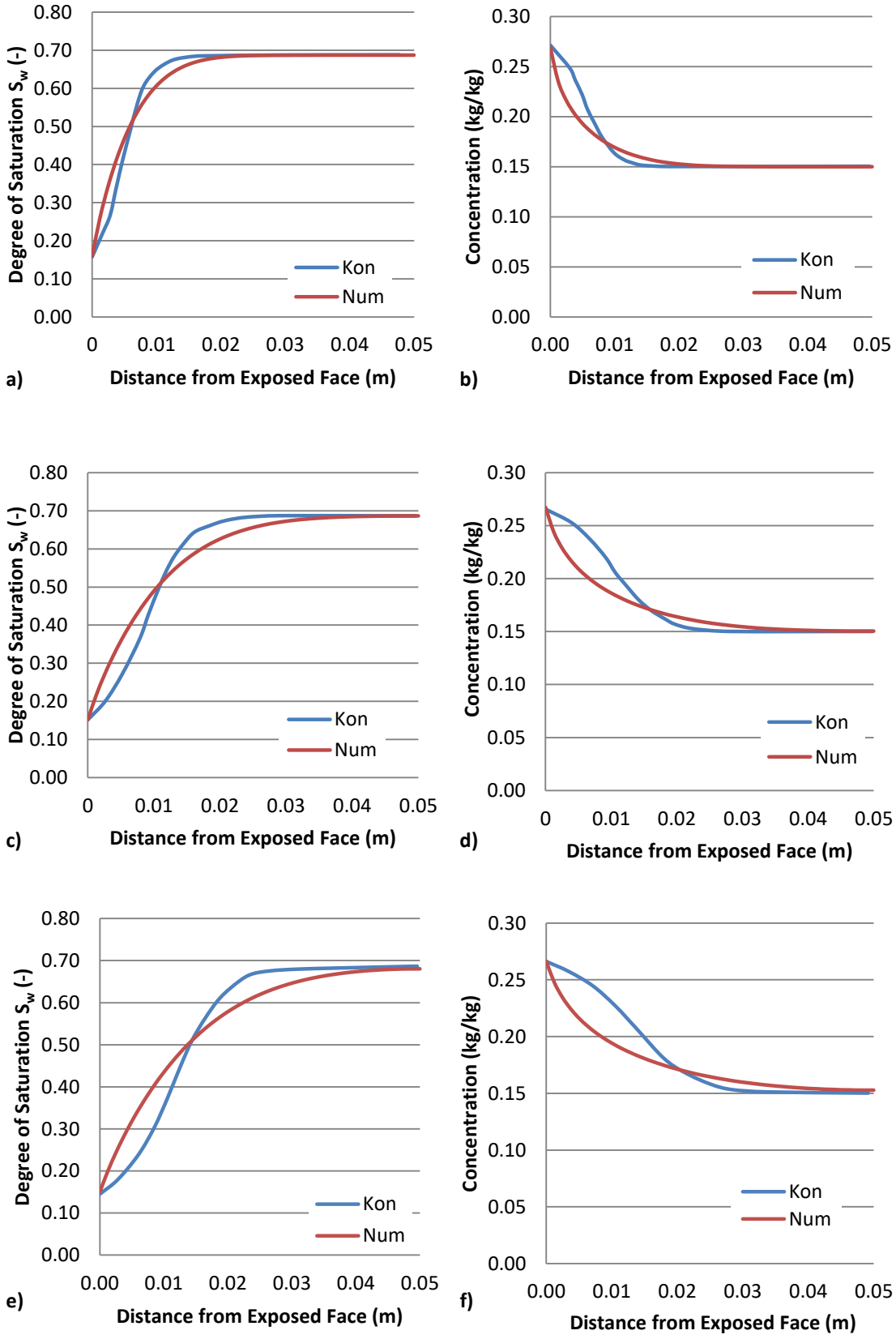

Figure 6.2 – Saturation and concentration profiles as predicted by the model and Koniorczyk (2010) a) S_w-20 hrs, b) c-20 hrs, c) S_w-60 hrs, d) c-60 hrs, e) S_w-100 hrs and f) c-100 hrs

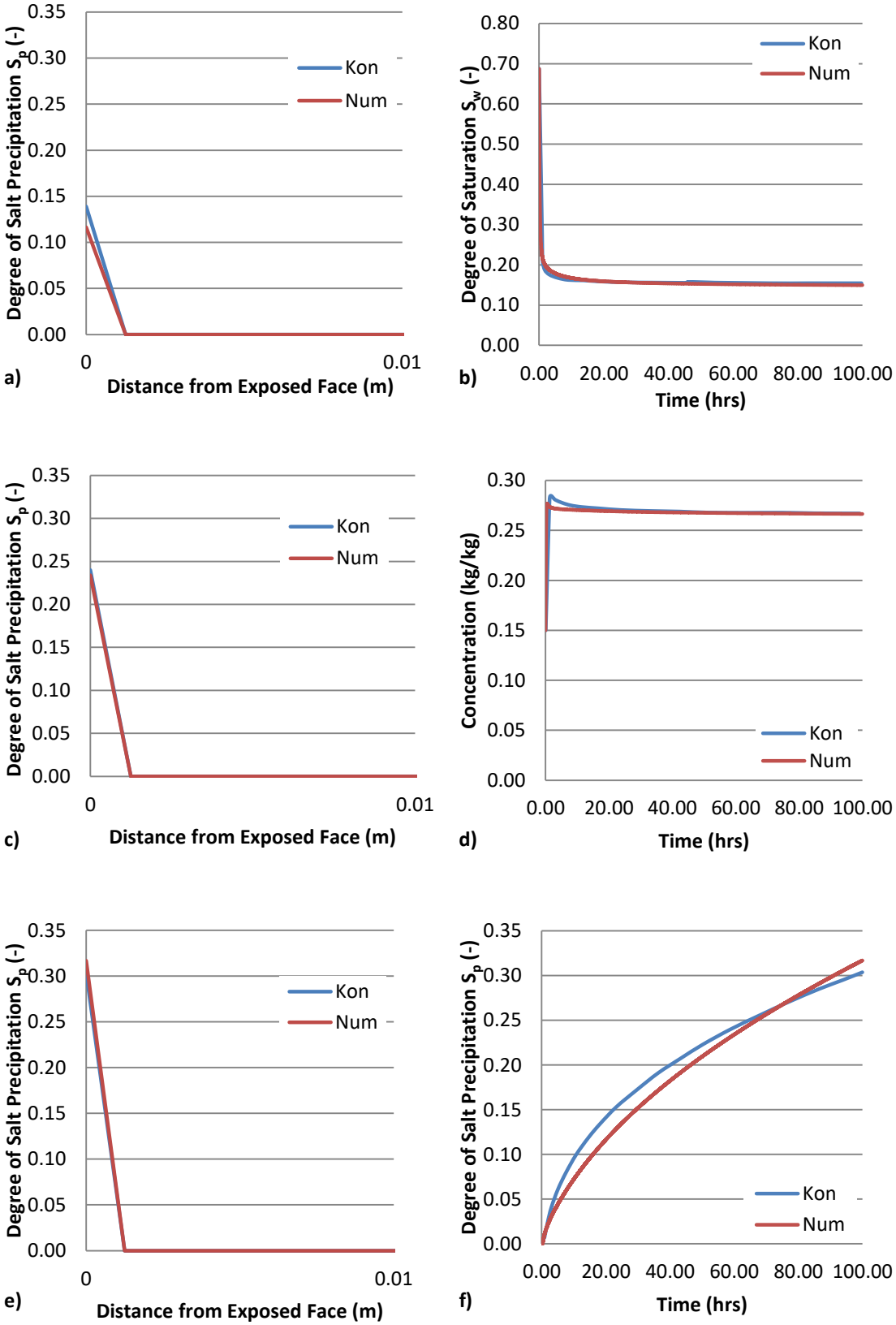

Figure 6.3 – Salt saturation and transient behaviour as predicted by the full model and Koniorczyk (2010) a) S_p-20 hrs, b) S_w (on the LHS boundary), c) S_p-60 hrs, d) c (on the LHS boundary), e) S_p-100 hrs and f) S_p (on the LHS boundary)

It can be seen from the profiles that the model is generally in good agreement with the results found in (Koniorczyk 2010). The degree of salt saturation shows good agreement for the 20, 60 and 100 hour profiles and the transient profiles of each of the variables are well matched. The profiles that are not as well matched are those of the liquid saturation and dissolved chemical concentration. The dissolved chemical concentration however depends on the degree of saturation as it is measured as mass per mass of liquid, and it can be seen that where the chemical concentration is over predicted the degree of saturation is under predicted and vice versa, therefore it is likely that the difference in concentration profiles is as a result of the difference in the liquid saturation profiles. The moisture models however are different and it is uncertain what values of parameters (such as the coefficients of both the moisture retention curve (eq. 3.19) and the permeability-saturation relation which were not reported by Koniorczyk (2010)) were used for the moisture flow. This difference may have arisen due to the fact that Koniorczyk (2010) has taken into account the effect of the salt on the moisture retention curve (Koniorczyk and Wojciechowski 2009), which can have a significant effect at high salt concentrations (Koniorczyk and Wojciechowski 2009) and which has not been accounted for in this thesis. The purpose of this example was to verify the chemical transport and precipitation, as the moisture transport will be validated later in section 6.3, meaning that it is justified to fit the model moisture results close to those of Koniorczyk (2010).

6.2.3 Example – Koniorczyk & Gawin (2012)

In 2012 Koniorczyk and Gawin (2012) developed the previous model (Koniorczyk 2010) further and considered the salt crystallisation pressure that is exerted on the solid skeleton. The salt crystallisation was considered with an assumption of non-equilibrium conditions using a Freundlich type isotherm as before, the difference being that in this approach the rate of precipitation was driven by the solution supersaturation ratio instead of the chemical concentration. The solution supersaturation ratio was calculated from the ion activity, which was calculated using an ion interaction model. To this end the Pitzer equations were preferred as a result of their higher range of validity than the Debye-Hückel or Davies models, which is important for the concentrations present in salt crystallisation problems. The examples

presented were of the drying of a wall saturated with a $NaCl$ solution. Two cases were considered, that of a brick wall and that of a concrete wall. The simulations chosen here are those of the concrete wall, and as the proposed model does not include a mechanical component the crystallisation pressures were not considered. The rate of reaction is of the general form of eq. (3.39) and is given by eqs. (3.40 & 3.41). Three different orders of reaction were considered, with the $\lambda=4.5$ case being chosen here.

6.2.3.1 Numerical Model Conditions

The dimensions of the concrete sample were 125x60 mm. The time period considered was 100 hours, a time step of $\Delta t = 3.6\, s$ and a uniform mesh of 100 bilinear quadrilateral elements were used, with element size of $\Delta x = 0.00125\, m$ and $\Delta y = 0.06\, m$. The finite element mesh used and problem geometry can be seen in Figure 6.4.

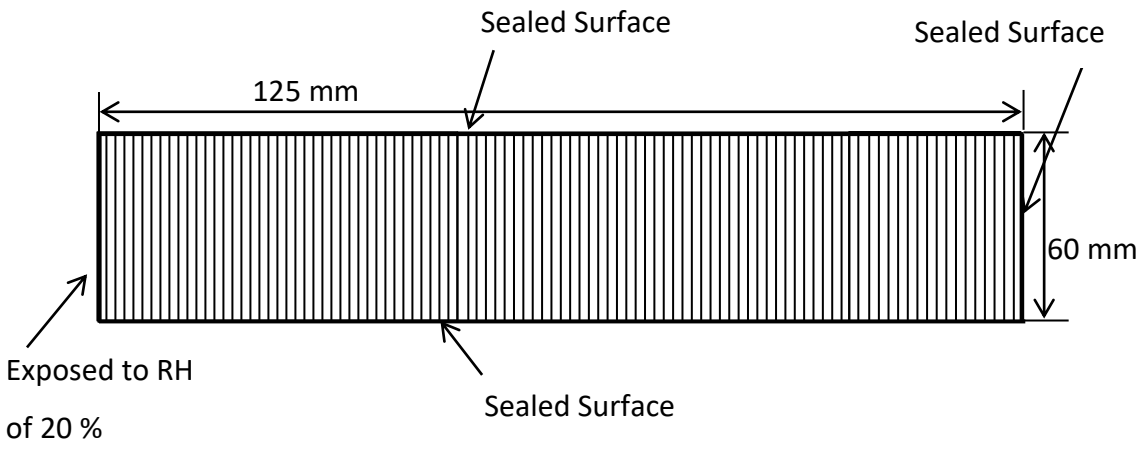

Figure 6.4 – Finite element mesh and problem geometry (not to scale)

The initial conditions along with the parameters used for the simulation can be seen in Table 6.3. The boundary conditions considered were of zero flux for the sealed sides and of the Cauchy type (eqs. 4.15-4.17) for the exposed surface, the values can be seen in Table 6.4. The Pitzer parameters used were taken from (Steiger et al. 2008).

Table 6.3 –Model parameters

Parameter		Values
Permeability (eqs. 3.11 & 3.18)	K_{i0}[a] $(10^{-21}\ m^2)$	3.0
	A_w[b]	1.0
Moisture Retention (eq. 3.19)	a_c[a]	183.834
	b[a]	2.27
Porosity	n[a]	0.131
Boundary (eqs. 4.15-4.17)	α_c $(W/Km2)$	8.0
	β_c $(10^{-3}\ m/s)$	2.6
Initial Values	S_w[a]	1.0
	c^a (kg/kg)	0.1
	S_p[a]	0.0
Reaction (eqs. 3.40 & 3.41)	A'	1.4
	λ[a]	4.5
	k_{da}[a]	1.0
	A'_2	1.3
Diffusion (eq. 3.38)	D_{mol}[c] $(10^{-9}\ m^2/s)$	1.0
	τ	0.45

[a]Taken from (Koniorczyk and Gawin 2012)
[b]Reported values between 1 and 6 (Koniorczyk and Gawin 2011)
[c]Taken from (Koniorczyk 2010)

Table 6.4 – Boundary conditions

Boundary	Boundary Type	Values
LHS	Cauchy	$RH=60\ \%$, $c=0\ kg/kg$, $T=293\ K$
Bottom	Sealed	-
RHS	Sealed	-
Top	Sealed	-

It should be noted that A' found in eq. (3.40) is the primary crystallisation coefficient, which is the supersaturation ratio needed for crystallisation to begin and A'_2 is the secondary crystallisation coefficient. It was unclear which values of A' and A'_2 were used by Koniorczyk and Gawin (2012) and so values of 1.4 and 1.3 were chosen here after an initial calibration exercise. The calibration exercise involved changing the

values of the parameters on a trial and error (beginning with the moisture parameters) basis until the resultant profiles were in good agreement with those of Koniorczyk and Gawin (2012). These values do not lie within the reported ranges quoted by Koniorczyk and Gawin (2012) however it should be noted that the solubility also depends on the pore size, needing a higher salt concentration to begin precipitation in smaller pores, which is not taken into account in this study. The influence of pore size on the solubility can be seen in Figure 6.5 for three different crystal shapes (reproduced from Koniorczyk and Gawin (2012), a and $ainf$ are the activities of a solution saturated with small and large crystals respectively and r is the pore radius). As with the previous example, it was found in this study that a tortuosity factor was needed to correctly predict the chemical transport, and the boundary mass transfer coefficient needed was lower than the value reported by Koniorczyk and Gawin (2012) ($8x10^{-3}$ m/s).

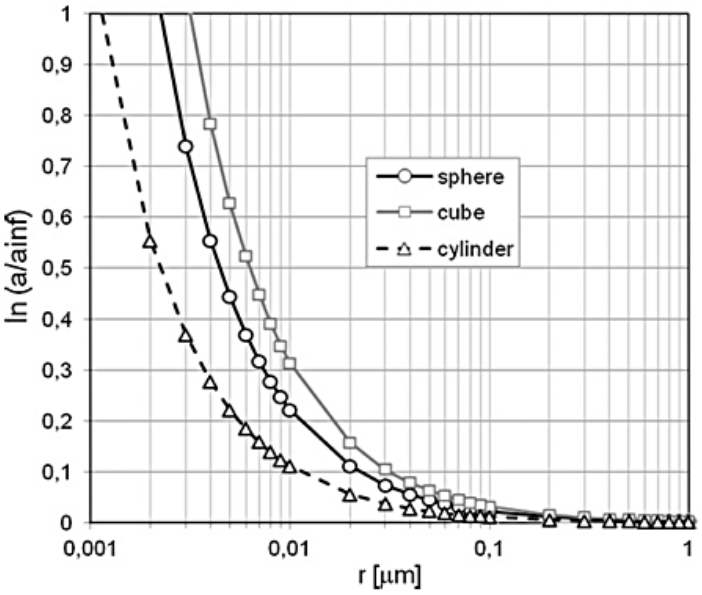

Figure 6.5 – Influence of pore size on salt solubility (after Koniorczyk and Gawin (2012))

6.2.3.2 Results and Discussions

The comparison of the results of the model and the results of Koniorczyk and Gawin (2012) can be seen in Figure 6.6 for the liquid saturation and supersaturation profiles and Figure 6.7 for the salt profiles and the transient behaviour. The transient profiles are measured at a point on the exposed surface.

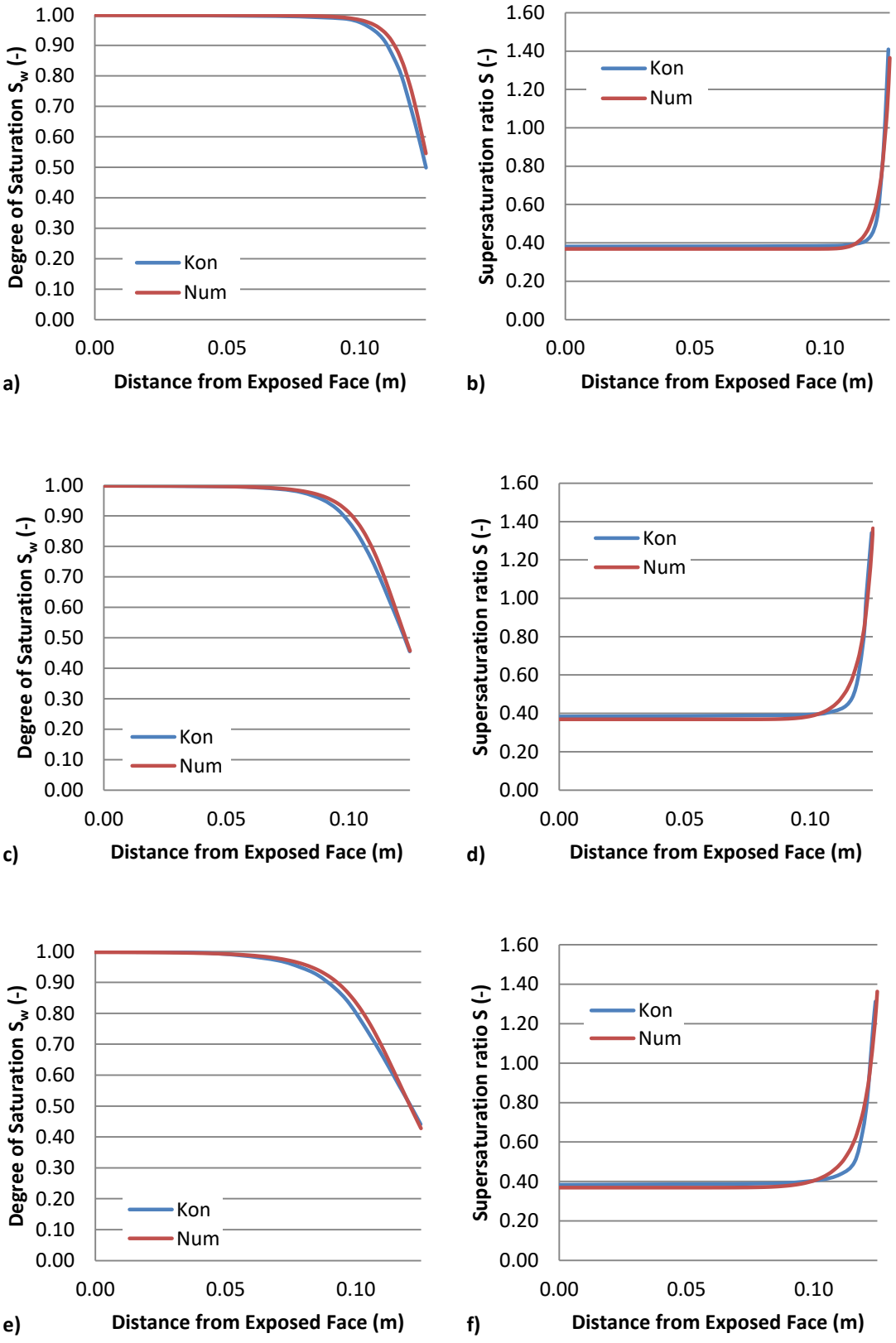

Figure 6.6 – Saturation and solution supersaturation profiles as predicted by the full model and Koniorczyk and Gawin (2012) a) S_w-20 hrs, b) S-20 hrs, c) S_w-60 hrs, d) S-60 hrs, e) S_w-100 hrs and f) S-100 hrs

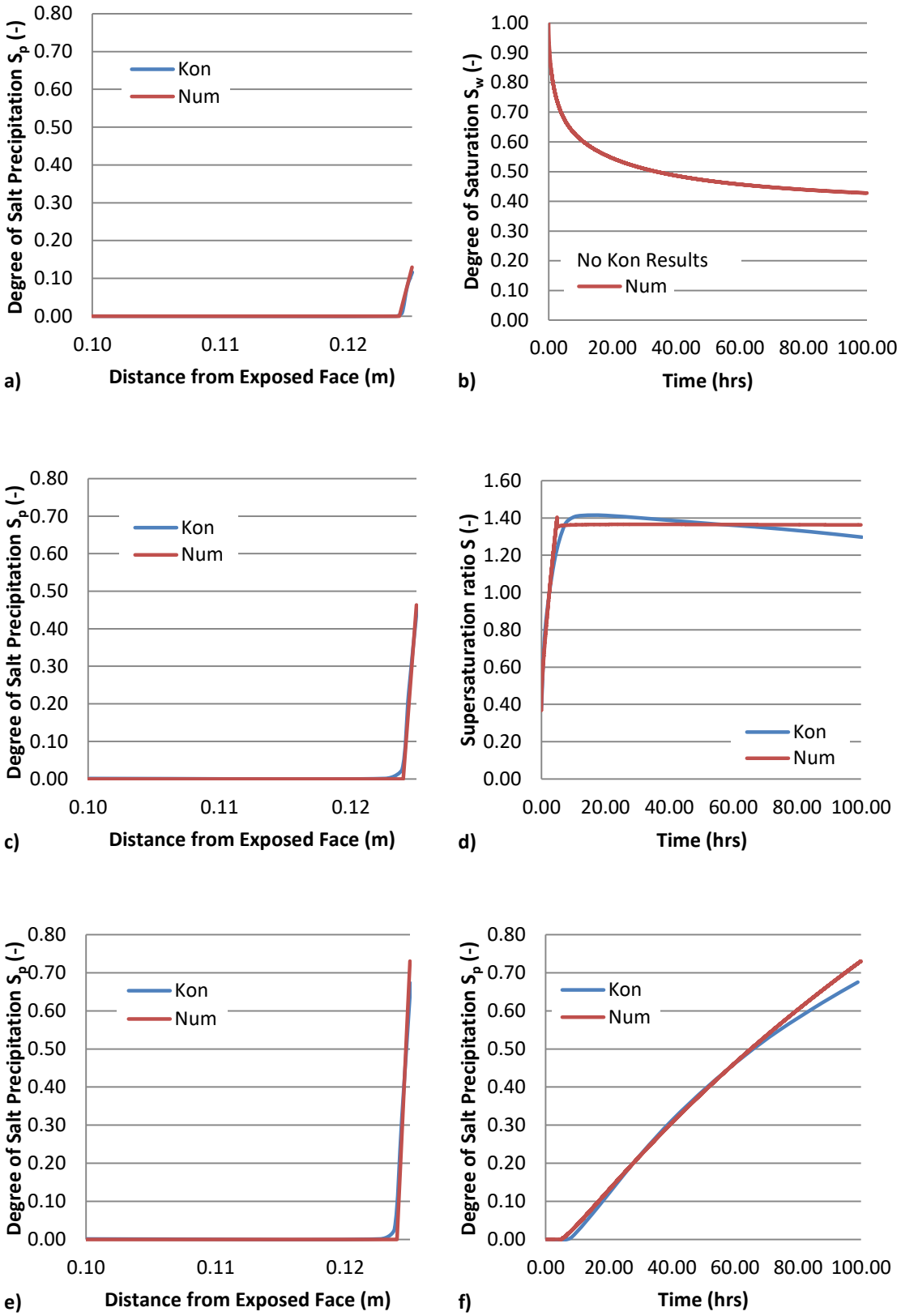

Figure 6.7 – Salt saturation and transient behaviour as predicted by full model and Koniorczyk and Gawin (2012) a) S_p-20 hrs, b) S_w (on the LHS boundary), c) S_p-60 hrs, d) S (on the LHS boundary), e) S_p-100 hrs and f) S_p (on the LHS boundary)

It can be seen from the profiles presented in Figures 6.6 and 6.7 that the model is in good agreement with the simulations of Koniorczyk and Gawin (2012). The precipitated salt profiles are the best match, with the liquid saturation being slightly over predicted, as is the supersaturation ratio. The transient behaviour the degree of salt precipitation is closely matched until around 70 hours where the model begins to over predict the amount. The solution supersaturation ratio was in the same range of values but the behaviour was slightly different, instead of increasing to a maximum at around 9 hours and then gradually decreasing, the model predicts it increasing to a maximum at around 6 hours, followed by a sharp decrease and then a relatively constant value therein. This behaviour arises due to the fact that following the initial salt precipitation the rate of increase of concentration due to the decrease in moisture content is almost equal to the rate of decrease of concentration due to the salt precipitation.

6.2.4 Example – Baroghel-Bouny et al. (2011)

In 2011 Baroghel-Bouny et al. (2011) presented a model for the simulation of multi-ionic transport in cementitious materials. The model included both the consideration of the chloride binding and formation of Friedel's salt. The formation of Friedel's salt was assumed to be instantaneous, whereas the chloride binding was investigated with assumptions of both equilibrium and non-equilibrium conditions. It was found that the non-equilibrium assumption gave a more accurate prediction of the total chloride content profiles (Tcc) measured in diffusion experiments, with the modelling under the equilibrium assumption greatly over predicting the Tcc near the surface and greatly under predicting the chloride penetration depth. It was also assumed that as the chloride ions bound to the cement matrix, hydroxide ions were simultaneously released to maintain the charge neutrality of the solution. The rate of reaction can be described by eq. (3.39), and the formation of Friedel's salt is given as:

$$S_p = \delta n_{C_3Aeq} \tag{6.2}$$

where δ is a factor derived from stoichiometric considerations and n_{C_3Aeq} is the equivalent content of the residual aluminates of the material.

The simulations were based upon the modelling of experiments carried out by Francy (1998), concerning the transport of Na^+, Cl^-, OH^- and K^+ ions through mortar specimens. Both advective-diffusive and diffusive cases were considered, with the diffusive case being chosen here for comparison.

6.2.4.1 Numerical Model Conditions

The sample was a cement disc of size 120x20 mm (diameter x thickness). The time period considered was 12 hours, a time step of $\Delta t = 0.9\ s$ and a uniform mesh of 20 bilinear quadrilateral elements were used, with element size of $\Delta x = 0.001\ m$ and $\Delta y = 0.12\ m$. The finite element mesh used and problem geometry can be seen in Figure 6.8.

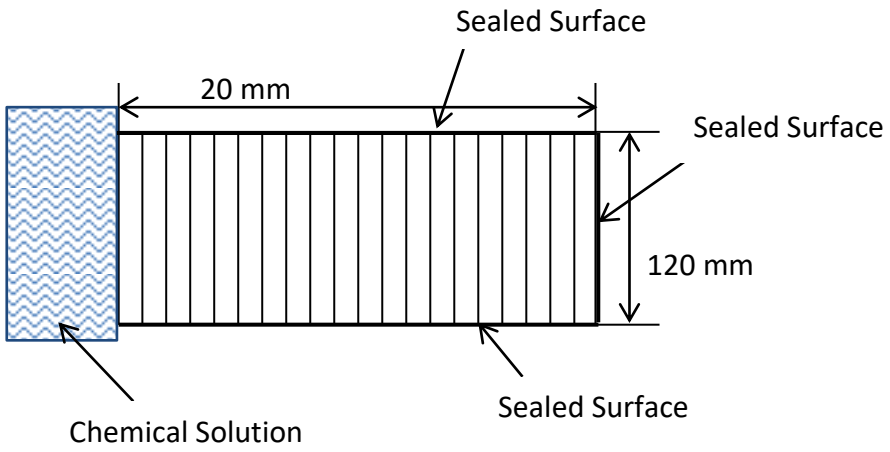

Figure 6.8 – Finite element mesh and problem geometry (not to scale)

The initial conditions along with the parameters used for the simulation can be seen in Table 6.5. The boundary conditions considered were of zero flux for the sealed sides and of the Cauchy type (eqs. 4.15-4.17) for the exposed surface, the values can be seen in Table 6.6. It was found in this example that different values of the diffusion coefficients than those reported by Baroghel-Bouny et al. (2011) were needed. This may be due to the fact that the current model deals with the charge neutrality condition in a different manner than Baroghel-Bouny et al. (2011), which would have an effect on the ion transport. The diffusion coefficients are however within the range of values reported in the literature (Baroghel-Bouny et al. 2011; Song et al. 2014). The boundary mass transfer coefficients were chosen based on an initial calibration

exercise (which involved changing the values on a trial and error basis until a good match was obtained).

Table 6.5 – Model parameters

Parameter			Values
Porosity	n^a		0.13
Boundary (eqs. 4.15-4.17)	α_c (W/Km^2)		8.0
	γ_c $(10^{-3}\ m/s)$		6.5
Initial Values	$S_w{}^a$		1.0
	Tcc^a (kg/kg)		0.01954
	Na^{+a} (kg/kg)		0.01352
	Cl^a (kg/kg)		0.01954
	OH^a (kg/kg)		0.00188
	K^{+a} (kg/kg)		0.00319
Reaction (eqs. 3.39 & 6.2)	$k_{da}{}^a$ (10^{-4})		1.305
	λ^a		0.61
	δ^a		2
	$n_{C_3Aeq}{}^a$ (mol/dm^3)		21
Diffusion (eq. 3.38)	D_{mol} $(10^{-10}\ m^2/s)$	Na^+	1.33
		Cl^-	2.1
		OH^-	5.3
		K^+	1.96

[a]Taken from (Baroghel-Bouny et al. 2011)

Table 6.6 –Boundary conditions

Boundary	Boundary Type	Values
LHS	Cauchy	$RH=100\ \%,\ T=293\ K,$ $Na^+=0.000299\ kg/kg,$ $Cl^-=0.0\ kg/kg,$ $OH^-=0.001105\ kg/kg,$ $K^+=0.002028\ kg/kg$
Bottom	Sealed	-
RHS	Sealed	-
Top	Sealed	-

6.2.4.2 Results and Discussions

The comparison of the results of the model and the results of Baroghel-Bouny et al. (2011) can be seen in Figure 6.9.

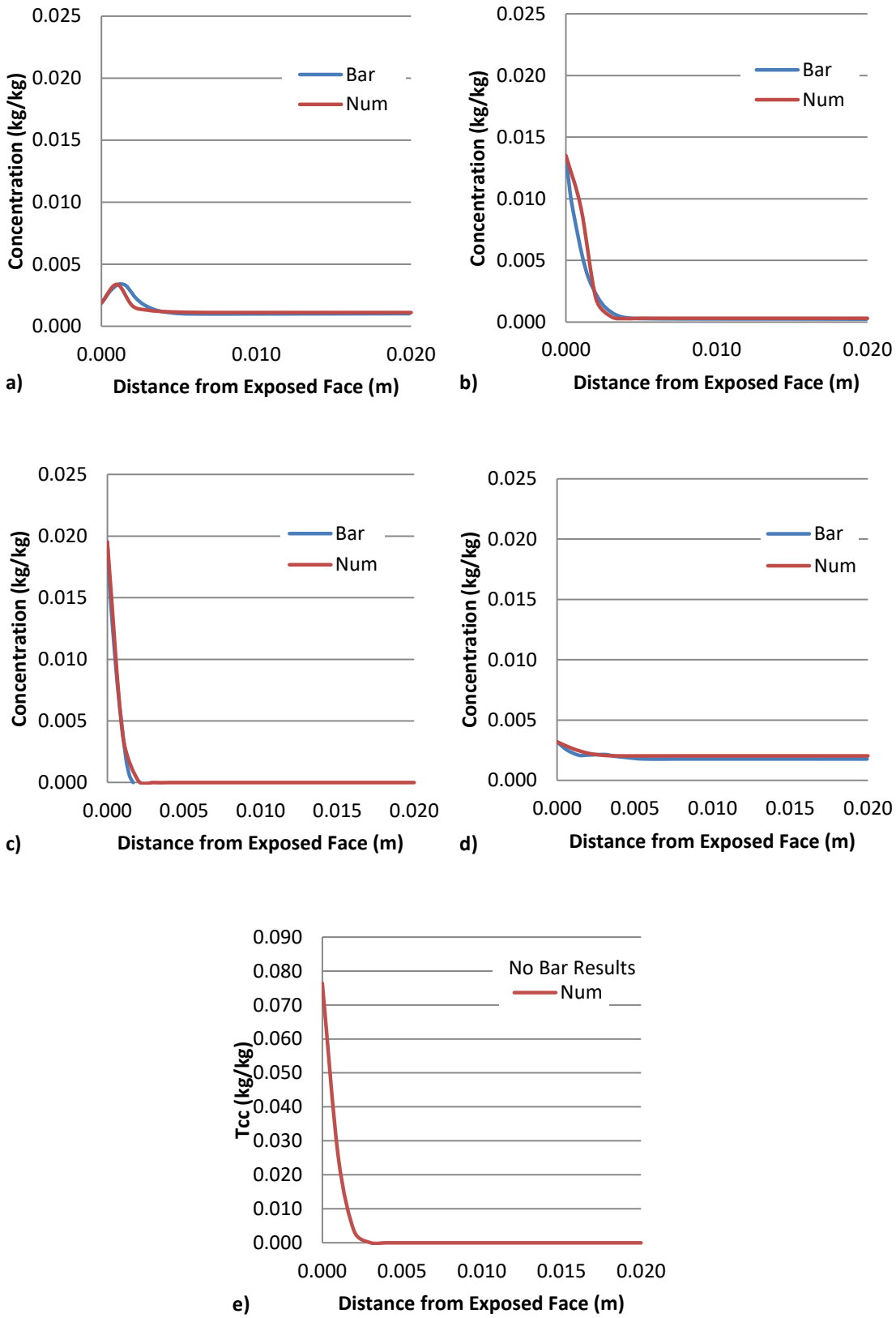

Figure 6.9 – Concentration and Tcc profiles as predicted by the full model and Baroghel-Bouny et al. (2011) (t=12 hours) a) OH^-, b) Na^+, c) Cl^-, d) K^+ and e) Tcc

In can be seen from the profiles above that the model predictions are in good agreement with the simulations of Baroghel-Bouny et al. (2011), with the biggest differences being the slight over prediction of the Na^{+} concentration near the exposed face and the under prediction of OH^{-} concentration near the peak that has arisen as a result of the chloride binding.

6.2.5 Example – Song et al. (2014)

In 2014 Song et al. (2014) developed a model to simulate the chloride transport in multiple-ionic solutions in cementitious materials, supplemented by experimental diffusion tests. It is the numerical simulations that are considered here as they provide results for all the chemical species and sorbed masses considered, whereas the experimental results concern only the total chloride content. The simulation considered the diffusion of chemical ions into a concrete specimen, the pore solution of which had an initial composition which included the presence of a number of ions, namely, Na^{+}, Ca^{2+}, K^{+}, OH^{-} and SO_4^{2-}. Two different scenarios were modelled, one of a $NaCl$ source solution and the other of a $CaCl_2$ source solution. The results of the $CaCl_2$ source solution case were considered here. A number of different reactions were considered in the model, including the dissolution of portlandite, and the dissolution of calcium and hydroxide from the C-S-H phases. The chemical chloride bindings onto the AFm phases were also considered, including formation of both Friedel's salt and Kuzel's salt. The physical absorption of the chloride ions onto the C-S-H phases was also taken into account, however their chemical binding onto the same phase was not considered. Finally the alkali bindings onto both the C-S-H and Afm phases were included. All of the reactions were considered with an assumption of non-equilibrium conditions and can be described using a Freundlich type isotherm, the rates of which are empirical but based on mass action law or empirical equations similar to mass action law. These reactions are given as:

$$r_1 = [CH]\left(k_d^{CH} - k_a^{CH}([Ca^{2+}][OH^{-}]^2)^{\lambda_1}\right) \tag{6.3}$$

$$r_2 = k_a^{CSH}[C/S] - k_d^{CSH}([Ca^{2+}][OH^{-}]^2)^{\lambda_2} \tag{6.4}$$

$$r_3 = k_a^{CSH.CaCl_2}[CSH.CaCl_2] - k_d^{CSH.CaCl_2}([Ca^{2+}][Cl^{-}]^2)^{\lambda_3} \tag{6.5}$$

$$r_4 = k_a^{CSH.NaCl}[CSH.NaCl] - k_d^{CSH.NaCl}([Na^+]^2[Cl^-]^2)^{\lambda_4} \quad (6.6)$$

$$r_5 = k_a^{CSH.2KCl}[CSH.2KCl] - k_d^{CSH.2KCl}([K^+]^2[Cl^-]^2)^{\lambda_5} \quad (6.7)$$

$$r_6 = k_a^{CSH.2NaOH}[CSH.2NaOH] - k_d^{CSH.2NaOH}([Na^+]^2[OH^-]^2)^{\lambda_6} \quad (6.8)$$

$$r_7 = k_a^{CSH.2KOH}[CSH.2KOH] - k_d^{CSH.2KOH}([K^+]^2[OH^-]^2)^{\lambda_7} \quad (6.9)$$

$$r_8 = k_a^{CAH}[CAH] - k_d^{CAH}([Ca^{2+}][OH^-]^2)^{\lambda_8} \quad (6.10)$$

$$r_9 = k_d^{CASH}[CASH]^{\alpha} - k_a^{CASH}([Ca^{2+}][SO_4^{2-}])^{\lambda_9} \quad (6.11)$$

$$r_{10} = k_d^{CAHCaCl_2}[CAH.CaCl_2] - k_a^{CCAHCaCl_2}([Ca^{2+}][Cl^-]^2)^{\lambda_{10}} \quad (6.12)$$

Reactions 1, 2, 8 and 9 all concern the reactions of the cement matrix, which are not taken into account in this study. These solids, however, show little change over the time period considered and so can be neglected with little loss of accuracy. This can be seen in Figure 6.10, which shows the comparison of the initial solid concentrations with the final values.

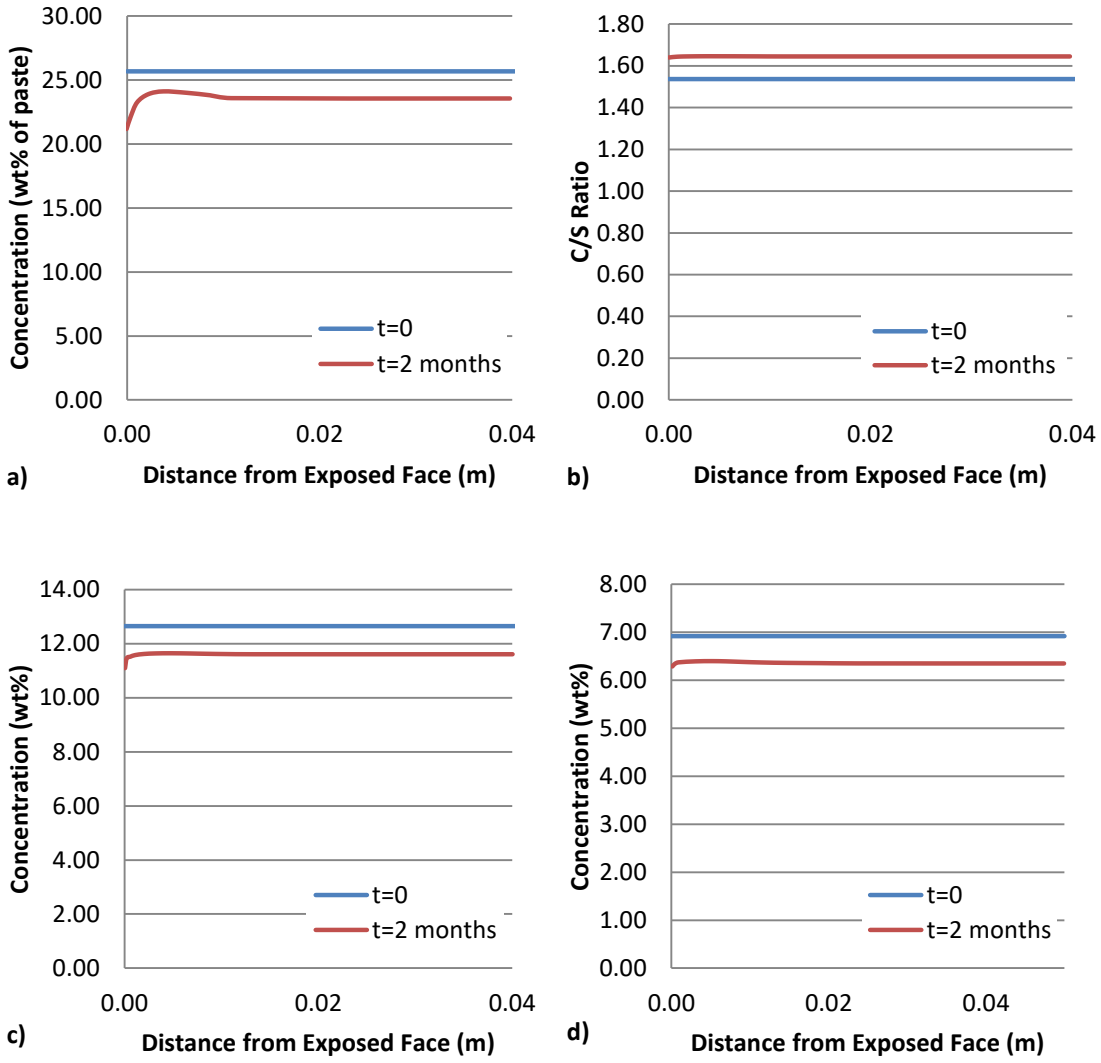

Figure 6.10 – Neglected solid profiles as predicted by Song et al. (2014) a) *CH*, b) *C/S Ratio*, c) *CAH* and d) *CASH*

6.2.5.1 Numerical Model Conditions

The concrete sample was a cylindrical core of size 100x50 mm (diameter x thickness). The time period considered was 2 months, a time step of $\Delta t = 360\ s$ and a uniform mesh of 25 bilinear quadrilateral elements were used, with element size of $\Delta x = 0.002\ m$ and $\Delta y = 0.12\ m$. The finite element mesh used and problem geometry can be seen in Figure 6.11.

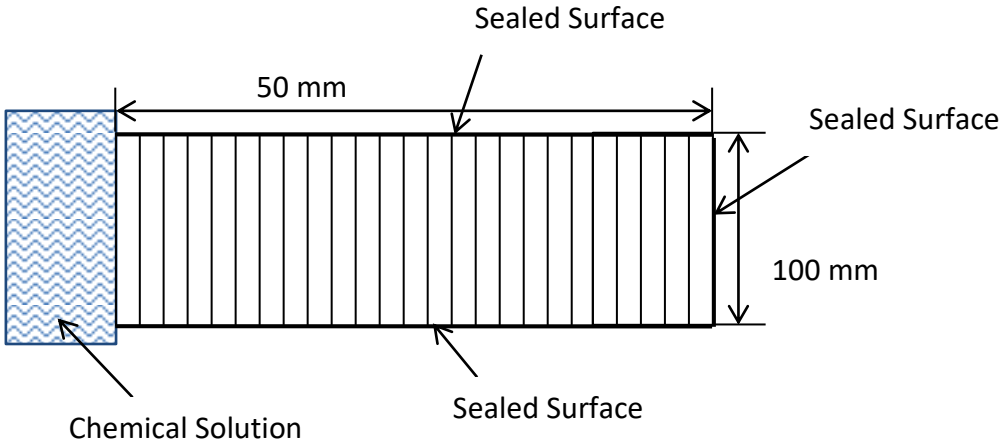

Figure 6.11 – Finite element mesh and problem geometry (not to scale)

The parameters used for the simulation can be seen in Table 6.7. The initial concentrations and diffusion coefficients of the chemical species along with the reaction parameters can be seen in Table 6.8. The boundary conditions considered were of zero flux for the sealed sides and of the Cauchy type (eqs. 4.15-4.17) for the exposed surface, the values can be seen in Table 6.9. Here a factor D_{es} was used to account for the effect of the electrostatic double layer; numerically it is treated in the same way as a tortuosity factor. It was found in this example that different values for both the D_{es} factors and the reaction rates than those reported by (Song et al. 2014) were needed. In this study these values –along with the porosity and boundary mass transfer coefficients- were chosen based on a calibration exercise following the approach of Song et al. (2014) who chose these values on a trial and error basis to match the experimental Tcc contents.

Table 6.7 –Model parameters

Parameter		Values
Porosity	n	0.13
Boundary (eqs. 4.15-4.17)	α_c (W/Km^2)	8.0
	γ_c $(10^{-4}\ m/s)$	1.0

Table 6.8 – Chemical parameters

Species	Initial Conc. (kg/kg)	D_{mol} $(10^{-9}\ m^2/s)$	D_{es}	Eq.	k_a (10^{-8})	k_d (10^{-8})	λ
Na^{+a}	0.001978	1.33	0.25	*r3*	12.0	18.0	0.35
OH^{a}	0.004573	5.3	0.25	*r4*	144.0	24.0	0.35
K^{+a}	0.007215	1.96	0.0875	*r5*	1375.0	330.0	0.35
Cl^{a}	0.0	2.1	0.25	*r6*	6.42	1.275	0.2
SO_4^{2-a}	0.000192	1.07	1.0	*r7*	5.4	0.75	0.2
Ca^{2+a}	0.00004	0.79	0.4	*r10*	1000.00	1200.0	0.35

[a]Taken from (Song et al. 2014)

Table 6.9 –Boundary conditions

Boundary	Boundary Type	Values
LHS	Cauchy	$RH=100\ \%$, $T=293\ K$, $Na^+=0.0\ kg/kg$, $Cl^-=0.01775\ kg/kg$, $OH^-=0.0\ kg/kg$, $K^+=0.0\ kg/kg$, $Ca^{2+}=0.01\ kg/kg$, $SO_4^{2-}=0.0\ kg/kg$
Bottom	Sealed	-
RHS	Sealed	-
Top	Sealed	-

6.2.5.2 Results and Discussions

The comparison of the results of the model and the results of Song et al. (2014) can be seen in Figure 6.12 for the concentration profiles and Figure 6.13 for the solid profiles.

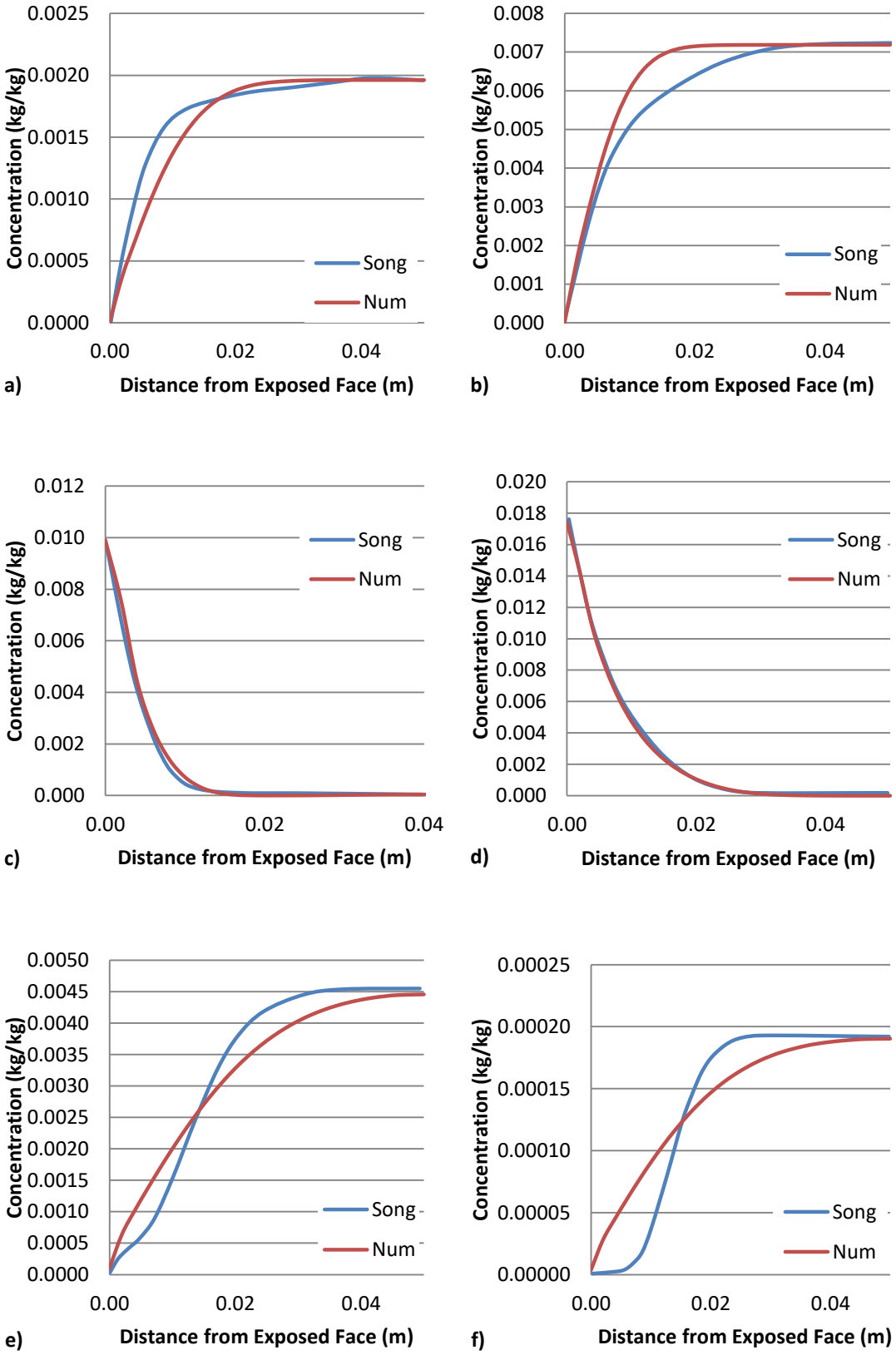

Figure 6.12 – Concentration profiles as predicted by the full model and Song et al. (2014) (t=2 months) a) Na^{+}, b) K^{+}, c) Ca^{2+}, d) Cl^{-}, e) OH^{-} and f) SO_4^{2-}

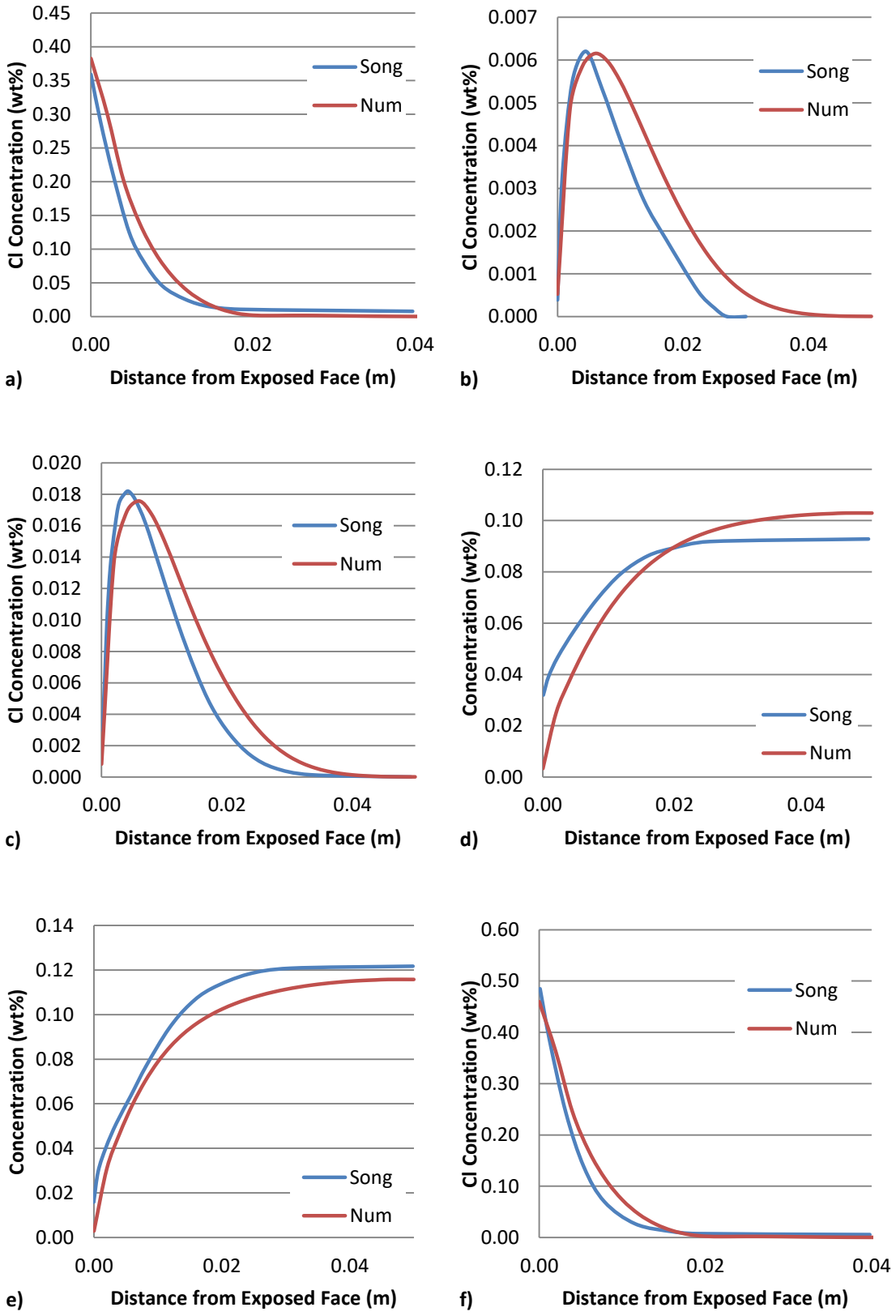

Figure 6.13 – Solid mass profiles as predicted by the full model and Song et al. (2014) (t=2 months) a) *CSH.CaCl*$_2$, b) *CSH.NaCl*, c) *CSH.2KCl*, d) *CSH.NaOH*, e) *CSH.2KCl* and f) *CAH.CaCl*$_2$

It can be seen from the profiles in Figure 6.12 that the model predictions are generally in good agreement with the simulations of Song et al. (2014), with the Ca^{2+} and Cl^{-} being almost identical. The diffusion of Na^{+} is slightly over predicted near the exposed face whereas the diffusion of K^{+} is under predicted from about 0.006 m to 0.03 m. The amount of transport of both OH^{-} and SO_4^{2-} is in agreement but the shapes of the curves are different, with the results of Song et al. (2014) showing a sharper concentration front.

The solid mass profiles also show a generally good agreement with $CSH.CaCl_2$ and $CAH.CaCl_2$ being the closest but slightly over predicted. The $CSH.2KOH$ and $CSH.2KCl$ are also both in good agreement but slightly under predicted and over predicted respectively. The $CSH.2NaOH$ profile is similar to the OH^{-} and SO_4^{2-} profiles in that it is over predicted in some areas and under predicted in others. In the case of the $CSH.NaCl$ the penetration is over predicted by the model. It is thought that the differences in predicted profiles are a result of the following factors:

1. Different numerical methods were used (finite element method vs finite difference method).
2. Charge neutrality was dealt with in a different way.
3. Reactions, 1,2, 8 and 9 were neglected in this study, but may have had a significant effect on certain profiles (for example SO_4^{2-} which is involved in reaction 9 and may be sensitive to small changes due to its low concentration).

6.3 Validation of the Coupled Model

6.3.1 Introduction

This section deals with validation of the moisture flow and chemical transport part of the model and involves the numerical simulation of experimental results carried out on the drying of cementitious materials by Kim and Lee (1999) and of the ion transport experiments reported in Chapter 5.

For both examples the mesh and time step sizes were chosen based on the results of a mesh convergence study.

6.3.2 Example – Kim and Lee (1999)

Kim and Lee (1999) reported results of an experimental study and numerical modelling of moisture diffusion and self-desiccation in concrete specimens. The results of the experimental study are used here to allow validation of the model developed in Chapter 4. Three different concrete mixes were considered, a high strength (H), medium strength (M) and a low strength (L). The materials used were ordinary Portland cement, river sand and crushed granite gravel of size <19 mm. The mix proportions for the three different mixes can be seen in Table 6.10 (reproduced from Kim and Lee (1999)).

Table 6.10 – Mix parameters

Mix	w/c	F.A./C.A.	Water (kg/m^3)	Cement (kg/m^3)	F.A. (kg/m^3)	C.A. (kg/m^3)	S.P. (Cx%)	f_c (MPa)
H	0.28	0.38	151	541	647	1055	2.0	76
M	0.40	0.42	169	423	736	1016	0.5	53
L	0.68	0.45	210	310	782	955	0.0	22

where F.A. stands for the fine aggregate, C.A. stands for the coarse aggregate, S.P. stands for super plasticiser, and f_c is the compressive strength. Once the beam specimens were cast they were moist cured for 28 days before testing. Following this, five sides were sealed with paraffin wax, with the remaining side being exposed to an environmental relative humidity of 50 %. The change in relative humidity was measured at three positions along the profile of the specimen, namely 3 cm, 7 cm and 12 cm from the exposed face. To take these measurements holes were drilled at the three locations, into which plastic sleeves were inserted, containing the humidity probes with a rubber plug, as shown in Figure 6.14. The measurements were taken using Vaisala HMP44 probes and Vaisala HMI41 indicators. The problem geometry and the position of the measuring points can be seen in Figure 6.15.

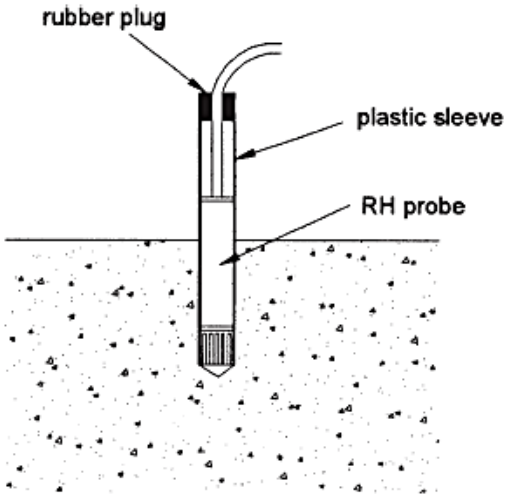

Figure 6.14 – Placement of probe (after Kim and Lee (1999))

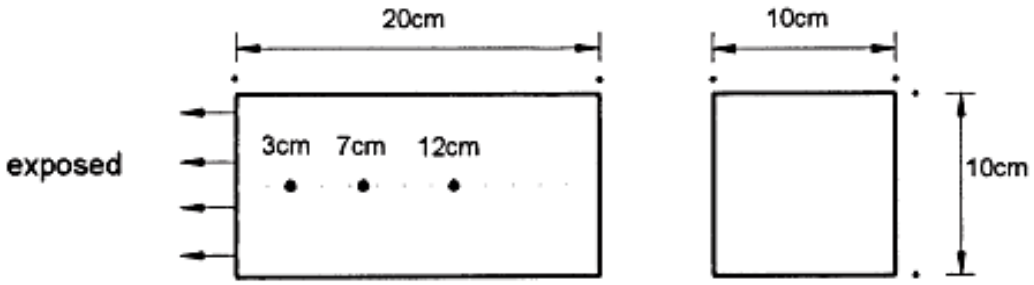

Figure 6.15 – Specimen geometry (after Kim and Lee (1999))

In order to measure the self-desiccation of the concrete additional specimens were cast and the experiment carried out with all sides sealed, the size of these specimens was 10x10x10 cm. The self-desiccation of concrete arises due to the on-going hydration reaction of the cement. This however, was not taken into account in the proposed model and so the results for the diffusion only case were considered here. In their study the moisture loss from the concrete was also measured and is included in the simulation described.

6.3.2.1 Numerical Model Conditions

The concrete sample was a beam of size 200x100 mm. The time period considered was 120 days, a time step of $\Delta t = 10800\ s$ and a uniform mesh of 80 bilinear quadrilateral elements were used, with element size of $\Delta x = 0.005\ m$ and $\Delta y = 0.05\ m$. It should

be noted however that as the analysis is essentially one dimensional this division in y is arbitrary. The finite element mesh used and problem geometry can be seen in Figure 6.16.

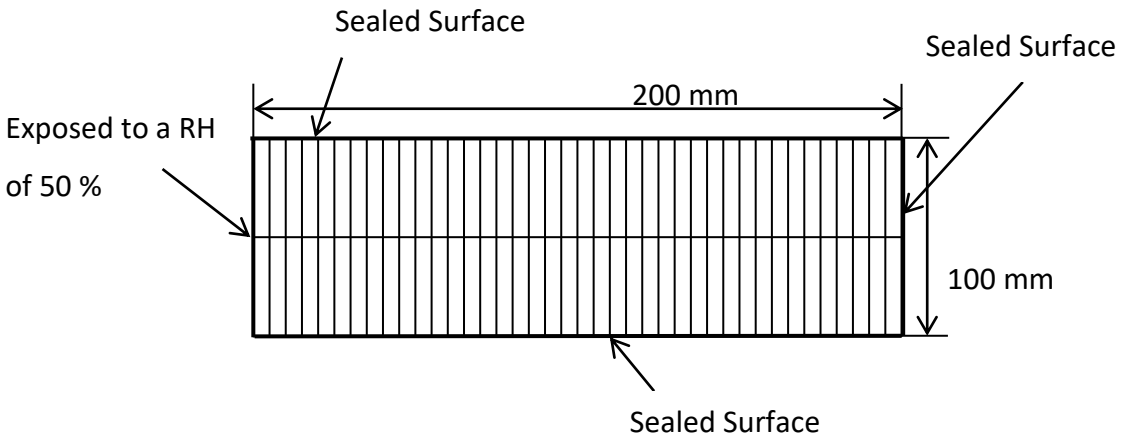

Figure 6.16 – Finite element mesh and problem geometry (not to scale)

It was assumed that the specimen was initially saturated following Kim and Lee (1999). The boundary conditions considered were of zero flux for the sealed sides and of the Cauchy type (eqs. 4.15-4.17) for the exposed surface. The values can be seen in Table 6.11. The moisture retention curve parameters used were the same for each mix, with the porosity, boundary mass transfer coefficients and intrinsic permeability varying. The values of the porosity, intrinsic permeability and boundary mass transfer coefficients were not measured by Kim and Lee (1999), and so were chosen here based on an initial calibration exercise (which involved changing the values on a trial and error basis until a good match was obtained). Full details of the parameters used in the simulation can be seen in Table 6.12.

Table 6.11 – Boundary conditions

Boundary	Boundary Type	Values
LHS	Cauchy	$RH=50\%$
Bottom	Sealed	-
RHS	Sealed	-
Top	Sealed	-

Table 6.12 – Model parameters

Parameter		Mix		
		L	M	H
Permeability (eqs. 3.11 & 3.18)	$K_{i0}\ (10^{-21}\ m^2)$	4.0	1.0	0.3
	A_w[a]	3.5	3.5	3.5
Moisture Retention (eq. 3.19)	a_c[b]	183.834	183.834	183.834
	b[b]	2.27	2.27	2.27
Porosity	n	0.15	0.125	0.1
Boundary (eqs. 4.15-4.17)	$\alpha_c\ (W/Km^2)$	8.0	8.0	8.0
	$\beta_c\ (10^{-4}\ m/s)$	2.5	1.0	0.8

[a]Reported values between 1 and 6 (Koniorczyk and Gawin 2011)
[b]Taken from (Koniorczyk and Gawin 2012)

6.3.2.2 Results and Discussions

The comparison between the numerical results of the model and the experimental results reported by Kim and Lee (1999) for the moisture profiles as well as the moisture lost from the specimens can be seen in Figure 6.17.

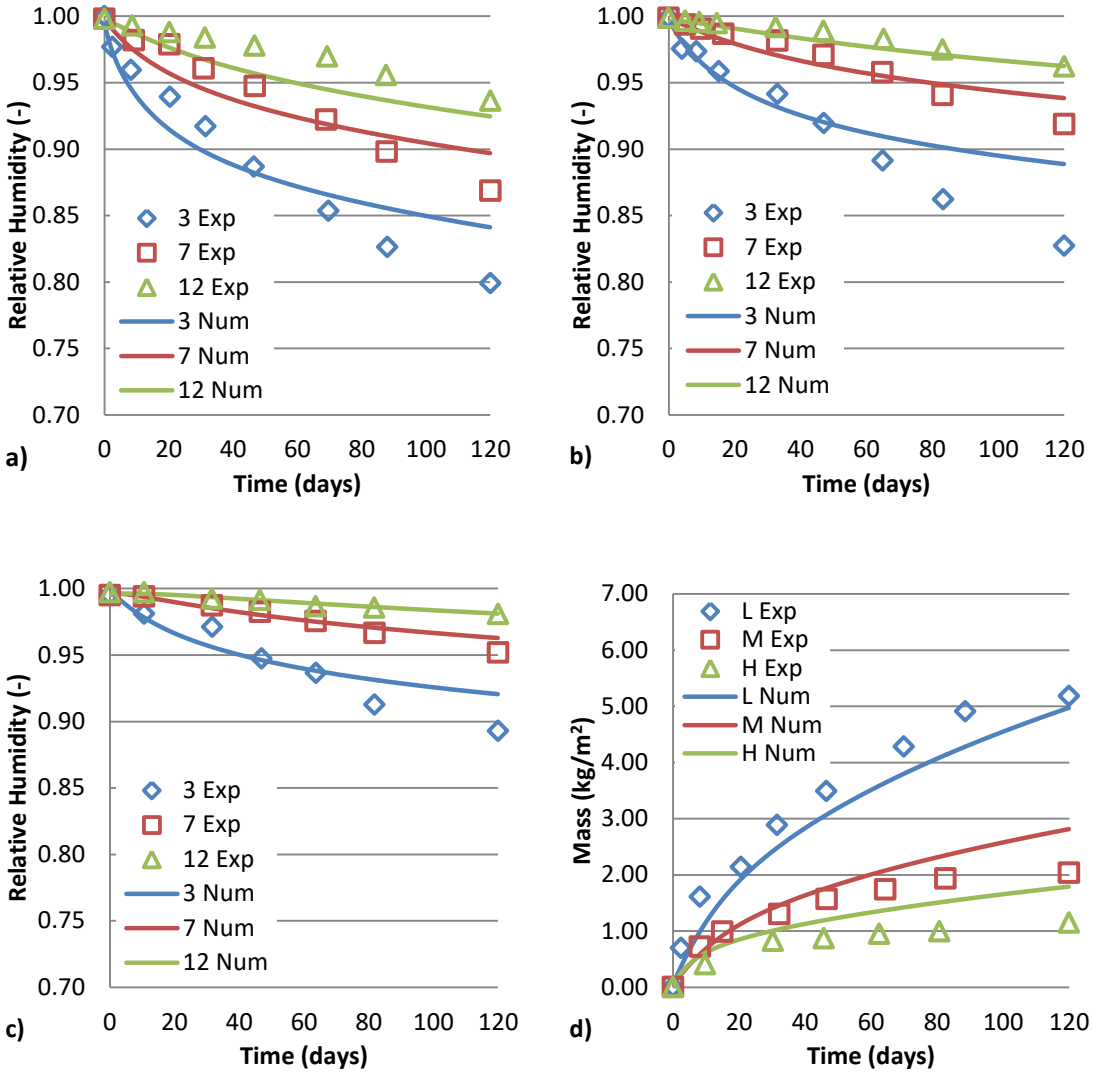

Figure 6.17 – Moisture profiles of experimental results and model predictions a) L, b) M, c) H and d) Moisture loss

It can be seen from the above figure that the profiles predicted by the model are generally in good agreement with the experimental results. The humidity at 7 cm and 12 cm are more accurately predicted, particularly for the M and H specimens, with the humidity at 3 cm being over predicted from around 60 days for all mixes. With regards to the moisture loss it can be seen that the predictions are accurate with a slight under prediction of the moisture loss for the L specimen and an over prediction for the M and H specimens from about 60 days onwards.

6.3.3 Ion Transport Experiments

This example uses data from the advective diffusive experiment presented in Chapter 5. A 10.3 % $NaCl$ solution was added to the left hand tank at a head of 540 mm (above the bottom of the beam), whilst the right tank was left empty. Tap water was added to the left hand tank, before the setup was left for one week, to allow the beam to become saturated. The test set up for the problem scenario can be seen in Figure 6.18 (where C1-3 denote the different sampling points).

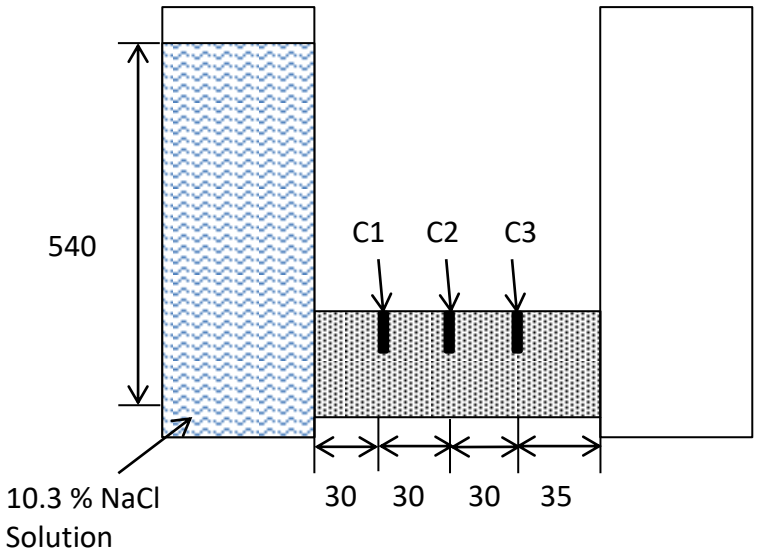

Figure 6.18 - Test setup (all dimensions in mm)

6.3.3.1 Numerical model conditions

The concrete sample was a beam of size 125x75 mm. The time period considered was 7 days, a time step of $\Delta t = 5400\ s$ and a uniform mesh of 100 bilinear quadrilateral elements were used, with element size of $\Delta x = 0.00125\ m$. The finite element mesh used and problem geometry can be seen in Figure 6.19. The coupling of the model was turned off such that only the chemical transport part was used.

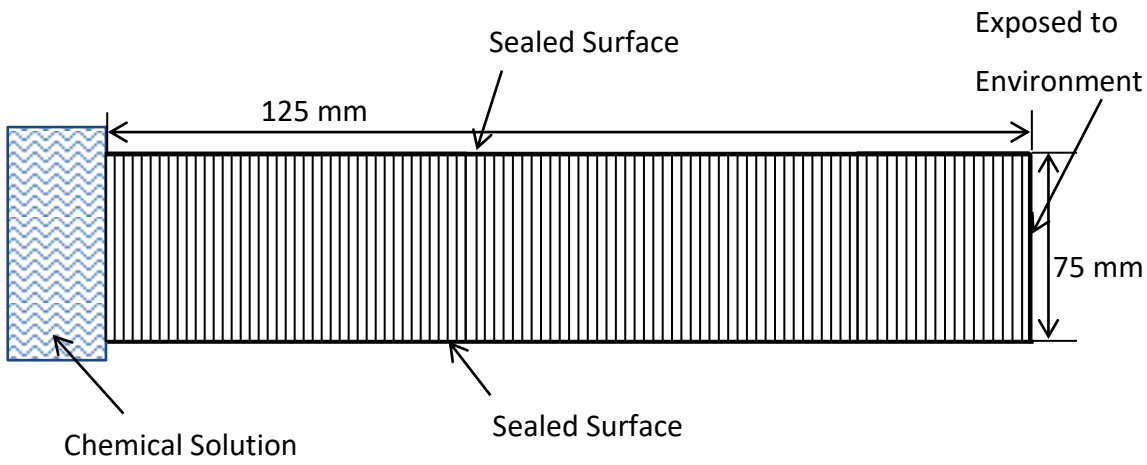

Figure 6.19 – Finite element mesh and problem geometry (not to scale)

It was assumed that the specimen was initially saturated (Baroghel-Bouny et al. (2011) have reported very high levels of saturation in cementitious specimens after just 48 hours) with no chemical ions present and moisture could be seen on the right hand boundary after just a few days. The boundary conditions considered were of zero flux for the sealed sides and of the Dirichlet type (eqs. 4.12-4.14) and Cauchy type (eqs. 4.15-4.17) for the exposed surfaces, the values can be seen in Table 6.13. The model parameters can be seen in Table 6.14. Chloride binding was taken into account and non-equilibrium conditions described by the Freundlich type isotherm (eq. 3.39) were assumed. It was also assumed that the Na^{+} and Cl^{-} ions were transported at the same rate to maintain charge neutrality. The concrete mix used in the experiments was designed to be a high porosity concrete that still contained enough fine aggregate to be comparable to an ordinary concrete. For this reason the parameters seen in Table 6.14 should be compared to the typical values for ordinary concrete and pervious/enhance porosity concrete (EPC). The values of reaction parameters were chosen based on an initial calibration exercise.

Table 6.13 – Boundary conditions

Boundary	Boundary Type	Values
LHS	Dirichlet	c_{Cl}=0.063 kg/kg, c_{Na}=0.041 kg/kg
Bottom	Sealed	-
RHS	Cauchy	c_{Cl}=0.0 kg/kg, c_{Na}=0.0 kg/kg
Top	Sealed	-

Table 6.14 – Model parameters

Variable	Value
n[a]	0.20
K_{i0}[b] (10^{-16} m^2)	6.59
D_{mol}[c] (10^{-10} m^2/s)	2.1
k_{da} (10^{-5})	1.305
λ	1.9

[a]Reported values of 0.10-0.13 (Baroghel-Bouny et al. 2011) and 0.16-0.264 for EPC (Neithalath et al. 2006)
[b]Reported values of the order $10^{-21}m^2$ (Baroghel-Bouny et al. 2011) and $10^{-10}m^2$ for EPC (Neithalath et al. 2006)
[c]Reported values of $2.1x10^{-9}m^2/s$ (Song et al. 2014) to $2.1x10^{-12}m^2/s$ (Baroghel-Bouny et al. 2011)

6.3.3.2 Results and discussions

The Cl^- and Na^+ profiles as measured from the experiment and predicted from the model after one week can be seen in Figure 6.20. It can be noted that due to the significant problems encountered with the experimental set up leaking these are the only set of viable results obtained.

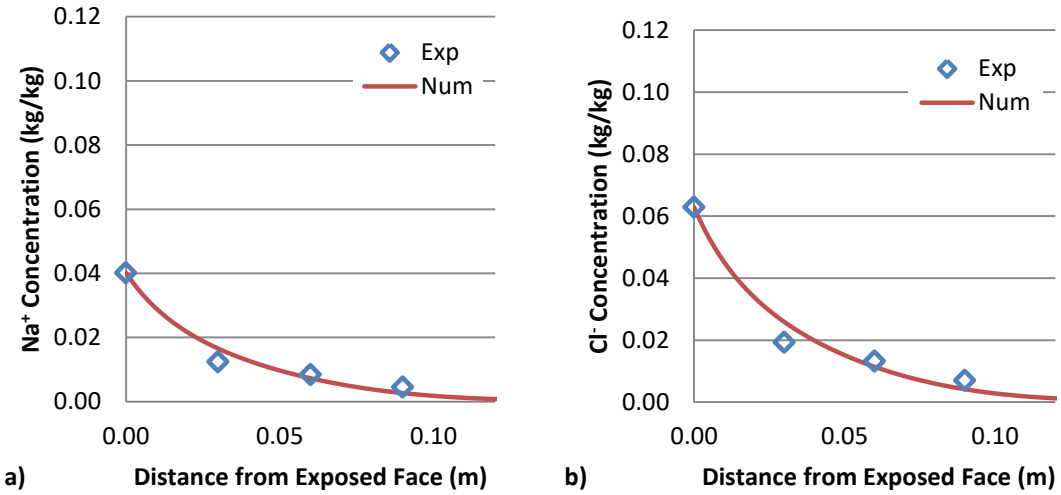

Figure 6.20 – Chloride profile as measured from the experiment and predicted by the coupled model (t=1 week)

As can be seen from the above profile the predictions of the numerical model are in good agreement with the experimental data, with the point at 30 mm being slightly over predicted and the 60 mm and 90 mm points being slightly under predicted. It is suggested that when considering variability in the results (which was not measured), the apparent difference between the predicted and measured data may become insignificant.

6.4 Conclusions

The purpose of this chapter was to investigate the ability of the fully coupled model to predict the reactive chemical transport in porous media. The verification was investigated, starting with the simulation of salt transport in building materials. The first example of this was presented by Koniorczyk (2010), where the salt precipitation was calculated as a function of concentration. The results show that the model accurately predicted the precipitated salt profiles, as well as the transient profiles of precipitated salt, degree of saturation and concentration. There were, however some differences in the degree of saturation and concentration profiles. The difference in the concentration profile was a direct result of the difference in saturation profile, and the difference in the saturation profile was justified as the moisture transport parameters were unclear and the moisture transport was validated in the previous

example. The second example was presented by Koniorczyk and Gawin (2012), where the salt precipitation was calculated as a function of solution supersaturation profile. The results showed good agreement between the model and the results from Koniorczyk and Gawin (2012), with the biggest difference being found in the transient profile of solution supersaturation ratio.

The next two examples investigated the ability of the model to predict multi-ionic transport. The first example of this was presented by Baroghel-Bouny et al. (2011) and concerned the transport of four chemical ions into a mortar specimen. The resultant profiles were in good agreement with a slight over prediction of the Na^{+} concentration near the exposed face and a slight under prediction of the OH^{-} concentration near the peak value caused by the reaction. The final example was presented by Song et al. (2014) and concerned the transport of six chemical ions in a concrete specimen and six different chemical reactions. The results showed good agreement between the model and the results presented by Song et al. with the Ca^{2+} and Cl^{-} being almost identical. The worst prediction was of the $CSH.NaCl$ profile where the penetration is over predicted by the model.

The validation of the moisture transport was then investigated through the simulation of drying experiments carried out by Kim and Lee (1999). It was found that the model accurately predicted the moisture profiles at 7 cm and 12 cm for all three mixes, as well as the moisture loss for the L specimen. The profiles at 3 cm were under predicted from around 60 days onwards, whilst the moisture loss for the M and H specimen was slightly over predicted from 60 days onwards. The validation of the chemical transport was investigated through the simulation of the results of the ion transport experiments; it was found that the model performed well in matching the concentration profiles.

It has been shown in this chapter that the developed model can accurately capture the chemical behaviour in porous media including moisture transport, multi-ionic chemical transport and chemical reactions.

Chapter 7. Applicability Investigation and Verification of the Problem Reduction Scheme

7.1 Introduction

In this chapter the performance of the problem reduction schemes is examined. This is split into two parts; first, each of the problem reduction schemes are tested to determine their range of applicability, using a hypothetical example problem concerning the reactive transport of 16 chemical species; secondly, the schemes are verified against a series of numerical simulations taken from, or based on, examples in the literature.

Section 7.2 describes an investigation into the range of applicability of each reduction schemes. As part of this study, the degree to which each PRS maintains mass balance is examined.

The verification of the PRSs is then presented in section 7.3, where each PRS is compared to an example problem taken from the literature and the accuracy of the predictions are discussed.

Section 7.4 presents the results of the reduction in computational cost achieved by the PRSs in terms of CPU time.

Section 7.5 details an investigation into the use of analytical relationships for the reduction scheme and the problems encountered.

Finally, in Section 7.6, a set of conclusions are drawn from the work on the calibration and performance of the PRSs.

7.2 Applicability Investigation of Reduction Schemes

The three reduction approaches presented will have different ranges of applicability in terms of the diffusion coefficient range over which they will give an acceptable approximation. It is expected that PRS 1 will be accurate over the smallest diffusion coefficient range as the transport is extrapolated as a multiple of the indicator species, whereas PRS 2 and 3 bound the solution using indicator species at either end of the diffusion coefficient range. The interpolation/extrapolation equations used to predict

concentrations in each of the 3 reduction schemes, presented in Chapter 4, are recalled (from eqs. 4.74, 4.75 & 4.76) in the following equations:

PRS 1;

$$c_i^{t+1} = c_i^t + \frac{\left(c_i^0 - c_i^b\right)}{\left(c_{ind}^0 - c_{ind}^b\right)} \frac{D_{mol}^i}{D_{mol}^{ind}} \Delta c_{ind} \tag{7.1}$$

PRS 2;

$$c_i^{t+1} = c_i^t + \frac{\left(c_i^0 - c_i^b\right)}{\left(c_{ind,l}^0 - c_{ind,l}^b\right)} \left(\frac{D_{mol}^{ind,u} - D_{mol}^i}{D_{mol}^{ind,u} - D_{mol}^{ind,l}} \right) \Delta c_{ind,l} + \frac{\left(c_i^0 - c_i^b\right)}{\left(c_{ind,u}^0 - c_{ind,u}^b\right)} \left(\frac{D_{mol}^i - D_{mol}^{ind,l}}{D_{mol}^{ind,u} - D_{mol}^{ind,l}} \right) \Delta c_{ind,u} \tag{7.2}$$

PRS 3;

$$\begin{aligned} c_i^{t+1} = \\ & c_i^t + \frac{\left(c_i^0 - c_i^b\right)}{\left(c_{ind,l}^0 - c_{ind,l}^b\right)} \left(\frac{\left(D_{mol}^{ind,m} - D_{mol}^i\right)\left(D_{mol}^{ind,u} - D_{mol}^i\right)}{\left(D_{mol}^{ind,m} - D_{mol}^{ind,l}\right)\left(D_{mol}^{ind,u} - D_{mol}^{ind,l}\right)} \right) \Delta c_{ind,l} + \\ & \frac{\left(c_i^0 - c_i^b\right)}{\left(c_{ind,m}^0 - c_{ind,m}^b\right)} \left(\frac{\left(D_{mol}^{ind,l} - D_{mol}^i\right)\left(D_{mol}^{ind,u} - D_{mol}^i\right)}{\left(D_{mol}^{ind,l} - D_{mol}^{ind,m}\right)\left(D_{mol}^{ind,u} - D_{mol}^{ind,m}\right)} \right) \Delta c_{ind,m} + \\ & \frac{\left(c_i^0 - c_i^b\right)}{\left(c_{ind,u}^0 - c_{ind,u}^b\right)} \left(\frac{\left(D_{mol}^{ind,l} - D_{mol}^i\right)\left(D_{mol}^{ind,m} - D_{mol}^i\right)}{\left(D_{mol}^{ind,l} - D_{mol}^{ind,u}\right)\left(D_{mol}^{ind,m} - D_{mol}^{ind,u}\right)} \right) \Delta c_{ind,u} \end{aligned} \tag{7.3}$$

A study is reported in this section which explores the accuracy and range of applicability of the three problem reduction approaches. The study employed a wick action test on a mortar sample in which the transport of 16 chemical species was simulated. The analysis undertaken in this study considered chemical reactions between the ions and the cement matrix, as well as advective and dispersive transport. The chemical species considered were artificial, allowing the choice of the diffusion coefficient values, giving greater control over the range and spread of the values. The reactions concerned the adsorption of the chemical ions onto the cement matrix, described by the non-equilibrium Freundlich isotherm (eq. 3.39). The time period considered was 24 hours and the initial concentrations of each ion, as well as the sorbed chemical mass for each species in the sample, were assumed to be zero. The mortar sample was assumed to be initially saturated, prior to the left hand side of the specimen being exposed to the chemical solution, and the right hand side being

exposed to an environmental humidity of 60 %, with all remaining sides being sealed, thereby ensuring 1D transport. Following a mesh and time step convergence study, a non-uniform mesh of 25 bilinear quadrilateral elements was used along the length of the specimen with a maximum element size of $\Delta x = 0.003\ m$ and a time step of $\Delta t = 36\ s$ was used. The mesh can be seen below in Figure 7.1 along with the problem geometry. The boundary conditions can be seen in Table 7.1.

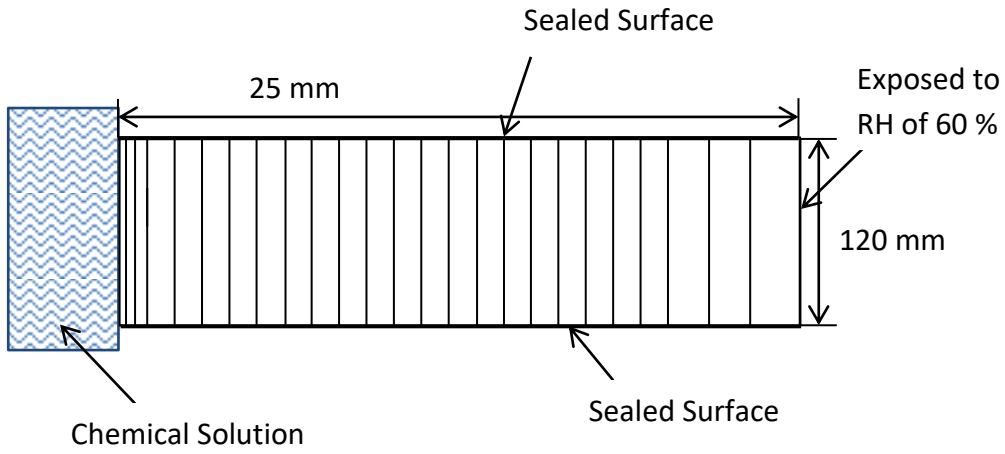

Figure 7.1 – Finite element mesh and problem geometry (not to scale)

Table 7.1 – Boundary conditions

Boundary	Boundary Type	Values
LHS	Cauchy	*RH=100 %, T=293 K, c=0.001 kg/kg**
Bottom	Sealed	-
RHS	Cauchy	*RH=60 %, T=293 K, c=0.0 kg/kg**
Top	Sealed	-

*Same for all species

The various model parameters, including the boundary mass transfer coefficients and reaction rates, are given in in Table 7.2. The diffusion coefficients for all chemical species can be seen in Table 7.3.

Table 7.2 – Model parameters

Parameter	Value
k_{da}	0.008
λ	2.0
n	0.13
β_c (m/s)	2.5×10^{-3}
γ_c (kg/m²s)	1×10^{-4}
ω_c (W/m²K)	8.0
K_{i0} (10^{-21} m²)	35.0
A_w	2.0

Table 7.3 – Chemical parameters

Species	D_{mol} (10^{-10} m²/s)	Species (cont'd)	D_{mol} (10^{-10} m²/s)
1	0.25	*9*	6
2	0.5	*10*	7
3	1	*11*	8
4	1.5	*12*	9
5	2	*13*	10
6	3	*14*	12
7	4	*15*	14
8	5	*16*	16

To determine the accuracy of the reduction schemes an analysis of the full problem has been undertaken. Once the results from the full model were obtained, the analysis could be carried out using each of the problem reduction schemes. The indicator species chosen for each of the techniques can be seen in Table 7.4. An artificial species labelled 'A' has been chosen for PRS 1 and 2 in order to allow the use of an indicator with a diffusion coefficient corresponding to the mean value of the species diffusion coefficients. Artificial indicator species may also be used for other reasons; for example, PRS 2 and 3 use indicator species with the highest and lowest diffusion coefficients, bounding the solution; in some cases the upper indicator species may be highly reactive, meaning that its rate of transport may no longer be the highest. In this situation, a non-reactive artificial indicator could be used in its place, maintaining the bounding of the solution.

Table 7.4 – Indicator species chosen and their diffusion coefficients (10^{-10} m^2/s)

PRS	Indicator 1	Indicator 2	Indicator 3
1	A (6.2)	-	-
2	1 (0.25)	16 (16)	-
3	1 (0.25)	A (6.2)	16 (16)

7.2.1 Results

The concentration profiles as predicted by the full model and each of the reduction schemes can be seen in Figures 7.2, 7.3 & 7.4, along with the saturation profile. The sorbed mass profiles can be seen in Figures 7.5, 7.6 & 7.7.

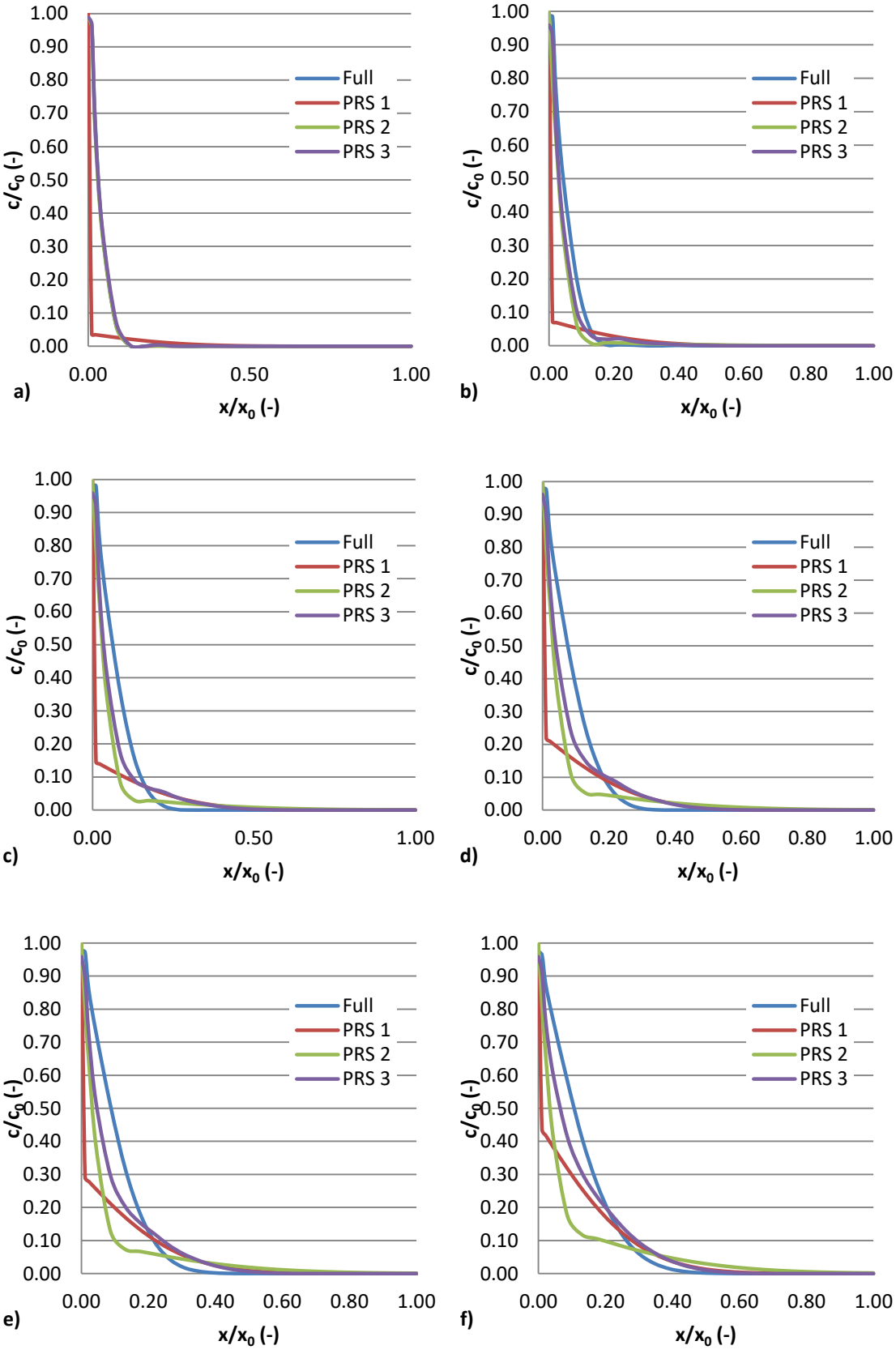

Figure 7.2 - Concentration profiles predicted by full model and PRS 1-3 (t=24 hours) species number: a) *1*, b) *2*, c) *3*, d) *4*, e) *5*, and f) *6*

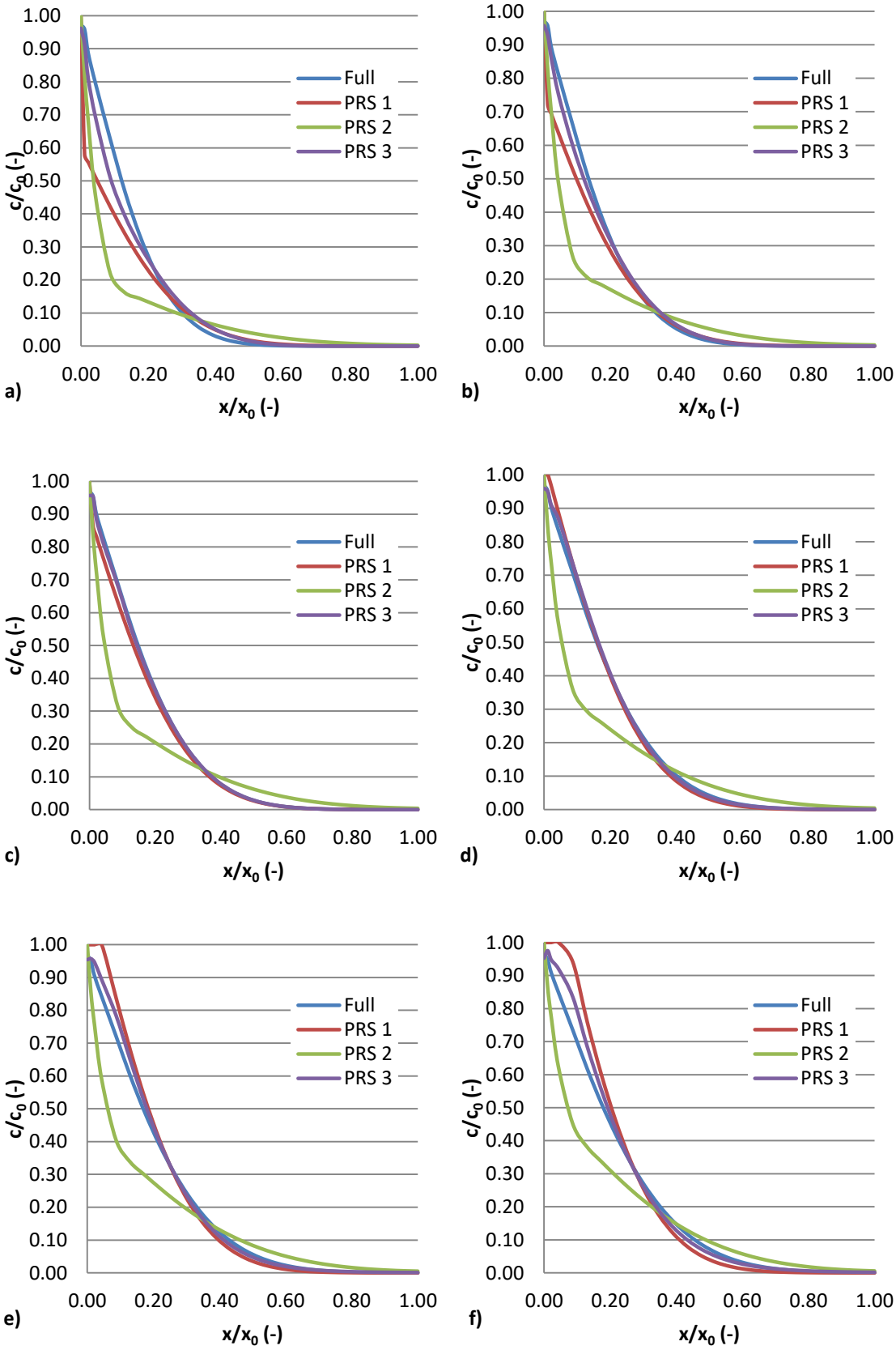

Figure 7.3 - Concentration profiles predicted by full model and PRS 1-3 (t=24 hours) species number: a) *7*, b) *8*, c) *9*, d) *10*, e) *11*, and f) *12*

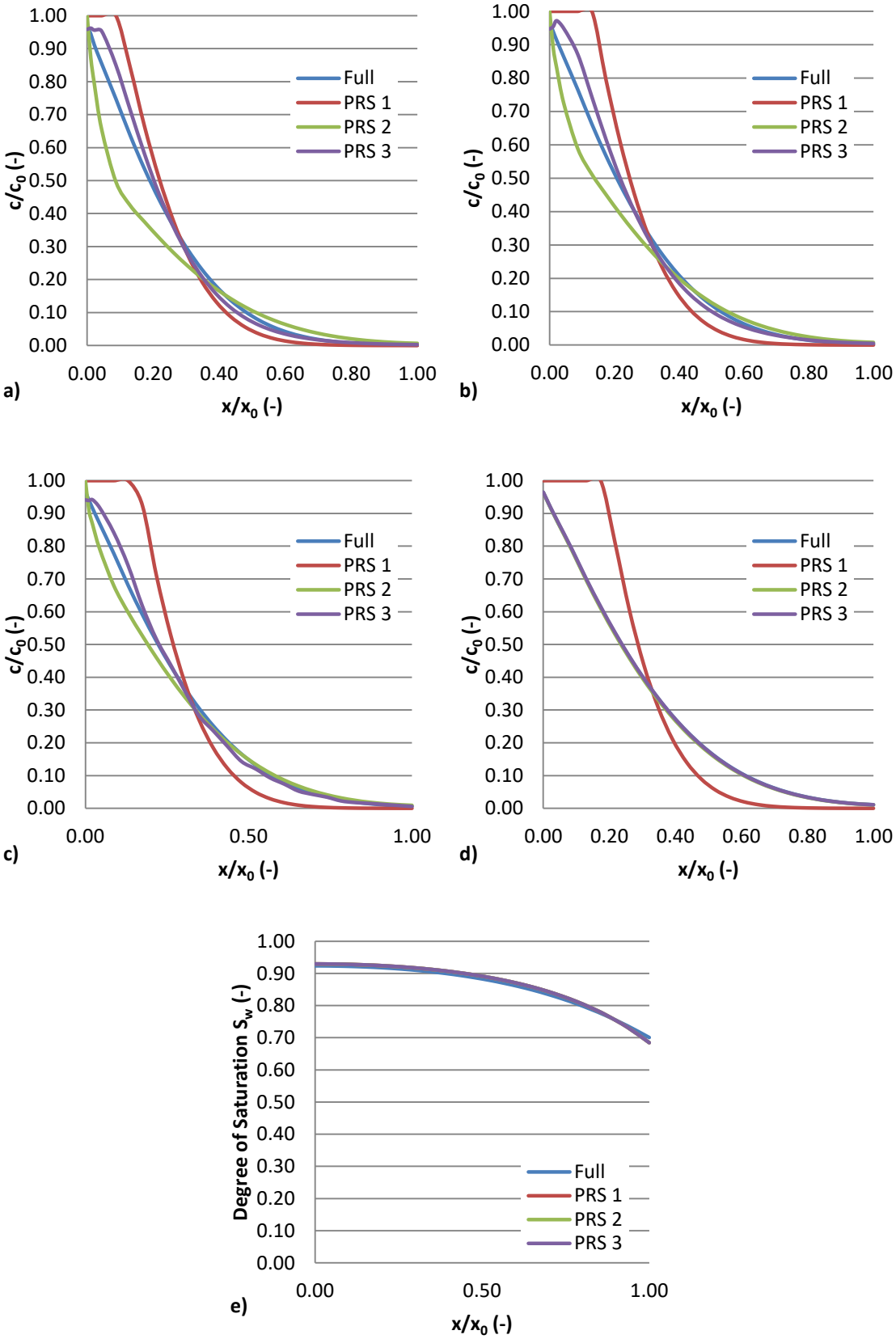

Figure 7.4 – Concentration and saturation profiles predicted by full model and PRS 1-3 (t=24 hours) species number: a) *13*, b) *14*, c) *15*, d) *16* and e) S_w

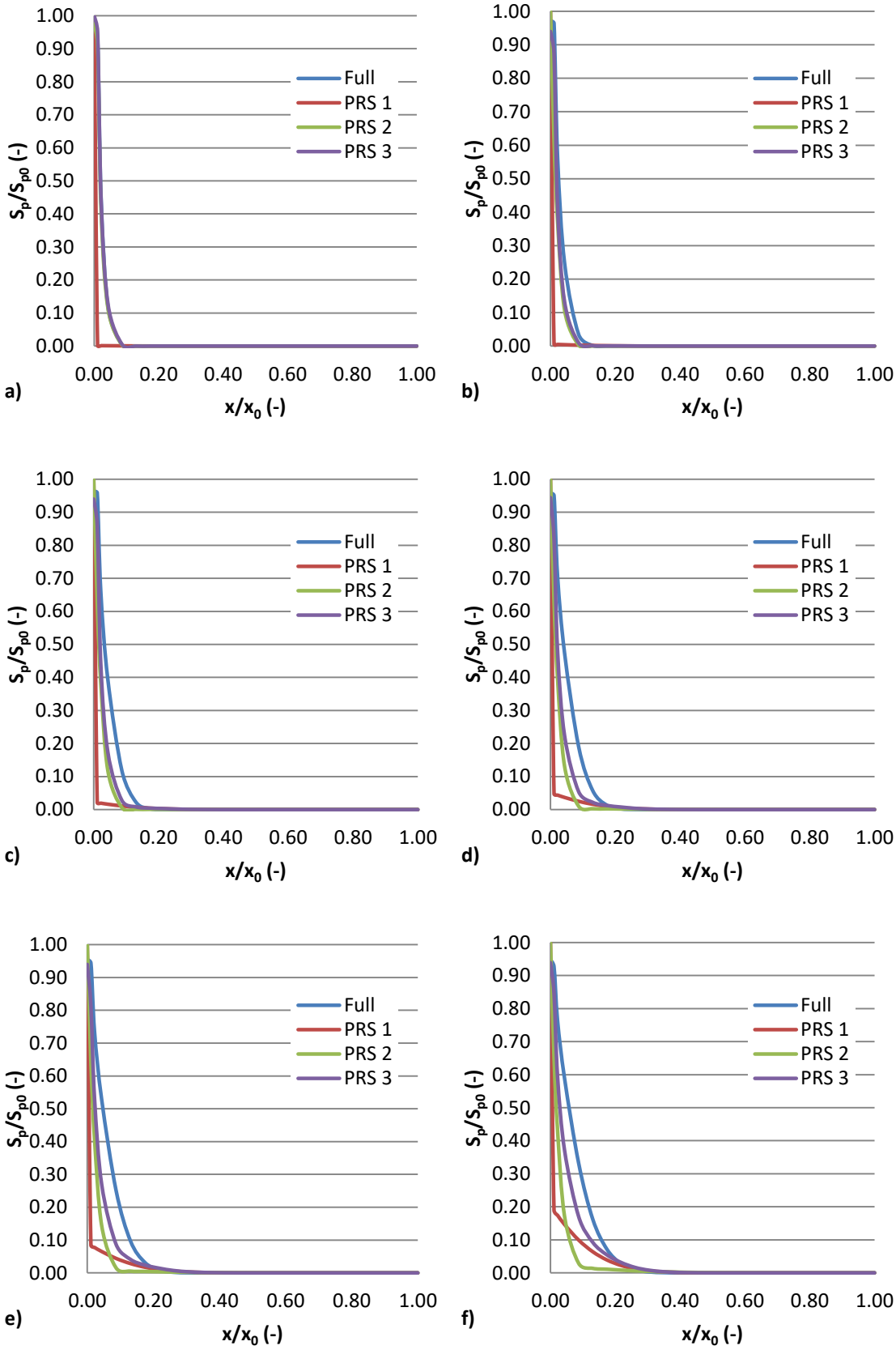

Figure 7.5 - Sorbed mass profiles predicted by full model and PRS 1-3 (t=24 hours) species number: a) *1*, b) *2*, c) *3*, d) *4*, e) *5*, f) *6*

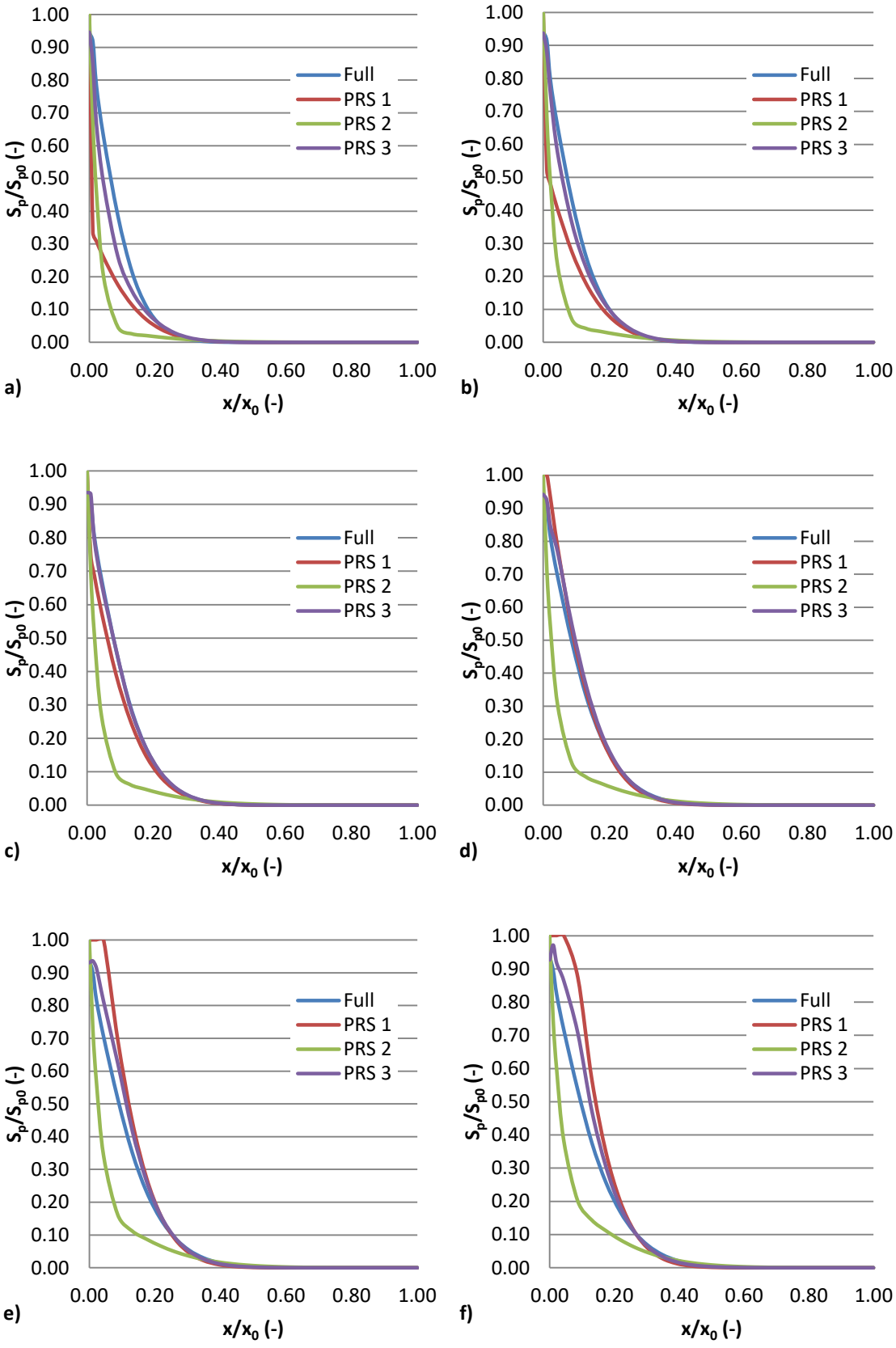

Figure 7.6 - Sorbed mass profiles predicted by full model and PRS 1-3 (t=24 hours) species number: a) *7*, b) *8*, c) *9*, d) *10*, e) *11*, f) *12*

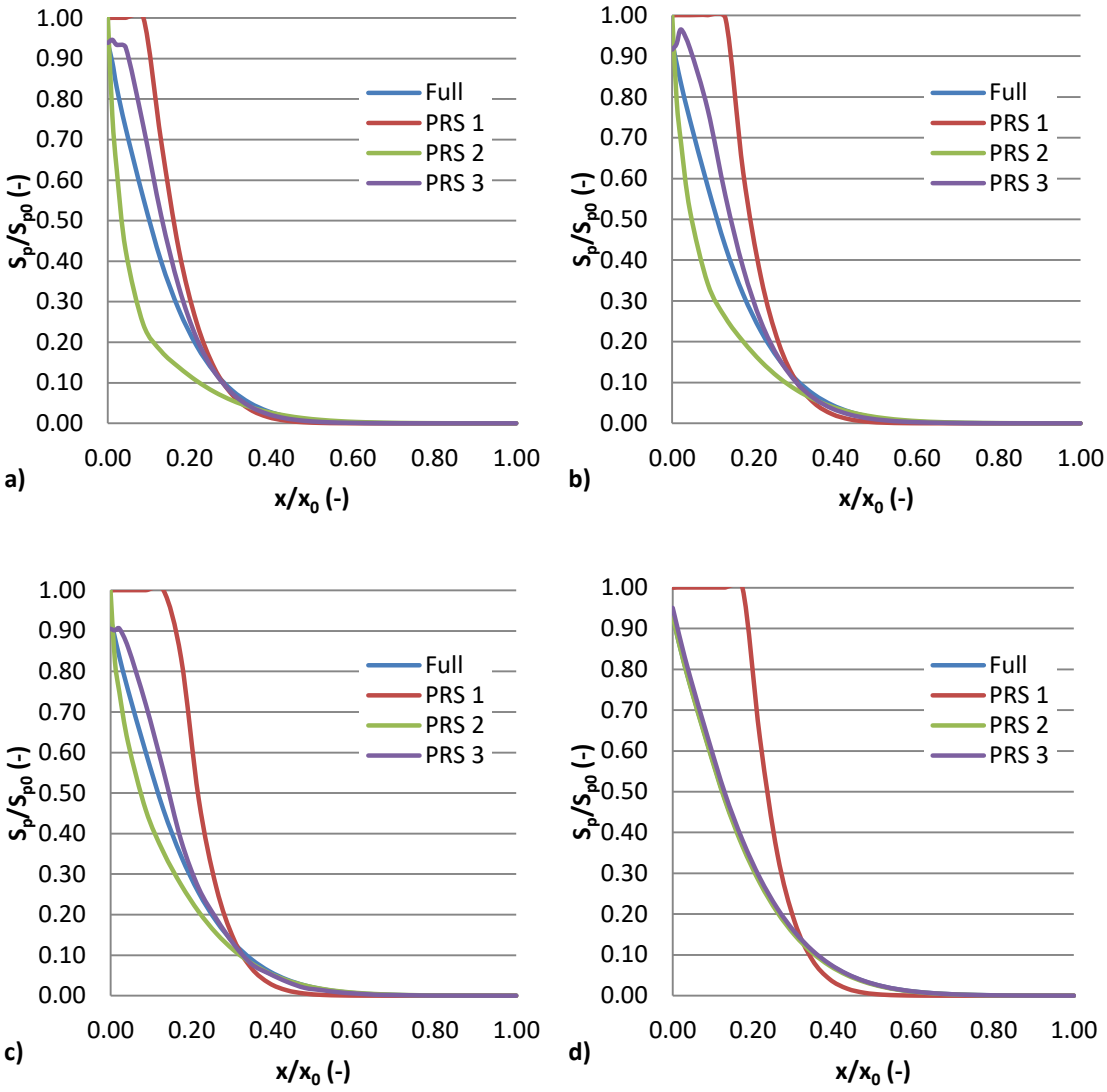

Figure 7.7 – Sorbed mass profiles predicted by full model and PRS 1-3 (t=24 hours) species number: a) *13*, b) *14*, c) *15* and d) *16*

It can be seen from the profiles that the ability of the reduction schemes to accurately predict the profiles increases with the order of the scheme. This is expected as their complexity and number of indicator species used also increases. The profiles are predicted most accurately for chemical species found near the indicator species, with the divergence increasing with the relative difference between the current and nearest indicator species. For PRS 1, this means that the best predictions are for the species with diffusion coefficients nearest the mean, with the worst being found at the limits, i.e. for species 1 and 16. For PRS 2, this means the best predictions are near species 1 and 16 and the worst are found near the mean (i.e. species 9). For PRS 3 the best

predictions are found near species 1, 9, & 16, with the worst profile being found at species 3, 4, 12 and 14.

7.2.1.1 Error and Correlation

In order to determine the accuracy of each reduction scheme, both the relative error between the reduced and full models and the correlation between the profiles has been investigated. The relative error is defined as:

$$R_E = 100 \cdot \frac{(c_i^{prs} - c_i^{full})}{c_i^b} \tag{7.4}$$

The relative error plots for the concentration can be seen in Figure 7.8, whilst the sorbed mass relative error can be seen in Figure 7.9.

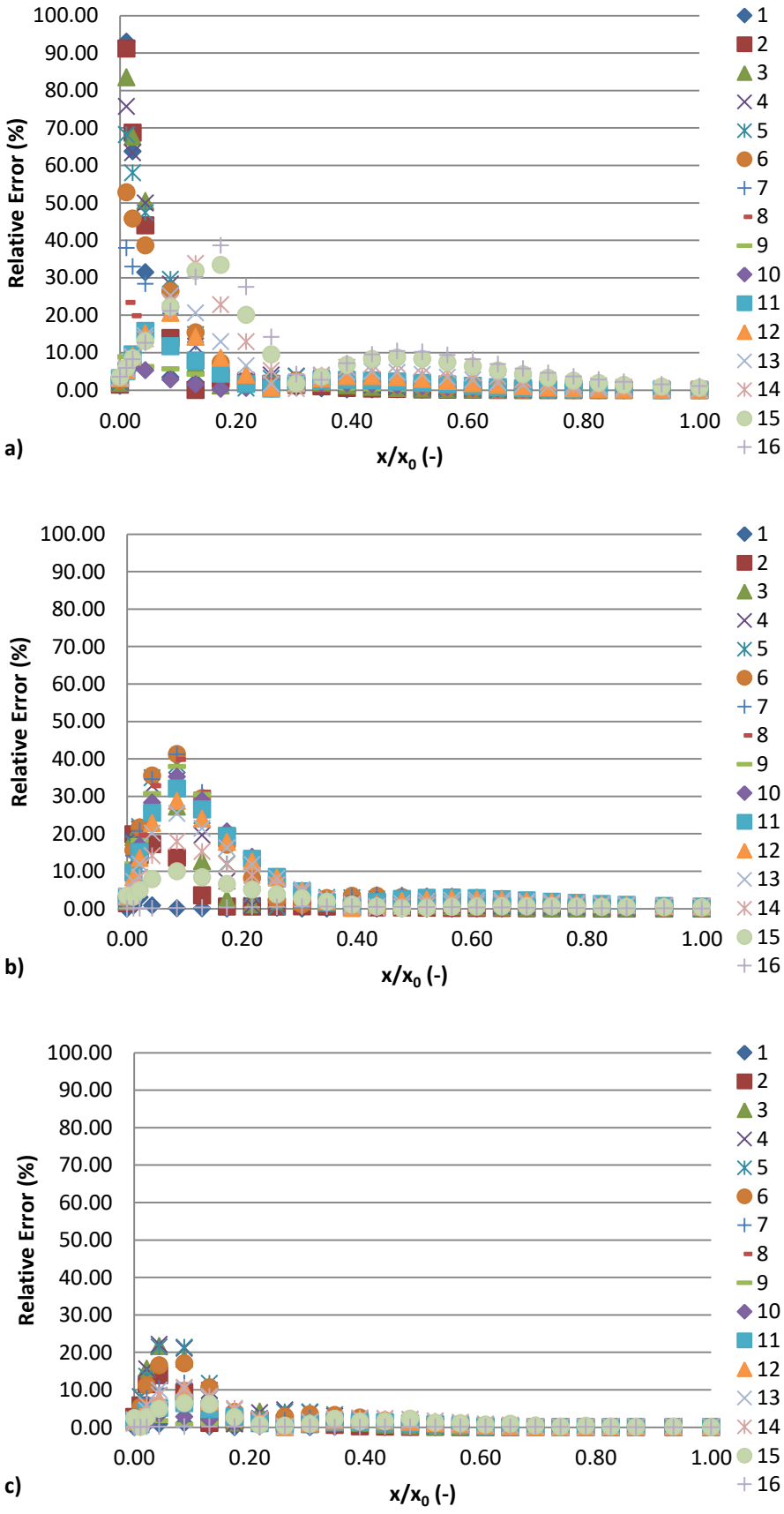

Figure 7.8 – Relative error of concentrations for a) PRS 1, b) PRS 2 and c) PRS 3

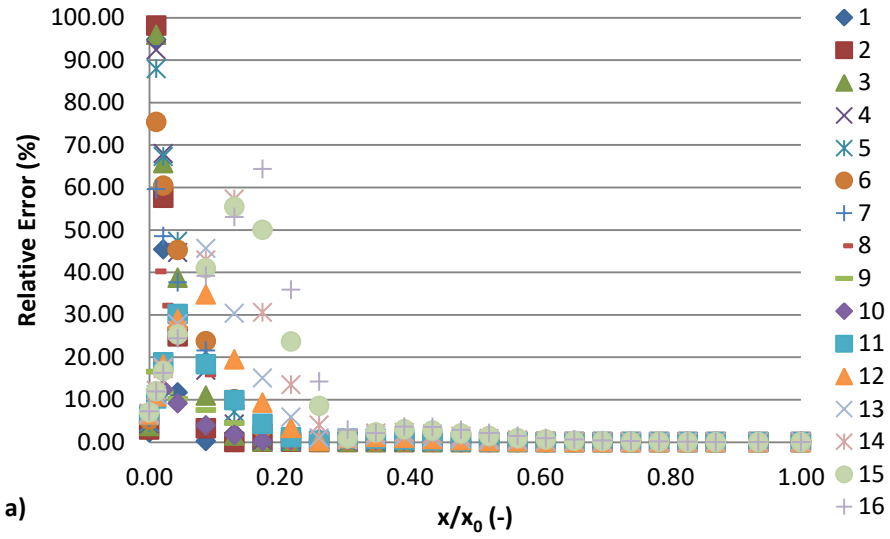

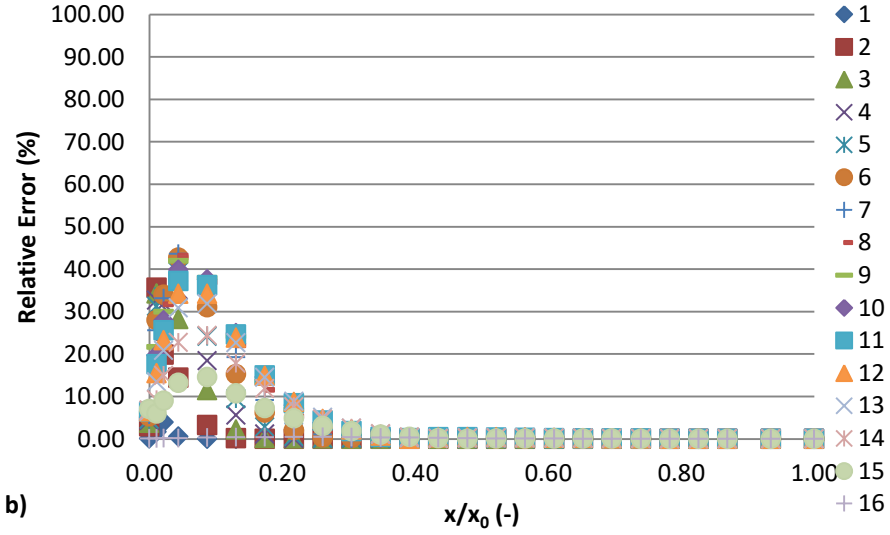

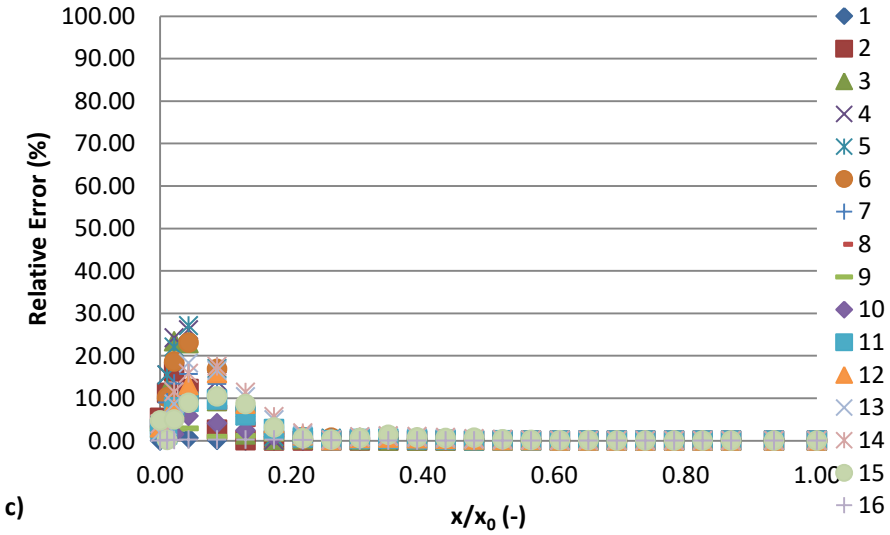

Figure 7.9 – Relative error of sorbed mass for a) PRS 1, b) PRS 2 and c) PRS 3

It is clear from the above figures that the relative error decreases with the increase in the order of the reduction scheme, such that PRS 3 has a smaller error. It can also be seen that the largest errors are found near the exposed face, this is to be expected as it is here that the concentration gradients are the largest. The sorbed mass error profiles are very similar to those of concentration but with slightly larger errors, this is because the error found in the concentration profiles is magnified by the reaction equation, which can lead to a larger error.

It may seem that some of the calculated errors are quite large. It can be noted, however, that these errors are caused by the sharp concentration gradients found near the left hand boundary and that the profiles still match well in this area. It is likely that there is a statistical analysis that better captures the closeness of the profiles than the relative error measure chosen here. To this end the correlation plots were investigated.

The correlation plots for the concentrations can be seen in Figure 7.10, in which the ordinates (y) represent the full solution values and the abscissae (x) give the PRS values. 100 % correlation corresponds with the line y=x, whilst the correlation plots for the sorbed mass can be seen in Figure 7.11.

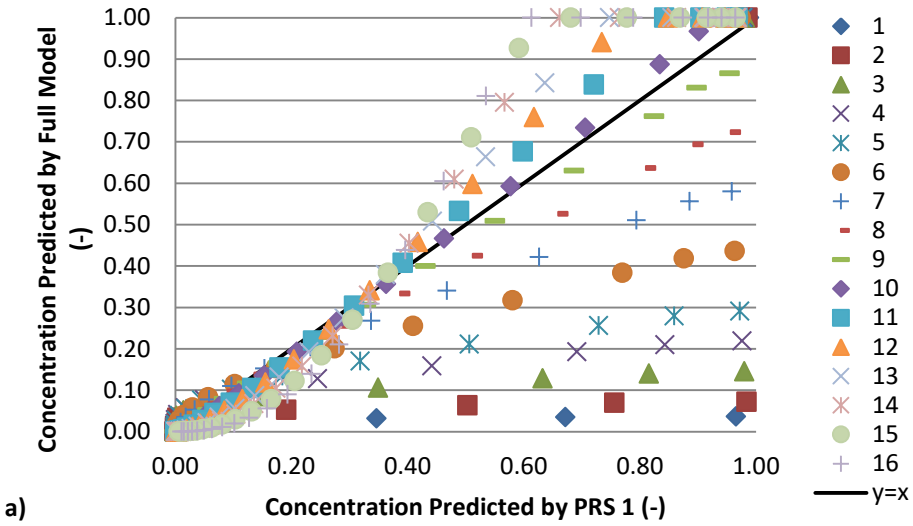

a)

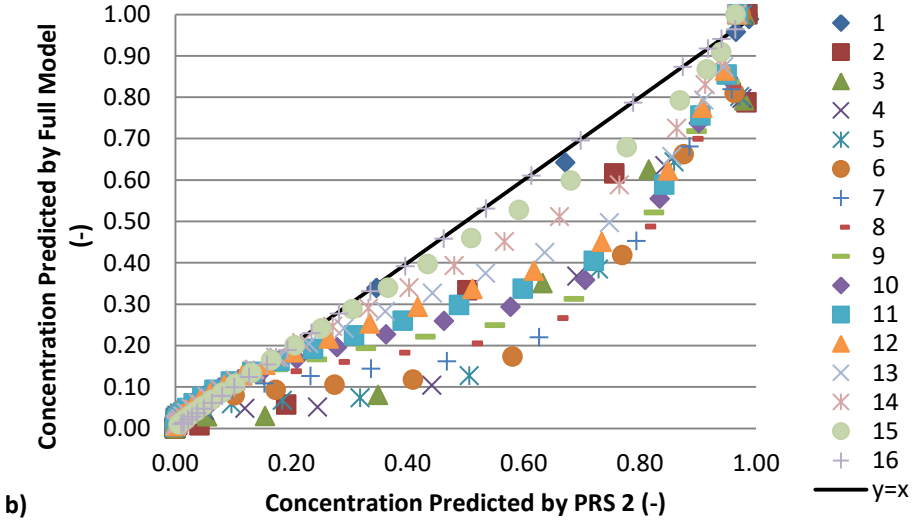

b)

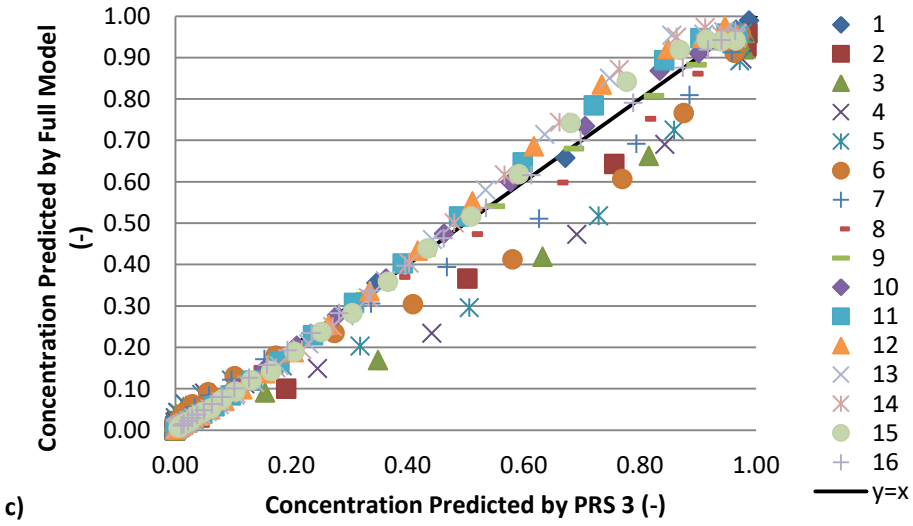

c)

Figure 7.10 – Correlation of concentration profiles for a) PRS 1, b) PRS 2 and c) PRS 3

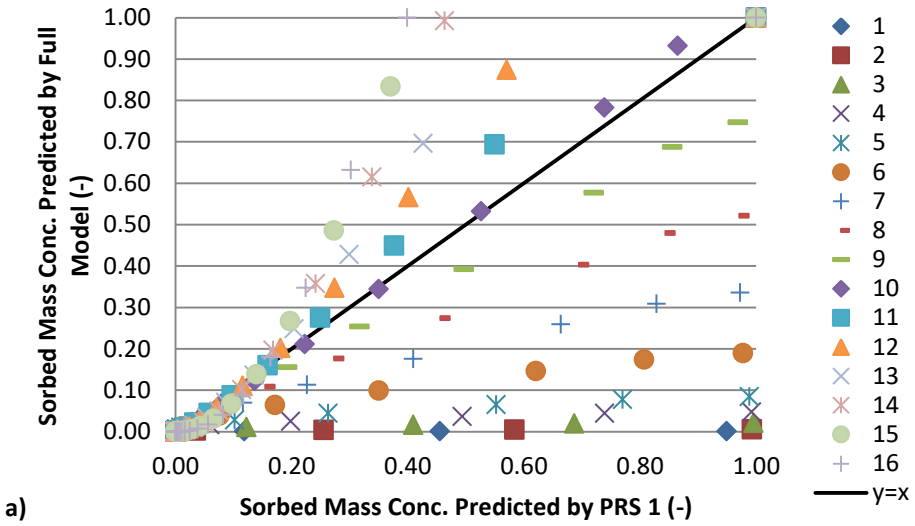

a)

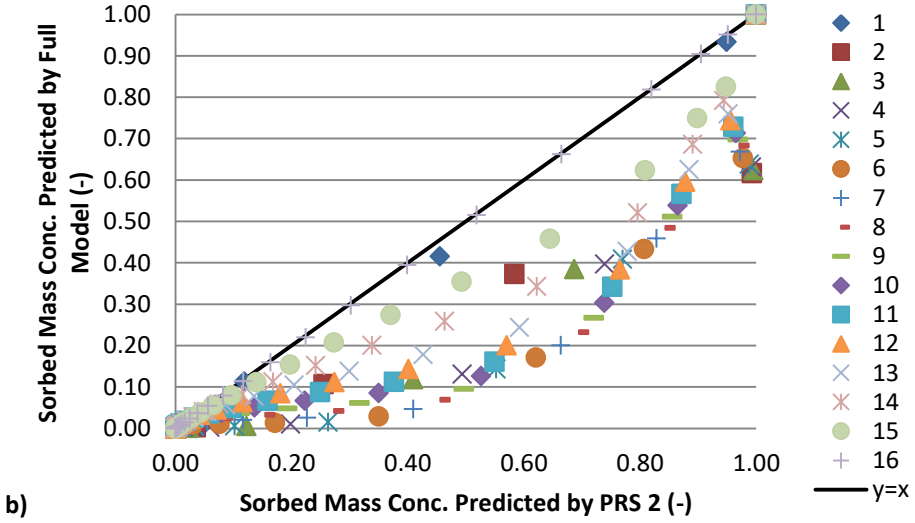

b)

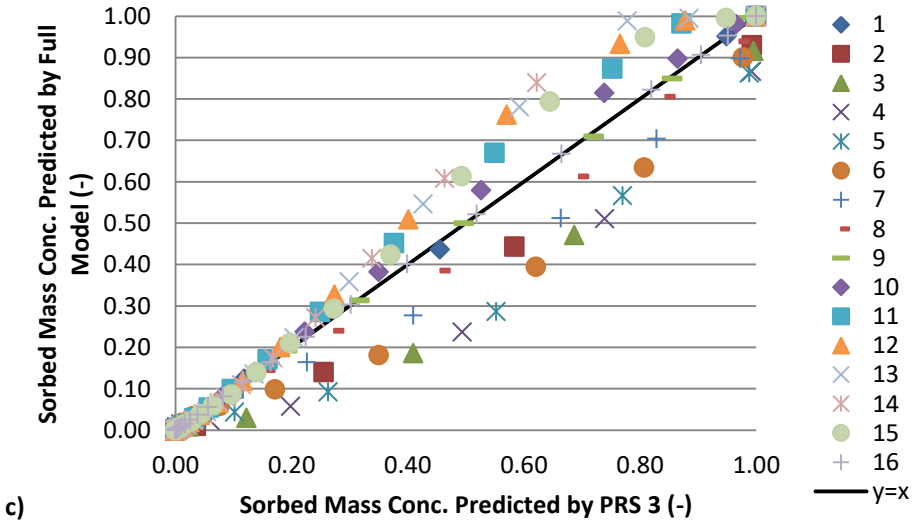

c)

Figure 7.11 – Correlation of sorbed mass profiles for a) PRS 1, b) PRS 2 and c) PRS 3

The above plots tell the same story as the error plots, with the correlation improving with the order of the reduction scheme, with the least correlated values being found at the exposed face where the concentration gradients are sharpest (represented here at the top right of the correlation plots). In addition, the sorbed mass profiles show the same behaviour as the concentration profiles but with slightly poorer correlation. As was the case with the error plots, the correlation plots don't capture the agreement between the profiles at the left hand boundary.

7.2.1.2 Diffusion Only and Reactive Diffusion Cases

Two other example problems were considered for the investigation into the applicability of the reduction schemes, a diffusive only and a reactive-diffusive case. These problems are essentially the same as the previous test problem in terms of the chemical species considered and the numerical model conditions. The difference is that in these test problems the right hand side is now sealed, eliminating the advection of the pore fluid, and in the case of the diffusion only problem, no chemical reactions are considered. The boundary conditions for these two test problems are summarised in Table 7.5.

Table 7.5 – Boundary conditions

Boundary	Boundary Type	Values
LHS	Cauchy	$RH=100\ \%$, $T=293\ K$, $c=0.001\ kg/kg$*
Bottom	Sealed	-
RHS	Sealed	-
Top	Sealed	-

*Same for all species

The concentration profiles for the diffusive and the diffusive reactive cases, along with the sorbed mass profiles for the diffusive reactive case can be seen in Appendix A2 Figures A2-10. The correlation plots for the concentration profiles for the diffusive only case can be seen in Figure 7.12. The correlation plots for the reactive-diffusive case for the concentration profiles and the sorbed mass profiles can be seen in Figures 7.13 and 7.14 respectively.

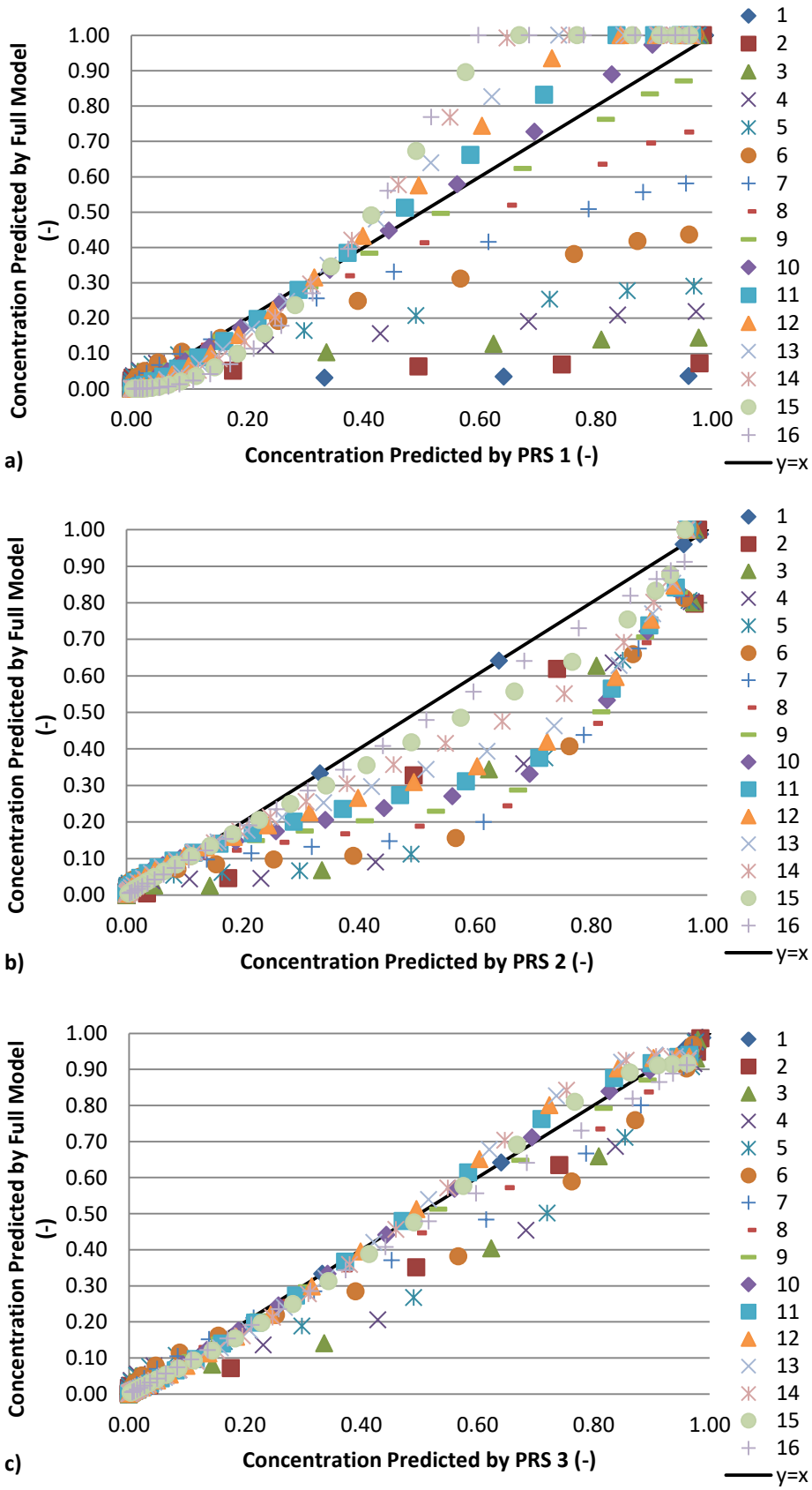

Figure 7.12 - Correlation of concentration profiles for diffusion only case a) PRS 1, b) PRS 2 and c) PRS 3

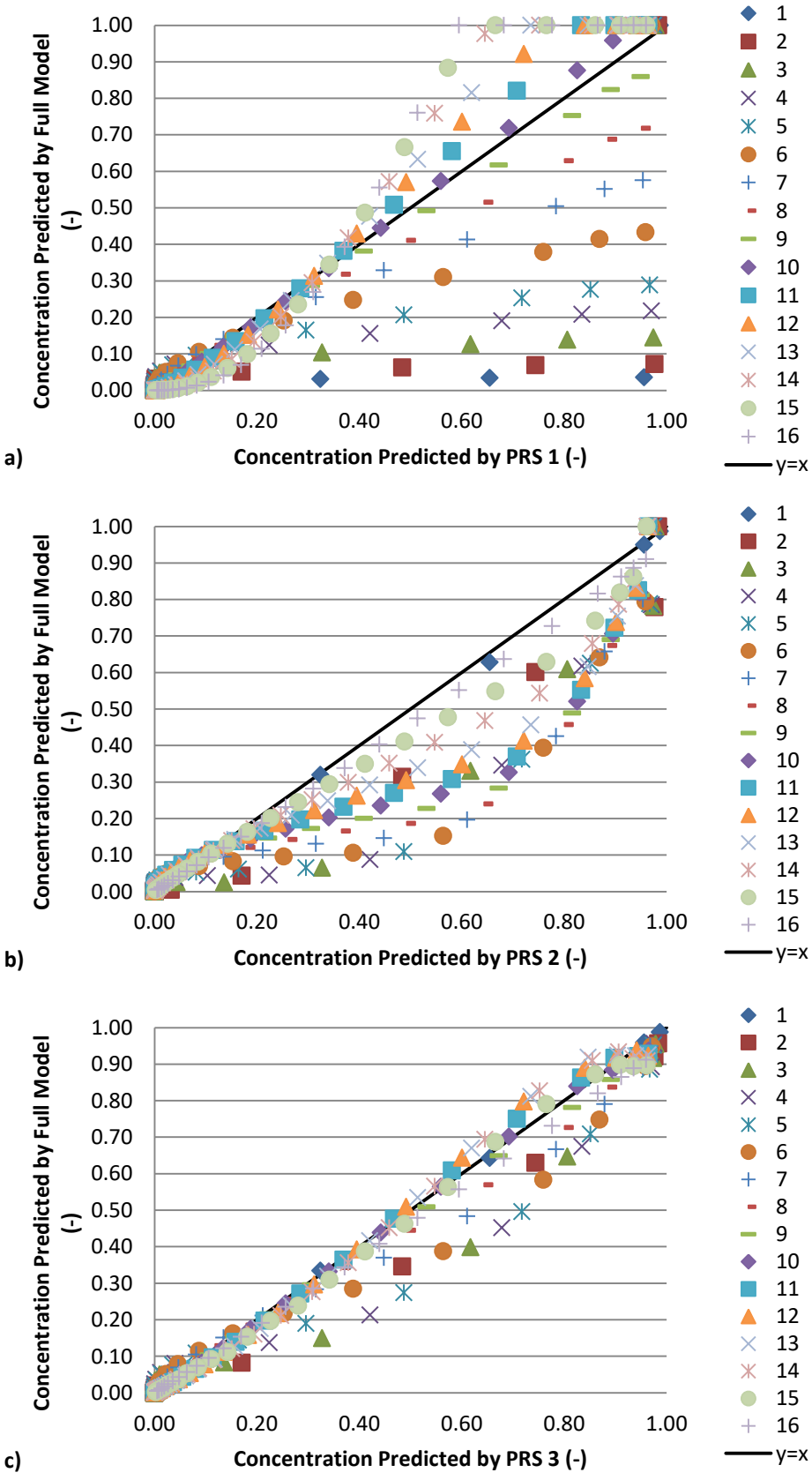

Figure 7.13 - Correlation of concentration profiles for diffusive reactive case a) PRS 1, b) PRS 2 and c) PRS 3

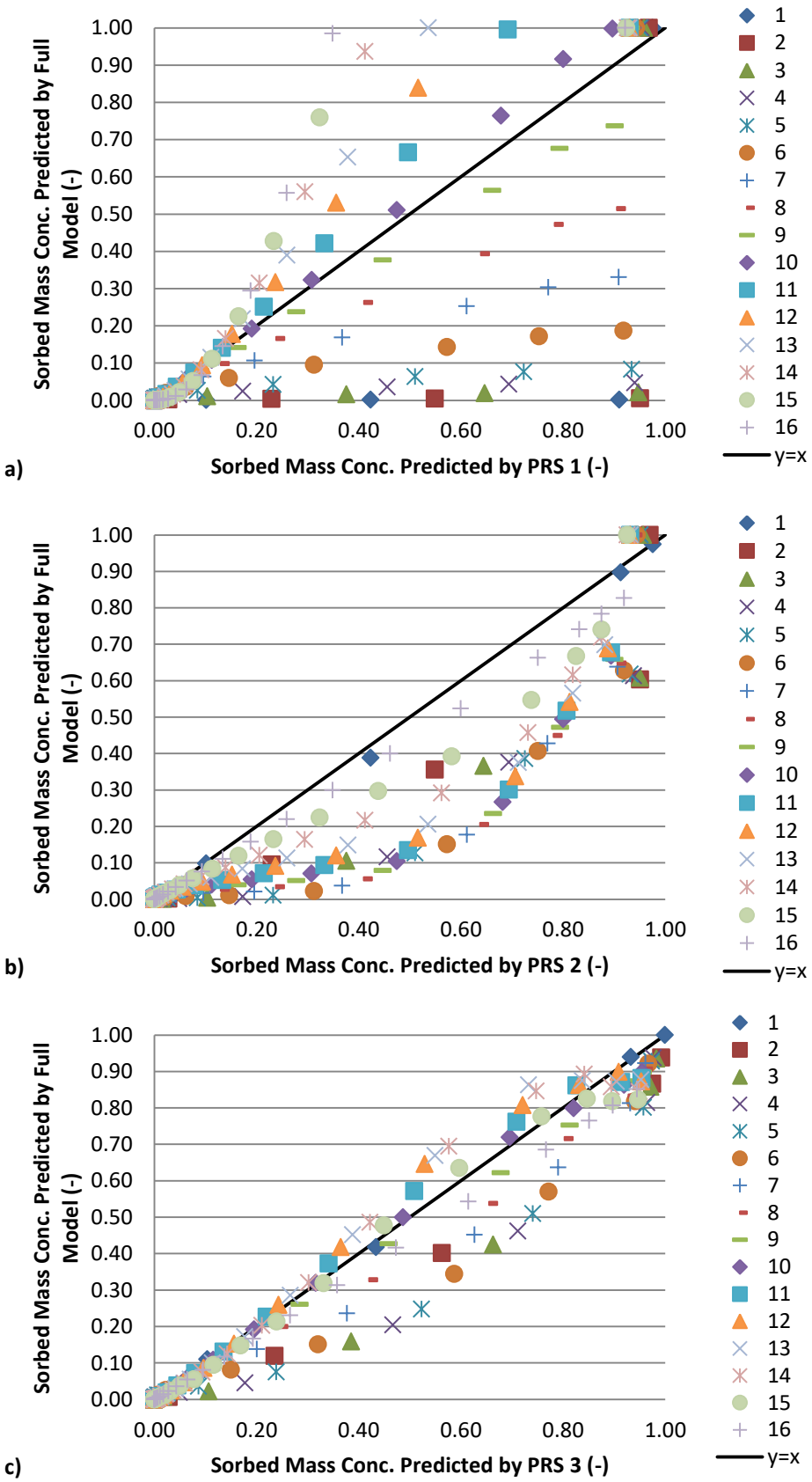

Figure 7.14 - Correlation of sorbed mass profiles for diffusive reactive case a) PRS 1, b) PRS 2 and c) PRS 3

As can be seen from the above plots, the correlation results are very similar to those of the full test case, with the correlations of the reactive diffusive case being slightly better and the correlations of the diffusive only case being slightly better again. This is as expected since the reduction schemes would be expected to perform better as the complexity of the analysis decreases.

7.2.2 Range of Applicability

The example problems presented above serve to determine the range of applicability of each of the PRSs. The full advective diffusive reactive case is chosen here for the calculation of the range as this is the most complex case and therefore will produce the most conservative range. The range of applicability of a PRS is decided based on a maximum allowable error in any one chemical species. The tolerance considered here is 25 % relative error. This may be relatively large but the concentration gradients found in the resultant profiles are sharp and a 25 % relative error represents a small difference in the predicted profiles.

The diffusion coefficient range over which each PRS can predict the concentration profile within this tolerance is defined as the applicable range. For PRS 1 it is possible to look above and below the indicator species until a profile exceeds this tolerance; however, this is not possible for PRS 2 and 3 as they use the extremes of the diffusion coefficient range as indicator species. To circumvent this, a series of analyses were carried out using different ranges until the maximum range that meets the tolerance was found. The profiles predicted by PRS 2 over the applicable range can be seen in Appendix A2 Figures A11-16. The ranges found over which each PRS is applicable can be seen in Table 7.6 (where D_{mol}^{i} and D_{mol}^{ind} are the diffusion coefficients a species and the indicator respectively and the u and l superscripts indicate upper and lower species respectively). For PRS 3 it was found that using the mean of the diffusion coefficient range for the middle indicator gave the best results. The use of indicator species for the applicable ranges can be seen in Figure 7.15. It can be noted that PRS 2 was tested at the lower and upper end of the diffusion coefficient range and that all schemes were initially tested on different (but similar) diffusion coefficient values than those used in the example and similar results were obtained.

Table 7.6 - Applicable ranges for PRSs

PRS	1	2	3
Diffusion Coefficient Range	$0.8D_{mol}^{ind}<D_{mol}^{i}<1.6D_{mol}^{ind}$	$D_{mol}^{ind,u}<16D_{mol}^{ind,l}$	$D_{mol}^{ind,u}<64D_{mol}^{ind,l}$

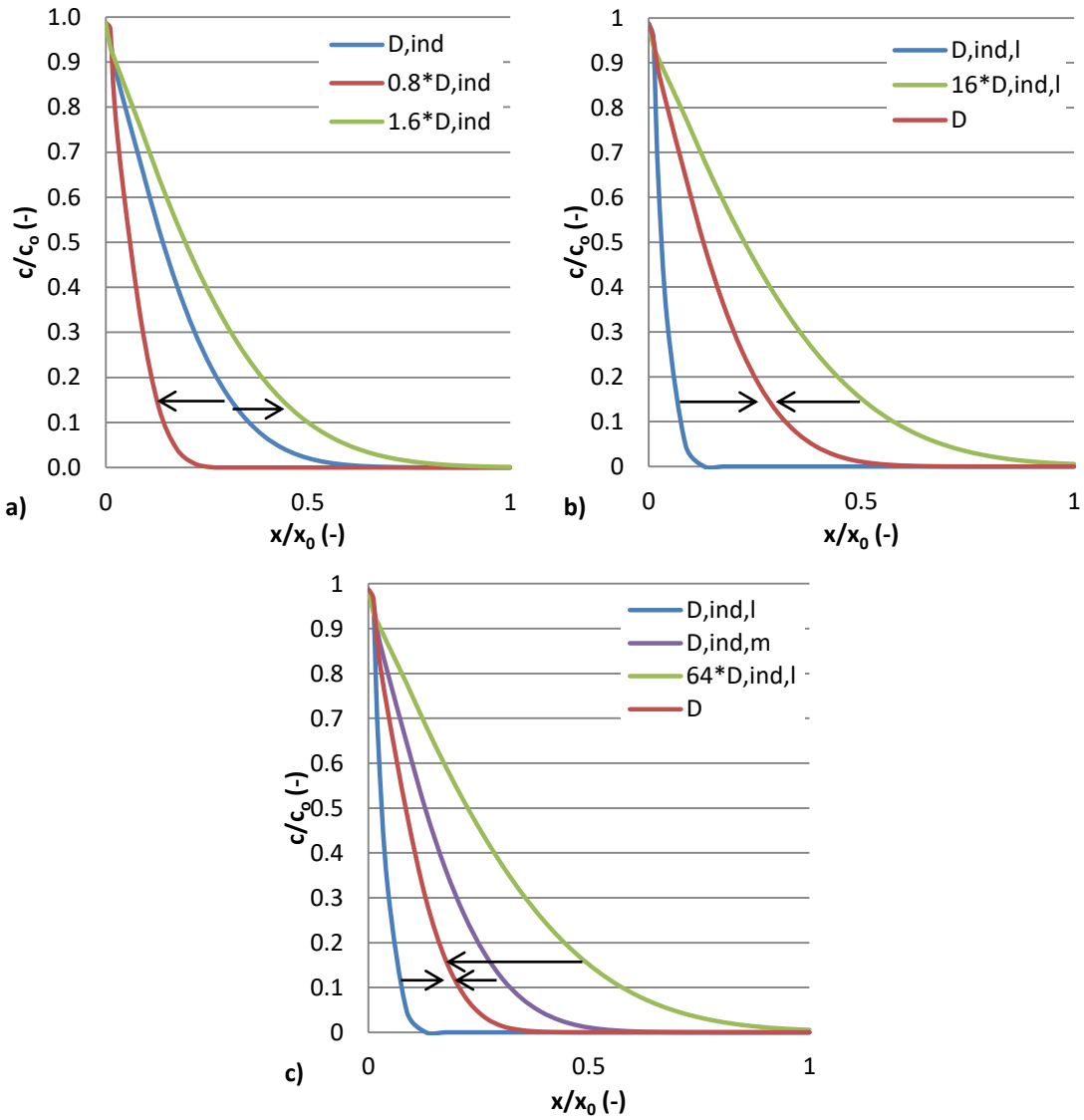

Figure 7.15 – Use of indicator species a) PRS 1, b) PRS 2 and c) PRS 3

7.2.3 Mass Balance

The PRSs have been shown to perform well in accurately predicting the chemical behaviour of various systems; one concern, however, is that as the governing balance equations are only solved for the indicator species and therefore mass balance may not be maintained for the remaining species. For this reason, the mass balance error of the PRSs has been investigated through the example problem. The total mass balance

errors for all of the chemical species within the applicable range of each reduction scheme are shown in Figure 7.16. It can be seen that the mass balance error is generally 10 % or less for each of the schemes, and that these errors generally decrease with time. This may be because the amount of diffusion is initially high and the concentration gradients are sharp. Under such conditions, the schemes may not perform as well, but over time, the gradients become smoother, and the predictions improve. It can be seen that the mass balance error of PRS 2 is greater than that of PRS 1. The results of PRS 1 show an over prediction of the chemical concentration near the boundary, and an under prediction further into the sample, whilst the mass balance error for each species is small. PRS 2 on the other hand shows a consistent under prediction of the concentration of the majority of chemical species, which leads to a larger mass balance error. It can be noted though that this is the mass balance error found when using the schemes at the extreme of their applicability and if a higher level of accuracy is required the range over which each scheme is applied could be reduced.

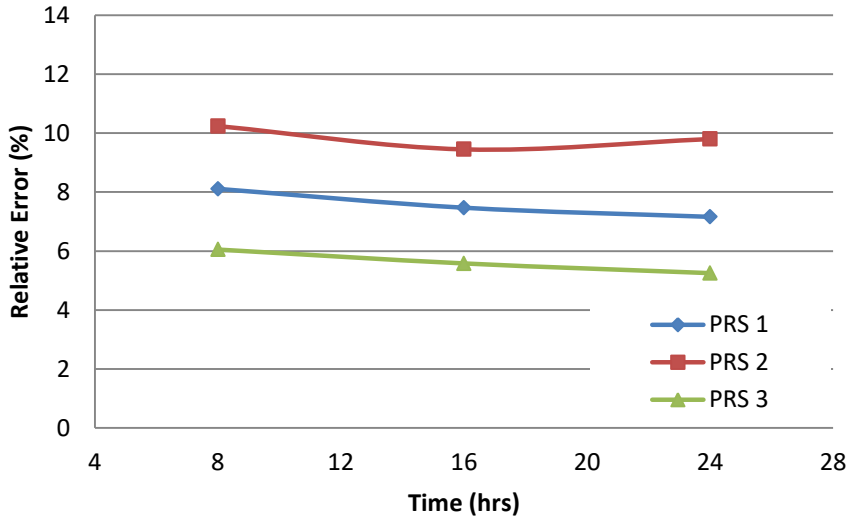

Figure 7.16 – Relative mass balance error for PRS 1-3 found in calibration problem

7.3 Verification of Reduction Schemes

Now that the range of applicability of the PRSs has been established, it is necessary to verify their application against a range of reported simulations. To do this, one problem for each PRS has been considered. The first two consider the diffusion and reactions of chemical species in mortar samples and are based alternative numerical

work presented by previous authors (Baroghel-Bouny et al. 2011; Song et al. 2014). The third is a hypothetical scenario and considers the 2D advective-diffusive-reactive transport in a mortar specimen based on the example found in Zhu et al. (1999).

For all examples the mesh and time step sizes were chosen based on the results of a mesh convergence study.

7.3.1 PRS 1 – Baroghel-Bouny et al. (2011)

The diffusion case, as reported by Baroghel-Bouny et al. (2011), is considered here. The simulation is based on experimental results by Francy (1998), who carried out experiments on cement discs of size (diameter x thickness = 120x20 mm). The left hand side of the sample was exposed to a salt solution whilst the remaining sides were sealed. The transport of the Na^+, OH^-, K^+ and Cl^- ions was considered and the non-equilibrium chloride binding has been taken into account as given in eq. (3.39). It was assumed that, as chloride ions sorbed onto the solid mass, hydroxide ions were released to preserve charge neutrality. The time period considered was 12 hours, a time step of $\Delta t = 0.9\ s$ was used, along with a uniform mesh of 20 bilinear quadrilateral elements with the element size of $\Delta x = 0.001\ m$.

PRS 1 was chosen to model this example due to the range of diffusion coefficients of the problem. The chosen indicator species was Na^+; it can be noted that the K^+ and Cl^- species lie within the range of validity of PRS 1, but OH^- does not; however, since there is very little transport of OH^- , this is considered to be acceptable in this case. The problem geometry can be seen in Figure 7.17. The boundary conditions can be seen in Table 7.7. The model parameters and boundary values can be seen in Table 7.8 and diffusion coefficients of the chemical species can be seen in Table 7.9.

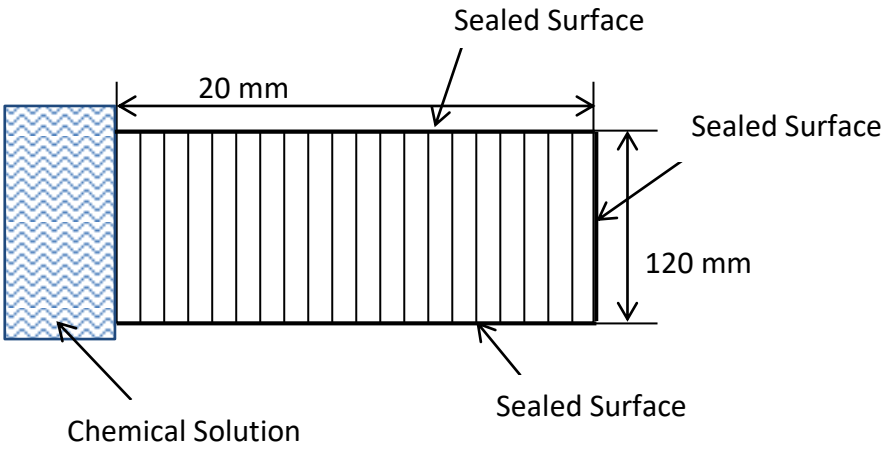

Figure 7.17 – Finite element mesh and problem geometry (not to scale)

Table 7.7 – Boundary conditions

Boundary	Boundary Type	Values
LHS	Cauchy	*RH=100 %, T=293 K, c**
Bottom	Sealed	-
RHS	Sealed	-
Top	Sealed	-

*See chemical parameters table

Table 7.8 – Model parameters

Parameter	Value
n	0.13
$\gamma_c\ (kg/m^2s)$	6.5×10^{-3}
$\omega_c\ (W/m^2K)$	8.0
k_{da}	0.000131
λ	0.61

Table 7.9 – Chemical parameters

Species	Initial Conc. (kg/kg)	Boundary Conc. (kg/kg)	D_{mol} $(10^{-10}\ m^2/s)$
Na^+	0.000299	0.01352	1.33
OH^-	0.001105	0.00188	5.3
K^+	0.002028	0.00319	1.96
Cl^-	0.0	0.01954	2.1
Tcc	0.0	0.01954	-

7.3.1.1 Results and Discussions

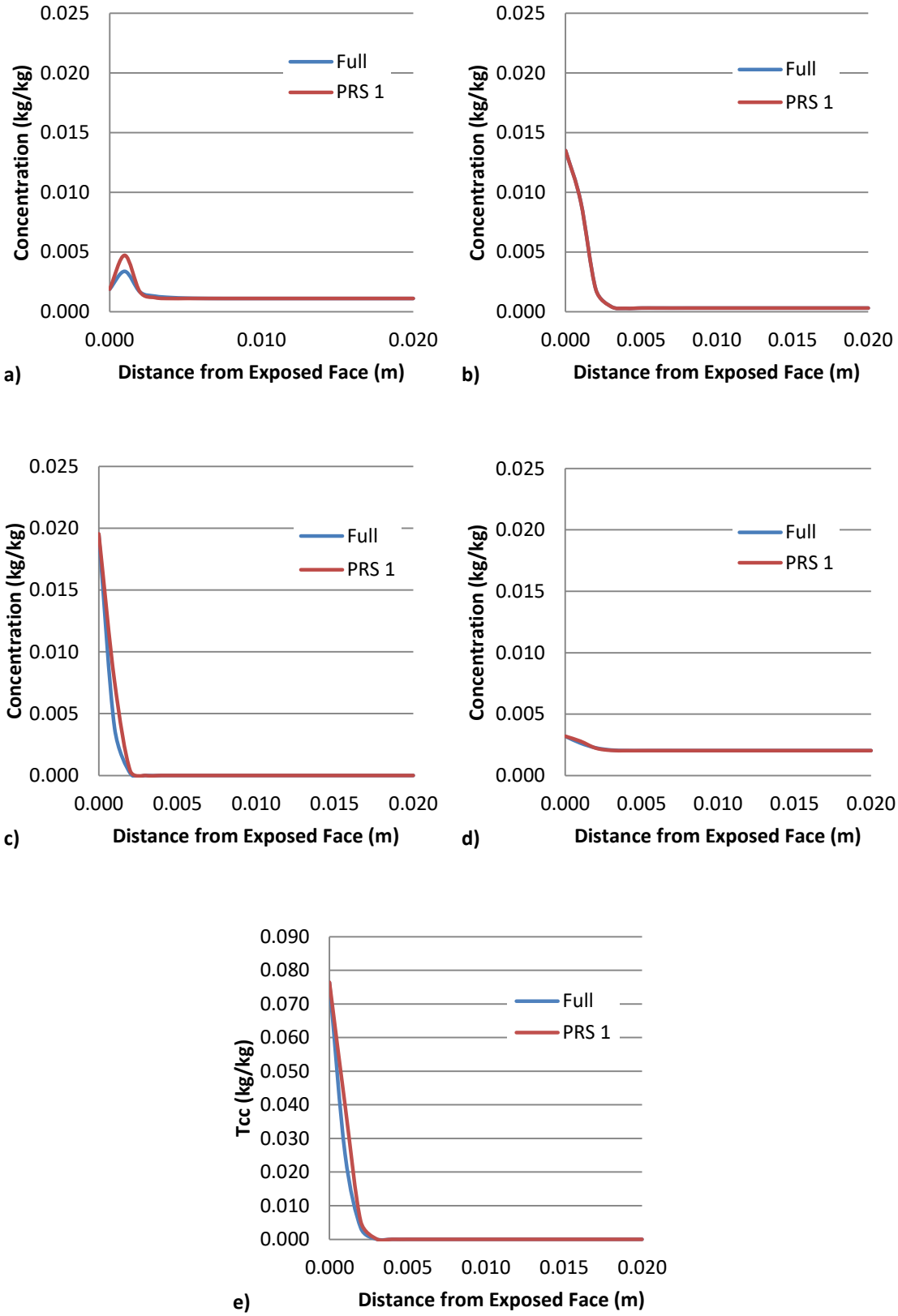

Figure 7.18 – Concentration and Tcc profiles predicted by full model and PRS 1 (t=12 hours) a) OH^-, b) Na^+, c) Cl^-, d) K^+ and e) Tcc

The concentration and Tcc profiles, as predicted by the full model and PRS 1 can be seen in Figure 7.18.

The above profiles show that PRS 1 is in good agreement with the full model, with the K^+, Cl^- and Tcc profiles being almost exactly the same. The biggest relative difference can be seen in the OH^- profile and is found at the peak value, this peak value corresponds to the release of OH^- ions due to the Cl^- adsorption, and so this difference may result from the fact that the Cl^- profile is slightly over predicted and the OH^- profile is more sensitive to the reaction due to its smaller concentration levels.

The relative error plots for both the concentrations and Tcc can be seen in Figure 7.19. The correlation plot can be seen in Figure 7.20.

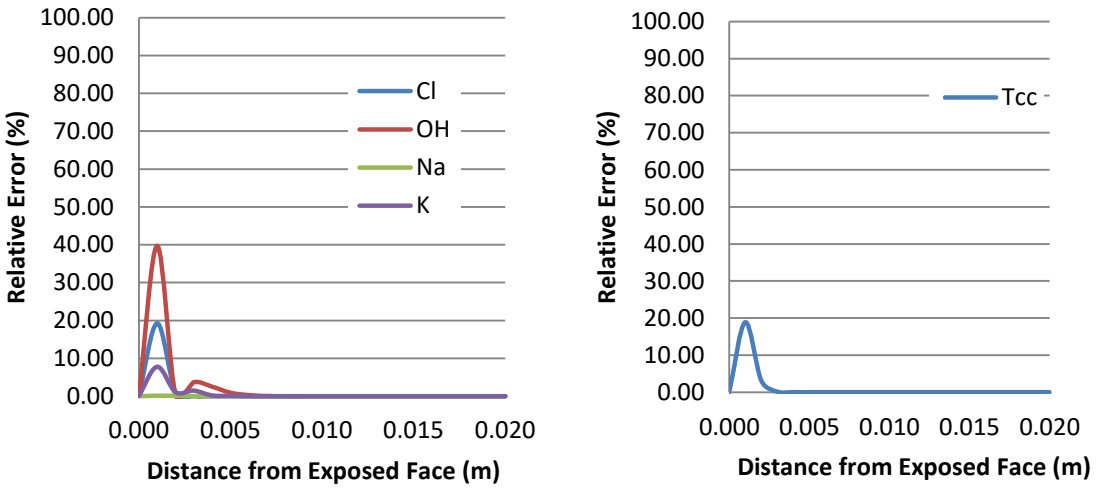

Figure 7.19 – Relative error of concentration and Tcc

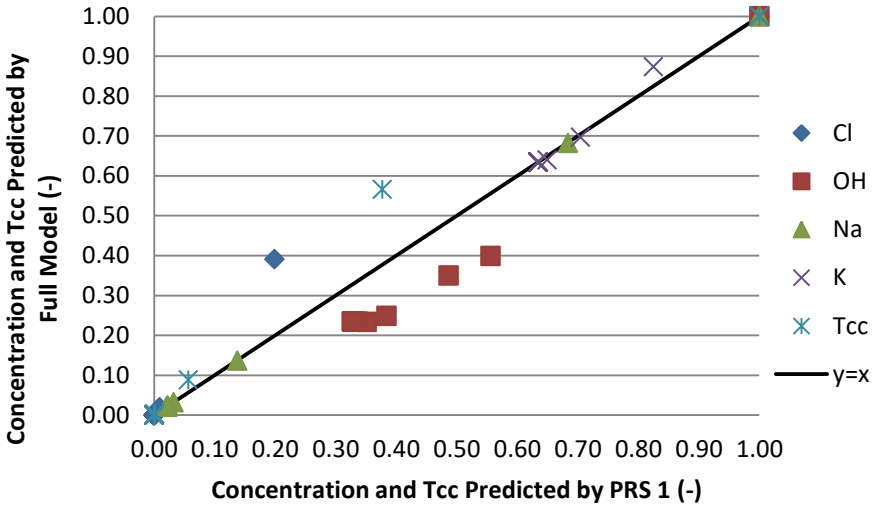

Figure 7.20 – Correlation plot of concentrations and Tcc

The above plots are in agreement with the profiles showing the largest error, and least correlation, for the OH^- profile.

A mass balance check was also carried out, from which the results are given in in Table 7.10. It can be seen from this table that the maximum mass balance error is 17 % and is found in the Cl^- profile not the OH^- profile which showed the largest relative error. This is due to the over prediction of the penetration of the Cl^- ions into the beam.

Table 7.10 – Relative mass balance error induced by PRS 1 (%)

Na^+	Cl^-	OH^-	K^+	Tcc
0.13	17.02	4.22	0.25	15.82

7.3.2 PRS 2 – Song et al. (2014)

The diffusion experiments and accompanying numerical simulations presented by Song et al. (2014) are considered here. In their work, a concrete slab was cured for 90 days and subsequently a set of 100x50 mm (diameter x thickness) cylindrical core of; the sides and bottom were sealed before the remaining surface was exposed to a salt solution for 6 months.

The boundary concentrations can be can be found in in Table 7.13 along with the diffusion coefficients and the D_{es} factors, which account for electrostatic double-layer

effects (Song et al. 2014). The sample was assumed to be initially saturated, with no solid masses present and the time period considered was 2 months. The time step size chosen was $\Delta t = 360\ s$ and a mesh of 52 bilinear quadrilateral elements was used with an element size of $\Delta x = 0.002\ m$. The problem geometry can be seen in Figure 7.21. The boundary conditions can be seen in Table 7.11. Table 7.12 shows the model parameters of the specimen. PRS 2 was chosen to model this example as the diffusion coefficient range is less than 6 ($D_{mol}^{ind,u}$<16$D_{mol}^{ind,l}$), the OH^- and K^+ species were chosen as the indicator species in this case as they are the species with the highest and lowest diffusion coefficients respectively (following multiplication by the D_{es} factors). The non-equilibrium Freundlich type isotherm describes the reactions, which were given in eqs. (6.5-6.9 & 6.12).

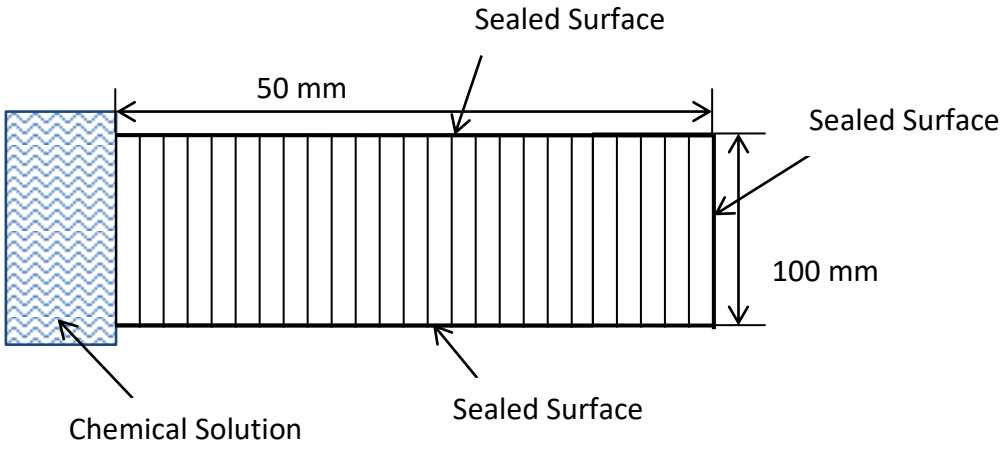

Figure 7.21 – Finite element mesh and problem geometry (not to scale)

Table 7.11 – Boundary conditions

Boundary	Boundary Type	Values
LHS	Cauchy	*RH=100 %, T=293 K, c**
Bottom	Sealed	-
RHS	Sealed	-
Top	Sealed	-

*See chemical parameters table

Table 7.12 – Model parameters

Parameter	Value
n	0.13
$\gamma_c\ (kg/m^2s)$	1e-4
$\omega_c\ (W/m^2K)$	8.0

Table 7.13 – Chemical parameters

Species	Initial Conc. (kg/kg)	Bound. Conc. (kg/kg)	D_{mol} $(10^{-9}\ m^2/s)$	D_{es}	Eq.	$k_a\ (10^{-8})$	$k_d\ (10^{-8})$	λ
Na^+	0.001978	0.0	1.33	0.25	*r1*	12.0	18.0	0.35
OH^-	0.004573	0.0	5.3	0.25	*r2*	144.0	24.0	0.35
K^+	0.007215	0.0	1.96	0.0875	*r3*	1375.0	330.0	0.35
Cl^-	0.0	0.01775	2.1	0.25	*r4*	6.42	1.275	0.2
SO_4^{2-}	0.000192	0.0	1.07	1.0	*r5*	5.4	0.75	0.2
Ca^{2+}	0.00004	0.01	0.79	0.4	*r6*	1000.00	1200.0	0.35

7.3.2.1 Results and Discussions

The concentration profiles as predicted by the full model and PRS 2 can be seen in Figure 7.22, whilst the solid mass profiles can be seen in Figure 7.23.

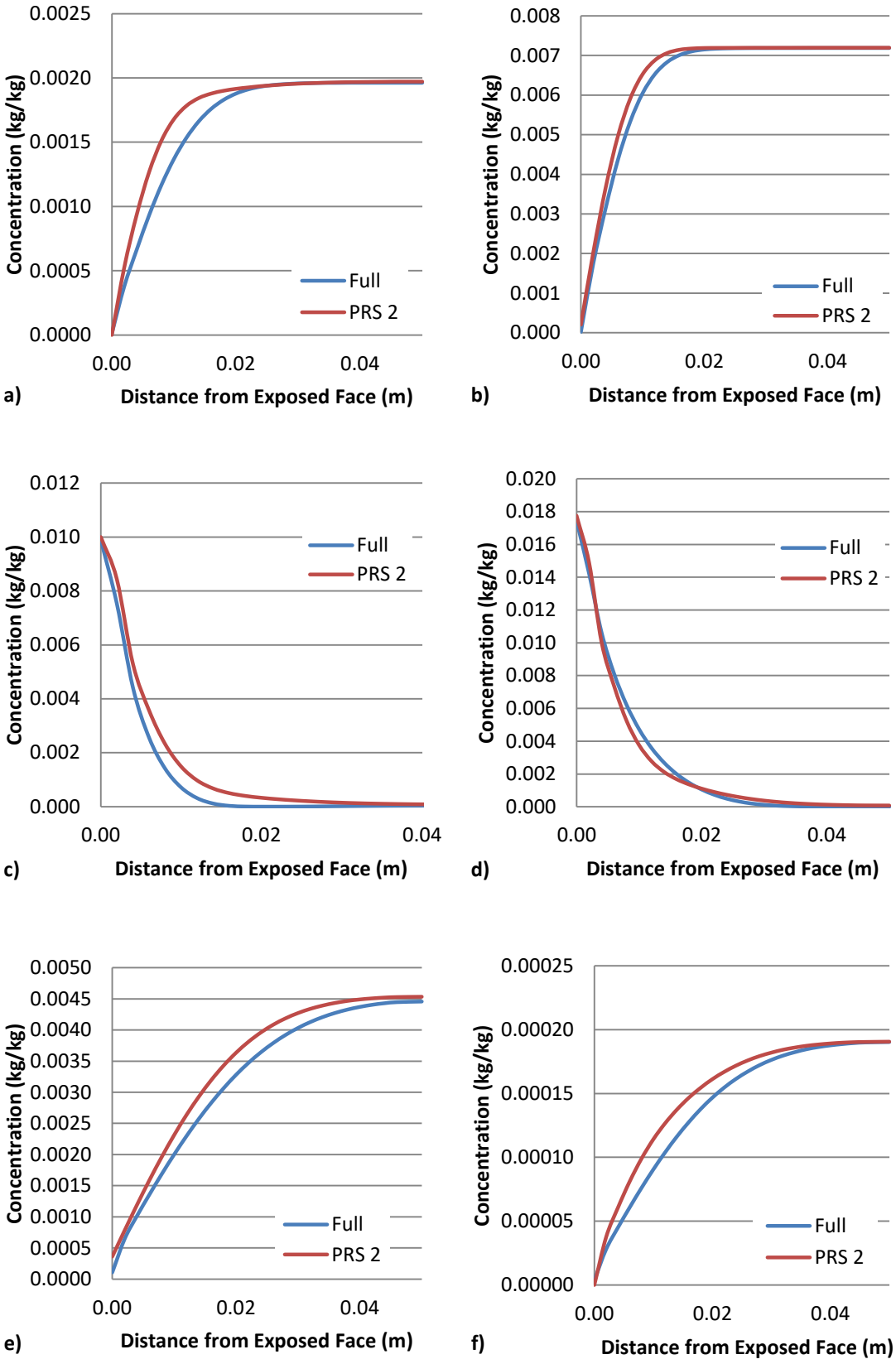

Figure 7.22 – Concentration profiles predicted by full model and PRS 2 (t=2 months) a) Na^{+}, b) K^{+}, c) Ca^{2+}, d) Cl^{-}, e) OH^{-} and f) SO_4^{2-}

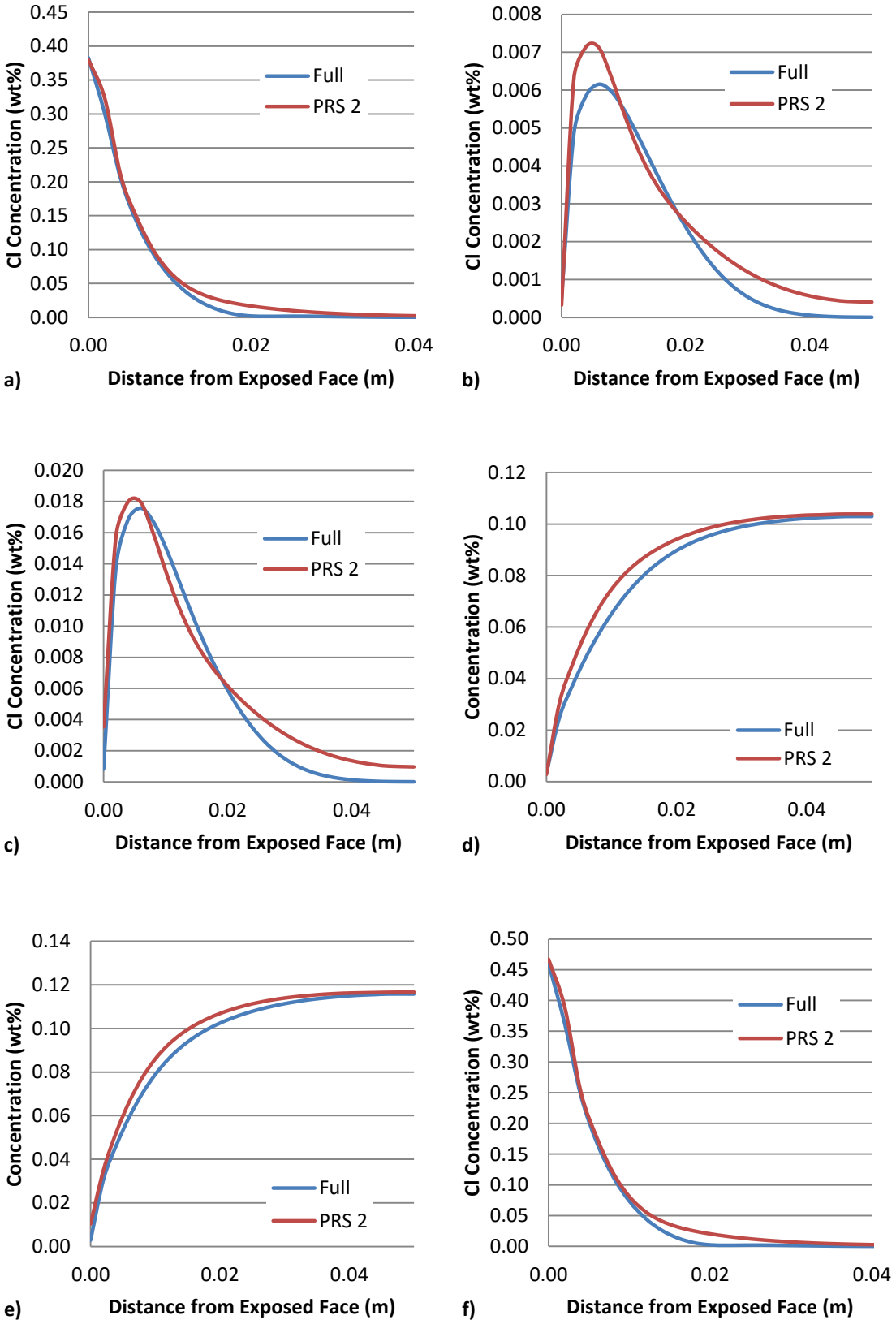

Figure 7.23 – Solid mass profiles predicted by full model and PRS 2 (t=2 months)
a) *CSH.CaCl$_2$*, b) *CSH.NaCl*, c) *CSH.2KCl*, d) *CSH.NaOH*, e) *CSH.2KCl* and f) *CAH.CaCl$_2$*

As can be seen from the figures, PRS 2 is in good agreement with the full model. The largest differences can be seen in the Na^+ and $CSH.NaCl$ profiles, with the Cl^-, $CSH.CaCl_2$ and $CAH.CaCl_2$ profiles being particularly close. This is not as expected as in terms of diffusion coefficient values since Cl^- is furthest away from the indicator species; however, this is due to the effect of the reaction. It can be noticed that both the K^+ and OH^- profiles are not in total agreement, despite being indicator species. It is thought that this is due to the effect of the reactions in this example. To investigate this, the example was simulated without reactions and the profiles then compared. It was found that profiles were in agreement in that case, and can be seen in Figure 7.24.

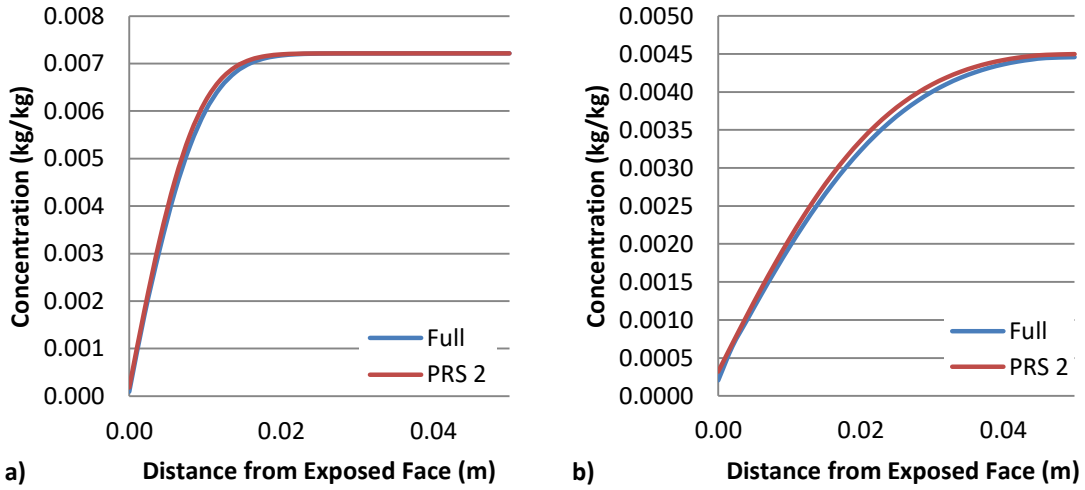

Figure 7.24 – Concentration profiles as predicted by the full model and PRS 2 for the non-reactive case (t=2 months) a) K^+ and b) OH^-

The relative error plots and the correlation plots can be seen in Figure 7.25.

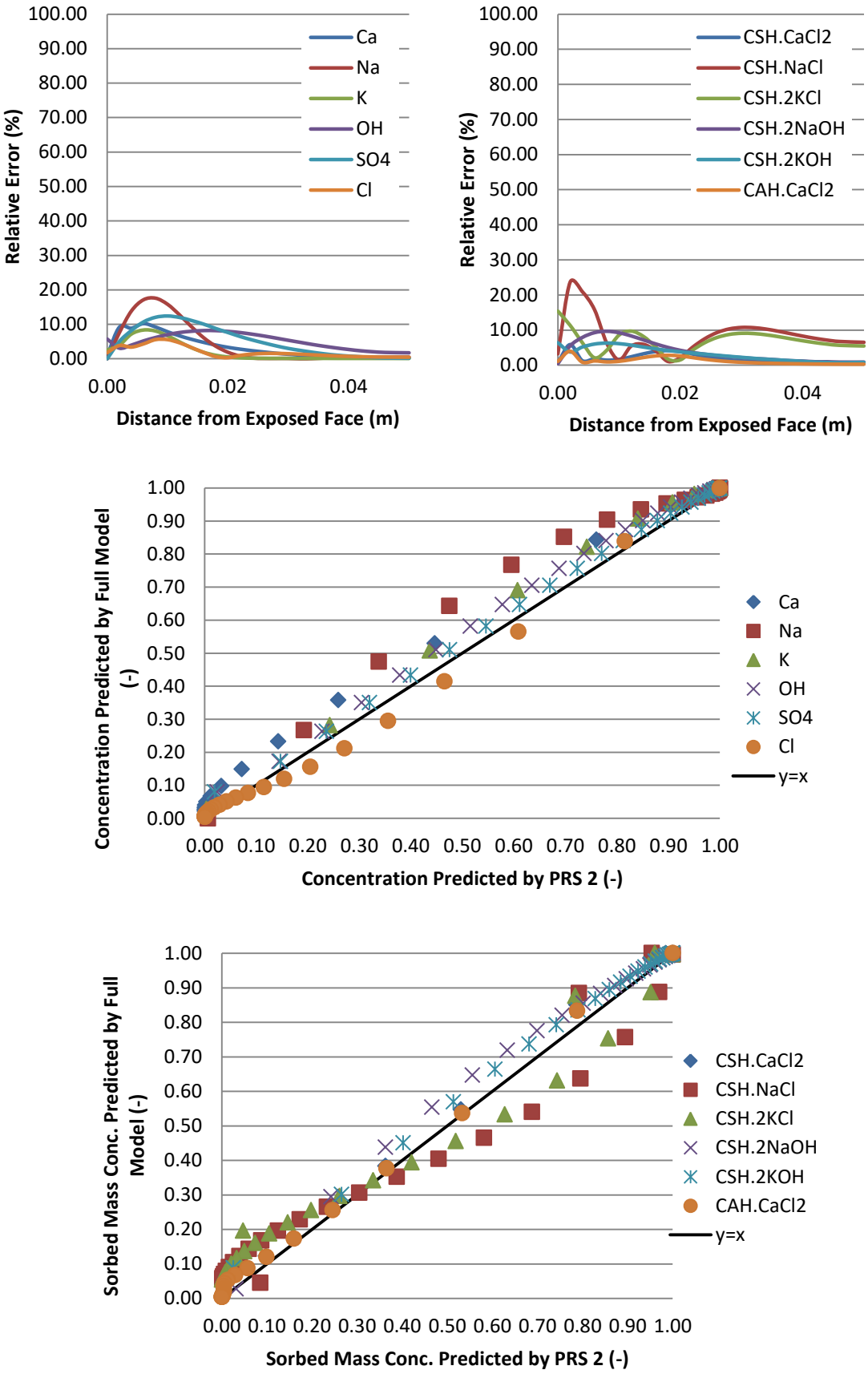

Figure 7.25 – Relative error and correlation plots of concentration and sorbed mass

The above plots are in agreement with the profiles showing the largest error and least correlation to be in the Na^+ and $CSH.NaCl$ profiles.

A mass balance check was also carried out, the results of which can be seen in Table 7.14. It can be seen that the largest error is in the Ca^{2+} profile with a value of 31.05 %, this is in agreement with the profiles as the Ca^{2+} shows a constant over-prediction.

Table 7.14 - Relative mass balance error induced by PRS 2 (%)

Ca^{2+}	Na^+	K^+	OH^-	SO_4^{2-}	Cl^-
31.05	5.23	2.30	7.35	7.07	2.16
$CSH.CaCl_2$	$CSH.NaCl$	$CSH.2KCl$	$CSH.2NaOH$	$CSH.2KOH$	$CAH.CaCl_2$
13.54	19.12	12.19	4.91	4.07	14.21

7.3.3 PRS 3 – Hypothetical based on Zhu et al. (1999)

The final simulation is based on the work of Zhu et al. (1999). It involves the transport of 10 chemical species, precipitation of 6 minerals and considers 1 immobile solid species. This is a 2D problem with a point source for the chemical species (marked A in Figure 7.26). The moisture transport was considered at a constant rate of $V=5.8x10^{-6}$ mm/s in the x direction. The total domain size was 12.5x10 mm. The problem geometry can be seen in Figure 7.26; due to the symmetry of the problem, it was only necessary to model half of the domain. The boundary conditions are of zero flux on all sides. It was assumed that the sample was initially saturated and the time period considered was 10 hours. The time step size chosen was $\Delta t=3.6\ s$ and a mesh of 286 bilinear quadratic elements was used with an element size of $\Delta x = 0.0005\ m$. The Freundlich type isotherm (eq. 3.39) describes the reactions, which were calculated based on the non-equilibrium assumption. The reaction equations for the 6 solid minerals considered are given as:

$$r_1 = k_d^{Al(OH)_3}[Al(OH)_3] - k_a^{Al(OH)_3}([Al^{3+}][OH^-]^3)^{\lambda_1} \quad (7.5)$$

$$r_2 = k_d^{CaSO_4.2H_2O}[CaSO_4.2H_2O] - k_a^{CaSO_4.2H_2O}([Ca^{2+}][SO_4^{2-}][OH^-]^2)^{\lambda_2} \quad (7.6)$$

$$r_3 = k_d^{K_{0.6}Mg_{0.25}Al_{2.3}Si_{3.5}O_{10}(OH)_2}[K_{0.6}Mg_{0.25}Al_{2.3}Si_{3.5}O_{10}(OH)_2] - k_a^{K_{0.6}Mg_{0.25}Al_{2.3}Si_{3.5}O_{10}(OH)_2}([K^+]^2[Mg^{2+}][H^+]^2[Al(OH)_4^-]^2[H_3SiO_4^-]^2)^{\lambda_4} \quad (7.7)$$

$$r_4 = k_d^{Fe(OH)_3}[Fe(OH)_3] - k_a^{Fe(OH)_3}([Fe^{3+}][OH^-]^3)^{\lambda_5} \quad (7.8)$$

$$r_5 = k_d^{CaCO_3}[CaCO_3] - k_a^{CaCO_3}([Ca^{2+}][CO_3^{2-}])^{\lambda_6} \quad (7.9)$$

$$r_6 = k_d^{H_4SiO_4}[H_4SiO_4] - k_a^{H_4SiO_4}([H^+]^2[SiO_2]^2)^{\lambda_3} \quad (7.10)$$

It was assumed that the initial concentration of solid masses is zero. The boundary conditions can be seen in Table 7.15. The boundary values, initial conditions, reaction rates and diffusion coefficients can be seen in Table 7.17. The model parameters can be seen in Table 7.16. PRS 3 was chosen to model this example as the diffusion coefficient range is greater than the range of applicability of both PRS 1 and PRS 2, the chosen indicator species were H^+, Al^{3+} and K^+.

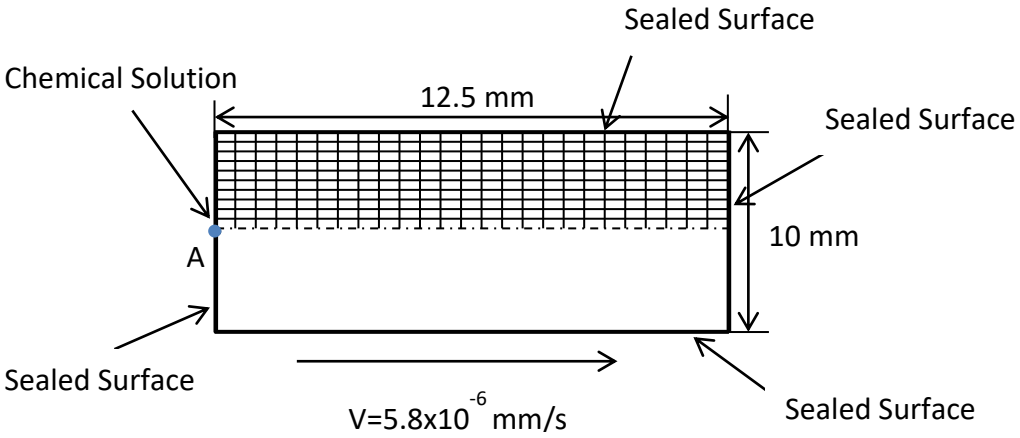

Figure 7.26 – Finite element mesh and problem geometry (not to scale)

Table 7.15 – Boundary conditions

Boundary	Boundary Type	Values
A	Cauchy	*RH=100 %, T=293 K, c**
LHS	Sealed	-
Bottom	q=0	-
RHS	Sealed	-
Top	Sealed	-

*See chemical parameters table

Table 7.16 – Model parameters

Parameter	Value
n	0.3
$\gamma_c\ (kg/m^2s)$	1e-4
$\omega_c\ (W/m^2K)$	8.0

Table 7.17 – Chemical parameters

Species	Initial Conc. (kg/kg)	Boundary Conc. (kg/kg)	D_{mol} $(10^{-9}\ m^2/s)$	Eq.	k_a (10^{-7})	k_d (10^{-8})	λ
H^+	0.000028	0.00005	9.311	r_1	2.6	29.6	0.61
Ca^{2+}	0.0003164	0.00048	0.792	r_2	0.6	8.67	0.2
Mg^{2+}	0.00102303	0.001944	0.706	r_3	1.4	9.0	0.07
HCO_3^-	0.00061	0.0000305	1.185	r_4	2.8	2.0	0.11
Al^{3+}	0.000837	0.00135	0.541	r_5	2.1	6.0	0.43
SO_4^2	0.016896	0.024	1.065	r_6	0.425	74.0	0.35
Fe^{3+}	0.00199206	0.00279	0.604				
K^+	0.00006123	0.000078	1.957				
Cl^-	0.0010295	0.001775	2.032				
Na^+	0.0018515	0.000345	1.334				
SiO_2	0.015	-	-				

7.3.3.1 Results and Discussions

The concentration contours as predicted by the full model can be seen in Figures 7.27 & 7.28, whilst the solid mass contours can be seen in Figures 7.29 & 7.30.

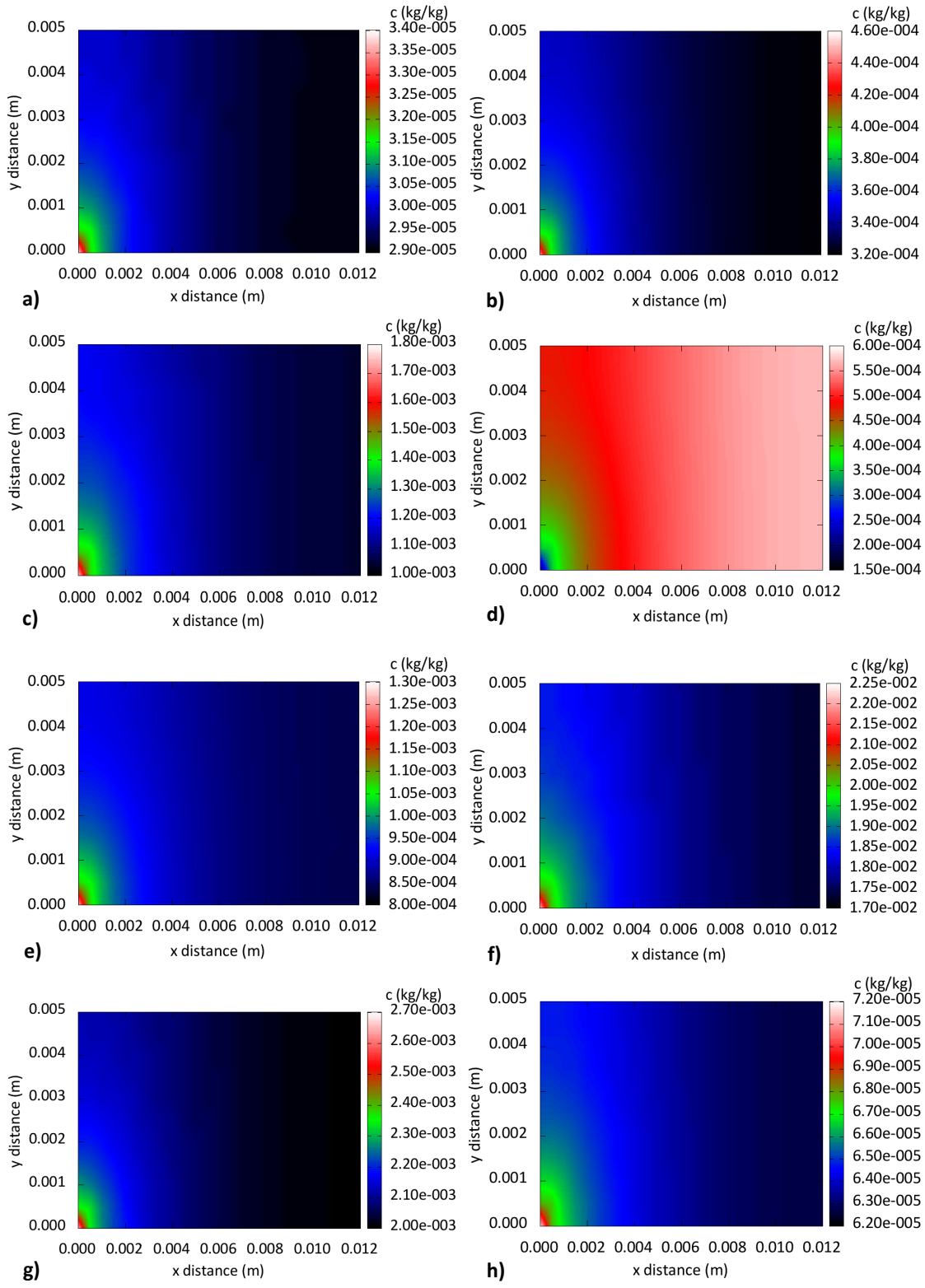

Figure 7.27 - Concentration contours predicted by the full model (t=10 hours) a) H^{+}, b) Ca^{2+}, c) Mg^{2+}, d) HCO_3^{2-}, e) Al^{3+}, f) SO_4^{2-}, g) Fe^{3+} and h) K^{+}

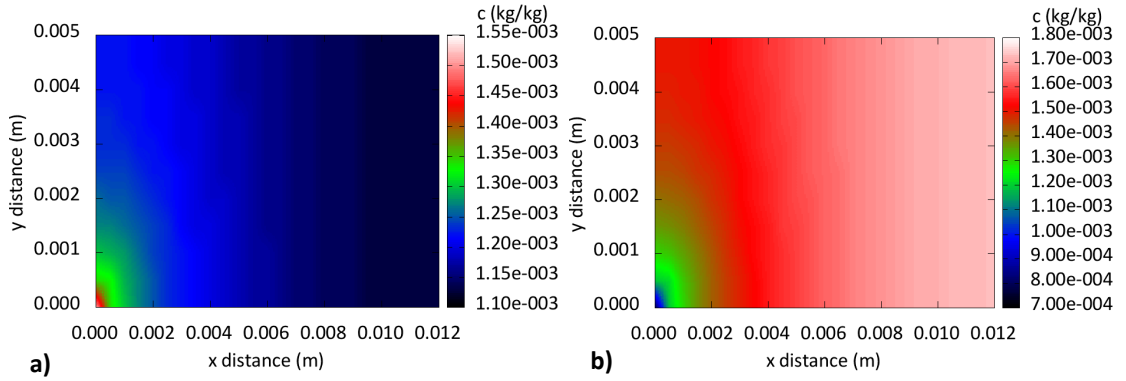

Figure 7.28 – Concentration contours predicted by the full model (t=10 hours) a) Cl^- and b) Na^+

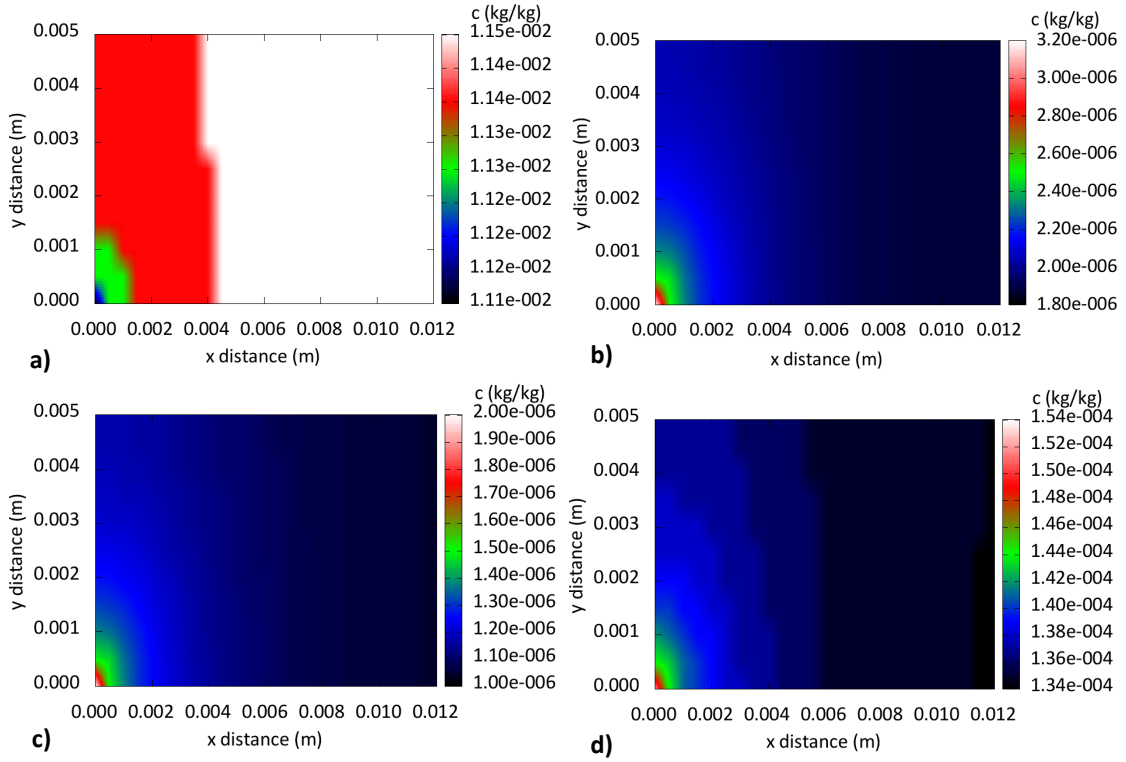

Figure 7.29 - Solid mass contours predicted by the full model (t=10 hours) a) $Al(OH)_3$, b) $CaSO_4.2H_20$, c) $K_{0.6}Mg_{0.25}Al_{2.3}Si_{3.5}O_{10}(OH)_2$ and d) $Fe(OH)_3$

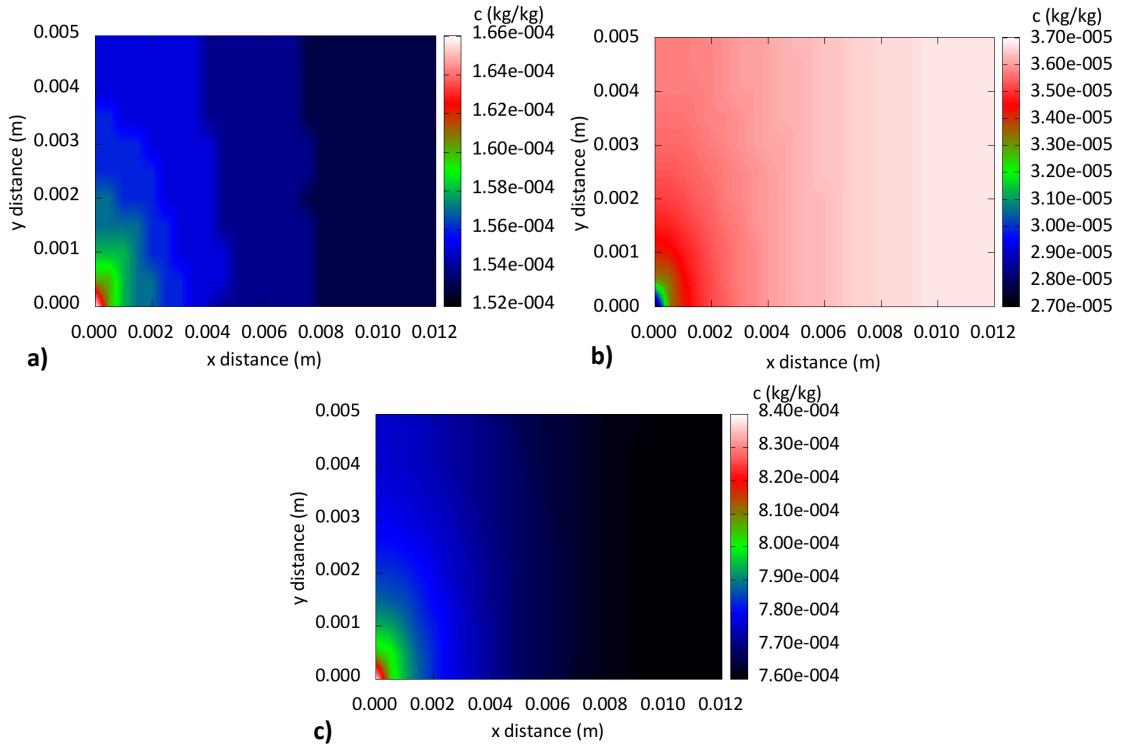

Figure 7.30 – Solid mass contours predicted by the full model (t=10 hours) a) $CaCO_3$, b) H_4SiO_4 and c) SiO_2

As can be seen from the contours, the behaviour is as expected with slightly higher penetration of the solutes in the x direction as a result of the pore water velocity. Two main types of behaviour are present in the chemical species; one relates to species for which the boundary concentration is higher than the initial concentration, where the chemical is transported into the domain, and the other for which concentrations are lower, and the chemical diffuses out of the domain in a direction contrary to the advective pore water flow.

The concentration profiles -as predicted by the full model and PRS 3- can be seen in Figures 7.32 & 7.33, whilst the solid mass profiles can be seen in Figures 7.34 & 7.35. These profiles are found by taking a cut along the x axis, line B-B seen in Figure 7.31. The y profiles, obtained by taking a cut along line A-A, showed similar results and can be seen in Appendix A2 Figures A19-22.

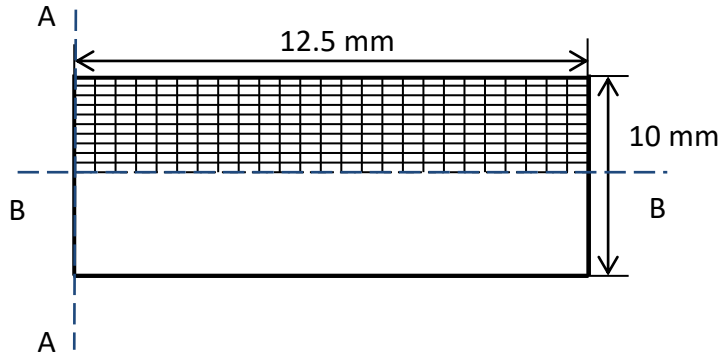

Figure 7.31 – Problem geometry and cut lines

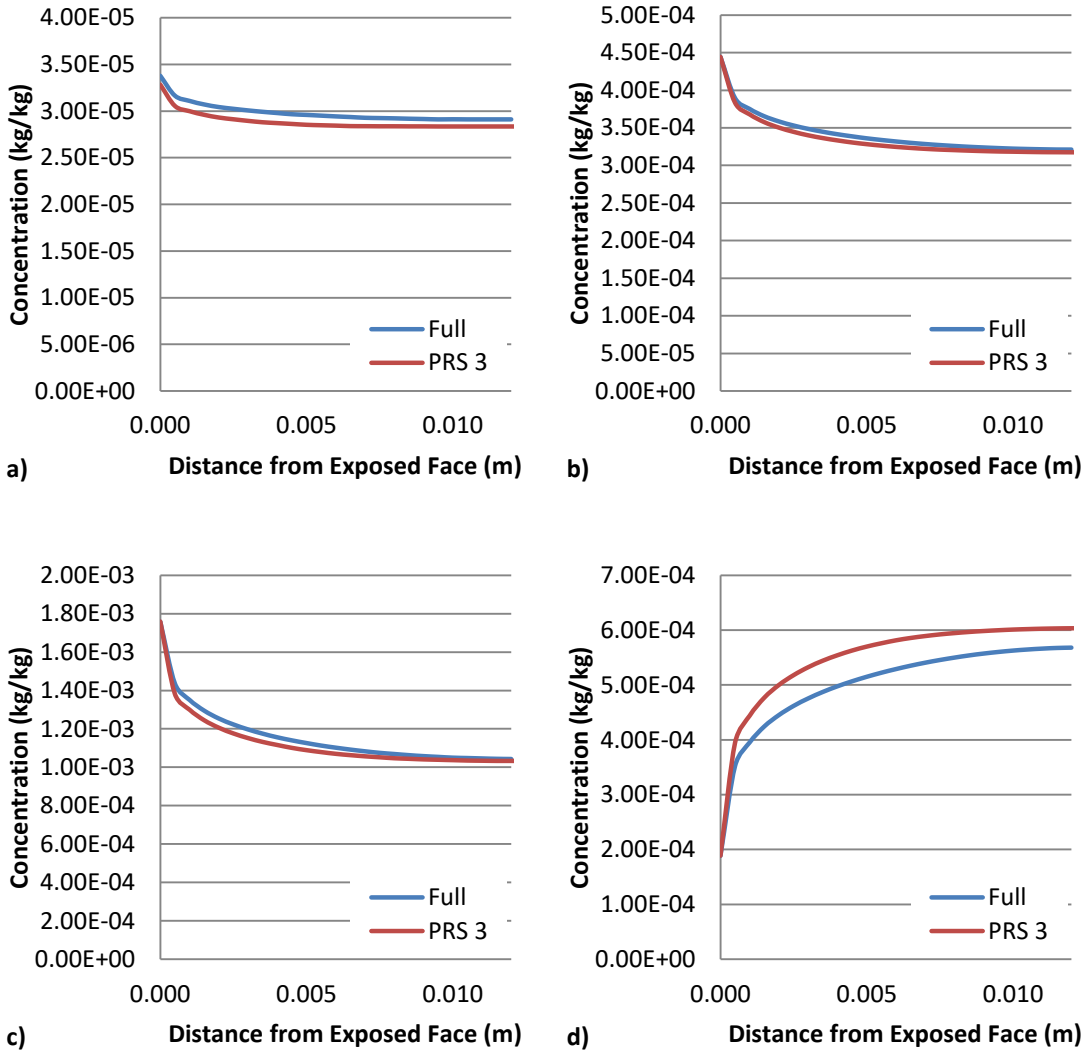

Figure 7.32 - Concentration profiles (taken along cut line B-B) predicted by the full model and PRS 3 (t=10 hours) a) H^{+}, b) Ca^{2+}, c) Mg^{2+} and d) HCO_3^{2-}

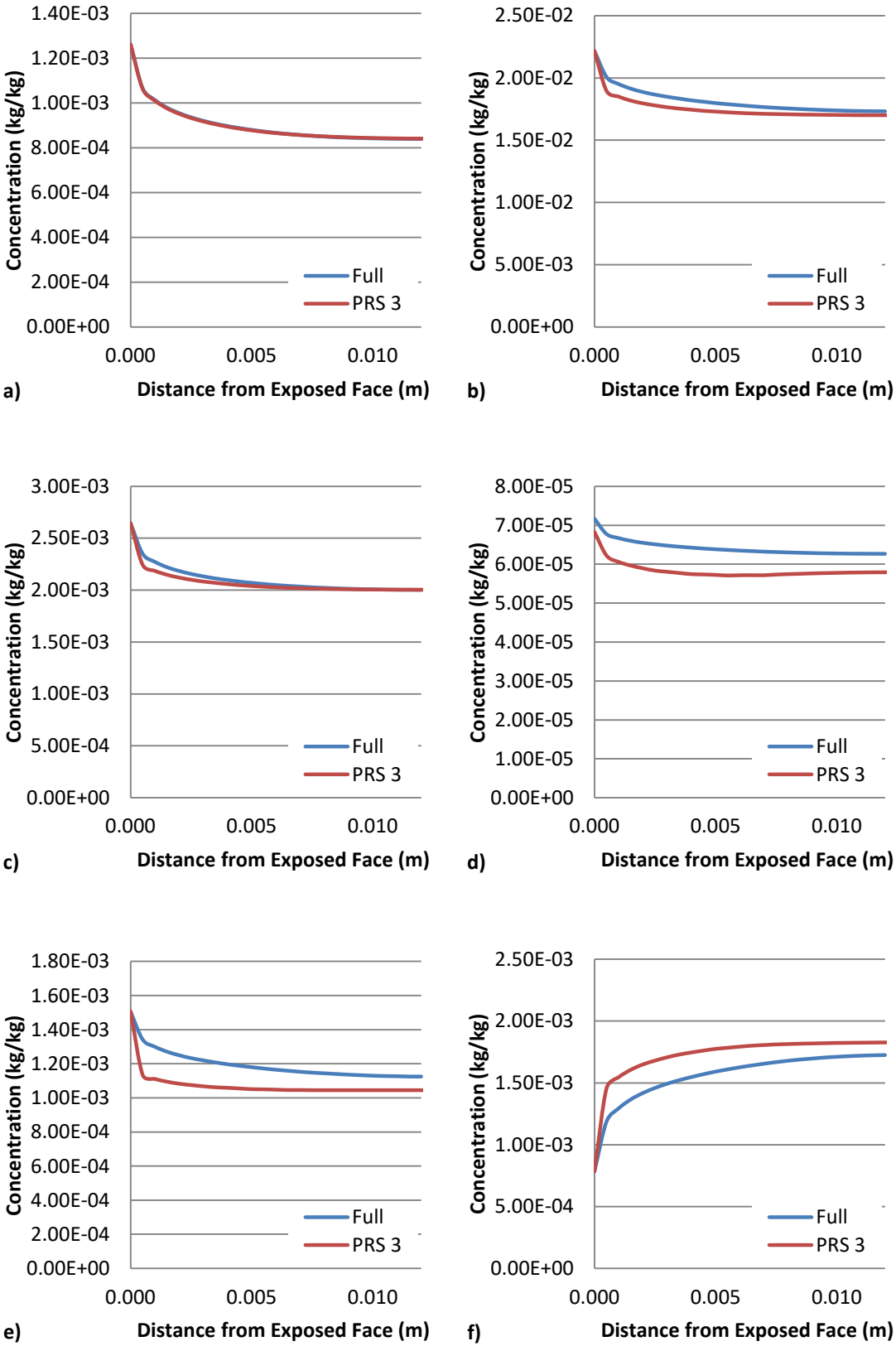

Figure 7.33 – Concentration profiles (taken along cut line B-B) predicted by the full model and PRS 3 (t=10 hours) a) Al^{3+}, b) SO_4^{2-}, c) Fe^{3+}, d) K^{+}, e) Cl^{-} and f) Na^{+}

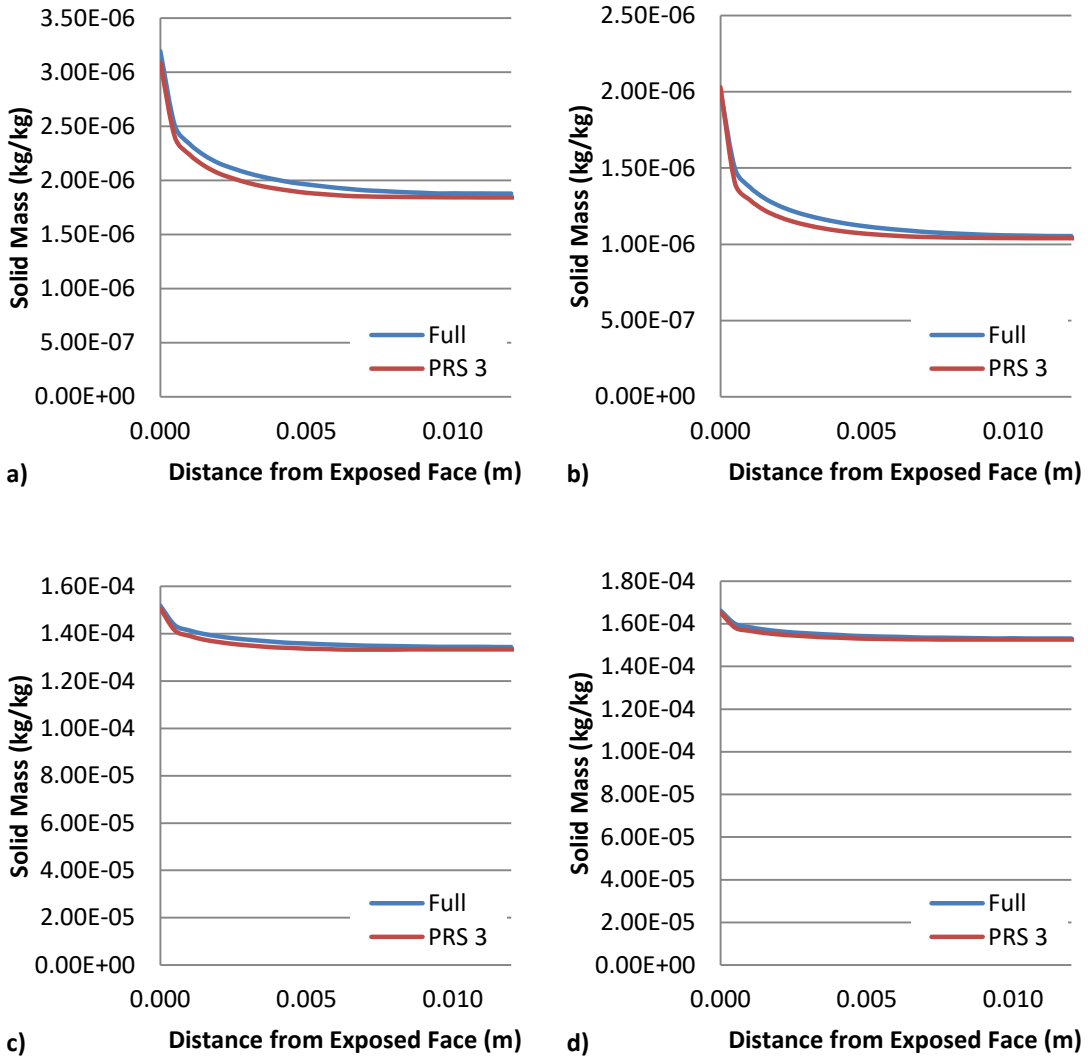

Figure 7.34 - Solid mass profiles (taken along cut line B-B) predicted by the full model and PRS 3 (t=10 hours) a) $Al(OH)_3$, b) $CaSO_4.2H_20$, c) $K_{0.6}Mg_{0.25}Al_{2.3}Si_{3.5}O_{10}(OH)_2$ and d) $Fe(OH)_3$

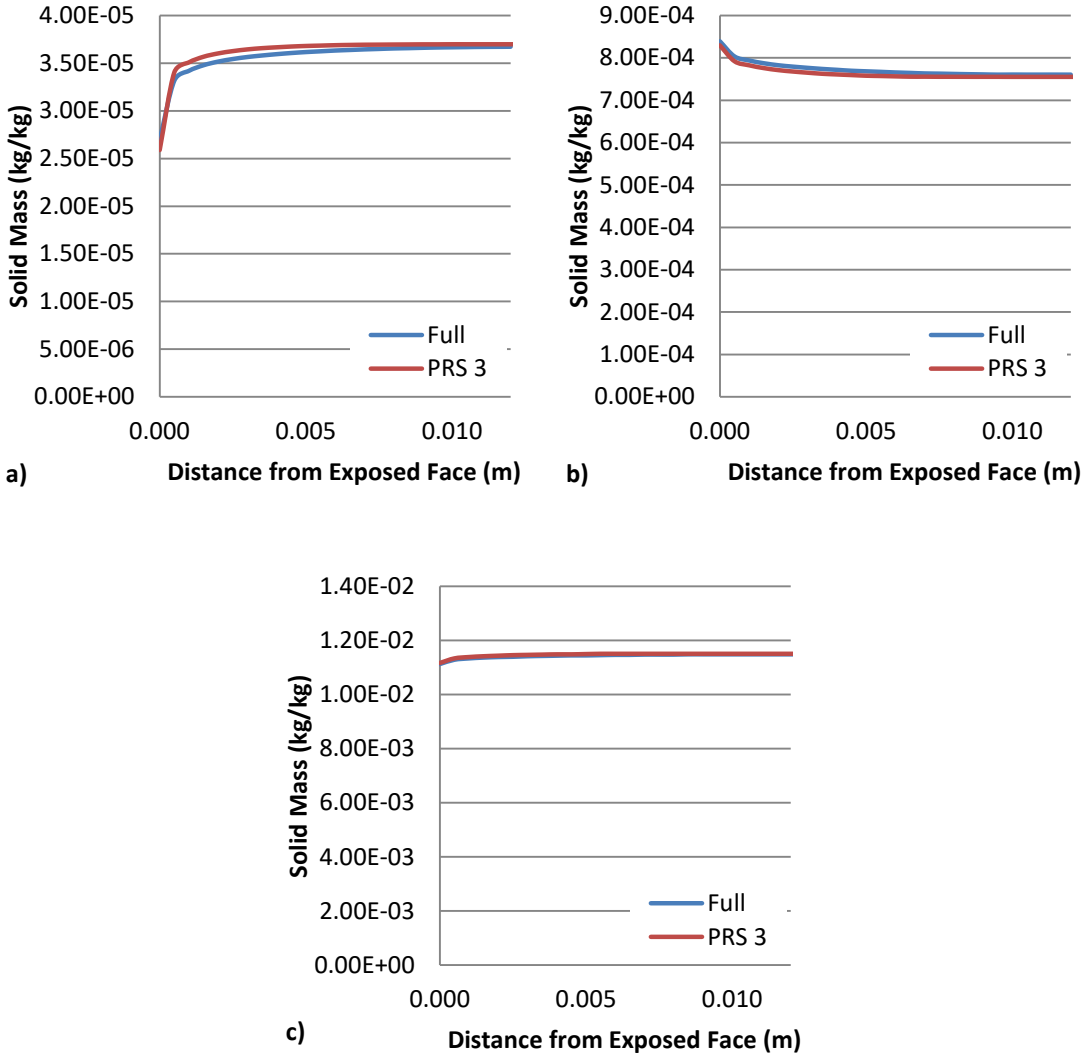

Figure 7.35 – Solid mass profiles (taken along cut line B-B) predicted by the full model and PRS 3 (t=10 hours) a) $CaCO_3$, b) H_4SiO_4 and c) SiO_2

It can be seen from the profiles that PRS 3 is in good agreement with the full model. The solid mass profiles are more accurately predicted in this example than the concentration profiles, contrary to previous examples. It is thought that this is because the error found in concentration profiles is reduced by the reaction equation in this case. The biggest differences can be seen in Cl^-, Na^+ and K^+ profiles. The Na^+ result is as expected since its diffusion coefficient is far from an indicator species; however, Cl^- is not as it is near to K^+ which is an indicator species. The K^+ is an indicator but shows a difference in concentration profiles, as does the H^+. This is thought to be due to the reactions as in the previous example; this was tested by simulating the problem again

without reactions. The results for the non-reactive case for K^+ and H^+ can be seen in Figure 7.36, which shows that they are in perfect agreement.

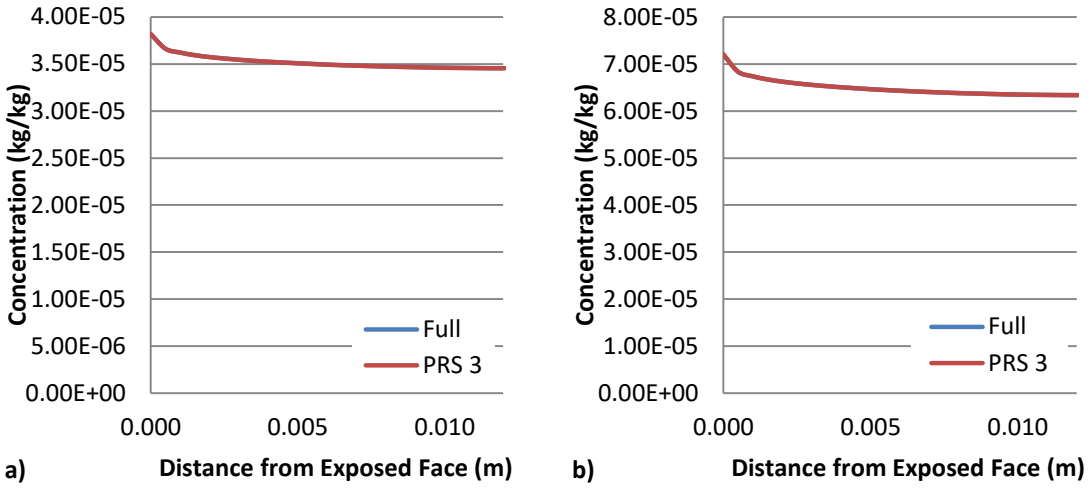

Figure 7.36 – Concentration profiles (taken along cut line B-B) as predicted by the full model and PRS 3 for the non-reactive case (t=10 hours) a) H^+ and b) K^+

The relative error plots for the concentration can be seen in Figures 7.37 & 7.38, whilst the solid mass error can be seen in Figures 7.39 & 7.40.

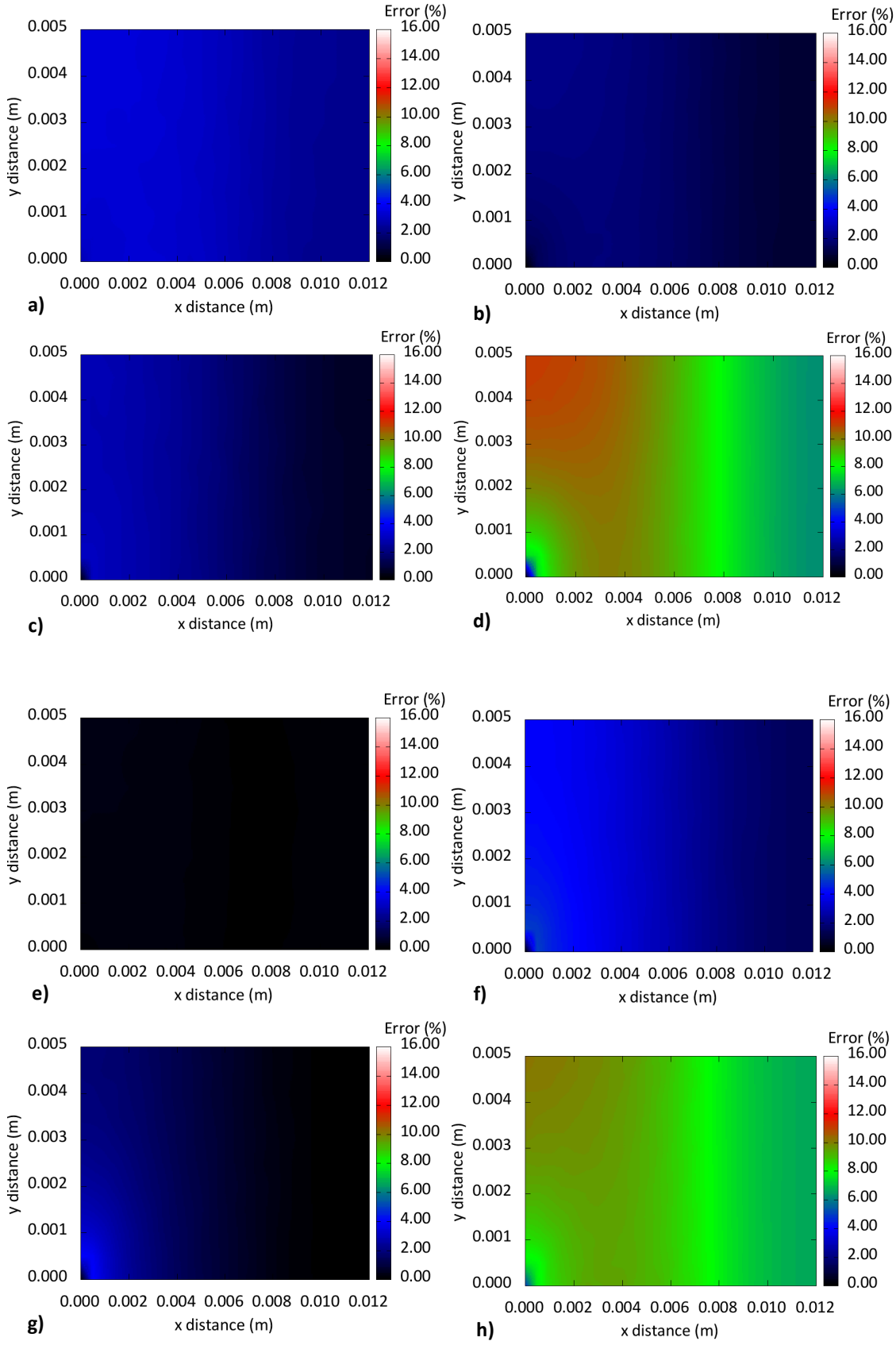

Figure 7.37 - Relative error contours of concentrations (t=10 hours) a) H^{+}, b) Ca^{2+}, c) Mg^{2+}, d) HCO_3^{2-}, e) Al^{3+}, f) SO_4^{2-}, g) Fe^{3+} and h) K^{+}

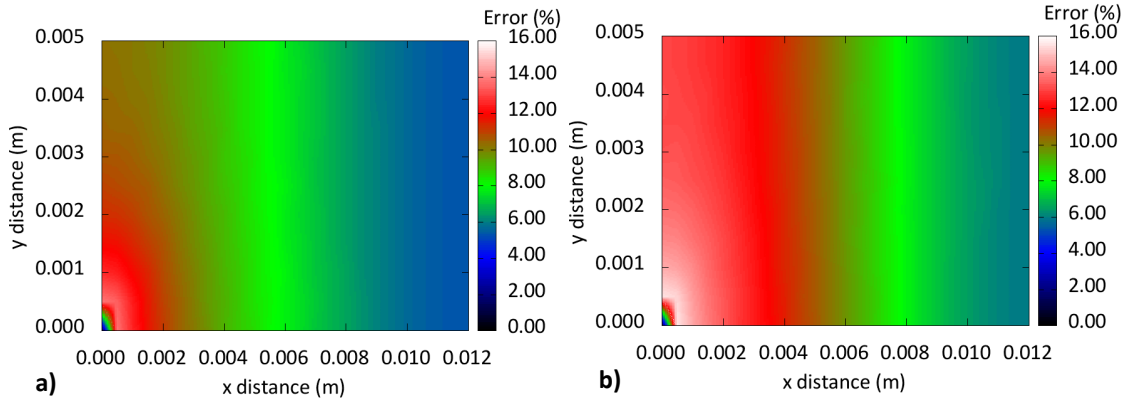

Figure 7.38 – Relative error contours of concentrations (t=10 hours) a) Cl^- and b) Na^+

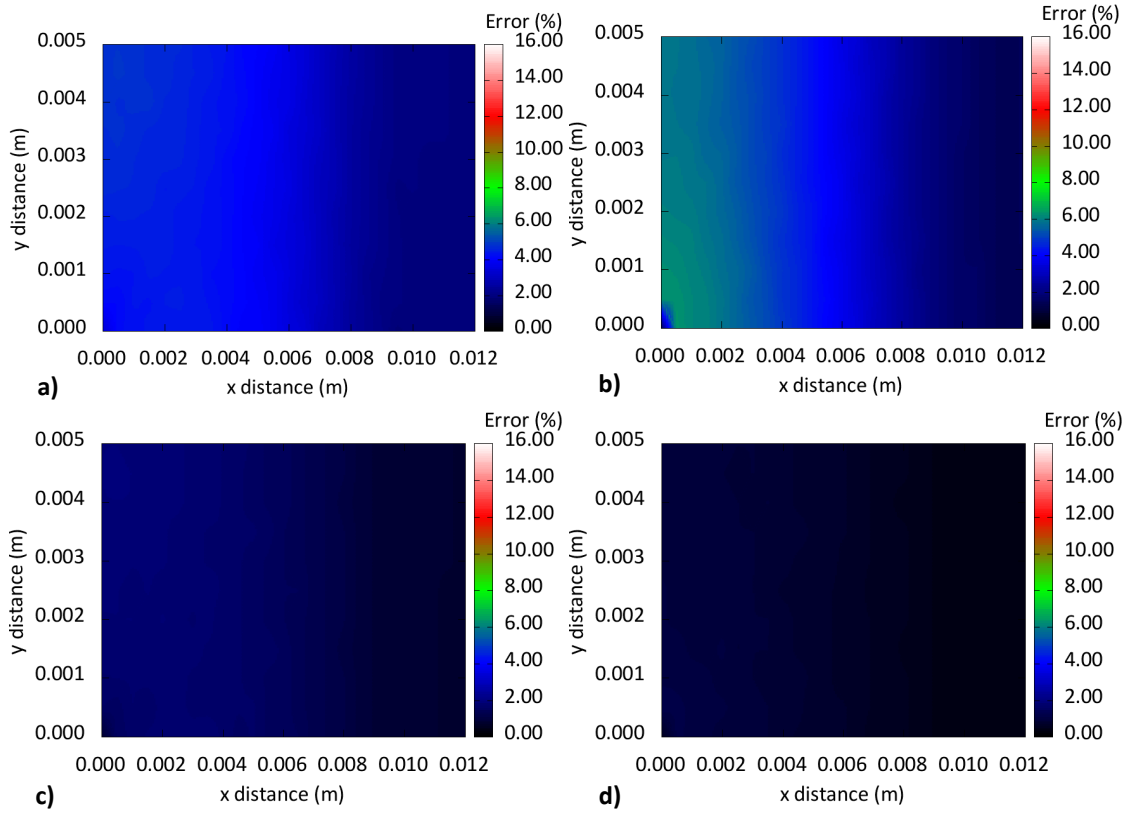

Figure 7.39 - Relative error contours of solid mass (t=10 hours) a) $Al(OH)_3$, b) $CaSO_4.2H_20$, c) $K_{0.6}Mg_{0.25}Al_{2.3}Si_{3.5}O_{10}(OH)_2$ and d) $Fe(OH)_3$

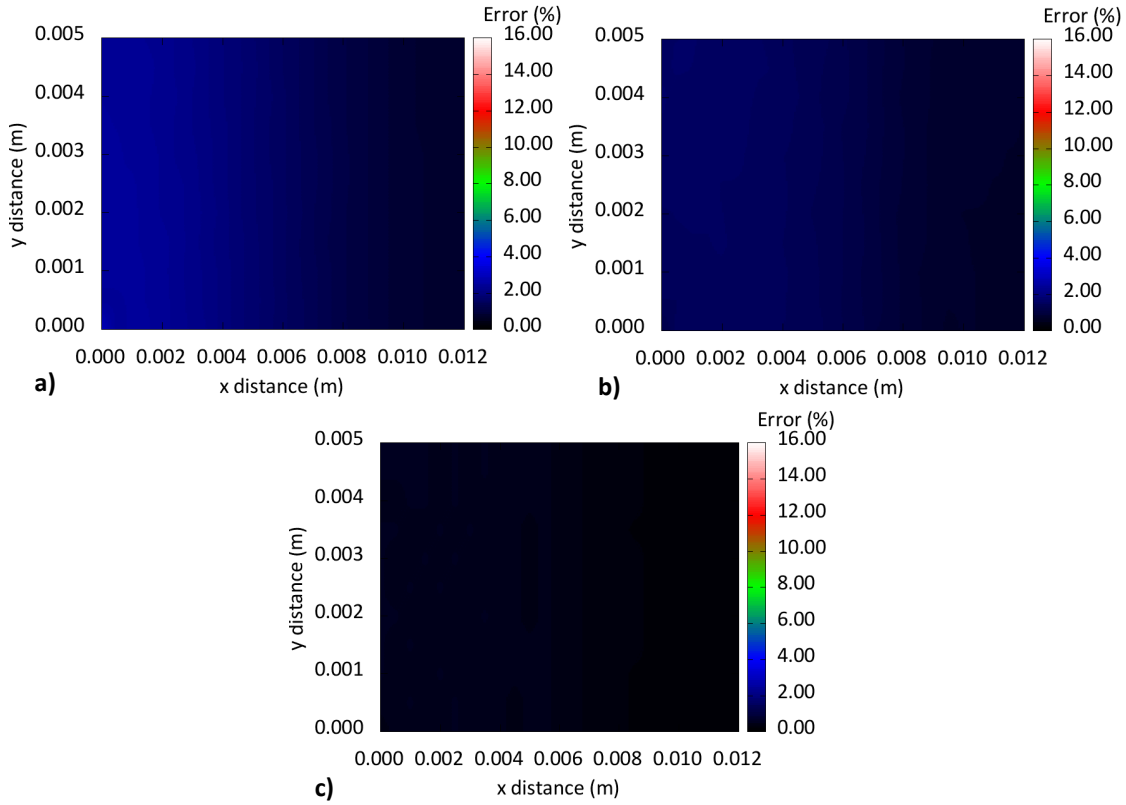

Figure 7.40 – Relative error contours of solid mass (t=10 hours) a) $CaCO_3$, c) H_4SiO_4 and c) SiO_2

As can be seen from the contours, the error is -on the whole- as expected. The solid masses indicate little error, and the larger concentration errors occur mainly near the chemical influx, where the concentration gradients are sharpest. Two exceptions to this are the HCO_3^{2-} and K^+ contours, which show their largest error in the top left corner of the domain, it is thought that this is due to the reactions that are taking place. The maximum error in any species is 15.58 % found in the Na^+ concentration.

The correlation plots found from the x profiles can be seen in Figure 7.41 for the concentration and solid mass, the equivalent y plots can be seen in Appendix A2 Figure A23.

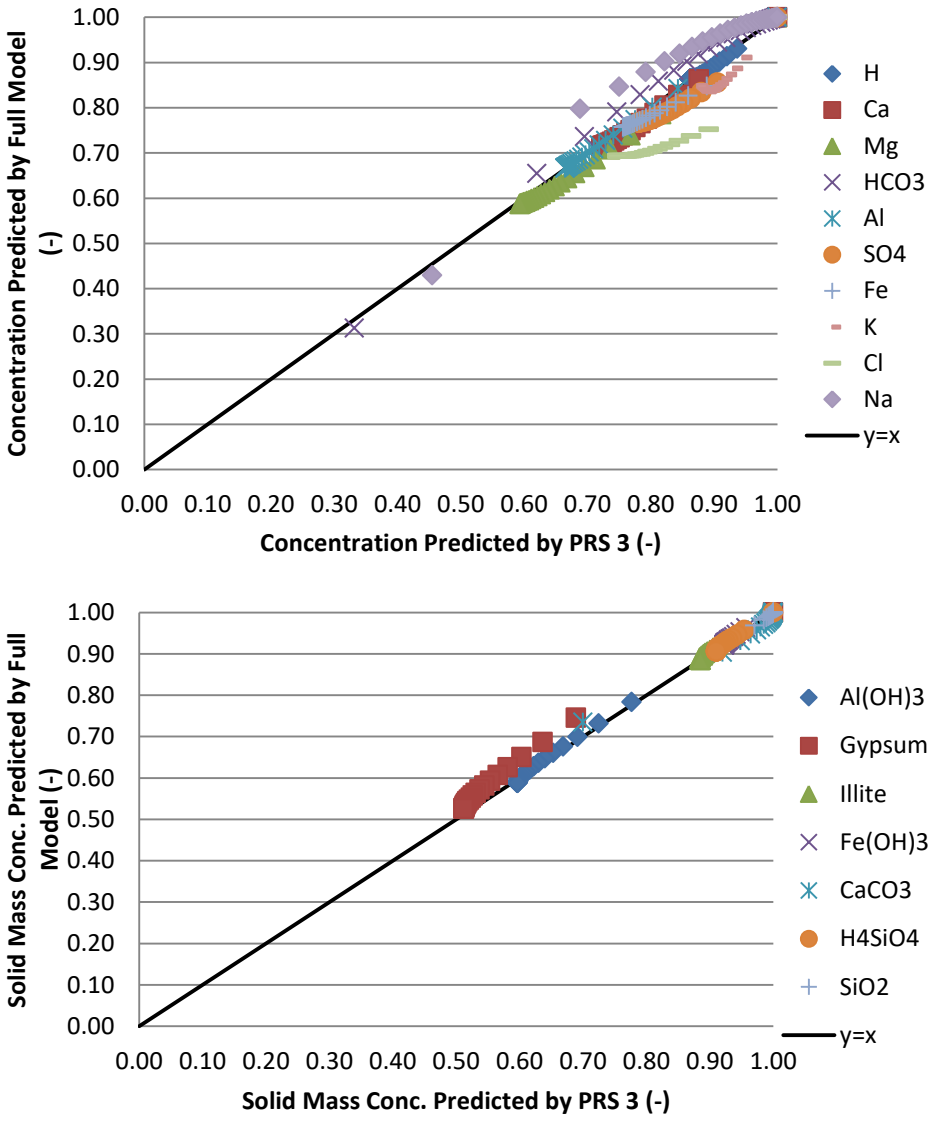

Figure 7.41 – Correlation of concentrations and solid mass

The above correlation and error plots are in agreement with the profiles showing the least correlation and largest error in the Na^+ and Cl^- profiles.

A mass balance check was also carried out, the results of which can be seen in Table 7.18. The largest mass balance errors are found where expected in the Na^+ and Cl^- concentrations of 10.01 % and 10.20 % relative error respectively. The solids masses are conserved well with a maximum error of only 3.62 %.

Table 7.18 - Relative mass balance error induced by PRS 3 (%)

H^+	Ca^{2+}	Mg^{2+}	HCO_3^{2-}	Al^{3+}	SO_4^{2-}	Fe^{3+}	K^+	Cl^-
3.23	1.96	2.68	9.36	0.11	3.35	1.18	9.36	10.01
Na^+	$Al(OH)_3$	*Gypsum*	*Illite*	$Fe(OH)_3$	$CaCO_3$	H_2SiO_4	SiO_2	
10.20	3.32	3.62	1.32	0.65	1.52	1.13	0.33	

7.4 Computational Cost

The purpose of the reduction scheme was to reduce the computational cost associated with solving transport problems. In the above examples it is clear that the computational cost has been reduced as the number of coupled non-linear equations solved has been reduced; however, in order to fully evaluate the effectiveness of the PRSs, this reduction needs to be quantified. To this end, the CPU time of the simulations has been measured and the results compared. The analysis was performed on a laptop with an Intel Core i5-3230M @2.60 GHz and 5.88 GB useable RAM. The CPU time of the time step loop was measured for a number of runs and an average taken. It should be noted that there is no trend in the measured CPU times for each of the examples as the mesh and time step sizes were different in each instance. The results for each of the problems considered can be seen in Table 7.19.

Table 7.19 – CPU times and percentage reduction for example problems

Problem	Full Model Time (s)	PRS Time (s)			Reduction (%)		
		1	2	3	1	2	3
4 Ion	620.07	293.90	-	-	52.60	-	-
6 Ion	240.00	-	92.64	-	-	61.40	-
10 Ion	26000.00	-	-	5508.33	-	-	78.81
16 Ion	1409.00	130.67	186.10	270.03	90.73	86.79	80.84

It can be seen from the above table that the PRSs greatly reduce the computational cost, with the greatest reduction being over than 90 % and the smallest reduction being over 50 %.

7.5 Investigation into the use of Analytical Relationships for the Reduction Scheme

Before developing the numerically based PRSs, presented previously, an investigation into the analytical relationship between the diffusion coefficient and the transport of a species over a time step was made. The analytical solution considered can be found in (Crank 1975), and is given for a semi-infinite medium as:

$$c = c^b \cdot erfc\left(\frac{x}{2\sqrt{D_{mol}t}}\right) \tag{7.11}$$

where x (>0) is the distance from the exposed face and $erfc$ is the complimentary error function. For this investigation, a problem concerning the 1D diffusion of ions into a semi-infinite domain with a boundary concentration of $1\ kg/kg$ was considered. The analytical formula was used to calculate the transient diffusion of a number of species with differing diffusion coefficients and the results used to analyse the relationship between the transport over a time step and the diffusion coefficient relative to an indicator species, such that the change in concentration ratio can be calculated as a function of the diffusion coefficient ratio as follows:

$$\frac{\Delta c_i}{\Delta c_{ind}} = f\left(\frac{D^i_{mol}}{D^{ind}_{mol}}\right) \tag{7.12}$$

An investigation was also made into the dependence of this, if any, on the time t and the distance from the boundary x. For the investigation, the indicator species had a diffusion coefficient of $1x10^{-9}\ m^2/s$.

The first discovery was that if any species with a higher diffusion coefficient than the indicator was included, the relationship of the concentration ratio to diffusion coefficient tended to infinity, as can be seen in Figure 7.42. This makes sense at the early stages of the problem since there would be some transport in the higher diffusion coefficient species whilst the indicator species transport would be near to zero.

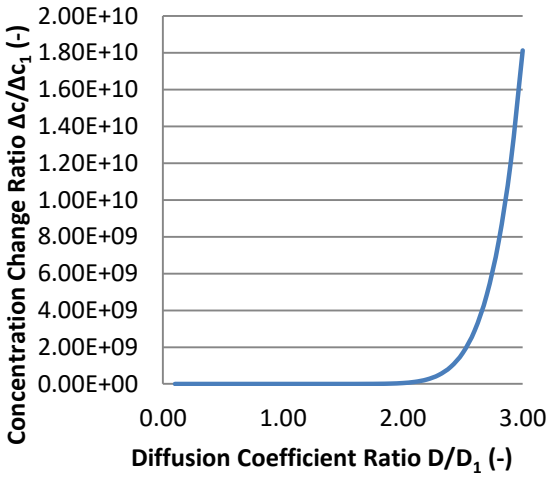

Figure 7.42 – Concentration ratio vs. Diffusion coefficient ratio for $x=0.05\ m$ and $t=5\ hours$

The second discovery was that while a relationship between the concentration ratio and diffusion coefficient ratio could be found, it was highly dependent on both time and distance, as can be seen in Figure 7.43. It is clear from these figures that any function used would need to be complex, and depend on the time and distance as well as the diffusion coefficients. It was concluded that such a function would be as complex as the analytical solution, and would not be suitable therefore for use in the problem reduction schemes. For this reason the numerical approach adopted was preferred due to its simplicity, accuracy and applicability to complex chemical systems, for which the analytical relation would not be suitable.

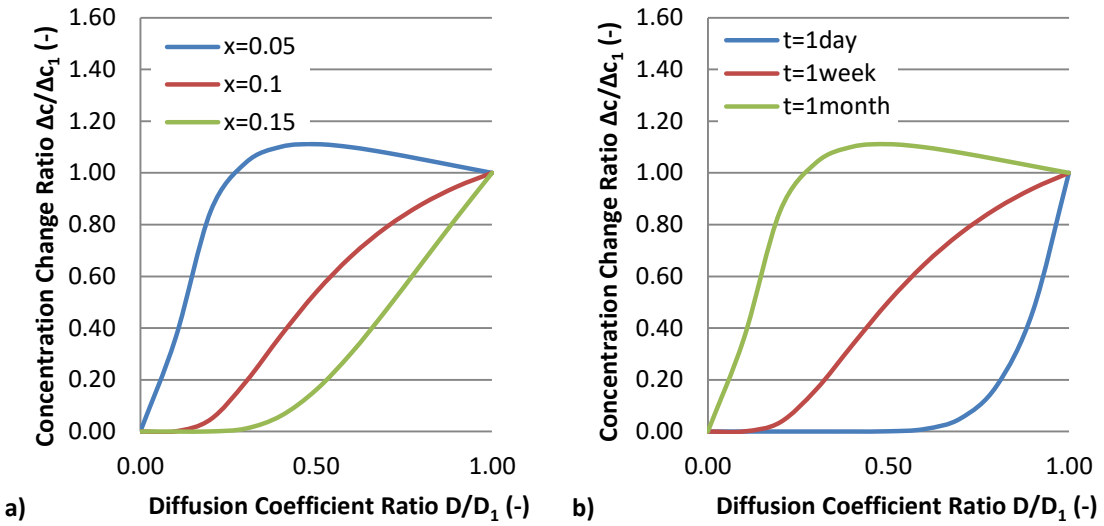

Figure 7.43 - Concentration ratio vs. Diffusion coefficient ratio for a) $t=1\ month$ and b) $x=0.05m$

7.6 Conclusions

The aims of the work described in this chapter were to determine the range of validity PRSs and to validate their predictive capabilities. The determination of the range of applicability of the schemes was achieved through the consideration of an example problem, concerning the advective-diffusive-reactive transport of the chemical species through a mortar specimen. The results showed that the PRSs predicted the profiles most accurately for chemical species found near the indicator species, with the divergence increasing with the relative difference between the current and nearest indicator species. Using these results, the range of applicability of each scheme was defined, based on the criterion that the concentration error should not exceed 25% for any chemical species, relative to the full model predictions. This resulted in the following ranges:

Table 7.20 – Applicable ranges for PRSs

PRS	1	2	3
Diffusion Coefficient Range	$0.8D_{mol}^{ind}<D_{mol}^{i}<1.6D_{mol}^{ind}$	$D_{mol}^{ind,u}<16D_{mol}^{ind,l}$	$D_{mol}^{ind,u}<64D_{mol}^{ind,l}$

The mass balance error introduced was investigated and was found to be both small, and to reduce with time for the example problem. It was suggested that this error could be diminished by reducing the range over which each scheme is applied.

The verification of each of the reduction schemes was then carried out using example simulations found in or based on the literature. PRS 1 was verified against an example from Baroghel-Bouny et al. (2011), which concerned the diffusion of four chemical species into a mortar specimen and the adsorption of the Cl^- ions. The resultant profiles were well matched, with the greatest difference being found in the OH^- profile, corresponding to the release of OH^- ions due to the chemical reaction. PRS 2 was verified against an example from Song et al. (2014), which concerned the diffusion of 6 chemical species within a concrete specimens and consideration of 6 different chemical reactions concerning the adsorption onto the cement matrix. The results were in good agreement with the full model with the largest differences being found in the Na^+ and $CSH.NaCl$ profiles. It was found in this example that as a result of the chemical reactions different results for the indicator species were being predicted by the full model and PRS 2. Finally, PRS 3 was verified against a hypothetical example based on an example found in Zhu et al. (1999) concerning the 2D advective-diffusive transport of 10 chemical species, 1 immobile species and 6 chemical reactions including precipitation of minerals. The results were in good agreement with the biggest differences seen in Cl^-, Na^+ and K^+ profiles. In this example, the solid profiles were predicted more accurately than the concentration profiles; it was thought that this concentration error was reduced by the reaction equations.

The reduction in computational cost was quantified for the considered example problems, through the investigation into the CPU time of the simulations. It was found that the reductions in cost were high for all of the PRSs, with reductions being achieved of over 90 %, with the smallest reductions being over 50 %.

An investigation into the use of an analytical relationship between the concentration and diffusion coefficient ratios was made. It was found that any relationship would be complex and therefore not fit the requirements of the reduction scheme, and so the numerical approach was preferred.

It is concluded from the work described in this chapter that each of the PRSs can successfully be used to reduce the computational cost of a simulation whilst maintaining a suitable accuracy of the results. The accuracy of the solutions can be increased further by reducing the range of diffusion coefficients over which each scheme is applied.

Chapter 8. Conclusions and Future Work

The work of this thesis had two main aims; firstly, to develop a numerical approach to the problem size reduction that would reduce the computational demand associated with the simulation of reactive transport problems; and secondly, to develop an experimental test procedure for the investigation of transport behaviour in cementitious materials, that allowed for different flow conditions and the measurement of transient behaviour, without requiring the removal of the specimen from the test setup. The development of a full coupled model, including the theory upon which it is based and the numerical implementation, was presented in Chapters 3 and 4, with the problem reduction scheme being introduced in Chapter 4. The development of the experimental procedure, including the test setup and concrete mix design, was discussed in Chapter 5.

The conclusions of this thesis are directly linked to the objectives of the study, which are recalled as:

1. Develop a coupled model based on a reliable mathematical framework for the simulation of reactive transport problems in porous media.
2. Investigate the behaviour of the coupled model for different chemical systems, including different boundary conditions, a range of transport behaviour and various reactions to determine the validity of the model.
3. Propose a problem reduction scheme for use in complex multi-ionic systems in order to reduce the computational cost of the simulations.
4. Investigate the problem reduction scheme through an example to determine the range of applicability of each of the approaches, before investigating the behaviour of the schemes for different chemical systems including different boundary conditions, a range of transport behaviour and various reactions to determine the validity of the approach.
5. Develop a simple alternative to column leaching tests for cementitious materials using lab scale concrete beams and carry out tests in order to determine different chemical parameters such as dispersion coefficients, as well as providing data for the validation of the proposed model.

The summary of the work of this study is as follows:

- The mathematical framework upon which the model is based allows for its application to different porous media and a range of chemical systems, including different reaction chemistry and multi-ionic transport. In terms of moisture transport, the model was found to perform well in the prediction of the moisture loss of drying experiments, and predicted accurate transient profiles of the moisture at near to the exposed face. The profile at the interior of the specimens however was under predicted following the initial drying period.
- In a numerically based drying example good agreement was obtained between the prediction of the moisture profiles of the current model and the results from Koniorczyk and Gawin (2012). Greater discrepancies in the prediction of the moisture profiles were found between the model and the results of Koniorczyk (2010). The general trend was in agreement, however the shape of the profiles was not. It was not clear in these examples however which values of the parameters of the moisture flow were used.
- The reactive chemical transport was validated against the experimental results, as well as verified against a number of examples from Baroghel-Bouny et al. (2011) and Song et al. (2014). It was found that the model accurately predicted both the concentration and solid mass profiles and their transient behaviour. The largest differences occurred either when the values of the reaction parameters were unclear, or the chemical in question was found in small concentrations and therefore was perhaps more sensitive to error.
- Three different problem reduction schemes were proposed, each of differing complexity, and each using a different number of indicator species. An investigation was made into the range of validity of each of the reduction schemes through an example problem concerning the advective diffusive reactive transport of 16 chemical species into a mortar specimen. It was found that the schemes had an increasing range of applicability and that PRS 3 covered the whole range of diffusion coefficients considered, which was higher than would normally be found in a real chemical system.

- Each of the reduction schemes were then verified using a single example problem. It was found that the reduction schemes accurately captured the chemical behaviour whilst reducing the number of coupled equations to be solved. The computational cost was investigated in terms of CPU time, which was found to be up to over 90 %.
- The mass balance error introduced through the use of the reduction schemes was investigated, with the maximum for the 16 ion example being around 10 % and showing a decrease with time.
- A simple approach to ion transport experiments was developed through the use of Perspex tanks that allow different heads of water, connected by a sealed concrete beam. The measurements of concentration were taken through the extraction of a pore water sample using a syringe and the tests were accelerated through the design of a porous concrete mix. It was found that the experiments were successful in providing results for the concentration profiles of a salt. A number of problems were encountered throughout the development, the main one being the leaking of the tanks through the seal of the concrete beams to the specimen.

The conclusions of this study are as follows:

1. The full model is able to accurately reproduce the results of experiments and alternative numerical models considering the reactive transport behaviour.
2. The problem reduction schemes were able to accurately capture the transport behaviour as predicted by the full model, whilst achieving reductions in cost of up to 90 % CPU time.
3. The ion transport experiments were successful in providing a simple solution to the problems associated with current approaches. The results obtained, however, were limited.

The suggestions for future research from this study are as follows:

1. Further investigation needs to be made into the performance of the PRSs including both:

a. The validity of the ranges of applicability for different chemical and flow conditions as these may have an effect on the range of diffusion coefficients over which the schemes give accurate results.
b. The mass balance error introduced by the PRSs for different chemical and flow conditions, with particular attention directed to its changes over time.

2. Concerning the ion transport experiments, further investigation is needed into different ways of sealing the beam in place to reduce the occurrence of leaks. It is thought that the use of a rubber gasket may provide an easier and more consistent way of sealing the beams into place.

The suggestions for future research based on the scope and limitations of this study are as follows:

1. The reactions considered were all kinetic and therefore an investigation is needed into the behaviour of the PRSs under chemical equilibrium conditions. Equilibrium reactions are found in a number of chemical systems in both cementitious materials and soils. The inclusion of equilibrium reactions would greatly widen the range of problems and applications for which the PRSs could be used (particularly for geochemical problems where equilibrium reactions are commonly used).
2. The example problems considered did not include temperature changes and neglected the enthalpy change of reactions; further investigation is therefore needed into this area. There is also coupling between the temperature and the chemistry (for example the rate of reactions which depend on temperature, enthalpy change of reactions, and effect of precipitated materials on specific heat of the medium). It is therefore important to investigate the sensitivity of the temperature to the problem chemistry to determine the effect of using the PRSs on the accuracy of the temperature profiles.
3. The effect of the dependence of the diffusion coefficients on both the degree of saturation and the chemical concentration should be investigated. As well as the effect of the chemical activity of the pore water on the transport

mechanisms should be investigated. This is important to determine the performance of the PRSs with an increased degree of coupling between the moisture and chemical phases.

References

Ahmad, S. and Azad, a 2013. An exploratory study on correlating the permeability of concrete with its porosity and tortuosity. *Advances in Cement Research* 25(5), pp. 288–294.

Al-amoudi, O.S.B., Al-kutti, W.A., Ahmad, S. and Maslehuddin, M. 2009. Correlation between compressive strength and certain durability indices of plain and blended cement concretes. *Cement and Concrete Composites* 31(9), pp. 672–676. Available at: http://dx.doi.org/10.1016/j.cemconcomp.2009.05.005.

Aliko-Benítez, A., Doblaré, M. and Sanz-Herrera, J.A. 2015. Chemical-diffusive modelling of the self-healing behavior in concrete. *International Journal of Solids and Structures* 70, pp. 392–402. Available at: http://www.sciencedirect.com/science/article/pii/S0020768315002218.

Allison, J.D., Brown, D.S. and Novo-Gradac, K.J. 1991. Minteqa2/Prodefa2, a Geochemical Assessment Model for Environmental Systems: Version 3.0 User'S Manual. *U. S. Environmental Protection Agency EPA/600/3-91/021* (March), p. 115.

Ashby, S.F. and Falgout, R.D. 1996. A parallel multigrid preconditioned conjugate gradient algorithm for groundwater flow simulations. *Nuclear Science and Engineering* 124, pp. 145–159. Available at: http://cat.inist.fr/?aModele=afficheN&cpsidt=3247969.

Baroghel-Bouny, V., Belin, P., Maultzsch, M. and Henry, D. 2007a. AgNO 3 spray tests : advantages , weaknesses , and various applications to quantify chloride ingress into concrete . Part 1 : AgNO 3 spray tests : advantages , weaknesses , and various applications. *Materials and structures* (2007), pp. 759–781.

Baroghel-Bouny, V., Belin, P., Maultzsch, M. and Henry, D. 2007b. AgNO 3 spray tests : advantages , weaknesses , and various applications to quantify chloride ingress into concrete . Part 2 : Non-steady-state migration tests and chloride diffusion coefficients. *Materials and structures* (2007), pp. 759–781.

Baroghel-Bouny, V., Kinomura, K., Thiery, M. and Moscardelli, S. 2011. Easy assessment of durability indicators for service life prediction or quality control of concretes with high volumes of supplementary cementitious materials. *Cement and Concrete Composites* 33(8), pp. 832–847. Available at: http://dx.doi.org/10.1016/j.cemconcomp.2011.04.007.

Baroghel-Bouny, V., Nguyen, T.Q. and Dangla, P. 2009. Assessment and prediction of RC structure service life by means of durability indicators and physical/chemical models. *Cement and Concrete Composites* 31(8), pp. 522–534. Available at: http://dx.doi.org/10.1016/j.cemconcomp.2009.01.009.

Baroghel-Bouny, V., Thiéry, M. and Wang, X. 2011. Modelling of isothermal coupled moisture-ion transport in cementitious materials. *Cement and Concrete Research* 41(8), pp. 828–841. Available at: http://dx.doi.org/10.1016/j.cemconres.2011.04.001.

Baroghel-Bouny, V., Wang, X., Thiery, M., Saillio, M. and Barberon, F. 2012. Prediction of chloride binding isotherms of cementitious materials by 'analytical' model or

'numerical' inverse analysis. *Cement and Concrete Research* 42(9), pp. 1207–1224. Available at: http://dx.doi.org/10.1016/j.cemconres.2012.05.008.

Bary, B., Ranc, G., Durand, S. and Carpentier, O. 2008. A coupled thermo-hydro-mechanical-damage model for concrete subjected to moderate temperatures. *International Journal of Heat and Mass Transfer* 51(11–12), pp. 2847–2862.

Bear, J. and Bachmat, Y. 1990. *Introduction to modelling of transport phenomena in porous media*. The Netherlands: Kluwer Academic Publishers.

Bear, J. and Verruijt, A. 1987. *Modelling Groundwater Flow and Pollution*. The Netherlands: D. Reidel Publishing Company.

Beisman, J.J., Maxwell, R.M., Navarre-Sitchler, A.K., Steefel, C.I. and Molins, S. 2015. ParCrunchFlow: an efficient, parallel reactive transport simulation tool for physically and chemically heterogeneous saturated subsurface environments. *Computational Geosciences* 19(2), pp. 403–422.

Bertocchi, A.F., Ghiani, M., Peretti, R. and Zucca, A. 2006. Red mud and fly ash for remediation of mine sites contaminated with As, Cd, Cu, Pb and Zn. *Journal of Hazardous Materials* 134(1–3), pp. 112–119.

Boggs, J.M. and Adams, E.E. 1992. Field study of dispersion in a heterogeneous aquifer 4. Investigation of adsorption and sampling bias. *Water Resources Research* 28(12), pp. 3325–3336.

British Standards Institution. 2013. *BS EN 12620:2013. Aggregates for concrete.* London: BSI.

Brooks, R.H. and Corey, a T. 1964. Hydraulic properties of porous media. *Hydrology Papers, Colorado State University. Fort Collins CO* 3(3), p. 27 pgs.

Buckingham, E. 1907. *Studies on the movement of soil moisture*. Bull. 38. Washington D.C.: USDA, Bureau of Soils.

Carrayrou, J., Kern, M. and Knabner, P. 2010. Reactive transport benchmark of MoMaS. *Computational Geosciences* 14(3), pp. 385–392. Available at: http://dx.doi.org/10.1007/s10596-009-9157-7.

Chitez, A.S. and Jefferson, A.D. 2015. Porosity development in a thermo-hygral finite element model for cementitious materials. *Cement and Concrete Research* 78, pp. 216–233. Available at: http://dx.doi.org/10.1016/j.cemconres.2015.07.010.

Chitez, A.S. and Jefferson, A.D. 2016. A coupled thermo-hygro-chemical model for characterising autogenous healing in ordinary cementitious materials. *Cement and Concrete Research* 88, pp. 184–197. Available at: http://dx.doi.org/10.1016/j.cemconres.2016.07.002.

Cleall, P.J. 1998. An investigation into the thermo/hydraulic/mechanical behaviour of unsaturated soils, including expansive clays. Cardiff University.

Cleall, P.J., Seetharam, S.C. and Thomas, H.R. 2007. Inclusion of Some Aspects of

Chemical Behavior of Unsaturated Soil in Thermo/Hydro/Chemical/Mechanical Models. I: Model Development. *Journal of Engineering Mechanics* 133(3), pp. 348–356. Available at: http://ascelibrary.org/doi/abs/10.1061/%28ASCE%290733-9399%282007%29133%3A3%28348%29.

Cleall, P.J., Thomas, H.R., Melhuish, T.A. and Owen, D.H. 2006. Use of parallel computing and visualisation techniques in the simulation of large scale geoenvironmental engineering problems. *Future Generation Computer Systems* 22(4), pp. 460–467. Available at: http://www.scopus.com/inward/record.url?eid=2-s2.0-29644438234&partnerID=40&md5=e97d1ecff92867bbe5a7becd7f140a61.

Conciatori, D., Grégoire, É., Samson, E., Marchand, J. and Chouinard, L. 2013. Statistical analysis of concrete transport properties. *Materials and Structures* 47(1–2), pp. 89–103. Available at: http://link.springer.com/10.1617/s11527-013-0047-z%5Cnpapers2://publication/doi/10.1617/s11527-013-0047-z.

Crank, J. 1975. The mathematics of diffusion. *Oxford University Press*, p. 414.

Davie, C.T., Pearce, C.J. and Bićanić, N. 2006. Coupled Heat and Moisture Transport in Concrete at Elevated Temperatures — Effects of Capillary Pressure and Adsorbed Water. *Numerical Heat Transfer Part A-Applications* 49(8), pp. 733–763.

Davie, C.T., Pearce, C.J. and Bićanić, N. 2010. A fully generalised, coupled, multi-phase, hygro-thermo-mechanical model for concrete. *Materials and structures* 43, pp. 13–33.

Debye, P. and Hückel, E. 1923. The Theory of Electrolytes I. Lowering of Freezing Point and Related Phenomena. *Physikalische Zeitschrift* 24, pp. 185–206.

Domenico, P.A. and Robbins, G.A. 1984. A dispersion scale effect in model calibrations and field tracer experiments. *Journal of Hydrology* 70, pp. 123–132.

Edlefsen, N.E. and Anderson, A.B.C. 1943. Thermodynamics of soil moisture. *Hilgardia* 15, pp. 31–298. Available at: http://hilgardia.ucanr.edu/Abstract/?a=hilg.v15n02p031.

Engesgaard, P. and Kipp, K.L. 1992. A geochemical transport model for redox-controlled movement of mineral fronts in groundwater flow systems: A case of nitrate removal by oxidation of pyrite. *Water Resources Research* 28(10), pp. 2829–2843.

Fetter C., W. 1998. *Contaminant Hydrogeology*. 2nd ed. USA: Prentice-Hall.

Francy, O. 1998. Modelling of chloride ions ingress in partially water saturated mortars. Paul Sabatier University.

Fredlund, D.G. and Rahardjo, H. 1993. Soil Mechanics for Unsaturated Soils. *Stress The International Journal on the Biology of Stress*, p. 517. Available at: http://books.google.com/books?hl=en&lr=&id=ltVtPOGuJJwC&oi=fnd&pg=PA1&dq=Soil+Mechanics+for+Unsaturated+Soils&ots=XIsVieTOHf&sig=7le-tXP6NbjK3xG0WUbc8JpXhJY.

Friedly, J.C. 1991. Extent of reaction in open systems with multiple heterogeneous reactions. *AIChE Journal* 37(5), pp. 687–693. Available at:

http://dx.doi.org/10.1002/aic.690370507.

Friedly, J.C. and Rubin, J. 1992. Solute transport with multiple equilibrium controlled or kinetically controlled chemical reactions. *Water Resources Research* 28, pp. 1935–1953.

Frind, E.O., Duynisveld, W.H.M., Strebel, O. and Boettcher, J. 1990. Modeling of multicomponent transport with microbial transformation in groundwater: The Fuhrberg Case. *Water Resources Research* 26(8), pp. 1707–1719. Available at: http://doi.wiley.com/10.1029/WR026i008p01707 [Accessed: 29 May 2017].

Galerkin, B.G. 1915. Series solution of some problems in elastic equilibrium of rods and plates. *Vestnik inzhenerov i tekhnikov* (19), pp. 897–908.

Gardner, D.R., Jefferson, A.D. and Lark, R.J. 2008. An experimental, numerical and analytical investigation of gas flow characteristics in concrete. *Cement and Concrete Research* 38(3), pp. 360–367. Available at: http://www.scopus.com/inward/record.url?eid=2-s2.0-38349129369&partnerID=40&md5=b4a2967bf5ed5744989b8fa5944b1221.

Gawin, D., Majorana, C.E. and Schrefler, B.A. 1999. Numerical analysis of hygrol thermal behaviour and damage of concrete at high temperature. *Mechanics of Cohesive-frictional Materials* 4(1), pp. 37–74. Available at: http://doi.wiley.com/10.1002/(SICI)1099-1484(199901)4:1%3C37::AID-CFM58%3E3.0.CO;2-S.

Gawin, D., Pesavento, F. and Schrefler, B.A. 2006. Hygro-thermo-chemo-mechanical modelling of concrete at early ages and beyond. Part I: hydration and hygro-thermal phenomena. *International Journal for Numerical Methods in Engineering* 67(3), pp. 299–331. Available at: http://dx.doi.org/10.1002/nme.1615.

Gawin, D., Pesavento, F. and Schrefler, B.A. 2009. Modeling deterioration of cementitious materials exposed to calcium leaching in non-isothermal conditions. *Computer Methods in Applied Mechanics and Engineering* 198(37–40), pp. 3051–3083. Available at: http://dx.doi.org/10.1016/j.cma.2009.05.005.

Gawin, D., Pesavento, F. and Schrefler, B.A. 2011a. What physical phenomena can be neglected when modelling concrete at high temperature? A comparative study. Part 1: Physical phenomena and mathematical model. *International Journal of Solids and Structures* 48(13), pp. 1927–1944. Available at: http://dx.doi.org/10.1016/j.ijsolstr.2011.03.004.

Gawin, D., Pesavento, F. and Schrefler, B.A. 2011b. What physical phenomena can be neglected when modelling concrete at high temperature? A comparative study. Part 2: Comparison between models. *International Journal of Solids and Structures* 48(13), pp. 1945–1961. Available at: http://dx.doi.org/10.1016/j.ijsolstr.2011.03.003.

Gawin, D., Schrefler, B.A. and Galindo, M. 1996. Thermo-hydro-mechanical analysis of partially saturated porous materials. *Engineering Computations* 13(7), pp. 113–143. Available at: http://dx.doi.org/10.1108/02644409610151584.

Gens, A., do N. Guimarães, L., Olivella, S. and Sánchez, M. 2004. Analysis of the Thmc Behaviour of Compacted Swelling Clay for Radioactive Waste Isolation. In: Stephanson, O. ed. *Coupled Thermo-Hydro-Mechanical-Chemical Processes in Geo-SystemsFundamentals, Modelling, Experiments and Applications*. Elsevier Geo-Engineering Book Series. Elsevier, pp. 317–322.

van Genuchten, M.T. 1980. A Closed-form Equation for Predicting the Hydraulic Conductivity of Unsaturated Soils. *Soil Science Society of America Journal* 44(5), p. 892.

Hartley, W., Edwards, R. and Lepp, N.W. 2004. Arsenic and heavy metal mobility in iron oxide-amended contaminated soils as evaluated by short- and long-term leaching tests. *Environmental Pollution* 131(3), pp. 495–504.

Hassanizadeh, M. and Gray, W.G. 1979. General conservation equations for multi-phase systems: 1. Averaging procedure. *Advances in Water Resources* 2(C), pp. 131–144.

Hillel, D. 1980. *Fundamentals of soil physics*. San Diego, Calif.: Academic.

Hoffmann, J., Kräutle, S. and Knabner, P. 2012. A general reduction scheme for reactive transport in porous media. *Computational Geosciences* 16(4), pp. 1081–1099.

Huo, J.X., Song, H.Z. and Wu, Z.W. 2014. Multi-component reactive transport in heterogeneous media and its decoupling solution. *Journal of Contaminant Hydrology* 166, pp. 11–22. Available at: http://dx.doi.org/10.1016/j.jconhyd.2014.07.009.

Irmay, S. 1954. On the hydraulic conductivity of unsaturated soils. *Eos, Transactions American Geophysical Union* 35(3), pp. 1–5.

Khan, A.U.H. and Jury, W.A. 1990. A laboratory study of the dispersion scale effect in column outflow experiments. *Journal of Contaminant Hydrology* 5(2), pp. 119–131.

Kim, J.K. and Lee, C.S. 1999. Moisture diffusion of concrete considering self-desiccation at early ages. *Cement and Concrete Research* 29(12), pp. 1921–1927.

Kim, Y.Y., Lee, K.M., Bang, J.W. and Kwon, S.J. 2014. Effect of W/C ratio on durability and porosity in cement mortar with constant cement amount. *Advances in Materials Science and Engineering* 2014.

Koniorczyk, M. 2010. Modelling the phase change of salt dissolved in pore water - Equilibrium and non-equilibrium approach. *Construction and Building Materials* 24(7), pp. 1119–1128. Available at: http://dx.doi.org/10.1016/j.conbuildmat.2009.12.031.

Koniorczyk, M. 2012. Salt transport and crystallization in non-isothermal, partially saturated porous materials considering ions interaction model. *International Journal of Heat and Mass Transfer* 55(4), pp. 665–679. Available at: http://dx.doi.org/10.1016/j.ijheatmasstransfer.2011.10.043.

Koniorczyk, M. and Gawin, D. 2008. Heat and Moisture Transport in Porous Building Materials Containing Salt. *Journal of Building Physics* 31(4), pp. 279–300.

Koniorczyk, M. and Gawin, D. 2011. Numerical Modeling of Salt Transport and

Precipitation in Non-Isothermal Partially Saturated Porous Media Considering Kinetics of Salt Phase Changes. *Transport in Porous Media* 87(1), pp. 57–76.

Koniorczyk, M. and Gawin, D. 2012. Modelling of salt crystallization in building materials with microstructure - Poromechanical approach. *Construction and Building Materials* 36, pp. 860–873. Available at: http://dx.doi.org/10.1016/j.conbuildmat.2012.06.035.

Koniorczyk, M., Gawin, D. and Schrefler, B.A. 2015. Modeling evolution of frost damage in fully saturated porous materials exposed to variable hygro-thermal conditions. *Computer Methods in Applied Mechanics and Engineering* 297, pp. 38–61. Available at: http://dx.doi.org/10.1016/j.cma.2015.08.015.

Koniorczyk, M. and Wojciechowski, M. 2009. Influence of salt on desorption isotherm and hygral state of cement mortar - Modelling using neural networks. *Construction and Building Materials* 23(9), pp. 2988–2996. Available at: http://dx.doi.org/10.1016/j.conbuildmat.2009.05.001.

Kräutle, S. 2008. General Multi-Species Reactive Transport Problems in Porous Media : Efficient Numerical Approaches and Existence of Global Solutions.

Kräutle, S. and Knabner, P. 2005. A new numerical reduction scheme for fully coupled multicomponent transport-reaction problems in porous media. *Water Resources Research* 41(9), pp. 1–17.

Kräutle, S. and Knabner, P. 2007. A reduction scheme for coupled multicomponent transport-reaction problems in porous media: Generalization to problems with heterogeneous equilibrium reactions. *Water Resources Research* 43(3).

Krueger, C.J., Radakovich, K.M., Sawyer, T.E., Barber, L.B., Smith, R.L. and Field, J.A. 1998. Biodegradation of the surfactant linear alkylbenzenesulfonate in sewage-contaminated groundwater: A comparison of column experiments and field tracer tests. *Environmental Science and Technology* 32(24), pp. 3954–3961.

Kuhl, D., Bangert, F. and Meschke, G. 2004. Coupled chemo-mechanical deterioration of cementitious materials. Part I: Modeling. *International Journal of Solids and Structures* 41(1), pp. 15–40.

Kulik, D.A., Wagner, T., Dmytrieva, S. V, Kosakowski, G., Hingerl, F.F., Chudnenko, K. V and Berner, U. 2012. GEM-Selektor geochemical modeling package: Numerical kernel GEMS3K for coupled simulation codes. *Computational Geosciences* 17(1), pp. 1–24.

Lagneau, V. and van der Lee, J. 2010. HYTEC results of the MoMaS reactive transport benchmark. *Computational Geosciences* 14(3), pp. 435–449.

Lasaga, A.C. 1981. The treatment of multicomponent diffusion and ion pairs in diagenetic fluxes: further comments and clarification. *American Journal of Science* 281(7), pp. 981–988.

Lewis, G.N., Randall, M., Pitzer, K.S. and Brewer, L. 1961. *Thermodynamics. 2nd edition.* New York, N.Y.: McGraw Hill.

Lewis R., W. and Schrefler B., A. 1998. *The finite element method in the static and dynamic deformation and consolidation of porous media*. 2nd ed. Great Britian: John Wiley and Sons Inc.

Lichtner, P.C. 1985. Continuum model for simultaneous chemical reactions and mass transport in hydrothermal systems. *Geochimica et Cosmochimica Acta* 49(3), pp. 779–800.

Liu, D., Jivkov, A.P., Wang, L., Si, G. and Yu, J. 2017. Non-Fickian dispersive transport of strontium in laboratory-scale columns: Modelling and evaluation. *Journal of Hydrology* 549, pp. 1–11. Available at: http://linkinghub.elsevier.com/retrieve/pii/S0022169417302032.

Matthäi, S.K., Geiger, S. and Roberts, S.G. 2001. Complex Systems Platform CSP3D3.0. (c).

Mayer, K.U. and MacQuarrie, K.T.B. 2010. Solution of the MoMaS reactive transport benchmark with MIN3P---model formulation and simulation results. *Computational Geosciences* 14(3), pp. 405–419. Available at: http://dx.doi.org/10.1007/s10596-009-9158-6.

McCutcheon, S.C., Martin, J.L. and Barnwell, T.O.J. 1993. Water Quality. In: Maidment, D. R. ed. *Handbook of Hydrology*. McGraw-Hill, pp. 346–414.

Mitchell, J.K. 1993. *Fundamentals of Soil Behavior*. Wiley.

Molins, S., Carrera, J., Ayora, C. and Saaltink, M.W. 2004. A formulation for decoupling components in reactive transport problems. *Water Resources Research* 40(10), pp. 1–13.

de Morais, M.V.G., Bary, B., Ranc, G., Pont, S.D. and Durand, S. 2009. Comparative Analysis of Coupled Thermo-Hydro-Mechanical Models for Concrete Exposed to Moderate Temperatures. *Numerical Heat Transfer Part A-Applications* 55(7), pp. 654–682. Available at: http://www.informaworld.com/smpp/content~db=all?content=10.1080/10407780902821516%5Cnpapers2://publication/doi/10.1080/10407780902821516.

Mualem, Y. 1976. A new model for predicting the hydraulic conductivity of unsaturated porous media. *Water Resources Research* 12(3), pp. 564–566.

Neithalath, N., Weiss, J. and Olek, J. 2006. Characterizing Enhanced Porosity Concrete using electrical impedance to predict acoustic and hydraulic performance. *Cement and Concrete Research* 36(11), pp. 2074–2085.

Netherlands Standardisation Institute. 1995. *NEN 7473. Leaching Characteristics of Solid Earthy and Stony Building and Waste Materials. Leaching Tests. Determination of the Leaching of Inorganic Components from Granular Materials with the Column Test.* Delft: NEN.

Nitao, J.J. and Bear, J. 1996. Potentials and their role in transport in porous media. *Water Resources Research* 32(2), pp. 225–250. Available at:

http://www.scopus.com/inward/record.url?eid=2-s2.0-0029744202&partnerID=40&md5=70ddc224a11eeeb3f42606fad3f3f752.

Nordtest. 1999. *NT Build 492. Concrete, mortar and cement-based repair materials: Chloride migration coefficient from non-steady-state migration experiments.* Espoo: Nordtest.

Parkhurst, D. l., Kipp, K. l. and Charlton, S. r. 2010. PHAST Version 2 - A program for simulating groundwater flow, solute transport, and multicomponent geochemical reactions. *Modeling Techniques, Book 6*, pp. 1–181. Available at: http://pubs.usgs.gov/tm/06A35/.

Parkhurst, D.L. and Wissmeier, L. 2015. PhreeqcRM: A reaction module for transport simulators based on the geochemical model PHREEQC. *Advances in Water Resources* 83, pp. 176–189. Available at: http://www.sciencedirect.com/science/article/pii/S0309170815001268.

Philip, J.R. and De Vries, D.A. 1957. Moisture movement in porous materials under temperature gradients. *Eos, Transactions American Geophysical Union* 38(2), pp. 222–232.

Pitzer, K.S. 1973. Thermodynamics of Electrolytes. I. Theoretical Basis and General Equations. *The Journal of Physical Chemistry* 77(2), pp. 268–277. Available at: http://pubs.acs.org/doi/abs/10.1021/j100621a026.

Pitzer, K.S. and Mayorga, G. 1973. Thermodynamics of electrolytes II. Activity and osmotic coefficients for strong electrolytes with one or both ions univalent. *Journal of Chemical Information and Modeling* 77(19), pp. 2300–2308.

Rees, S.W., Adjali, M.H., Zhou, Z., Davies, M. and Thomas, H.R. 2000. Ground heat transfer effects on the thermal performance of earth-contact structures. *Renewable & sustainable energy reviews* 4(3), pp. 213–265.

Richards, L.A. 1931. Capillary conduction of liquids through porous mediums. *Journal of Applied Physics* 1(5), pp. 318–333.

Robbins, G.A. 1989. Methods for determining transverse dispersion coefficients of porous media in laboratory column experiments. *Water Resources Research* 25(6), pp. 1249–1258.

Rubin, J. 1983. Transport of reacting solutes in porous media: Relation between mathematical nature of problem formulation and chemical nature of reactions. *Water Resources Research* 19(5), pp. 1231–1252.

Rubin, J. and James, R. V 1973. Dispersion-affected transport of reactive solutes in saturated porous media: Galerkin method applied to equilibrium-controlled exchange in unidirectional steady state water flow. *Water Resour. Res.* 9(5), pp. 1332–1356.

Saaltink, M.W., Carrera, J. and Ayora, C. 2001. On the behavior of approaches to simulate reactive transport. *Journal of Contaminant Hydrology* 48(3–4), pp. 213–235.

Samson, E. and Marchand, J. 2007a. Modeling the effect of temperature on ionic transport in cementitious materials. *Cement and Concrete Research* 37(3), pp. 455–468.

Samson, E. and Marchand, J. 2007b. Modeling the transport of ions in unsaturated cement-based materials. *Computers and Structures* 85(23–24), pp. 1740–1756.

De Schutter, G. and Taerwe, L. 1995. General hydration model for portland cement and blast furnace slag cement. *Cement and Concrete Research* 25(3), pp. 593–604.

Song, H.W., Lee, C.H. and Ann, K.Y. 2008. Factors influencing chloride transport in concrete structures exposed to marine environments. *Cement and Concrete Composites* 30(2), pp. 113–121.

Song, Z., Jiang, L., Chu, H., Xiong, C., Liu, R. and You, L. 2014. Modeling of chloride diffusion in concrete immersed in CaCl2 and NaCl solutions with account of multi-phase reactions and ionic interactions. *Construction and Building Materials* 66, pp. 1–9. Available at: http://dx.doi.org/10.1016/j.conbuildmat.2014.05.026.

Steefel, C.I., Appelo, C.A.J., Arora, B., Jacques, D., Kalbacher, T., Kolditz, O., Lagneau, V., Lichtner, P.C., et al. 2015. *Reactive transport codes for subsurface environmental simulation*.

Steiger, M., Kiekbusch, J. and Nicolai, A. 2008. An improved model incorporating Pitzer's equations for calculation of thermodynamic properties of pore solutions implemented into an efficient program code. *Construction and Building Materials* 22(8), pp. 1841–1850.

Sun, G., Zhang, Y., Sun, W., Liu, Z. and Wang, C. 2011. Multi-scale prediction of the effective chloride diffusion coefficient of concrete. *Construction and Building Materials* 25(10), pp. 3820–3831. Available at: http://dx.doi.org/10.1016/j.conbuildmat.2011.03.041.

Thomas, H.R., Cleall, P.J., Li, Y., Harris, C. and Kern-Luetschg, M. 2009. Modelling of cryogenic processes in permafrost and seasonally frozen soils. *Geotechnique* (3), pp. 173–184. Available at: http://orca.cf.ac.uk/8408/.

Thomas, H.R. and He, Y. 1995. Analysis of coupled heat, moisture and air transfer in a deformable unsaturated soil. *Géotechnique* 45(4), pp. 677–689. Available at: http://dx.doi.org/10.1680/geot.1995.45.4.677.

Thomas, H.R. and He, Y. 1997. A coupled heat–moisture transfer theory for deformable unsaturated soil and its algorithmic implementation. *International Journal for Numerical Methods in Engineering* 40(18), pp. 3421–3441. Available at: http://dx.doi.org/10.1002/(SICI)1097-0207(19970930)40:18%3C3421::AID-NME220%3E3.0.CO;2-C%5Cnhttp://onlinelibrary.wiley.com/store/10.1002/(SICI)1097-0207(19970930)40:18%3C3421::AID-NME220%3E3.0.CO;2-C/asset/220_ftp.pdf?v=1&t=hd68fgbc&s=eda2fdc2a06a854b1c67.

Thomas, H.R., Sedighi, M. and Vardon, P.J. 2012. Diffusive Reactive Transport of Multicomponent Chemicals Under Coupled Thermal, Hydraulic, Chemical and

Mechanical Conditions. *Geotechnical and Geological Engineering* 30(4), pp. 841–857.

Thompson, J.B. 1982a. Composition space; an algebraic and geometric approach. *Reviews in Mineralogy and Geochemistry* 10(1), pp. 1–31. Available at: http://rimg.geoscienceworld.org/content/10/1/1.

Thompson, J.B. 1982b. Reaction space; an algebraic and geometric approach. *Reviews in Mineralogy and Geochemistry* 10(1), pp. 33–52. Available at: http://rimg.geoscienceworld.org/content/10/1/33.

Tie-hang, W. and Li-jun, S. 2009. Equation for Calculating Change in Moisture Content Caused by Water Vapor Transfer in Unsaturated Soil. *Journal of Hydrologic Engineering* 14(11), pp. 1235–1239.

Truc, O., Ollivier, J.P. and Carcassès, M. 2000. New way for determining the chloride diffusion coefficient in concrete from steady state migration test. *Cement and Concrete Research* 30(2), pp. 217–226.

Valocchi, A.J. and Malmstead, M. 1992. Accuracy of operator splitting for Advection-Dispersion-Reaction Problems. *Water Resources Research* 28(5), pp. 1471–1476.

Valocchi, A.J., Street, R.L. and Roberts, P. V 1981. Transport of ion-exchanging solutes in groundwater: Chromatogrphoc theory and field simulation. *Water Resources Research* 17(5), pp. 1517–1527.

Walter, A.L., Frind, E.O., Blowes, D.W., Ptacek, C.J. and Molson, J.W. 1994. Modeling of multicomponent reactive transport in groundwater. 1.Model development and evaluation. *Water Resources Research* 30(1), pp. 3137–3148.

Wierenga, P.J. and Van Genuchten, M.T. 1989. Solute transport through small and large unsaturated soil columns. *Ground Water* 27(1), pp. 35–42.

Xu, T., Spycher, N. and Sonnenthal, E. 2012. TOUGHREACT User's Guide: A Simulation Program for Non-isothermal Multiphase Reactive Transport in Variably Saturated Geologic Media, version 2.0. *Lawrence Berkeley …* (October), pp. 1–5. Available at: http://esd.lbl.gov/FILES/research/projects/tough/documentation/TOUGHREACT_V2_Users_Guide.pdf.

Yamamoto, H., Nakajima, K., Zhang, K. and Nanai, S. 2014. Performance of parallel simulators on peta-scale platforms for coupled multi-physics modelling of CO2 geologic sequestration. *Energy Procedia* 63, pp. 3795–3804. Available at: http://dx.doi.org/10.1016/j.egypro.2014.11.408.

Yamamoto, H., Zhang, K., Karasaki, K., Marui, A., Uehara, H. and Nishikawa, N. 2009. Large-scale numerical simulation of CO2 geologic storage and its impact on regional groundwater flow: A hypothetical case study at Tokyo Bay, Japan. *Energy Procedia* 1(1), pp. 1871–1878. Available at: http://dx.doi.org/10.1016/j.egypro.2009.01.244.

Yang, C.C., Cho, S.W. and Wang, L.C. 2006. The relationship between pore structure and chloride diffusivity from ponding test in cement-based materials. *Materials Chemistry and Physics* 100(2–3), pp. 203–210.

Yang, J. and Jiang, G. 2003. Experimental study on properties of pervious concrete pavement materials. *Cement and Concrete Research* 33(3), pp. 381–386.

Yapparova, A., Gabellone, T., Whitaker, F., Kulik, D.A. and Matthäi, S.K. 2017. Reactive Transport Modelling of Dolomitisation Using the New CSMP++GEM Coupled Code: Governing Equations, Solution Method and Benchmarking Results. *Transport in Porous Media* 117(3), pp. 385–413.

Yeh, G. and Tripathi, V.S. 1991. A Model for Simulating Transport of Reactive Multispecies Components: Model Development and Demonstration. *Water Resources Research* 27(12), pp. 3075–3094.

Yeh, G.T. and Tripathi, V.S. 1989. A critical evaluation of recent developments in hydrogeochemical transport models of reactive mutichemical components. *Water Resources Research* 25(1), pp. 93–108.

Zhang, K., Doughty, C., Wu, Y., Pruess, K. and Berkeley, L. 2007. Efficient Parallel Simulation of CO 2 Geologic Sequestration in Saline Aquifers. In: *SPE 106026*. pp. 26–28.

Zhu, C., Fang, H., Anderson, G. and Burden, D. 1999. Reactive mass transport modeling of natural attenuation of an acid plume at a uranium mill tailings site. *Abstracts with Programs - Geological Society of America* 31, pp. 69–70.

Zienkiewicz, O.C., Taylor, R.L. and Zhu, J.Z. 2013. *Finite Element Method: Its Basis and Fundamentals*. Elsevier, Inc.

Appendices

A1 – Model Parameters

The model parameters used throughout this thesis can be seen in Table A1.

Table A1 – Model Parameters

Parameter		Value
D_d **(eq. 3.33)**	α_L [a]	1.4×10^{-4}
	α_T [a]	1.4×10^{-5}
D_v **(eq. 3.24)**	D_{v0} [b] (m^2/s)	2.47×10^{-5}
	f_s [c]	0.01
	A_v [c]	1.0
	B_v [c]	1.667
k_t **(eq. 3.30)**	k_{t0} [c] $(W/m*K)$	1.7
	A_λ [c]	5×10^{-4}
K_{int} **(eq. 3.17)**	A_k [c]	5×10^{-3}
μ_w **(eq. 3.16)**	A_1 [d]	1.85
	A_2 [d]	4.1
	A_3 [d]	44.5
ρ_{vs} **(eq. 3.14)**	b_1 [e]	133.322
	b_2 [e]	8.07131
	b_3 [e]	1730.63
	b_4 [e]	233.426
	b_5 [e]	273
ρ_w **(eq. 3.15)**	a_1 [e]	1000
	a_2 [e]	288.94
	a_3 [e]	3.99
	a_4 [e]	50892.92
	a_5 [e]	68.13
$\overline{\rho C}$ **(eq. 3.28)**	C_{ps} [f] $(J/(K*kg)$	820
	C_{pw} [f] $(J/(K*kg)$	4050
	C_{pg} [g] $(J/(K*kg)$	1400
$g\ (m/s^2)$		9.81
$P_{atm}\ (Pa)$		101325
$R\ (J/K*kmol)$		8314.37
T_r [c] (K)		293
ρ_s [h] (kg/m^3)		2400

[a] Taken from (Fetter 1998)
[b] Taken from (Baroghel-Bouny et al. 2011)
[c] Taken from (Gawin et al. 1999)
[d] Taken from (Koniorczyk 2010)
[e] Taken from (Chitez and Jefferson 2016)
[f] Taken from (Bary et al. 2008)
[g] Taken from (Chitez and Jefferson 2015)
[h] Taken from (Samson and Marchand 2007a)

A2 – PRS Results

Calibration Problem

The example problem presented here is similar to that of Chapter 7 section 7.2 but without the exposed right hand side. The problem geometry and finite element mesh can be seen in Figure A1. The boundary conditions can be seen in Table A2. The model and chemical parameters used can be seen in Tables A3 and A4.

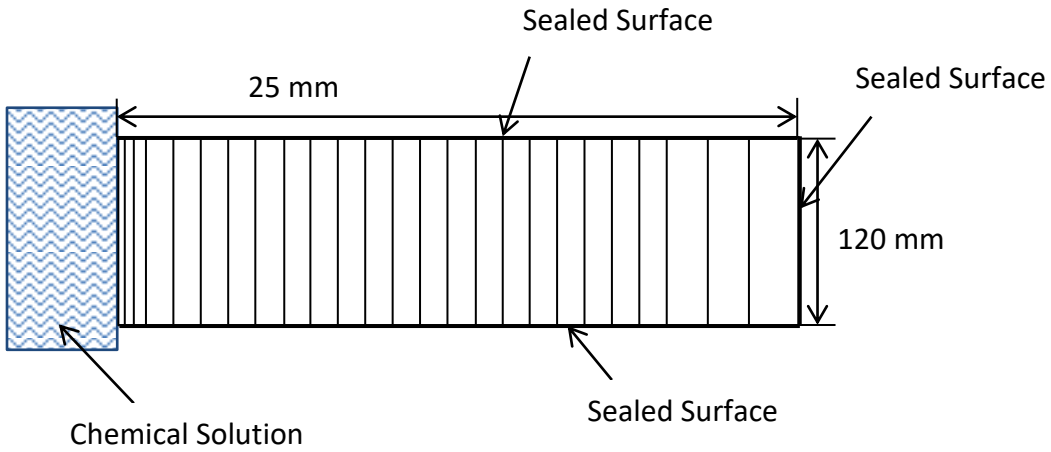

Figure A1 – Finite element mesh and problem geometry (not to scale)

Table A2 – Boundary conditions

Boundary	Boundary Type	Values
LHS	Cauchy	*RH=100 %, T=293 K, c=0.001 kg/kg**
Bottom	Sealed	-
RHS	Sealed	-
Top	Sealed	-

*Same for all species

Table A3 – Model parameters

Parameter	Value
μ	0.008
λ	2.0
n	0.13
β_c (m/s)	2.5×10^{-3}
γ_c (kg/m²s)	1×10^{-4}
ω_c (W/m²K)	8.0
K_{i0} (10^{-21} m²)	35.0
A_w	2.0

Table A4 – Chemical parameters

Species	D_{mol} $(10^{-10}\ m^2/s)$	Species (cont'd)	D_{mol} $(10^{-10}\ m^2/s)$
1	0.25	*9*	6
2	0.5	*10*	7
3	1	*11*	8
4	1.5	*12*	9
5	2	*13*	10
6	3	*14*	12
7	4	*15*	14
8	5	*16*	16

Non-reactive Diffusion

The first case considered the above boundary conditions with no chemical reactions. The profiles as predicted by the full model and PRS 1-3 can be seen in Figures A2, A3 & A4.

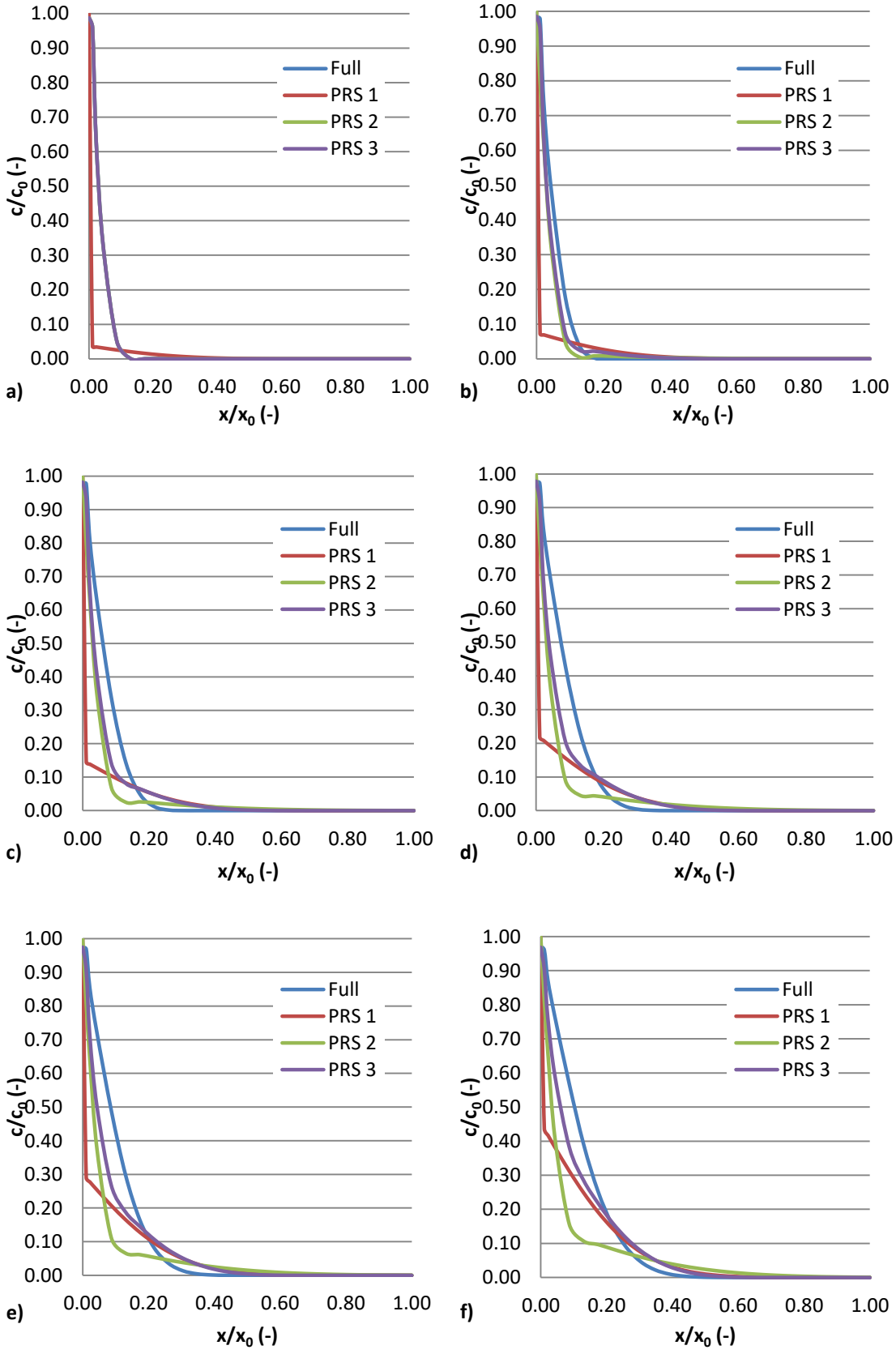

Figure A2 - Concentration profiles predicted by full model and PRS 1-3 (t=24 hours) species number: a) *1*, b) *2*, c) *3*, d) *4*, e) *5* and f) *6*

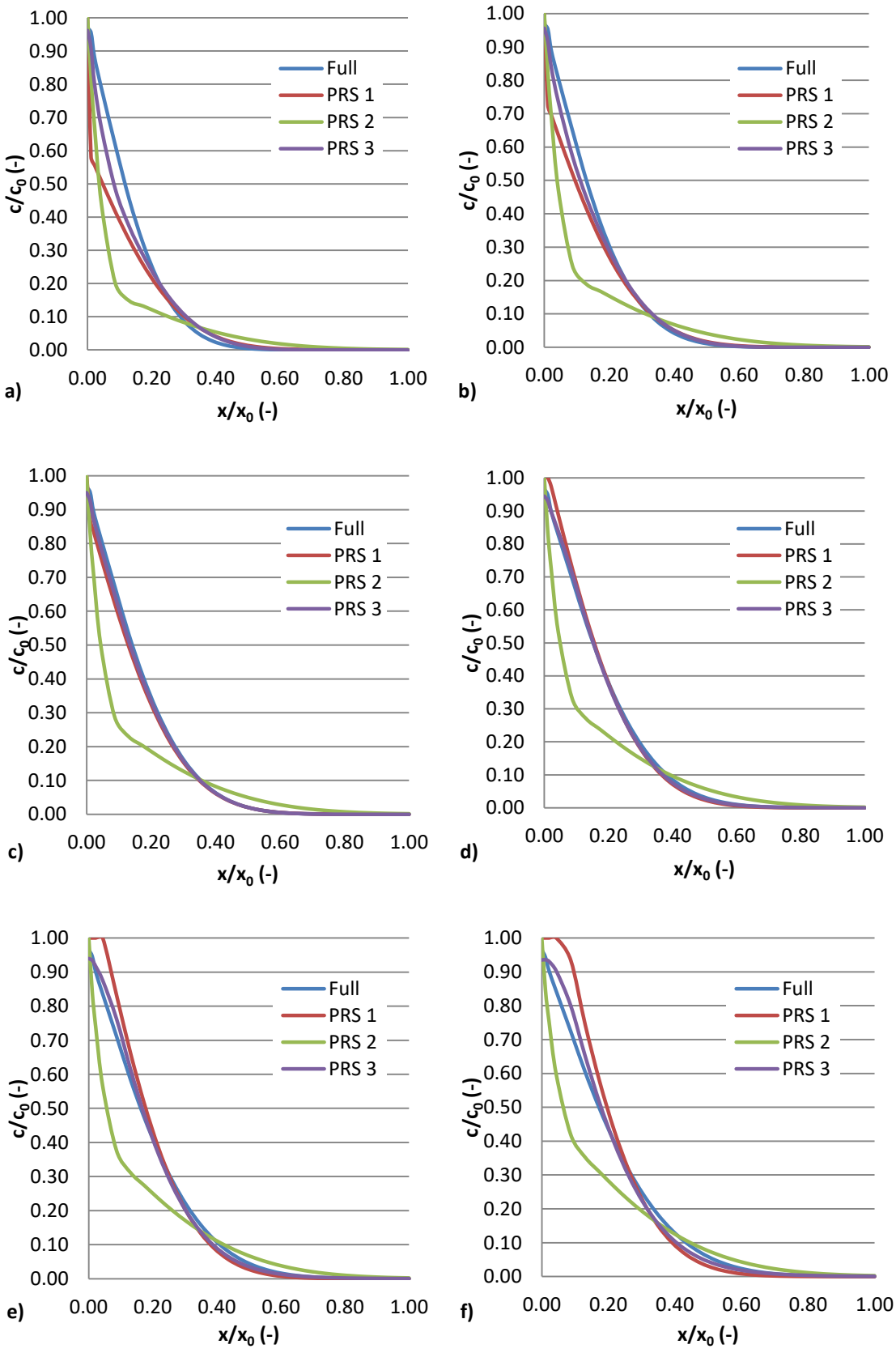

Figure A3 - Concentration profiles predicted by full model and PRS 1-3 (t=24 hours) species number: a) *7*, b) *8*, c) *9*, d) *10*, e) *11* and f) *12*

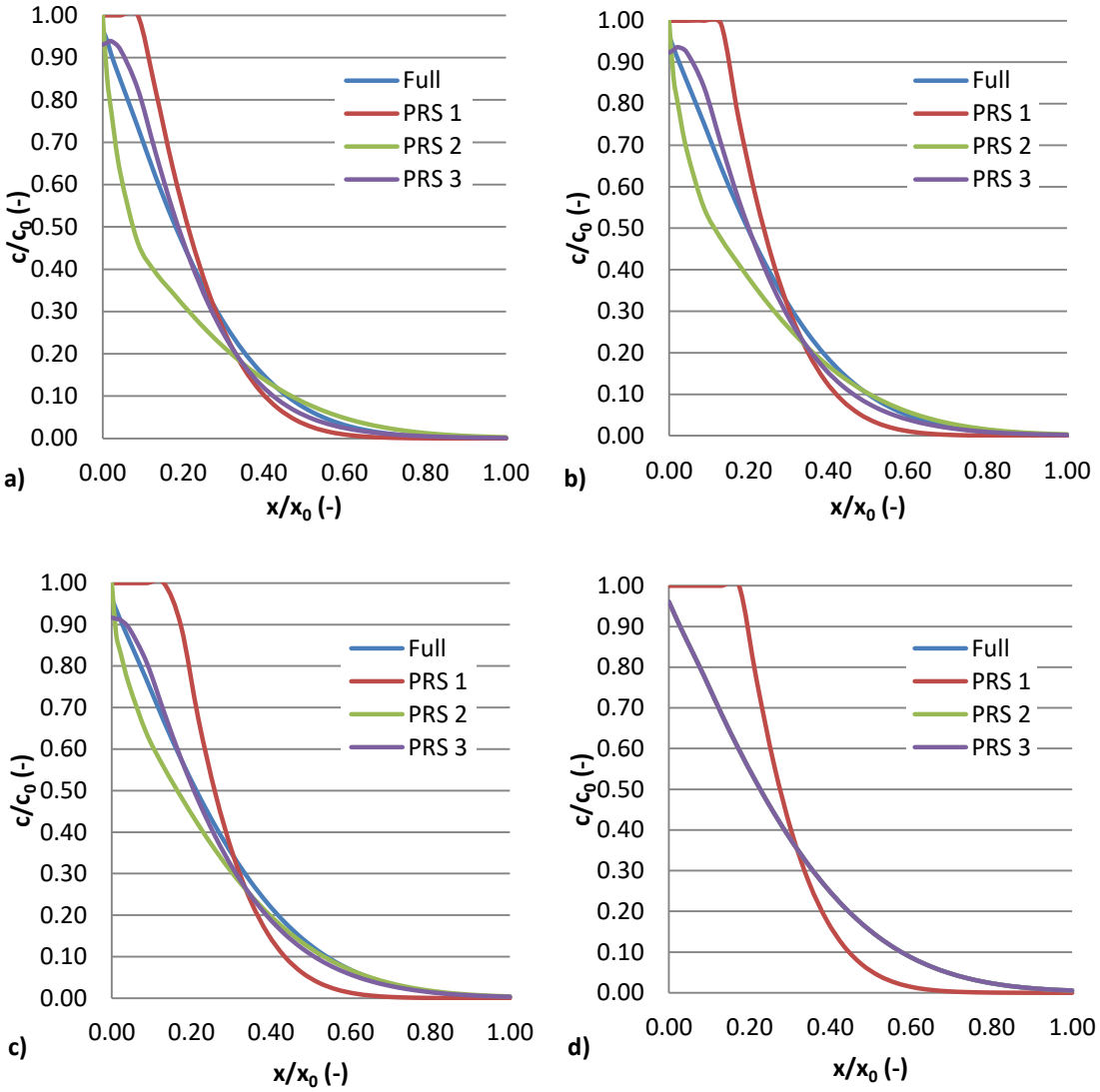

Figure A4 - Concentration profiles predicted by full model and PRS 1-3 (t=24 hours) species number: a) *13*, b) *14*, c) *15* and d) *16*

Reactive Diffusion

The next case considered was as above but with sorption reactions, as described by the Freundlich isotherm (eq. 3.39) with an assumption of non-equilibrium conditions. The predicted profiles for the full model and PRS 1-3 can be seen in Figures A5, A6, A7, A8, A9 & A10.

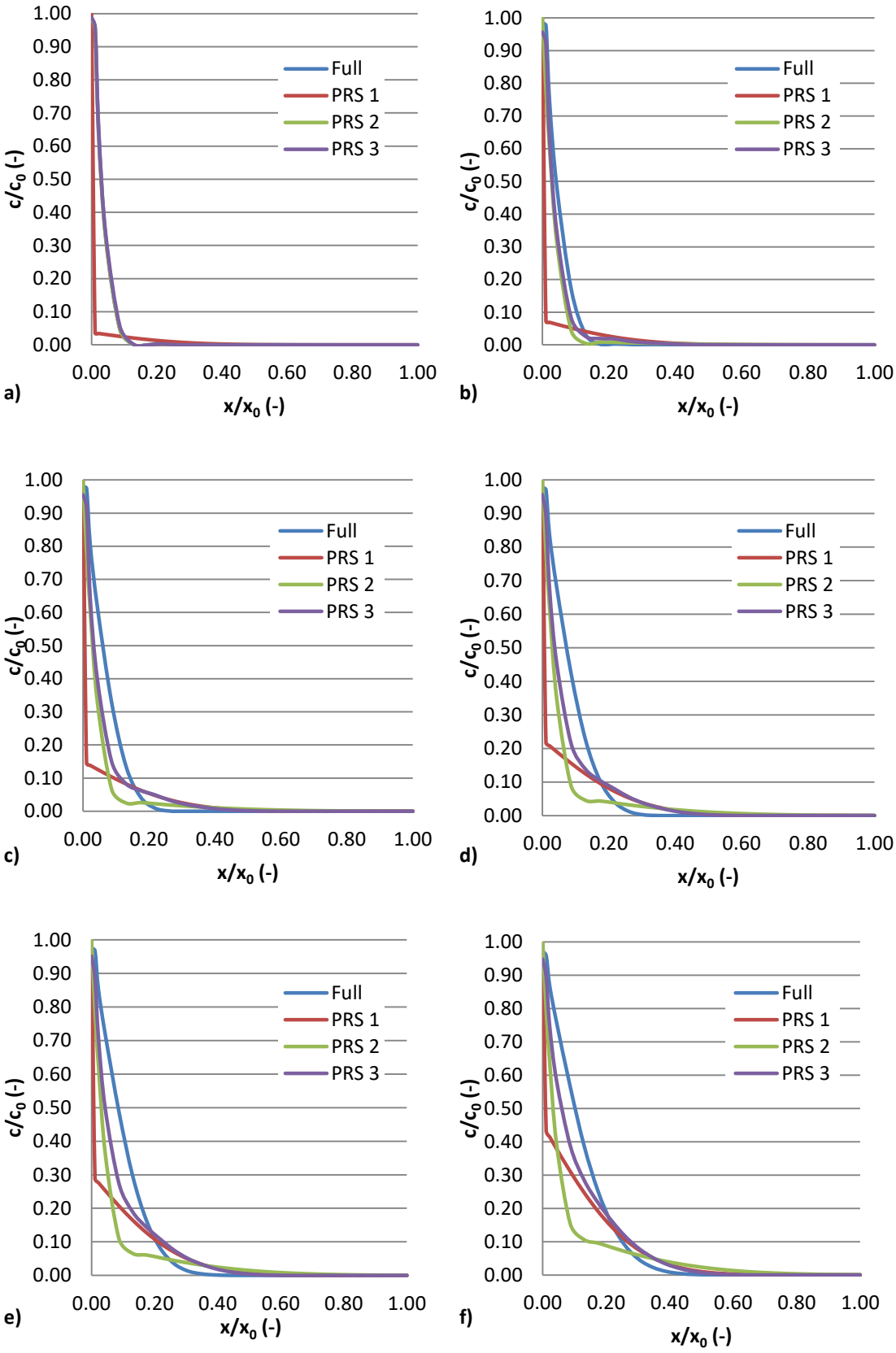

Figure A5 - Concentration profiles predicted by full model and PRS 1-3 (t=24 hours) species number: a) *1*, b) *2*, c) *3*, d) *4*, e) *5* and f) *6*

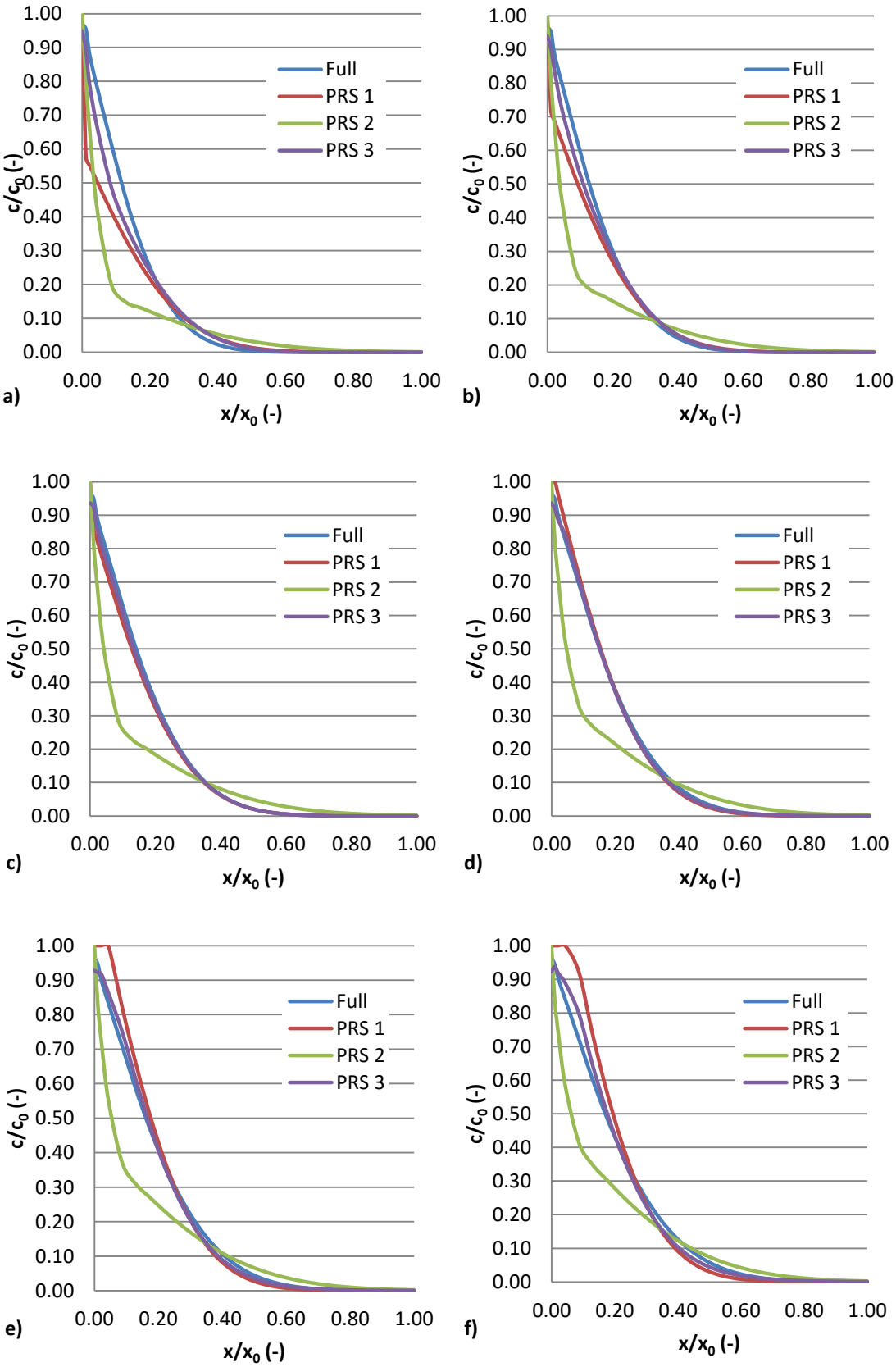

Figure A6 - Concentration profiles predicted by full model and PRS 1-3 (t=24 hours) species number: a) *7*, b) *8*, c) *9*, d) *10*, e) *11* and f) *12*

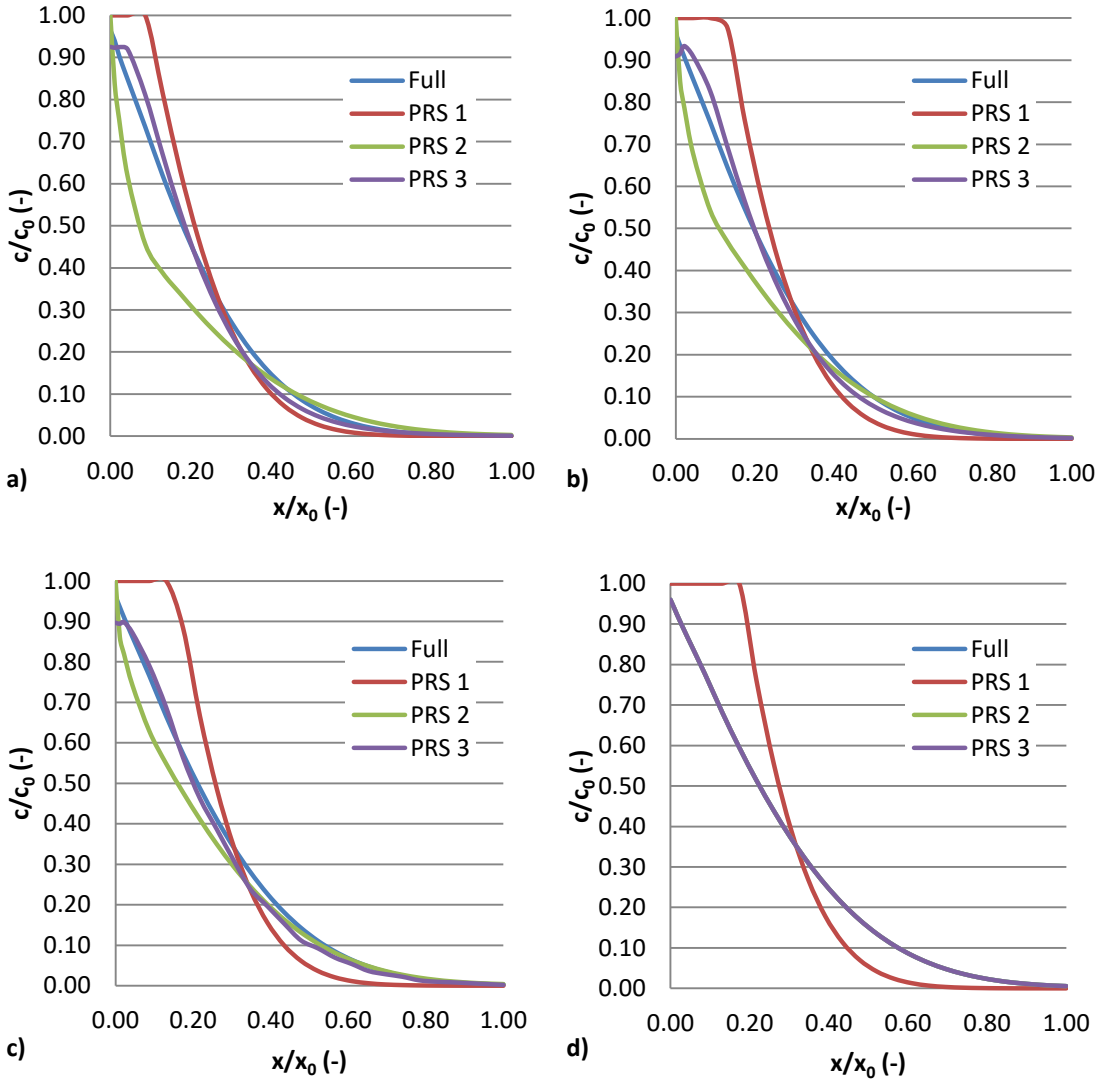

Figure A7 - Concentration profiles predicted by full model and PRS 1-3 (t=24 hours) species number: a) *13*, b) *14*, c) *15* and d) *16*

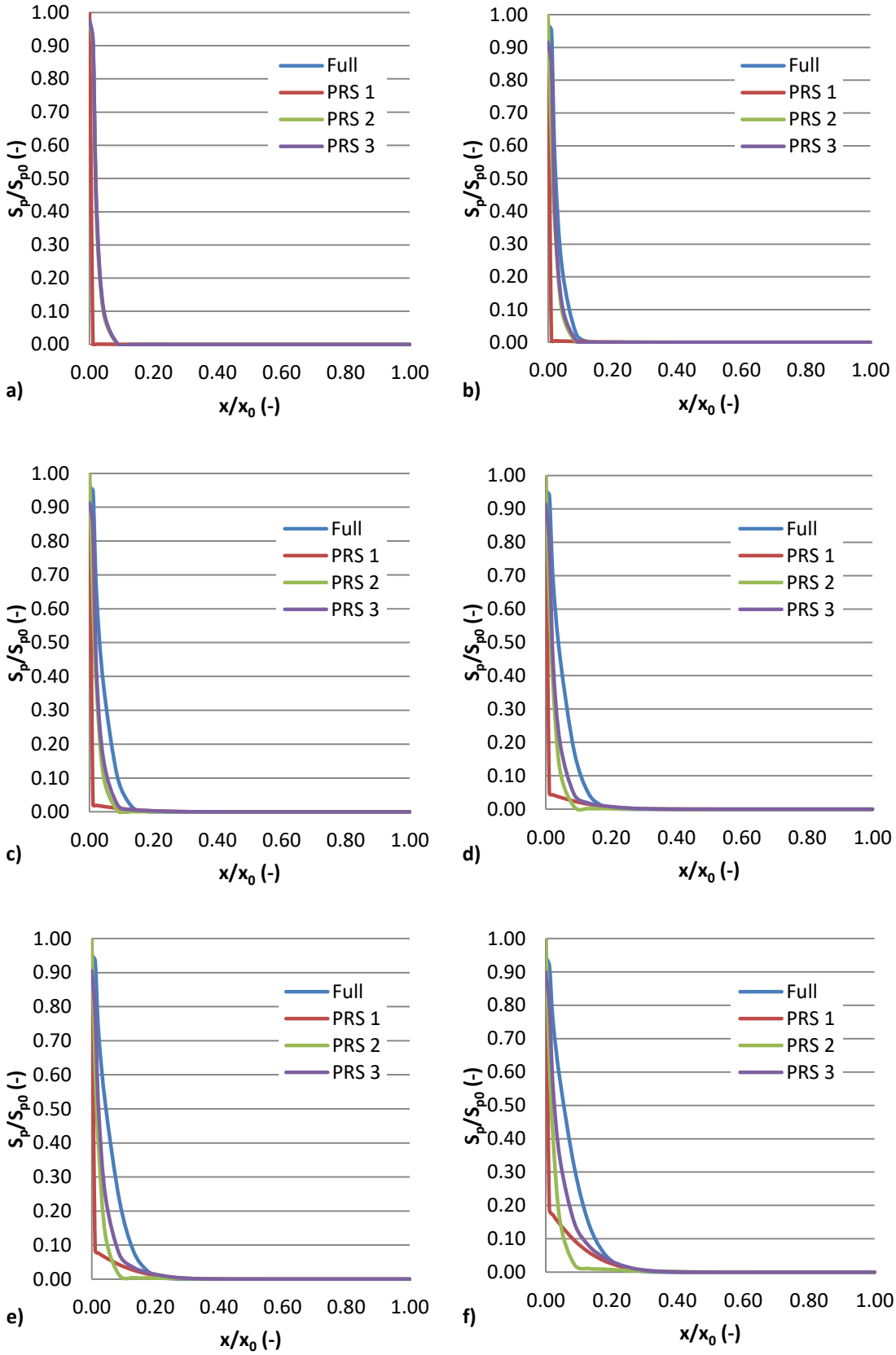

Figure A8 - Sorbed mass profiles predicted by full model and PRS 1-3 (t=24 hours) species number: a) *1*, b) *2*, c) *3*, d) *4*, e) *5* and f) *6*

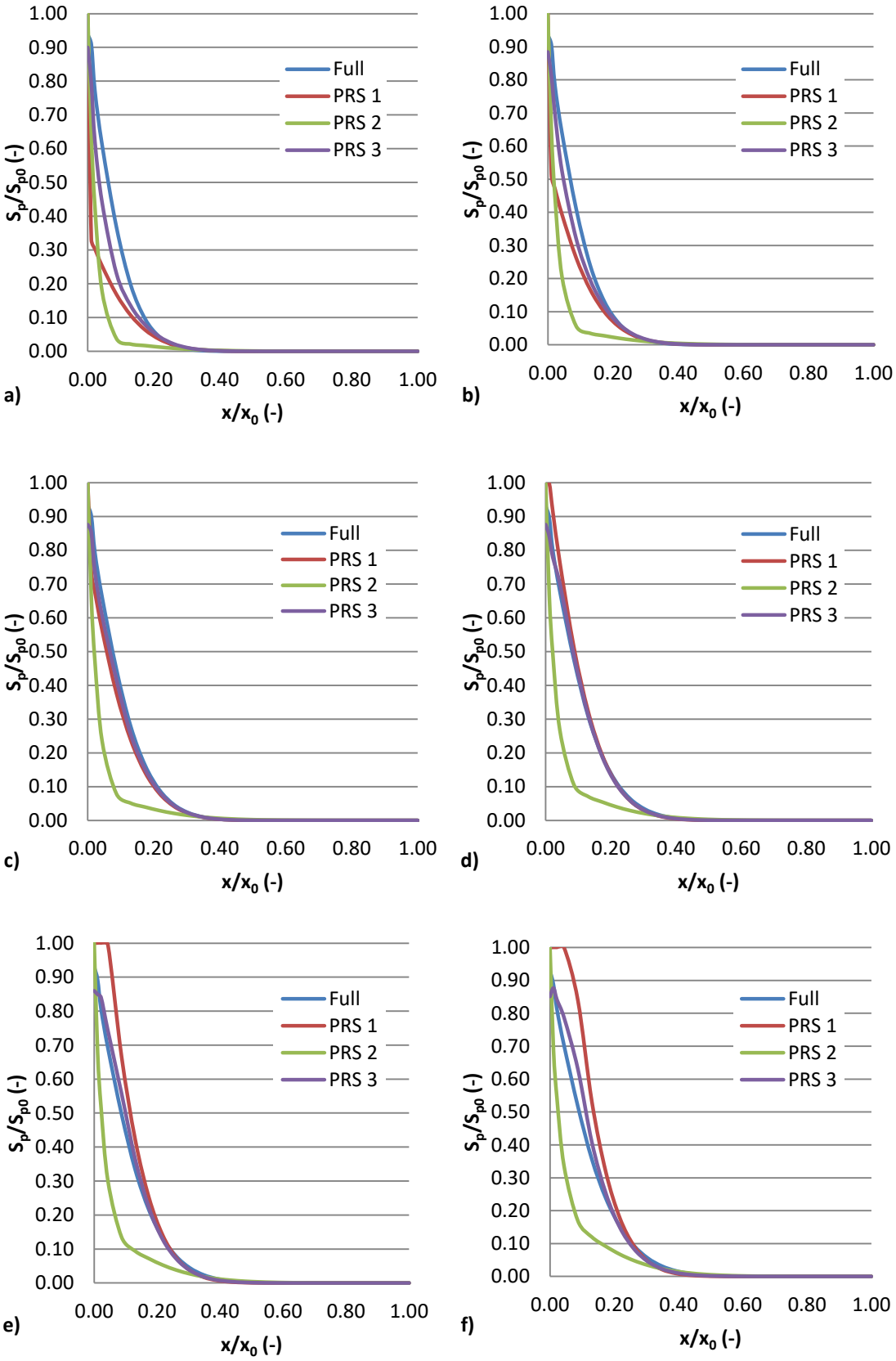

Figure A9 - Sorbed mass profiles predicted by full model and PRS 1-3 (t=24 hours) species number: a) *7*, b) *8*, c) *9*, d) *10*, e) *11* and f) *12*

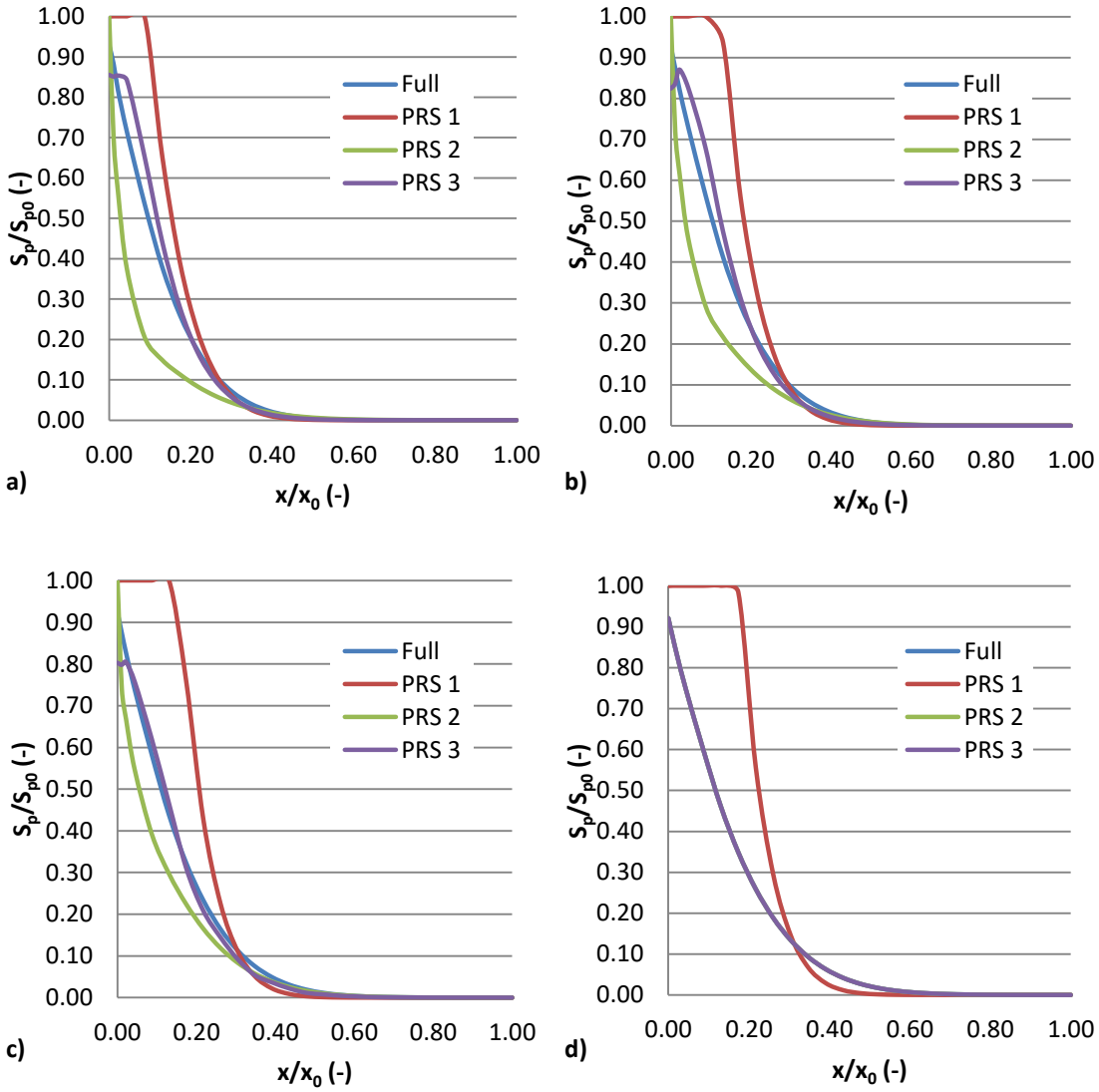

Figure A10 – Sorbed mass profiles predicted by full model and PRS 1-3 (t=24 hours) species number: a) *13*, b) *14*, c) *15* and d) *16*

PRS 2 – Results over Valid Range for Advective-Diffusive-Reactive Problem

In Chapter 7 section 7.2.2 the range of applicability of the PRSs was investigated. In order to determine the maximum range over which PRS 2 is valid, different indicator species were tested. Figures A11, A12, A13, A14, A15 & A16 show the predicted profiles for the applicable range for PRS 2. A reminder of the boundary conditions of the advective diffusive reactive case can be seen in Table A5.

Table A5 – Boundary conditions

Boundary	Boundary Type	Values
LHS	Cauchy	*RH=100 %, T=293 K, c=0.001 kg/kg**
Bottom	Sealed	-
RHS	Cauchy	*RH=60 %, T=293 K, c=0.0 kg/kg**
Top	Sealed	-

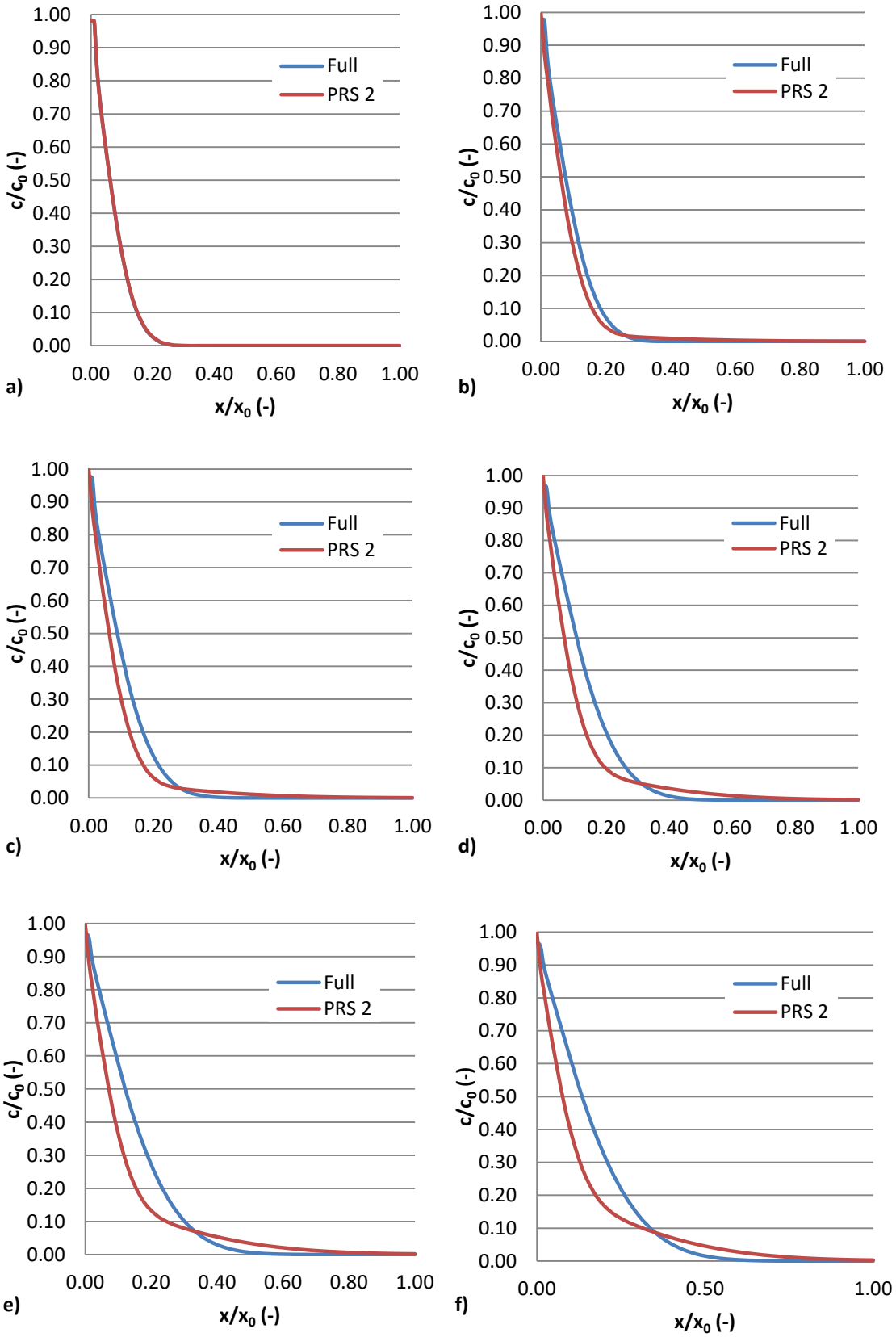

Figure A11 - Concentration profiles predicted by full model and PRS 2 (t=24 hours) species number: a) *3*, b) *4*, c) *5*, d) *6*, e) *7* and f) *8*

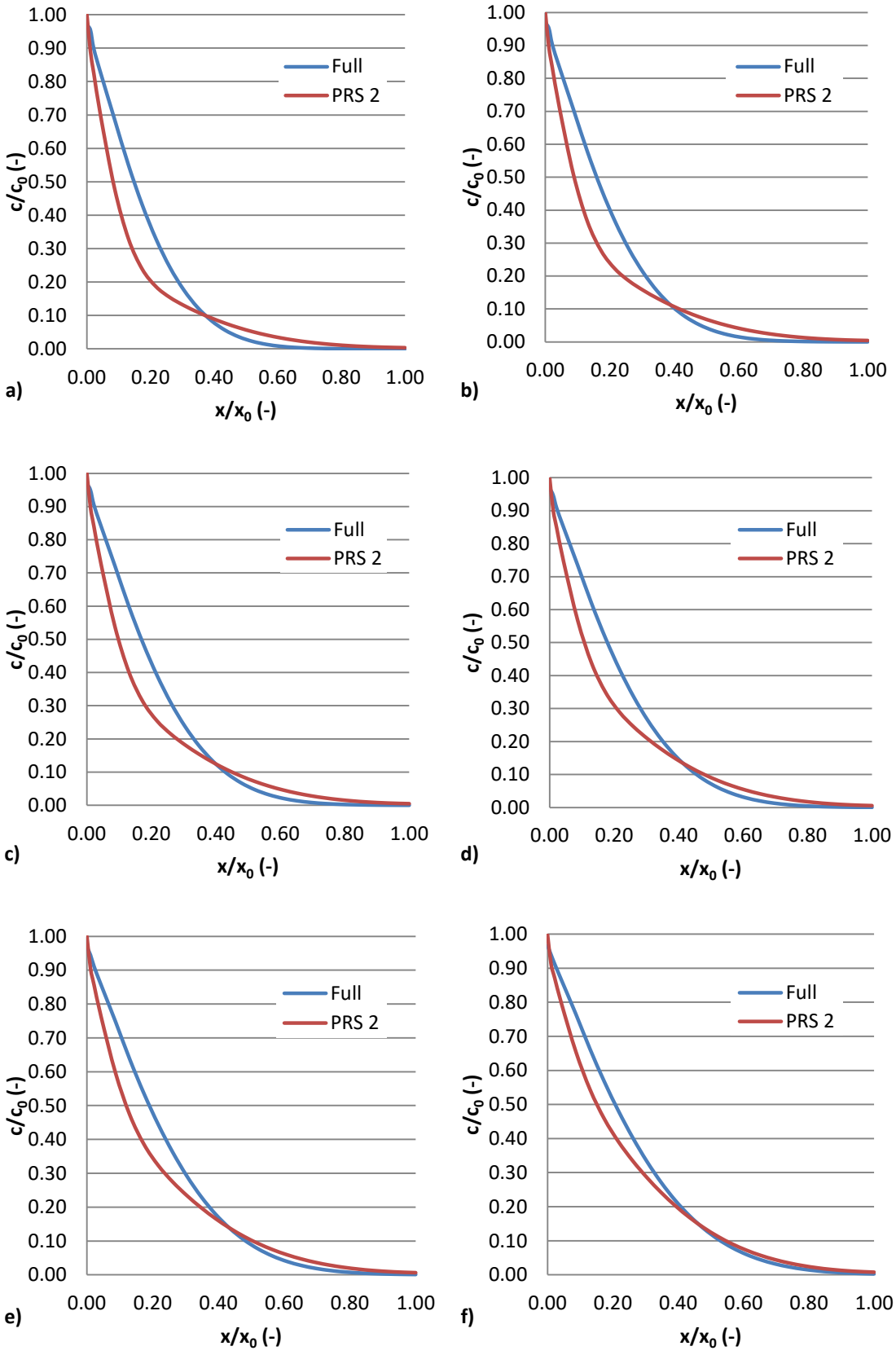

Figure A12 - Concentration profiles predicted by full model and PRS 2 (t=24 hours) species number: a) *9*, b) *10*, c) *11*, d) *12*, e) *13* and f) *14*

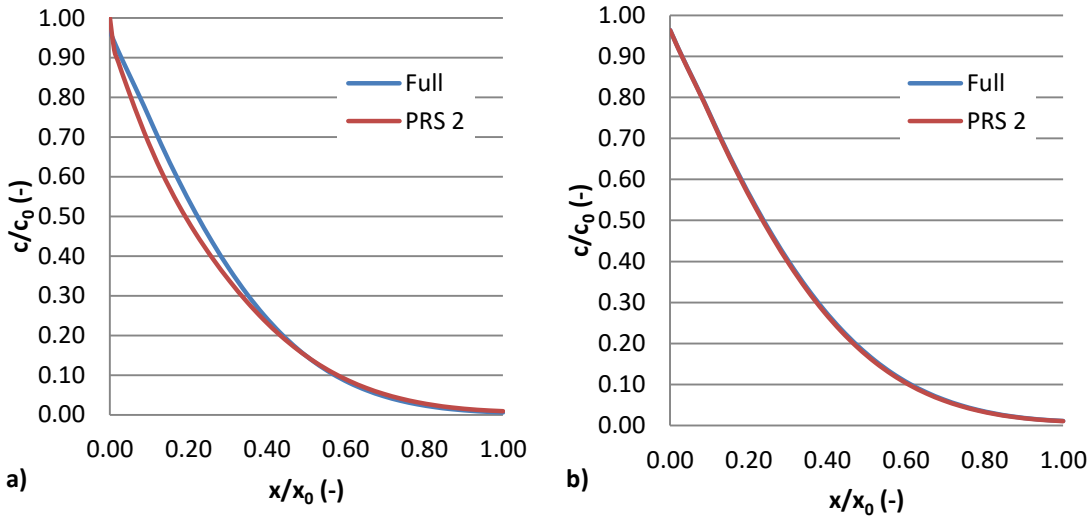

Figure A13 - Concentration profiles predicted by full model and PRS 2 (t=24 hours) species number: a) *15* and b) *16*

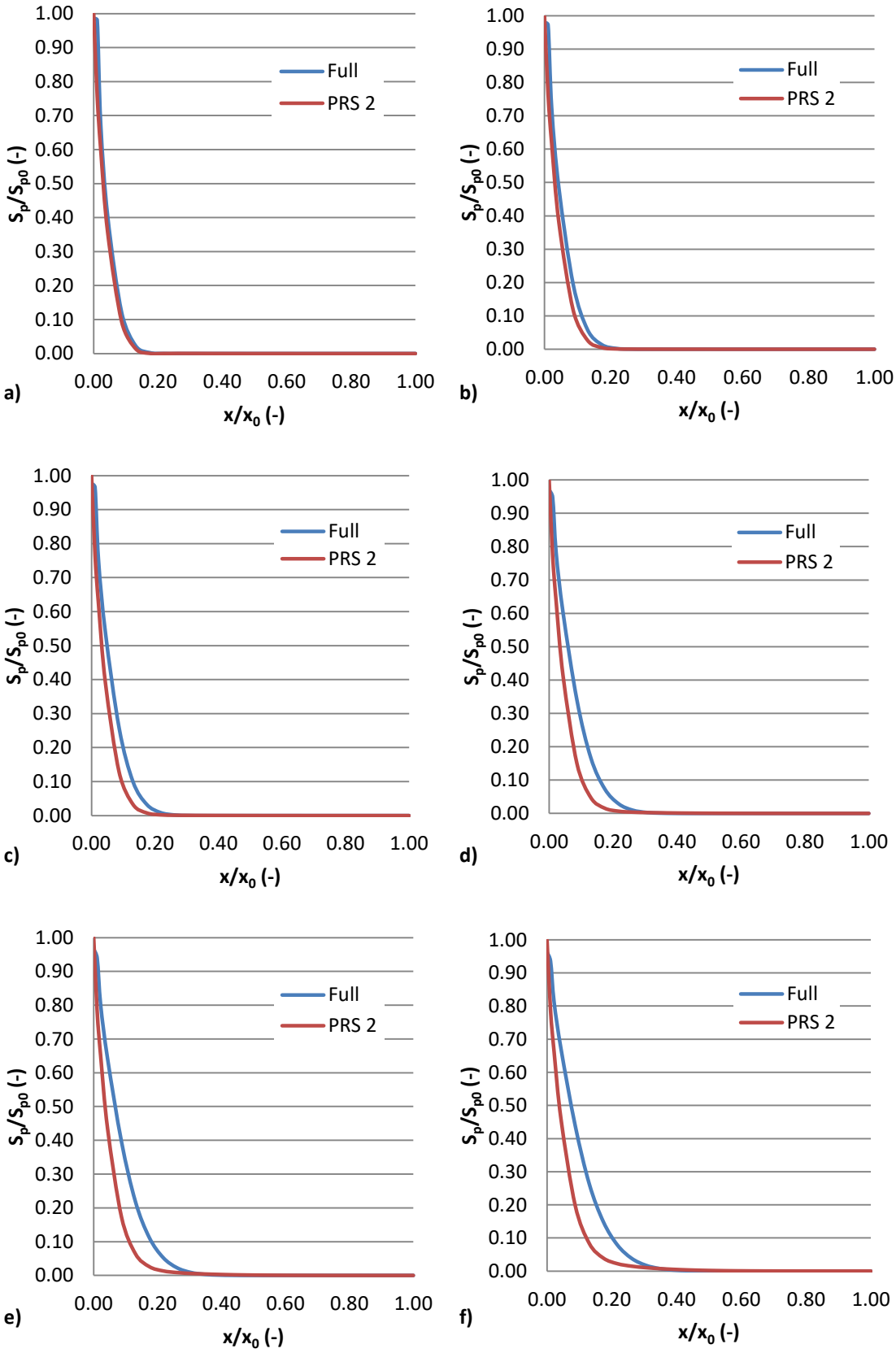

Figure A14 - Sorbed mass profiles predicted by full model and PRS 2 (t=24 hours) species number: a) *3*, b) *4*, c) *5*, d) *6*, e) *7* and f) *8*

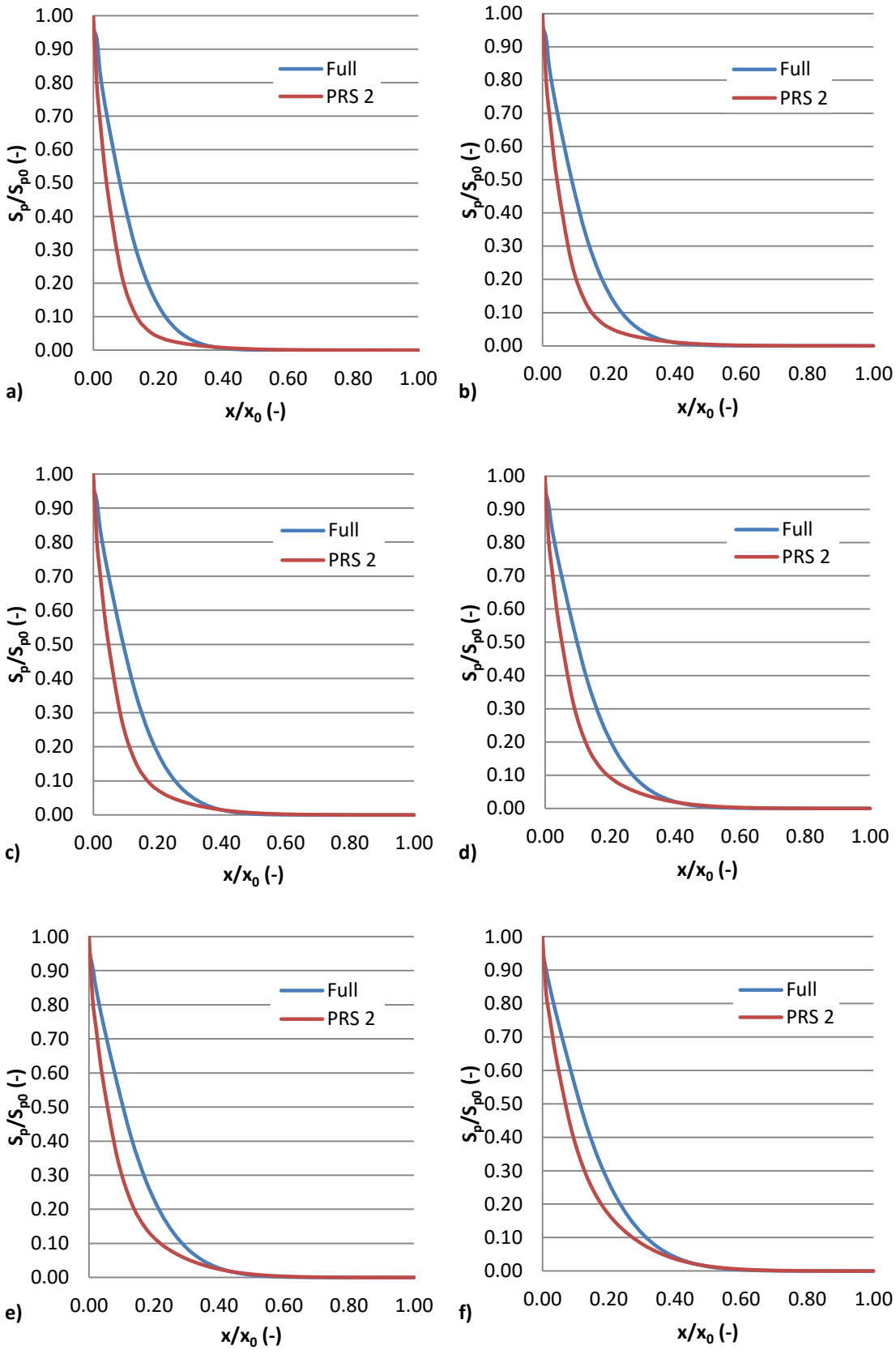

Figure A15 - Sorbed mass profiles predicted by full model and PRS 2 (t=24 hours) species number: a) *9*, b) *10*, c) *11*, d) *12*, e) *13* and f) *14*

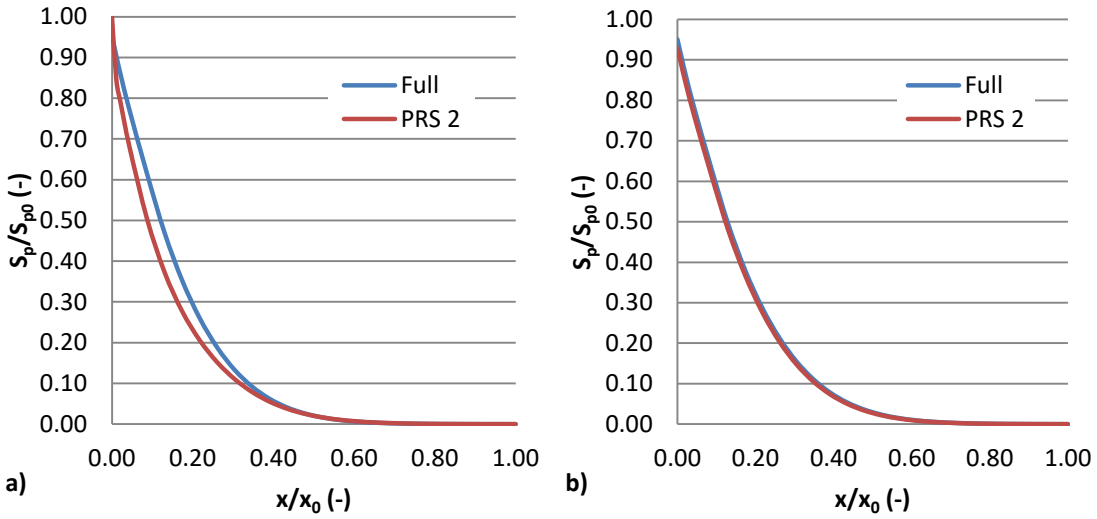

Figure A16 – Sorbed mass profiles predicted by full model and PRS 2 (t=24 hours) species number: a) *15* and b) *16*

Verification Example 3 Results

This section will present the remaining results of the verification example 3, detailed in Chapter 7 section 7.3.3. A reminder of the problem geometry and finite element mesh can be seen in Figure A17, whilst the boundary conditions can be seen in Table A6.

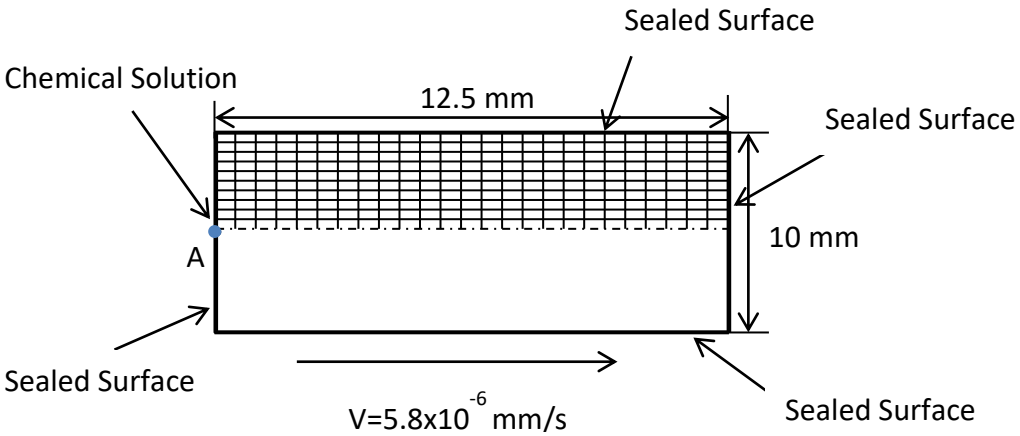

Figure A17 – Finite element mesh and problem geometry (not to scale)

Table A6 – Boundary conditions

Boundary	Boundary Type	Values
LHS	Cauchy	*RH=100 %, T=293 K, c**
Bottom	q=0	-
RHS	Sealed	-
Top	Sealed	-

*See chemical parameters table

The model and chemical parameters used in the model can be seen in Table A7 and Table A8 respectively.

Table A7 – Model parameters

Parameter	Value
n	0.3
$\gamma_c\ (kg/m^2s)$	1e-4
$\omega_c\ (W/m^2K)$	8.0

Table A8 – Chemical parameters

Species	Initial Conc. (kg/kg)	Boundary Conc. (kg/kg)	D_{mol} $(10^{-9}\ m^2/s)$	Eq.	k_a (10^{-7})	k_d (10^{-8})	λ
H^+	0.000028	0.00005	9.311	r_1	2.6	29.6	0.61
Ca^{2+}	0.0003164	0.00048	0.792	r_2	0.6	8.67	0.2
Mg^{2+}	0.00102303	0.001944	0.706	r_3	1.4	9.0	0.07
HCO_3^-	0.00061	0.0000305	1.185	r_4	2.8	2.0	0.11
Al^{3+}	0.000837	0.00135	0.541	r_5	2.1	6.0	0.43
SO_4^2	0.016896	0.024	1.065	r_6	0.425	74.0	0.35
Fe^{3+}	0.00199206	0.00279	0.604				
K^+	0.00006123	0.000078	1.957				
Cl^-	0.0010295	0.001775	2.032				
Na^+	0.0018515	0.000345	1.334				
SiO_2	0.015	-	-				

The concentration profiles along the y axis -obtained by taking a cut along line A-A seen in Figure A18- as predicted by the full model and PRS 3 can be seen in Figures A19 & A20, whilst the sorbed mass profiles can be seen in Figures A21 & A22. Finally the correlation plots can be seen in Figure A23.

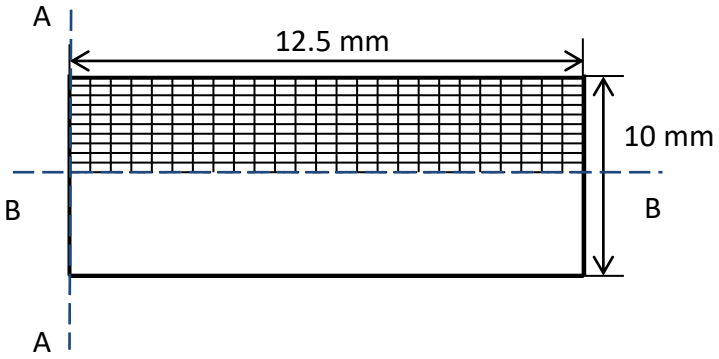

Figure A18 - Problem geometry and cut lines

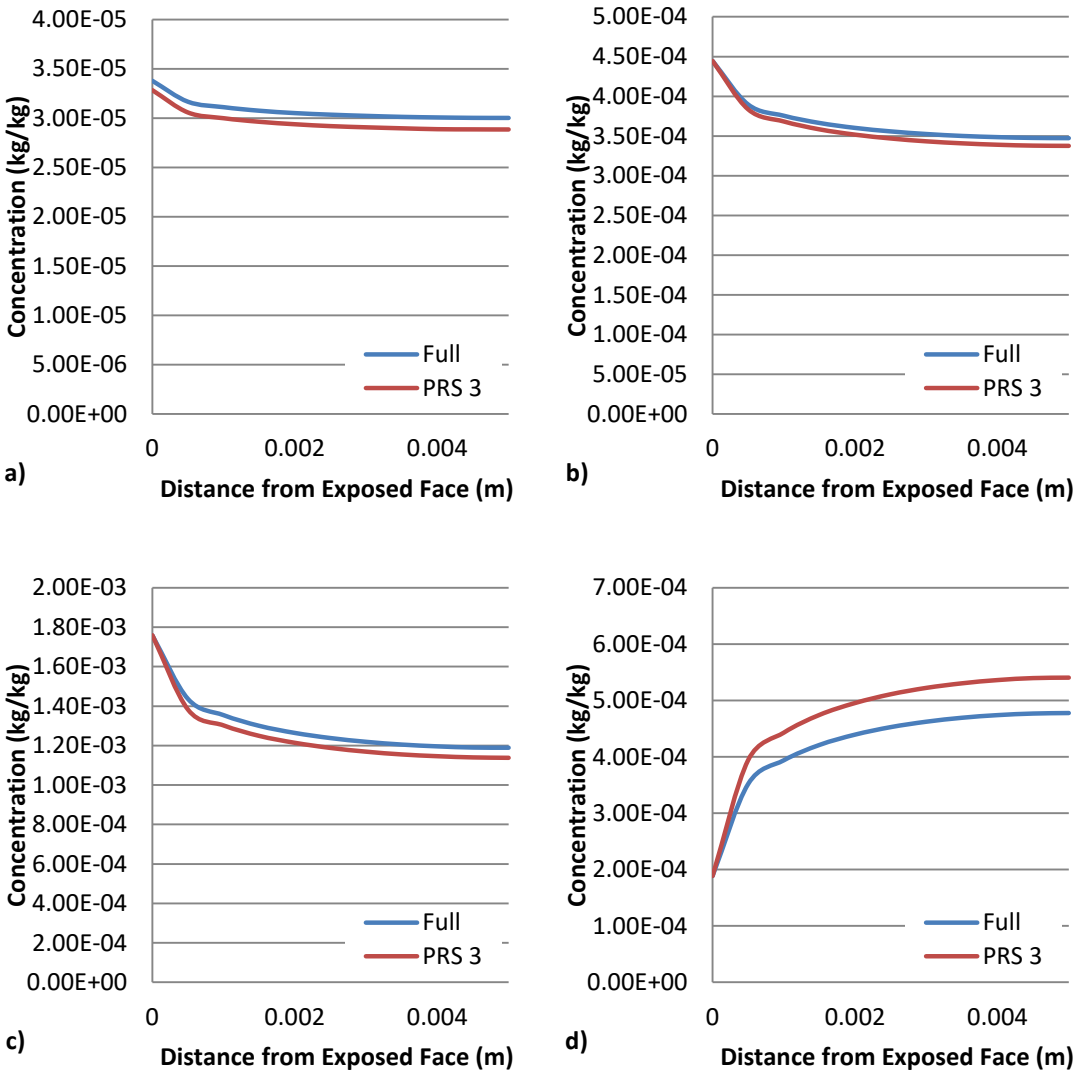

Figure A19 - Concentration profiles (taken along cut line A-A) predicted by the full model and PRS 3 (t=10 hours) a) H^{+}, b) Ca^{2+}, c) Mg^{2+} and d) HCO_3^{2-}

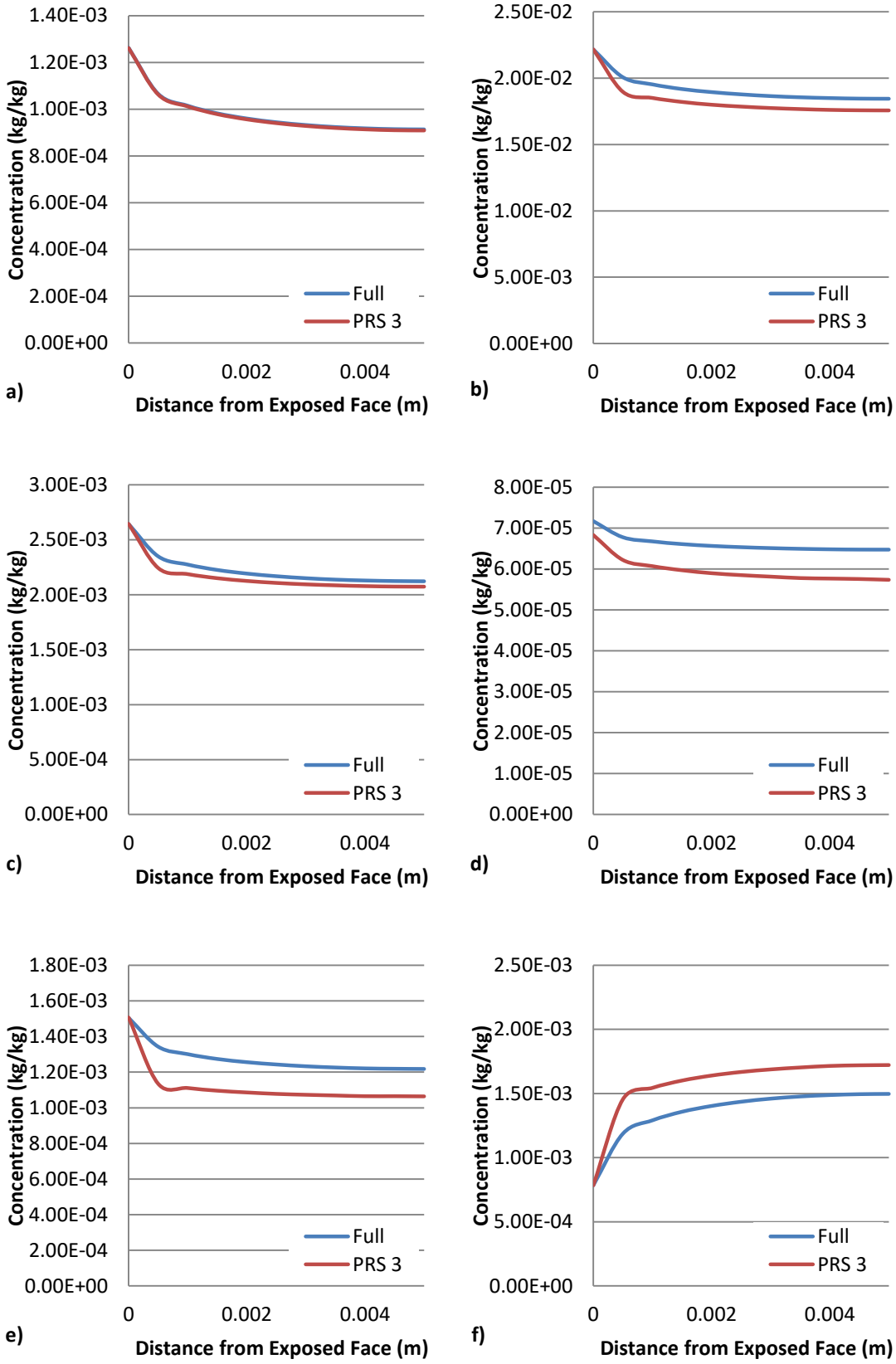

Figure A20 - Concentration profiles (taken along cut line A-A) predicted by the full model and PRS 3 (t=10 hours) a) Al^{3+}, b) SO_4^{2-}, c) Fe^{3+}, d) K^{+}, e) Cl^{-} and f) Na^{+}

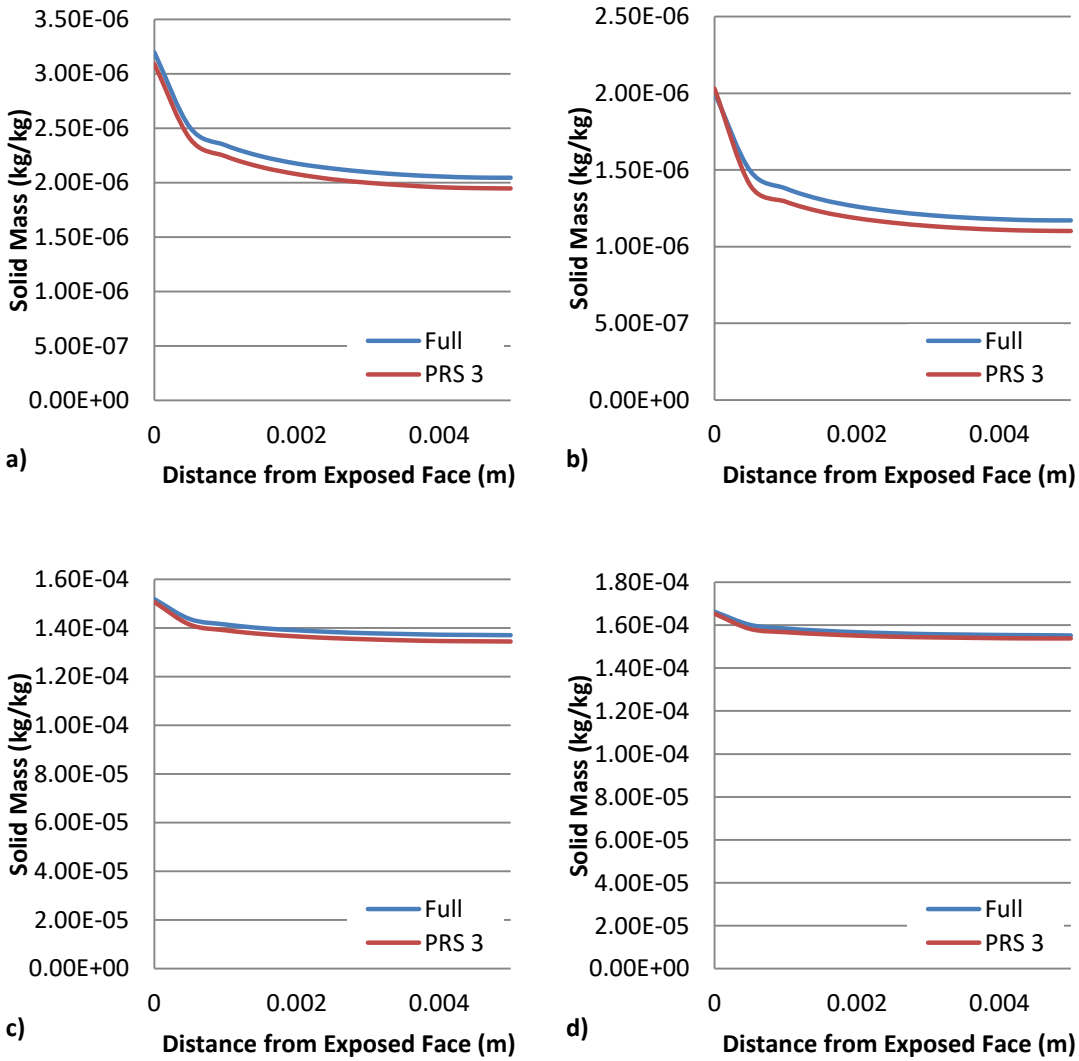

Figure A21 - Solid mass profiles (taken along cut line A-A) predicted by the full model and PRS 3 (t=10 hours) a) $Al(OH)_3$, b) $CaSO_4.2H_20$, c) $K_{0.6}Mg_{0.25}Al_{2.3}Si_{3.5}O_{10}(OH)_2$ and d) $Fe(OH)_3$

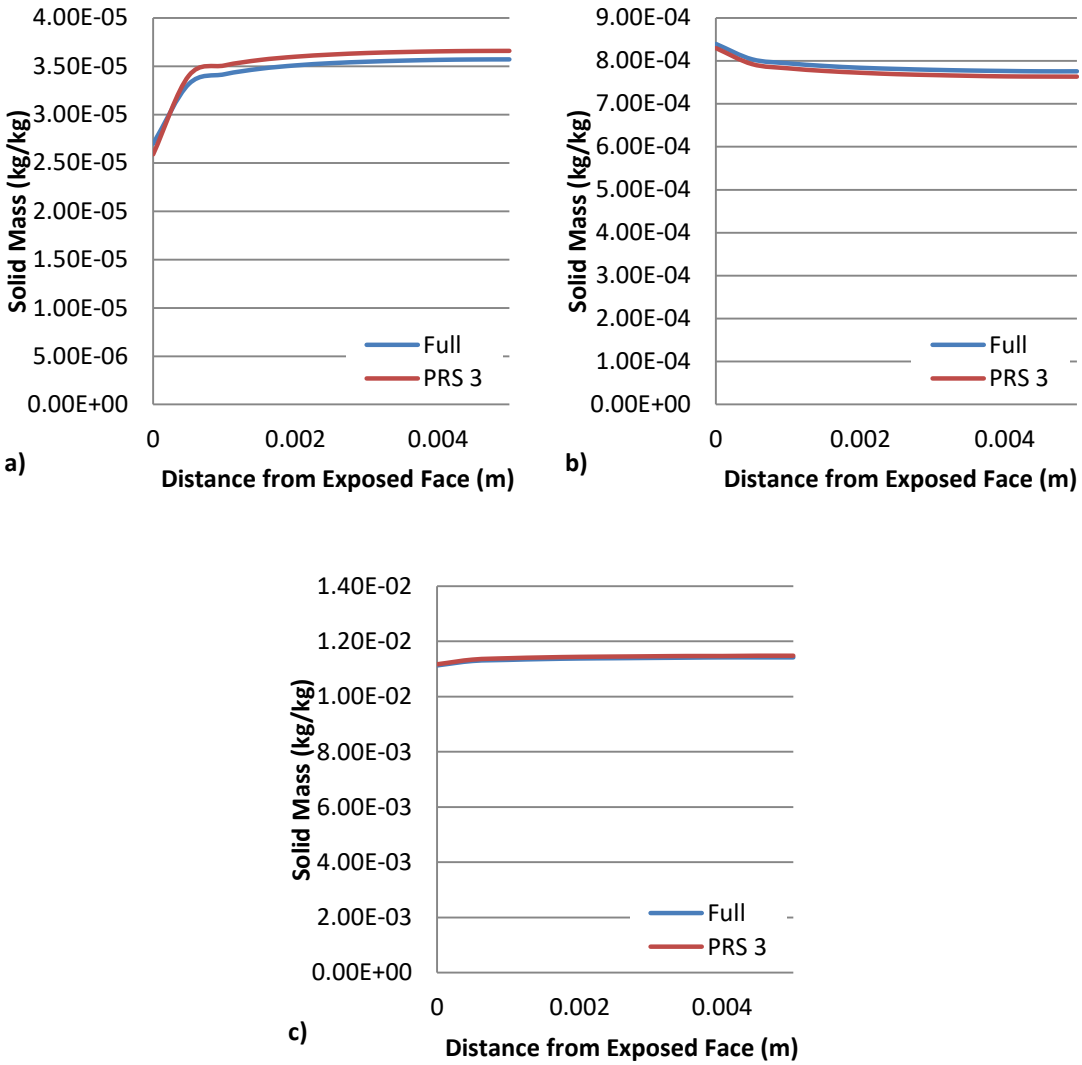

Figure A22 - Solid mass profiles (taken along cut line A-A) predicted by the full model and PRS 3 (t=10 hours) a) $CaCO_3$, b) H_4SiO_4 and c) SiO_2

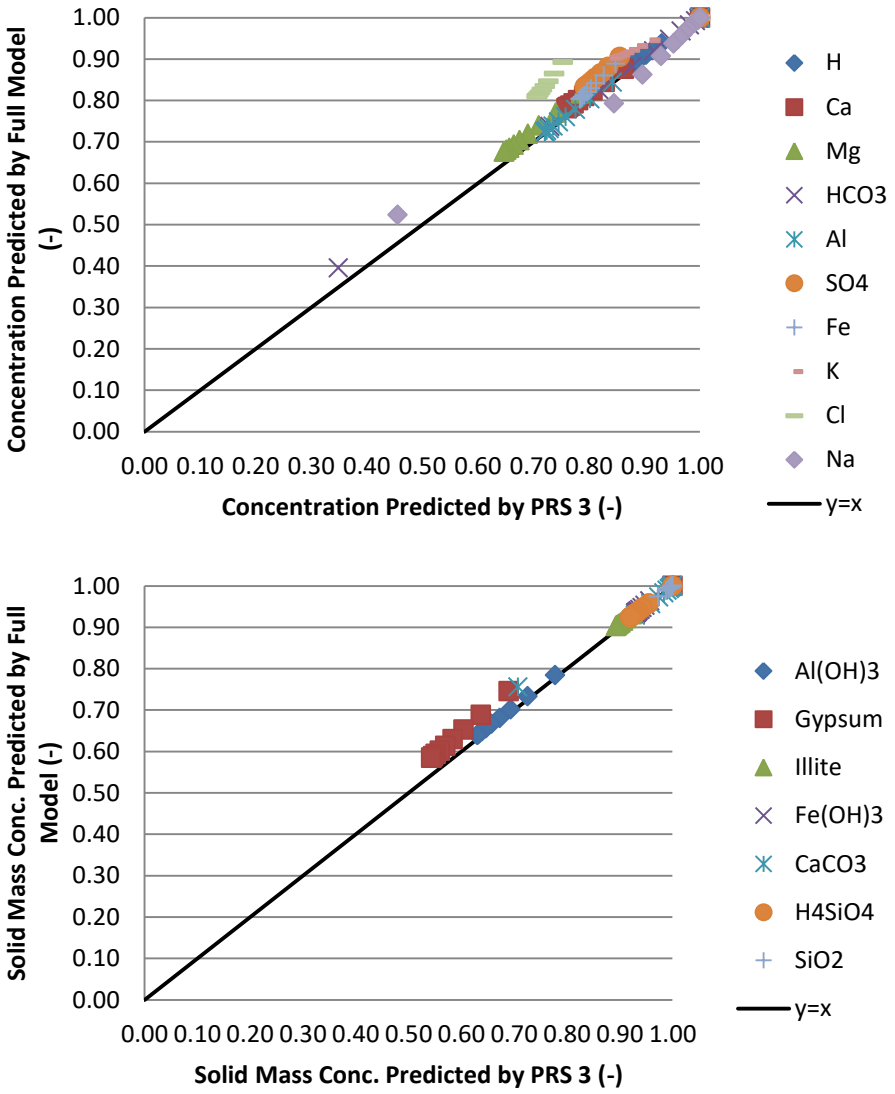

Figure A23 - Correlation of concentrations and solid mass